UNIVERSITY OF CALIFORNIA

Santa Barbara

Characterization and Consequences of Atomic-Scale Catalyst Structure on Performance for Hydrodeoxygenation of Lignin Model Compounds

A dissertation submitted in partial satisfaction of the requirements for the degree Doctor of Philosophy in Chemical Engineering

By

Justin Marlowe

Dissertation Committee:

Professor Phillip Christopher, Co-Chair

Professor Mahdi M. Abu-Omar, Co-Chair

Professor Bradley Chmelka

Professor Peter C. Ford

June 2024

The dissertation of Justin Marlowe is approved.

_____

Bradley Chmelka

_____

Peter C. Ford

_____

Phillip Christopher, Co-Chair

_____

Mahdi M. Abu-Omar, Co-Chair

June 2024

Characterization and Consequences of Atomic-Scale Catalyst Structure on Performance for Hydrodeoxygenation of Lignin Model Compounds

By

Justin Marlowe

Acknowledgments

The chance to acknowledge those in my life who are most responsible for the completion of this chapter is a moment that I have always looked forward to. And yet, I will admit for posterity's sake, this section is the last contribution to be made to this dissertation. Which is to say, simply enough, that putting into words the profound appreciation I have for the assistance, guidance, and support of these individuals is a more daunting task than composing the other 260 pages of this document. All I can ask for is forgiveness when I inevitably fall short of capturing the totality of contributors.

I must, of course, start with my Ph.D. committee members who have sat through the candidacy, annual review, and now Ph.D. defense presentations that have all, invariably, gone longer than scheduled because of my "disinterest in brevity". I am indescribably grateful for the opportunity to have not one, but two, advisors in Phil and Mahdi who have given me their time, attention, advice, and technical experience. Phil and Mahdi gave me the freedom to pursue my curiosities, the freedom to be wrong, and the freedom to be myself. In allowing me these freedoms, they have given me the most holistic learning experience of my life, one that I can only hope to have repaid in a few laughs and a few new scientific insights. To repeat the cliché shared in many an acknowledgment, I have grown as a researcher and a person at the behest of their guidance. Such is the mark of a truly successful academic research group, and I was fortunate enough to be a part of both.

I am also grateful to the other members of my committee, Peter and Brad, who have been continually generous with their time and their suggestions, and to my undergraduate advisor, Dr. George Tsilomelekis, who managed to instill in me a love for catalysis research through a technique (Raman) that is as often frustrating as it is fruitful. I should also thank my first research colleagues, Adam and Trang, who gave their time to mentor an undergraduate who could barely pipette correctly. Regardless, I never felt lesser working alongside them, a lesson I hope I have extended to my own undergraduate assistants.

I can sincerely say that my experience would be inherently less enjoyable without the combined Christopher and Abu-Omar groups that I've worked and laughed alongside during my time at UCSB. This includes Chithra, Greg, Jordan, and Bao, who taught me how to troubleshoot the many instruments that broke in my first few years, which may be the most important skill one can have in research and in life. I hope I have passed this along in some

way to the group members who will follow me, including Anika, Kelsey, Ryan, and Thanh. I am both grateful and always impressed by the impact that the post-docs have had in their short time in our group, including but not limited to, Jae Ha, Samji, and Sylvia.

To those who have not played a direct technical role in this dissertation, I instead turn to the wise adage that once said, “The point of life is love and friendship.” First and foremost on this list is my mother, Kathy, who has been a role model, a friend, a supporter, a provider, a confidant – the list could go on. My mom is a paragon of strength, resilience, intelligence, and compassion, and so I can only be honored when people continue to point out that we look alike.

A special thanks goes to the friends who have tolerated my inconsistent availability and maintained contact with me while living across the country. To PS, who I could never deny considering you are tattooed on me forever - good thing I’d never want to. To APK, who have grown alongside me in ways I never would have expected and braved flights and pandemics to meet me in Lake Tahoe. To Victoria, Thalia, and Sharon, I thank a group project for bringing us together. To Nick, Kat, Tanner, and Karl, who turned a virtual game of Catan in the depth of the pandemic into a long-winded campaign. To Cass and Rachel, my favorite coworkers.

And then there are the people who have been there for me, in person, throughout the twists and turns of this experience - I have them to thank for my sanity and good humor. In Zach, Emily, and Kevin I have found friends, roommates, and intimidatingly successful scholars – to find roommates with one of these traits would be rare, but to find all three is a once-in-a-lifetime, lottery kind of luck. Daniel, Graham, Starry, and Isabel have been there from San Clemente to Mt. Pinos and everywhere in between. Alyssa and Arik have shared a few M.Special beers, caught a couple of party waves, and appreciated some good rocks with me – until next time.

And finally, to Bridgette, who has made real the abstract from the moment I met her. There are so preciously few reasons that I would choose to continue to live in a semi-arid climate with no autumn and no snow – I am glad that you are one of them.

VITA of Justin Marlowe

June 2024

Education

June 2024 University of California Santa Barbara

Ph.D., Chemical Engineering

May 2019 Rutgers University

B.S., Chemical Engineering Summa Cum Laude

Publications

In Press

1. Beck, A., **Marlowe, J.**, Gordon, M., Christopher, P. Is there a discernable photochemical effect beyond heating for visible photon mediated NH3 decomposition over Ru/Al2O3? *J. Phys. Chem. C,* **2024**, 128, 21, 8590-8600.
2. **Marlowe, J.**, Deshpande, S., Vlachos, D., Abu-Omar, M. M., Christopher, P. Effect of Dynamic and Preferential Decoration of Pt Surfaces by WO_x on Hydrodeoxygenation Reactions. *J. Am. Chem. Soc*., **2024**, 146, 20, 13862-13874.
3. Barraza Alvarez, I., Le, T., Hosseini, H., Samira, S., Beck, A., **Marlowe, J.**, Montemore, M., Wang, B., Christopher, P. Bond Selective Photochemistry at Metal Nanoparticle Surfaces: CO Desorption from Pt and Pd. *J. Am. Chem. Soc.,* **2024**, 146, 18, 12431-12443.
4. Lin, Z., Deshpande, S., Denny, S. R., Porter, W. N., Wang, C., **Marlowe, J.**, Christopher, P., Zheng, W., Caratzoulas, S., Vlachos, D. G., Chen, J. G. Mechanistic Understanding of Ring-Opening of Tetrahydrofurfuryl Alcohol over WO_x-Modified Pt Model Surfaces and Powder Catalysts. *ACS Catalysis,* **2023**, 13, 12, 8014-8024.
5. **Marlowe, J.**, Ford, P., Abu-Omar, M. M., Christopher, P. Structure sensitivity in Pt-catalyzed hydrodeoxygenation of multi-oxygenated lignol model compounds. *Cat. Sci. Tech.,* **2023**, 13, 5662-5678.
6. Gomez, L. A., Babarik, R., Komarneni, M. R., **Marlowe, J.**, Salvati-fard, T., D'Amico, A. D., Wang, B., Christopher, P., Crossley, S. P. Selective Reduction of Carboxylic Acids to Aldehydes with Promoted MoO3 Catalysts. *ACS Catalysis,* **2022**, 12, 11, 6313-6324.

7. **Marlowe, J.**, Acharya, S., Zuber, A., Tsilomelekis, G. Characterization of Sulfated SnO2-ZrO2 Catalysts and Their Performance on the tert-Butylation of Phenol. *Catalysts,* **2020**, 10, 7, 726.
8. **Marlowe, J.**, Tsilomelekis, G. Accessible and interactive learning of spectroscopic parametrization through computer-aided training. *J. Chem. Education,* **2020**, 97, 12, 4527-4532.
9. Li, Z., Zuber, A., Wang, X., **Marlowe, J.**, Vekeria, A., Lu, Y., Zhang, H., Tsilomelekis, G. Towards the coupling of microbial biosynthesis and catalysis for the production of alkylated phenolic compounds. *AIChE Journal,* **2020**, 66, 12, 16547.

In Preparation

1. **Marlowe, J.**, Abraham, L., Zakem, G., Jalil, A., Christopher, P. Particle-Size Dependent Penetration Depth of DRIFTS and Consequences for Temperature-Programmed Techniques.
2. **Marlowe, J.**, Abu-Omar, M. M., Christopher, P. Determination of Oxide Role in HDO over MO_x/Pt Catalysts: Spectator or Active Site?
3. Lee, J., Zang, W., **Marlowe, J.**, Pan, X., Christopher, P. Dynamic Burial of Isolated Pt Between TiO2 Grains

Presentations

1. 28th Meeting of the North American Catalysis Society
2. 2022 National Meeting of the American Institute of Chemical Engineering
3. 18th Annual Clorox-Amgen Graduate Student Symposium
4. UCSB Chemical Engineering 1st Year Research Symposium
5. 2019 National Meeting of the American Institute of Chemical Engineering

Awards

1. National Science Foundation Graduate Research Fellowship Program
   Honorable Mention
2. North American Catalysis Society Kokes Award
   Honorable Mention
3. UCSB Dow Discovery Fellowship
   Finalist

4. Rutgers Department of Chemical Engineering Researcher-Scholar Award
5. Rutgers CBE Annual Research Symposium, 1st Place

Abstract

Characterization and Consequences of Atomic-Scale Catalyst Structure on Performance for Hydrodeoxygenation of Lignin Model Compounds

by

Justin Marlowe

A variety of technical, economic, and societal factors require a global shift in the consumption of goods and the production of energy towards routes that are broadly more sustainable. A shift toward the use of biomass as a feedstock for carbon-based chemicals is one promising component of such a future shift, spurred on recently by rapid electrification of transportation and energy sectors. Lignin, a component of biomass that is currently underutilized as waste generated during cellulose production, represents a promising, drop-in replacement for current carbon feedstocks such as petroleum for the production of aromatic monomers such as benzene, toluene, and xylene (BTX). This route of lignin-to-chemicals would, in principle, provide a net-zero carbon emissions source of these high-value chemicals currently produced on the scale of hundreds of millions of tons annually across the globe. However, one of the primary technical challenges preventing the adoption of such a process is the removal of oxygen from lignin-derived monomers through catalytic hydrodeoxygenation (HDO). Oxygenated lignin monomers provide a range of reactive functionalities that are activated by the catalysts typically explored to date, namely supported transition metal nanoparticles. Thus, high selectivity of catalyst activation towards solely C-O bonds is essential to avoid off-target product formation.

Recently, a class of catalysts involving noble metal-reducible metal oxide interactions has been identified as promising for the HDO of lignin-derived compounds. Despite initial reports of high selectivity for C-O bond cleavage over other competing reactions such as aromatic ring hydrogenation, there remains a lack of fundamental understanding of the active site, hampered primarily by vast uncertainty regarding the mechanism of deoxygenation, the structure of the catalysts under reaction conditions, and the subsequent structure-activity relationships. While it is generally known that the reduced oxide decorates the metal nanoparticle surfaces, it is unclear whether or not the oxide participates directly in catalysis either as the active site itself, a modifier to the base metal reactivity, or solely as a spectator or inhibitor. Because of this uncertainty, a number of plausible mechanisms have been proposed, including direct deoxygenation, acid-catalyzed dehydration, and Mars-van Krevelen-type deoxygenation, among others.

This work contained within this dissertation seeks to clarify the role of the reducible metal oxide as it pertains to HDO catalysis, specifically, but also to expound upon the understanding of metal-oxide interactions more broadly, especially concerning the so-called strong metal-support interaction (SMSI). The development of a model catalyst system with high tunability which facilitates a number of different characterization techniques to probe catalyst structure and develop structure-activity relationship is critical to this goal. Through this developed catalyst framework, this dissertation explores the effects on HDO catalysis of nanoparticle size (Chapter 2), the metal oxide surface density (Chapter 3), metal oxide identity (Chapter 4), and support identity (Chapter 5).

Through a combination of *in situ* and *ex-situ* characterization techniques (DRIFTS, TEM, chemisorption) and measured reactivity of diverse model compounds for lignin, the role

of MO_x promotion of Pt in HDO is clarified. MO_x decoration on the surfaces of metal sites serves primarily as a site-blocker, selectively inhibiting the undesired aromatic hydrogenation by limiting the number of metal ensembles large enough to facilitate planar aromatic adsorption through the preferential decoration of these ensembles. However, the oxide-metal interface formed during catalysis also plays a lesser role in facilitating deoxygenation through the conversion of metastable surface intermediates. The results suggest that both modified and unmodified Pt catalysts transit through a shared mechanism in the HDO of phenolics, with tautomerization of the phenolic functionality being an essential characteristic to facilitate deoxygenation under the conditions studied.

Table of Contents

Chapter 1: Introduction

1.1 Motivation and Rationale

The global reliance on fossil fuels, including coal, oil, and natural gas, for transportation, heating, and electricity has resulted in the emission of at least 450 billion tons of carbon into the atmosphere since the dawn of the industrial age[1]. This unfettered emission has overwhelmed the ecologic and geologic processes responsible for carbon sequestration, resulting in current atmospheric CO_2 levels above 400 ppm which continue to rise. Continued emissions at this scale are predicted to cause average global temperatures to rise well above the 2˚C goal set forth by the Paris Agreement, resulting in climatic change that will necessarily result in significant global hardship, likely shouldered disproportionately, at least initially, by the poorest groups across the world who have contributed the least to total anthropogenic CO_2 emissions to date. To mitigate the worst of these consequences, collaborative and sweeping efforts are needed to simultaneously reduce or eliminate net anthropogenic CO_2 emissions and explore strategies to actively reduce current CO_2 levels, such as carbon capture and storage (CCS)[2,3], among other approaches.

One avenue that is essential to this goal is the growth of alternative energy resources such as wind, solar, hydroelectric, and nuclear energies in order to reduce the net CO_2 emissions associated with electricity production and transportation. Models suggest that by 2050, electric vehicles could account for up to 30% of transportation energy and renewables could provide up to 60% of all energy generation[4]. Electric vehicle growth in the United States has outpaced most estimates to date, indicating that economic approaches such as tax breaks and technical breakthroughs enabling the production of historically inexpensive batteries have been successful in accelerating uptake. Wind and solar have similarly outperformed

expectations. The overall result is that energy usage is expected to significantly shift towards electricity generation over the next few decades, signaling a large shift in both production and consumption routes.

Though this progress is necessary and exciting, it is crucial to consider the butterfly effects that these shifts to our global energy landscape will have. The petroleum refining industry today is highly integrated and efficient, conserving >95% of the input carbon atoms in crude oil in final products and achieving total energy efficiencies (η):

$$\eta = \frac{Energy\ Density\ of\ Products}{Energy\ Density\ of\ Crude\ Oil + External\ Energy\ Used}$$

of almost 90%[5]. In large part, this efficient design stems from the diverse portfolio of products that have been developed to take advantage of what was (and still is, albeit to a progressively lesser degree) a relatively inexpensive and plentiful resource. These diverse products include liquid petroleum natural gas (LPNG), gasoline, jet fuel, petrochemicals, and higher-boiling fractions such as asphalt, highlighting that crude oil provides not only primary use products such as transportation fuels but also chemical feedstocks such as petrochemicals which find their way into nearly every consumer product manufactured today.

Disrupting this efficiency through the growth of renewable energy, however, comes at a cost. Current models suggest that depending on the aggressiveness of carbon taxes and other institutional limitations on CO_2 emissions, demand for petroleum will decline by 20-70% between 2019 and 2050, from ~100 million barrels per day to 75 million barrels per day in the most conservative estimates or only 20 million barrels per day in the most aggressive case of emissions reduction[4]. This drop in projected demand is overwhelmingly caused by the

aforementioned electrification of consumer ground transportation. However, transportation fuels, specifically gasoline and diesel, make up a majority of refinery output, meaning that overall refinery output is predominantly affected by the demand for transportation fuels. Consequently, in response to declining demand for ground transportation fuels, refinery output must decline to avoid a crash in the valuation of crude oil products. Critically, this decline in refinery output will necessarily affect the supply of each product in the petroleum refining pipeline, including the non-transportation components such as petrochemicals and asphalt. Troublingly, the demand for these same components is only expected to rise, counter to the trends of transportation fuels. Figure 1.1a shows the projected demand for crude oil and petrochemicals between 2020 and 2050. It can be seen that while crude oil demand overall falls drastically in all projected scenarios, petrochemical demand only increases as a result of continued industrialization and global population growth. Thus, barring significant and sweeping changes to current refinery models as they exist today, namely, the development of

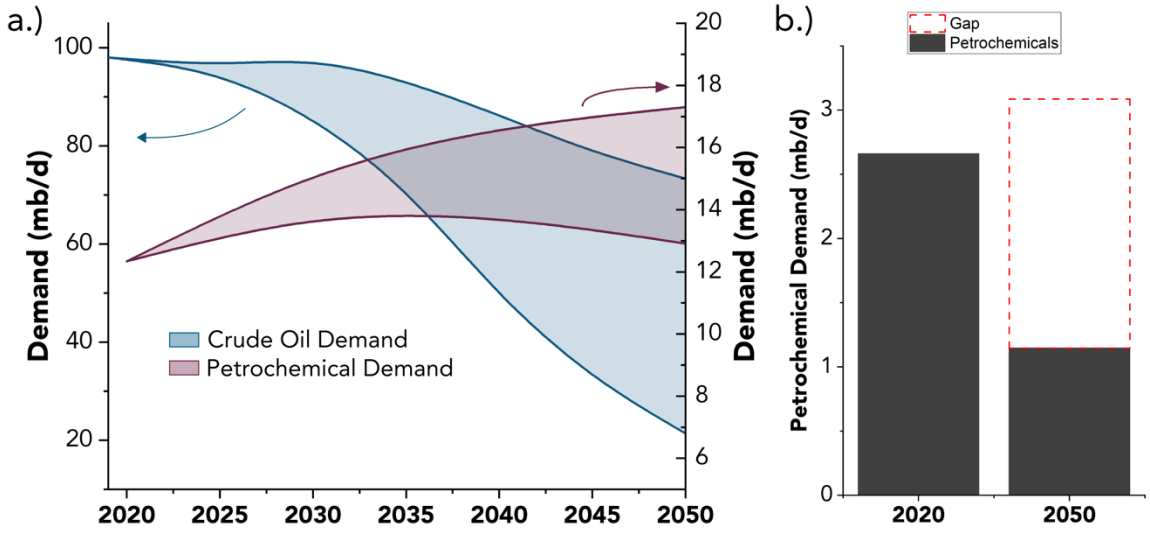

Figure 1.1: (a) Projected trends in crude oil and petrochemical demand between 2020 and 2050 in millions of barrels per day (mb/d). Shaded area represents the bounds of model projections based on conservation or aggressive legislative and technical assumptions, respectively. (b) Projected gap in petrochemical supply created by assuming that the fractional output of crude oil products remains constant. A dropping supply of petrochemicals due to reduced refinery throughput at the same time that petrochemical demand increases creates a gap unfilled by current technologies and feedstocks. Data compiled from Ref. 4.

new processes that can reform ground transportation fuels into higher-value and higher-boiling fractions such as jet fuel, a gap between growing petrochemical demand and shrinking petrochemical supply from crude oil is likely to form (Figure 1.1b).

A similar challenge was recently experienced in the production of propylene, which experienced a so-called "propylene gap"[6]. Domestic declines in refinery throughput due to stagnating demand for gasoline in the 2010s, coupled with a shift to ethane as a primary feedstock rather than propane due to the exploitation of domestic shale gas deposits, resulted in a decline in refinery propylene production. At the same time, however, propylene demand was only rising due to the increasing usage of polypropylene and other products globally. Thus, a gap between supply and demand occurred, demanding the development of new propylene production technologies distinct from traditional stream cracking to supplement propylene production. These on-demand technologies such as methanol-to-olefin (MTO) and propane dehydrogenation (PDH) were commercialized successfully and have been employed in various iterations to close the propylene gap.

However, unlike in the case of the propylene gap, there is currently an absence of technologies that enable the production of petrochemicals from other crude oil streams. The closest example currently in utilization is the increasing use of ZSM-5 in fluidized catalytic cracking (FCC) catalyst blends to increase aromatics yield[7]. FCC technology utilizes acidic zeolites, predominantly some form of zeolite Y, to crack heavy oils of C_{20+} into gasoline and diesel fractions[6]. While it has been found that introducing a small fraction of ZSM-5 into the catalyst blend can improve aromatics yield, which has been ascribed to a confinement effect stemming from the different cage size of ZSM-5 compared to zeolite Y, the total aromatics achieved by the process are relatively small and insufficient to meet total the projected gap.

Thus, other technologies will be needed in order to supplement petrochemical production, ideally utilizing existing infrastructure and downstream processes to reduce the complexity of

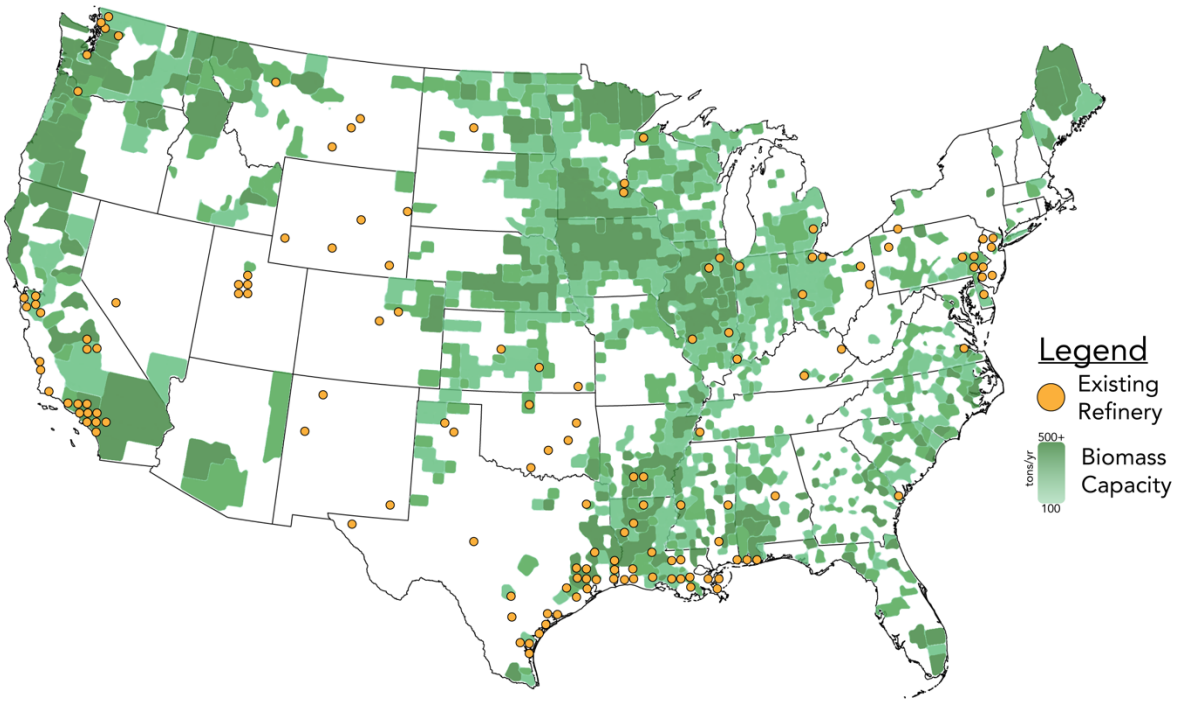

Figure 1.2: Map of current domestic crude oil refineries. Co-location of refineries in regions which have been identified to exhibit high biomass potential by NREL suggests reasonable transportation costs and logistics. Data compiled from Ref. 5.

the transition while at the same time reducing overall production carbon footprint.

Considering these design constraints, second-generation biomass is a promising candidate. Second-generation biomass encompasses a broad range of non-edible, plant-derived materials from the residential, commercial agricultural, and residential sectors that are typically considered waste and used for low-value applications such as combustion, if used at all[8,9]. The central tenet guiding the valorization of biomass into industrially relevant carbon feedstocks is the hypothetical "carbon neutrality" of the products – that is, CO_2 is extracted from the atmosphere during biomass growth and may be returned to the atmosphere upon product decomposition at the end of life. In this process, the CO_2 cycle is significantly accelerated compared to fossil resources, which on relevant time scales represent only a source

of CO_2 emission today – the sequestration of which through natural processes will take millions of years. Additionally, biomass is abundant both regionally and globally, mitigating the geopolitical issues associated with geographically scarce resources such as petroleum.

Biomass consists of a range of carbonaceous polymers that lend themselves to diverse applications as a result of their distinct structures. For example, much of the research to date has been focused on the valorization of sugar monomers derived from cellulose and hemicellulose components abundant in agricultural sources such as corn stover and residential waste[10–12]. Depolymerization of the native biopolymers lends itself to the release of these structurally consistent sugar monomers, primarily glucose, which can then be used in fermentative or thermocatalytic processes to generate products such as ethanol[10,13], 5-hydroxymethylfurfural (5-HMF)[14–16], and others[17]. Of these routes, only ethanol production from cellulosic fermentation has achieved much commercial implementation.

Biomass also consists of a significant fraction (~25% dry mass) of lignin, a complex biopolymer consisting of oxygenated aromatic units linked through radical polymerization processes to provide structural stability in plants. This composition of primarily aromatic monomers, in fact making lignin the largest known natural source of aromatic compounds[18], lends lignin unique potential for use as a feedstock, specifically targeting high-value petrochemicals. Of the five chemical feedstocks typically comprising the "high-value chemicals" or "primary" (ethylene, propylene, benzene, toluene, and xylene), three are aromatic monomers (benzene, toluene, and xylene)[19]. These species, also known as BTX collectively, are produced on the order of 100 million tons per year and find use in a range of consumer goods including pharmaceuticals, plastics, and textiles[20]. It is these species that are projected to grow in demand while crude oil supply begins to wane with decreased gasoline

and diesel demand, demanding the exploration of new feedstocks for BTX, ideally one that can exploit current processes while reducing the overall carbon footprint of BTX growth.

Thus, considering the likely discrepancies between fossil resource supply and aromatics demands in coming years, lignin could prove to be a viable, sustainable, drop-in substrate to close the supply gap left by petroleum. Valorization of lignin is also considered an integral component towards the economic realization of biorefineries, as the low-value utilizations of lignin today, primarily as a combustible fuel, reduce overall refinery profitability[21]. However, while there are demonstrated, commercial-scale processes which target cellulose and hemicellulose valorization, the technical space for lignin is far less mature.

Realizing a lignin-inclusive biorefinery for aromatics production requires two broad technical steps, namely 1.) extraction and depolymerization and 2.) deoxygenation[22–24]. Depolymerization, from a technical standpoint, is significantly more challenging for lignin than for the analogous biopolymers cellulose and hemicellulose due to the complex and stochastic chemical bonds formed during lignin's radical polymerization *in vivo*. A full overview of the challenges for lignin separation and depolymerization is outside of the scope of this dissertation but can be found in a number of detailed reviews[25–27]. For the sake of this work, there have been multiple routes identified, including liquid-phase solvolysis[28,29], catalyst-mediated reductive fractionation[30–32], and thermal pyrolysis[33–37] which enable the depolymerization of lignin. However, in all cases, the resulting monomers are a pool of mixed structures, exhibiting varying degrees of oxygenation in the form of hydroxy and methoxy species and hydrocarbon chains bonded to the aromatic ring of interest[38]. Such diversity in the product stream lends itself to low intrinsic value, susceptibility to repolymerization and fouling, and high oxygen content. In order to realistically be a drop-in replacement for current

petroleum feedstocks, which can tolerate some degree of structure heterogeneity considering the state of current separations processes, the oxygen content of the resulting monomers must be reduced. This both improves the chemical properties of the monomer pool and funnels the monomers into greater structural similarity. Considering the strength of the C-O bond energy[39], thermal and chemical routes alone have been ineffective in activating the C-O bond, especially considering the need to maintain the desired aromatic structure. In order to realize the bond-selective cleavage of C-O bonds in lignin-derived monomers at high rates, heterogeneous catalytic hydrogenation (HDO) is required.

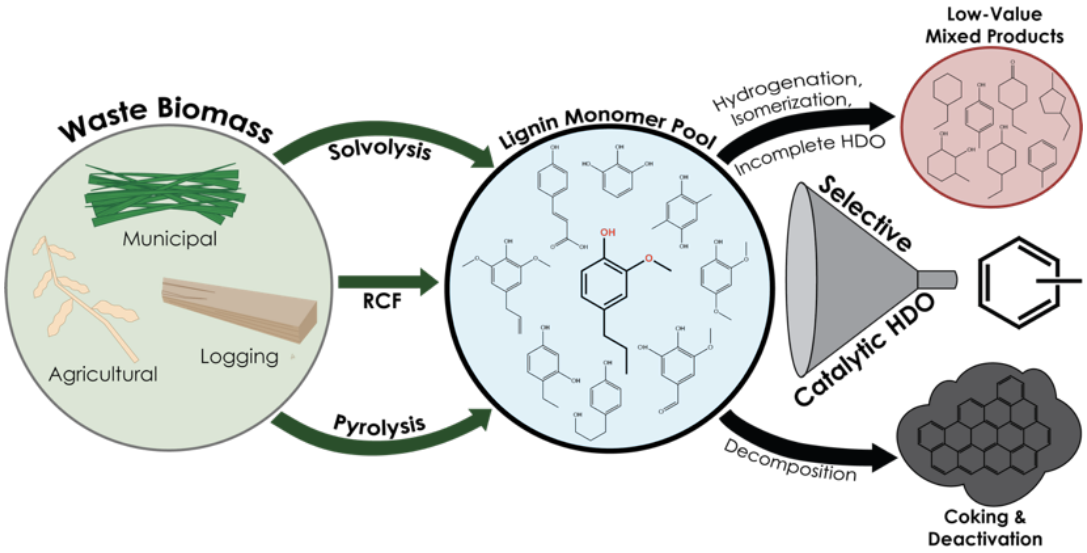

Figure 1.3: Overview of biomass valorization strategies targeting aromatic monomers from lignin-rich feedstocks.

Heterogeneous catalysts are materials that participate in a reaction by lowering the barriers of key reaction steps but are importantly not consumed during the reaction itself, instead lowering barriers by transiently stabilizing key transition states. By careful design of the catalyst structure, properties, and composition, performance can be tuned to theoretically achieve selective activation of specific transition states over others, thus enabling the facilitation of specific reactions, such as the cleavage of C-O bonds.

1.2 Current HDO Catalysts

Early work into the investigation of effective catalysts for HDO relied on the closest approximation to the process available and present in industry, which are hydrodesulfurization (HDS) catalysts employed in the reduction of sulfur content in transportation fuels. Combustion of sulfur-containing fuel results in sulfur oxide (SO_x) emissions that are both a human health and ecological concern. As a result, environmental agencies globally have placed restrictions on the amount of sulfur that transportation fuels can contain, which today stands at a maximum of 10 ppm in the United States. Crude oil, on the other hand, has a sulfur content between 0.4 to 5%, or up to 50,000 ppm[40], meaning that sulfur removal has been an essential component of refinery operation since the late 1990's.

Sulfur content in crude oil is primarily composed of thiophenes and sulfides, though the full range of sulfur-containing compounds is as diverse as the number of compounds comprising crude oil[41]. Thus, HDS catalysts have undergone multiple evolutions as increasingly more sulfur-containing compounds and functionalities are required to undergo HDS as environmental regulations become stricter. The current state-of-the-art is CoMoP/HY-Al_2O_3 catalysts, wherein bimetallic CoMo sites are the active site for sulfur removal, phosphoric acid is present as a structure-directing agent to increase the density of active CoMo sites, and the HY-Al_2O_3 support facilitates isomerization to more reactive sulfur-containing compounds compared to Al_2O_3 alone[42].

While a large commercial push to reduce the oxygen content in crude oil never occurred, as oxygenated byproducts are inherently not an emissions concern (CO_2, H_2O, etc.), early academic interest in HDO spurred by biomass-to-chemical processes initially utilized HDS catalysts. The inspiration for this primarily comes from the chemical similarity of

oxygen- and sulfur-containing functional groups in organic compounds as a result of their proximity in the periodic table under Group 8. There are also important analogs between HDO and HDS regarding the diversity of substrates that are likely present under reaction conditions, either in the form of sulfided hydrocarbons in the case of crude oil or oxygenated aromatics in the case of lignin. Thus, in both cases, catalysts should be active towards a broad range of chemical and structural moieties. Examples of HDS catalysts abound in early HDO literature[43–46], primarily utilizing the prototypical sulfided CoMo formulation at temperatures above 300˚C and pressure greater than 20 bar H_2. Under these conditions, there are reports of both mono-oxygenate and multi-oxygenated lignin model compounds undergoing HDO to deoxygenated aromatics such as benzene at high selectivity, with hydrogenation of the aromatic ring representing a minor side-reaction.

Though the CoMoS formulation was shown to be effective in obtaining high yields of aromatics from oxygenated lignin model compounds, there are significant plant-scale drawbacks that limit its desirability in HDO reactions. Namely, although the as-prepared catalytic formulation of the state-of-the-art HDS catalyst is composed of CoMoP/HY-Al_2O_3, extensive research with the goal of optimizing HDS catalyst performance identified that active sites are CoMoS bimetallic sulfide domains, specifically at the defective corner sites where S vacancies form[47,48]. Thus, in order to obtain active catalysts for HDO using similar catalytic formulations, sulfur compounds must be co-fed to continually regenerate the CoMoS active phase. The presence of sulfur on the surface of the catalyst leads to unavoidable contamination of the product stream with trace levels of sulfur, which requires downstream removal. Contrary to petroleum refineries where desulfurization is inherent to the plant design, particularly after HDS where H_2S is a stoichiometric product, proposed biorefinery models are not expected to

employ large-scale desulfurization units, especially in the downstream monomers process units. Additionally, though the selectivity to aromatics is favorable, even under harshly reducing conditions, deoxygenation rates are generally too low for industrial application.[49] As a result, alternative catalyst formulations have been explored for commercial-scale implementation in HDO processes.

Of these alternative catalysts, supported metal nanoparticles such as Pt, Pd, Ni, and Ru have received the most attention in HDO research[50–58]. Of these catalysts, early screening studies identified Pt as particularly active and stable in the HDO of model compounds. However, at reaction conditions needed to achieve reasonable HDO rates greater than 1 mmol $g_{cat}^{-1}hr^{-1}$ (250˚C+, ≥1 bar H_2), Pt simultaneously hydrogenates the aromatic ring and isomerizes substrates to 5-member ring and open-chain saturated alkane products, which are lower-value and challenging to separate from the desired aromatic products. Deactivation via coking and irreversible intermediate adsorption to the catalyst have also been challenging for transition metal catalysts[59–61].

Studies have been conducted that investigate the influence of the support composition on the HDO activity of reduced metals. Supports can influence the reactivity of metals by providing distinct active sites, modifying metal electronic characteristics, and dictating the transport of substrates and products to the active sites. For instance, zeolite-supported Pt catalysts have been proposed for HDO primarily due to their high Brønsted acid site density[62,63], which facilitates deoxygenation through dehydration of alcohols formed from hydrogenation of phenolic substrates. However, the product selectivity on these catalysts is often dominated by saturated cycloalkane species with low utility and value compared to the desired aromatics.

High yields of aromatics in the HDO of lignin model compounds were observed with Pt supported on reducible metal oxides, as compared to irreducible supports. For example, the activity and selectivity to aromatics over Pt supported on ZrO_2, TiO_2, and Nb_2O_5 increased with more reducible supports[64]. Another study investigated Pt/TiO_2 reduced at 250˚ - 550˚C and found a relationship between oxygen vacancy concentration and the TOF of *m*-cresol to toluene[65]. Importantly, characterization showed decreasing acid site density on more active catalysts treated under harsher reducing conditions, indicating selective HDO over Pt catalysts supported on reducible oxides does not proceed through acid-catalyzed pathways.

For Pt/TiO_2 catalysts, SMSI was hypothesized to play a role in balancing catalytic activity and selectivity[65]. SMSI describes the *in situ* formation of reducible oxide overlayers on the surface of metal nanoparticles under high temperatures, reducing atmospheres, such as those during HDO. It has been speculated that the formation of incomplete oxide overlayers on metal surfaces may optimize HDO selectivity to BTX products by maximizing the metal-oxide interfacial length beyond what can be achieved for metals sitting on supports (no oxide decoration). For catalysts supported directly onto reducible metal oxides, however, obtaining incomplete overlayers is a challenge via SMSI due to the stoichiometric excess of reducible oxide available, which favors the formation of overlayers that cover the entire metal surface.

Recent work has addressed this limitation by using atomic layer deposition (ALD) to deposit reducible metal oxides such as WO_3, Nb_2O_5, and TiO_2 onto metal nanoparticles supported on SMSI-inactive supports (e.g. SiO_2)[66–69]. Importantly, the reducible oxide content relative to the metal surface area is tailorable, allowing control of the extent of overlayer formation since the support (SiO_2) does not exhibit SMSI. In the HDO of *m*-cresol, WO_x-modified Pt/C catalysts exhibited a remarkably high selectivity of 98% to the desired aromatic product, toluene, even under 36 bar of H_2, see Figure 1.4[68]. Under similar conditions, Pt/C catalysts were only 62% selective to toluene, with the balance being hydrogenated products, and deactivated within 4 hours. Conversely, the WO_x-modified Pt/C catalyst conversion was stable for at least 7 hours.

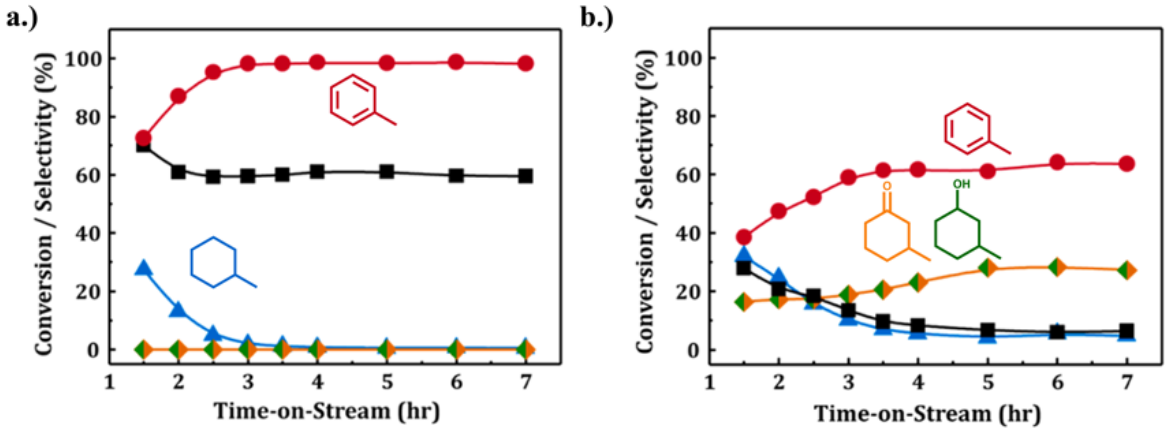

Figure 1.4: HDO of *m*-cresol catalyzed by a.) WO_x/Pt/C and b.) Pt/C. WO_x-modified Pt catalysts exhibit far improved selectivity to toluene and stability compared to unmodified Pt catalysts. Reaction conditions: 573 K, 36 bar, 2 mol% *m*-cresol/dodecane, WHSV = 0.6 hr^{-1}. Black data points represent conversion, colored data points represent selectivity. Adapted from Ref. 68.

1.3 Goals of this Dissertation

Despite this exciting progress toward identifying potentially viable catalyst architectures for the HDO of lignin, there has been no conclusive work furthering the understanding of the structure of the active site. The development of such a structure-activity relationship is essential for the realistic implementation of these catalysts on a commercial

scale. Recently, a list of suggested metrics for catalytic processes that produce fuels and chemicals has been published, which seeks to provide realistic industrial benchmarks that lab-scale catalysts can be compared against to shrink the gap between academic research, which tends to target only fundamental progress, and industrial implementation, which strongly values performance metrics such as reactor volume, catalyst stability, and process conditions. This report suggests that reactor productivity be greater than 0.1 metric tons per cubic meter per hour for a sustainable catalytic process[70]. Assessing the literature available for WO_x/Pt and other inverse catalysts in the HDO of lignin model compounds, there appears to be a need for ~10-fold improvement in catalyst rates to meet the provided performance benchmark. Improvement may need to be even greater considering the costs associated with catalysts containing noble metals, such as Pt, and the price of products derived from lignin. Such improvement will require a fundamental understanding of the active site for deoxygenation in these catalysts.

Regarding the current understanding of the active site structure, it is generally been observed that catalysts containing oxide-on-metal structures exhibit increased activity and selectivity to BTX products, despite presumably lower metal site accessibility compared to unmodified catalysts due to the presence of the oxide decorating surface metal sites. However, while activity has been reported to increase, improvements to the rates of initial reactivity have been quite modest (never more than 3-fold) compared to unmodified Pt[68] catalysts. Hampering confident assessment of the reactivity of modified and unmodified catalysts on a per-site basis are the technical challenges associated with direct measurement site density due to the inherently dynamic nature of oxide decoration. The small changes in rates (on a per mass of catalyst basis) comparing bare and oxide-promoted Pt for HDO is suggestive of a shared

mechanism and active site, drawing into question whether WO_x-modification of Pt is responsible for generating a novel active site at the Pt-WO_x interface or if WO_x moderates the observed activity of bare Pt through other means.

Importantly, there is no consensus on the mechanism of phenolics HDO for either modified or unmodified Pt catalysts. Reports have consistently shown that supported reducible oxides such as MoO_3 and WO_3 alone exhibit far suppressed reactivity, if any, in HDO compared to WO_x-modified Pt catalysts[39,71]. On the other hand, Pt is known to be active by itself in the HDO of phenolics[72]. Theoretical work has suggested that under-coordinated sites, such as those present on the steps and edges of Pt nanoparticles might be more reactive than well-coordinated sites in the direct cleavage of C-O bonds present in phenolics[73]. However, experimental work on Pt/SiO_2 catalysts has proposed a tautomerization mechanism for the HDO of phenolics, meaning that direct C-O cleavage may not play a role under experimental conditions. Despite this disagreement, no work has been conducted seeking to understand the role of Pt structure, namely that of well-coordinated and under-coordinated sites on the surface of Pt nanoparticles, on the experimentally observed HDO reactivity.

It is perhaps unsurprising, then, that without a functional understanding of the mechanism at play in unmodified Pt-catalyzed HDO reactions, even more uncertainty surrounds the reactivity and mechanism of WO_x-modified Pt catalysts for HDO. A number of mechanisms have been proposed, ranging from Brønsted acid-catalyzed dehydration, reverse Mars-van Krevelen mechanisms, direct C-O cleavage, and other interfacial phenomena between the oxide and metal components. One report studying WO_x-modified Pt/TiO_2 catalysts using deuterated polyol substrates and NMR concluded that the resultant products exhibited D-labelling inconsistent with a Mars van Krevelen-type mechanism, though the reactivity of

saturated polyol substrates and phenolics might be considerably different[74]. Others have pointed to the *in situ* formation of acid sites associated with the oxide-metal interface, bolstered once again by observed HDO activity of saturated alcohols[75,76]. Such results cannot by themselves be extended to aromatic oxygenates, which are stable under acidic conditions even when strong mineral acids are used.

Thus, the work presented in this dissertation seeks to gain a fundamental understanding of oxide-promoted Pt catalysts in the HDO of phenolic compounds by taking a ground-up approach. The work presented in Chapter 2 seeks to identify the inherent structure-activity relationships of unmodified Pt/SiO_2 catalysts by varying Pt particle size, thus varying the fraction of well-coordinated and under-coordinated sites, to assess the role of direct C-O cleavage in the HDO of phenolics compared to other mechanisms, such as tautomerization. Using the fundamental understanding built on this system, Chapter 3 utilizes a stepwise synthesis to produce WO_x-modified Pt/SiO_2 catalysts of consistent size with varied WO_x loading. Characterization of these materials sheds light on a new aspect of oxide-on-metal catalyst architectures which contextualizes the high aromatics selectivity of this class of catalysts in the HDO of phenolics. In Chapter 4, the results of the previous 2 chapters are tested against a wider range of modifying oxides to elucidate the physical and chemical properties dictating reducible oxide-modified Pt catalyst performance in the HDO of phenolics. Chapter 4 briefly investigates the confluence of metal-support and oxide-support interactions using an Al_2O_3 support instead of SiO_2 as used throughout the rest of the dissertation work. In conclusion, an atomic-scale perspective of HDO reactivity over modified Pt catalysts is achieved for the case of phenolic substrates, complemented by a rich mechanistic

understanding of deoxygenation under mild conditions and the materials science phenomenon underpinning the structure of heterogeneous catalysts.

1.4 References

1. Friedlingstein, P. *et al.* Global carbon budget 2019. *Earth Syst Sci Data* **11**, 1783–1838 (2019).
2. Zhao, K. *et al.* Recent Advances and Future Perspectives in Carbon Capture, Transportation, Utilization, and Storage (CCTUS) Technologies: A Comprehensive Review. *Fuel* **351**, (2023).
3. Rubin, E. S., Mantripragada, H., Marks, A., Versteeg, P. & Kitchin, J. The outlook for improved carbon capture technology. *Progress in Energy and Combustion Science* vol. 38 630–671 Preprint at https://doi.org/10.1016/j.pecs.2012.03.003 (2012).
4. bp. *Bp Energy Outlook 2023*.
5. Wang, M. *Estimation of Energy Efficiencies of U.S. Petroleum Refineries*. http://www.eia.doe.gov/pub/oil_gas/petroleum/analysis_publications/oil_market_basics/paddma (2008).
6. Akah, A. & Al-Ghrami, M. Maximizing propylene production via FCC technology. *Appl Petrochem Res* **5**, 377–392 (2015).
7. Liu, C. *et al.* Effect of ZSM-5 on the aromatization performance in cracking catalyst. *J Mol Catal A Chem* **215**, 195–199 (2004).
8. Naik, S. N., Goud, V. V., Rout, P. K. & Dalai, A. K. Production of first and second generation biofuels: A comprehensive review. *Renewable and Sustainable Energy Reviews* vol. 14 578–597 Preprint at https://doi.org/10.1016/j.rser.2009.10.003 (2010).
9. Alonso-Pippo, W., Luengo, C. A., Felfli, F. F., Garzone, P. & Cornacchia, G. Energy recovery from sugarcane biomass residues: Challenges and opportunities of bio-oil production in the light of second generation biofuels. *Journal of Renewable and Sustainable Energy* **1**, 063102 (2009).
10. Badger, P. C. *Ethanol From Cellulose: A General Review*. (2002).
11. He, J. *et al.* Synthesis of 1,6-Hexanediol from Cellulose Derived Tetrahydrofuran-Dimethanol with Pt-WOx/TiO2 Catalysts. *ACS Catal* **8**, 1427–1439 (2018).
12. Collard, F. X. & Blin, J. A review on pyrolysis of biomass constituents: Mechanisms and composition of the products obtained from the conversion of cellulose, hemicelluloses and lignin. *Renewable and Sustainable Energy Reviews* vol. 38 594–608 Preprint at https://doi.org/10.1016/j.rser.2014.06.013 (2014).
13. Lynd, L. R. *OVERVIEW AND EVALUATION OF FUEL ETHANOL FROM CELLULOSIC BIOMASS: Technology, Economics, the Environment, and Policy*. *Annual Reviews LYNDDUN.TXT AR016-15 Annu. Rev. Energy Environ* vol. 9 www.annualreviews.org (1996).
14. Luo, J., Arroyo-Ramírez, L., Gorte, R. J., Tzoulaki, D. & Vlachos, D. G. Hydrodeoxygenation of HMF over Pt/C in a continuous flow reactor. *AIChE Journal* **61**, 590–597 (2015).

15. Du, Q. *et al.* One-pot conversion of cellulose to HMF under mild conditions through decrystallization and dehydration in dimethyl sulfoxide/tetraethylammonium chloride. *Chemical Engineering Journal* **475**, (2023).
16. Tsilomelekis, G. *et al.* Molecular structure, morphology and growth mechanisms and rates of 5-hydroxymethyl furfural (HMF) derived humins. *Green Chemistry* **18**, 1983–1993 (2016).
17. Hopper, J. T., Ma, R., Rawlings, J. B., Ford, P. C. & Abu-Omar, M. M. Markedly Improved Catalytic Dehydration of Sorbitol to Isosorbide by Sol-Gel Sulfated Zirconia: A Quantitative Structure-Reactivity Study. *ACS Catal* **13**, 10137–10152 (2023).
18. Meng, Q. *et al.* Sustainable production of benzene from lignin. *Nat Commun* **12**, (2021).
19. Lopez, G., Keiner, D., Fasihi, M., Koiranen, T. & Breyer, C. From fossil to green chemicals: sustainable pathways and new carbon feedstocks for the global chemical industry. *Energy Environ Sci* **16**, 2879–2909 (2023).
20. Icca. *The Global Chemical Industry: Catalyzing Growth and Addressing Our World's Sustainability Challenges Report for ICCA*. (2019).
21. Sudarsanam, P. *et al.* Towards Lignin-Derived Chemicals Using Atom-Efficient Catalytic Routes. *Trends in Chemistry* vol. 2 898–913 Preprint at https://doi.org/10.1016/j.trechm.2020.07.011 (2020).
22. Abu-Omar, M. M. *et al.* Guidelines for performing lignin-first biorefining. *Energy and Environmental Science* vol. 14 262–292 Preprint at https://doi.org/10.1039/d0ee02870c (2021).
23. Renders, T., Van den Bossche, G., Vangeel, T., Van Aelst, K. & Sels, B. Reductive catalytic fractionation: state of the art of the lignin-first biorefinery. *Current Opinion in Biotechnology* vol. 56 193–201 Preprint at https://doi.org/10.1016/j.copbio.2018.12.005 (2019).
24. Balakshin, M. Y. *et al.* New Opportunities in the Valorization of Technical Lignins. *ChemSusChem* vol. 14 1016–1036 Preprint at https://doi.org/10.1002/cssc.202002553 (2021).
25. Pandey, M. P. & Kim, C. S. Lignin Depolymerization and Conversion: A Review of Thermochemical Methods. *Chemical Engineering and Technology* vol. 34 29–41 Preprint at https://doi.org/10.1002/ceat.201000270 (2011).
26. Alherech, M. *et al.* From Lignin to Valuable Aromatic Chemicals: Lignin Depolymerization and Monomer Separation via Centrifugal Partition Chromatography. *ACS Cent Sci* **7**, 1831–1837 (2021).
27. Abu-Omar, M. M. & Ford, P. C. The lignin challenge in catalytic conversion of biomass solids to chemicals and fuels. *RSC Sustainability* vol. 1 1686–1703 Preprint at https://doi.org/10.1039/d3su00117b (2023).
28. Nishide, R. N., Truong, J. H. & Abu-Omar, M. M. Organosolv Fractionation of Walnut Shell Biomass to Isolate Lignocellulosic Components for Chemical Upgrading of Lignin to Aromatics. *ACS Omega* **6**, 8142–8150 (2021).
29. Liu, B., Sanchez, M., Truong, J., Ford, P. C. & Abu-Omar, M. M. Catalytic conversion of high S-lignin to a sustainable tri-epoxide polymer precursor. *Green Chemistry* **24**, 4958–4968 (2022).
30. Anderson, E. M. *et al.* Flowthrough Reductive Catalytic Fractionation of Biomass. *Joule* **1**, 613–622 (2017).

31. Anderson, E. M. *et al.* Reductive Catalytic Fractionation of Corn Stover Lignin. *ACS Sustain Chem Eng* **4**, 6940–6950 (2016).
32. Van Den Bosch, S. *et al.* Reductive lignocellulose fractionation into soluble lignin-derived phenolic monomers and dimers and processable carbohydrate pulps. *Energy Environ Sci* **8**, 1748–1763 (2015).
33. Liu, C., Wang, H., Karim, A. M., Sun, J. & Wang, Y. Catalytic fast pyrolysis of lignocellulosic biomass. *Chemical Society Reviews* vol. 43 7594–7623 Preprint at https://doi.org/10.1039/c3cs60414d (2014).
34. Zhou, G., Jensen, P. A., Le, D. M., Knudsen, N. O. & Jensen, A. D. Atmospheric Hydrodeoxygenation of Biomass Fast Pyrolysis Vapor by MoO3. *ACS Sustain Chem Eng* **4**, 5432–5440 (2016).
35. Bai, X. *et al.* Formation of phenolic oligomers during fast pyrolysis of lignin. *Fuel* **128**, 170–179 (2014).
36. Ma, Z., Troussard, E. & Van Bokhoven, J. A. Controlling the selectivity to chemicals from lignin via catalytic fast pyrolysis. *Appl Catal A Gen* **423–424**, 130–136 (2012).
37. Jiang, G., Nowakowski, D. J. & Bridgwater, A. V. Effect of the temperature on the composition of lignin pyrolysis products. *Energy and Fuels* **24**, 4470–4475 (2010).
38. Ház, A. *et al.* Chemical composition and thermal behavior of kraft lignins. *Forests* **10**, (2019).
39. Prasomsri, T., Shetty, M., Murugappan, K. & Román-Leshkov, Y. Insights into the catalytic activity and surface modification of MoO 3 during the hydrodeoxygenation of lignin-derived model compounds into aromatic hydrocarbons under low hydrogen pressures. *Energy Environ Sci* **7**, 2660–2669 (2014).
40. Demirbas, A., Alidrisi, H. & Balubaid, M. A. API gravity, sulfur content, and desulfurization of crude oil. *Pet Sci Technol* **33**, 93–101 (2015).
41. Vetere, A., Pröfrock, D. & Schrader, W. Qualitative and Quantitative Evaluation of Sulfur-Containing Compound Types in Heavy Crude Oil and Its Fractions. *Energy and Fuels* **35**, 8723–8732 (2021).
42. Fujikawa, T. Development of New CoMo HDS Catalyst for Ultra-low Sulfur Diesel Fuel Production. *Journal of the Japan Petroleum Institute* **50**, 249–261 (2007).
43. Lin, Y. C., Li, C. L., Wan, H. P., Lee, H. T. & Liu, C. F. Catalytic hydrodeoxygenation of guaiacol on Rh-based and sulfided CoMo and NiMo catalysts. *Energy and Fuels* **25**, 890–896 (2011).
44. Yoosuk, B., Tumnantong, D. & Prasassarakich, P. Amorphous unsupported Ni-Mo sulfide prepared by one step hydrothermal method for phenol hydrodeoxygenation. *Fuel* **91**, 246–252 (2012).
45. Viljava, T.-R., Komulainen, R. S. & Krause, A. O. I. *Effect of H 2 S on the Stability of CoMo/Al 2 O 3 Catalysts during Hydrodeoxygenation*. *Catalysis Today* vol. 60 (2000).
46. Laurent, E. & Delmon, B. Influence of water in the deactivation of a sulfided NiMo γ-Al2O3 catalyst during hydrodeoxygenation. *J Catal* **146**, (1994).
47. Li, M., Li, H., Jiang, F., Chu, Y. & Nie, H. The relation between morphology of (Co)MoS2 phases and selective hydrodesulfurization for CoMo catalysts. *Catal Today* **149**, 35–39 (2010).
48. Leliveld, R. G., Van Dillen, A. J., Geus, J. W. & Koningsberger, D. C. *Structure and Nature of the Active Sites in CoMo Hydrotreating Catalysts Conversion of Thiophene*. *JOURNAL OF CATALYSIS* vol. 175 (1998).

49. Yan, P. *et al.* The role of acid and metal sites in hydrodeoxygenation of guaiacol over Ni/Beta catalysts. *Catalysis Science and Technology* **10**, 810–825 (2020).
50. Bejblová, M., Zámostný, P., Červený, L. & Čejka, J. Hydrodeoxygenation of benzophenone on Pd catalysts. *Appl Catal A Gen* **296**, 169–175 (2005).
51. Bowker, R. H. *et al.* Synthesis and hydrodeoxygenation properties of ruthenium phosphide catalysts. *ACS Catal* **1**, 917–922 (2011).
52. Lee, E. H. *et al.* Hydrodeoxygenation of guaiacol over Pt loaded zeolitic materials. *Journal of Industrial and Engineering Chemistry* **37**, 18–21 (2016).
53. Lan, X., Hensen, E. J. M. & Weber, T. Hydrodeoxygenation of guaiacol over Ni2P/SiO2–reaction mechanism and catalyst deactivation. *Appl Catal A Gen* **550**, 57–66 (2018).
54. Gao, D., Xiao, Y. & Varma, A. Guaiacol Hydrodeoxygenation over Platinum Catalyst: Reaction Pathways and Kinetics. *Ind Eng Chem Res* **54**, 10638–10644 (2015).
55. Rivoira, L., Martínez, M. L. & Beltramone, A. Hydrodeoxygenation of guaiacol over Pt-Ga-mesoporous catalysts. *Microporous and Mesoporous Materials* **312**, (2021).
56. Olcese, R. N. *et al.* Gas-phase hydrodeoxygenation of guaiacol over Fe/SiO 2 catalyst. *Appl Catal B* **115–116**, 63–73 (2012).
57. Salakhum, S., Saenluang, K. & Wattanakit, C. Stability of monometallic Pt and Ru supported on hierarchical HZSM-5 nanosheets for hydrodeoxygenation of lignin-derived compounds in the aqueous phase. *Sustain Energy Fuels* **4**, 1126–1134 (2020).
58. Kumar, A. *et al.* Hydrodeoxygenation of m-Cresol over Ru based catalysts: Influence of catalyst support on m-Cresol conversion and methylcyclohexane selectivity. *Renew Energy* **151**, 687–697 (2020).
59. Bykova, M. V., Zavarukhin, S. G., Trusov, L. I. & Yakovlev, V. A. Guaiacol hydrodeoxygenation kinetics with catalyst deactivation taken into consideration. *Kinetics and Catalysis* **54**, 40–48 (2013).
60. De Souza, P. M. *et al.* Hydrodeoxygenation of Phenol over Pd Catalysts. Effect of Support on Reaction Mechanism and Catalyst Deactivation. *ACS Catal* **7**, 2058–2073 (2017).
61. Cordero-Lanzac, T. *et al.* Revealing the pathways of catalyst deactivation by coke during the hydrodeoxygenation of raw bio-oil. *Appl Catal B* **239**, 513–524 (2018).
62. Hellinger, M. *et al.* Catalytic hydrodeoxygenation of guaiacol over platinum supported on metal oxides and zeolites. *Appl Catal A Gen* **490**, 181–192 (2015).
63. Duan, H. *et al.* Effects of crystallite sizes of pt/hzsm-5 zeolite catalysts on the hydrodeoxygenation of guaiacol. *Nanomaterials* **10**, 1–19 (2020).
64. Mäkelä, E. *et al.* Liquid-phase Hydrodeoxygenation of 4-Propylphenol to Propylbenzene: Reducible Supports for Pt Catalysts. *ChemCatChem* **12**, 4090–4104 (2020).
65. Wu, X., Liu, C. jun, Wang, H., Ge, Q. & Zhu, X. Origin of strong metal-support interactions between Pt and anatase TiO2 facets for hydrodeoxygenation of m-cresol on Pt/TiO2 catalysts. *J Catal* **418**, 203–215 (2023).
66. Wang, C. *et al.* Hydrodeoxygenation of m-Cresol Over Pt-WOx/C Using H2 Generated In Situ by n-Hexane Dehydrogenation. *Catal Letters* **150**, 913–921 (2020).
67. Lin, Z. *et al.* Mechanistic Understanding of Ring-Opening of Tetrahydrofurfuryl Alcohol over WOx-Modified Pt Model Surfaces and Powder Catalysts. *ACS Catal* **13**, 8014–8024 (2023).
68. Wang, C. *et al.* Mechanistic Study of the Direct Hydrodeoxygenation of m -Cresol over WOx-Decorated Pt/C Catalysts. *ACS Catal* **8**, 7749–7759 (2018).

69. Huang, R., Kwon, O., Lin, C. & Gorte, R. J. The effects of SMSI on m-Cresol hydrodeoxygenation over Pt/Nb2O5 and Pt/TiO2. *J Catal* **398**, 102–108 (2021).
70. Lange, J.-P. Performance metrics for sustainable catalysis in industry. *Nat Catal* **4**, 186–192 (2021).
71. Saraeian, A., Burkhow, S. J., Jing, D., Smith, E. A. & Shanks, B. H. Catalyst Property Effects on Product Distribution during the Hydrodeoxygenation of Lignin Pyrolysis Vapors over MoO3/γ-Al2O3. *ACS Sustain Chem Eng* **9**, 6685–6696 (2021).
72. Nie, L. & Resasco, D. E. Kinetics and mechanism of m-cresol hydrodeoxygenation on a Pt/SiO 2 catalyst. *J Catal* **317**, 22–29 (2014).
73. Liu, R. & An, W. Stepped M@Pt(211) (M = Co, Fe, Mo) single-atom alloys promote the deoxygenation of lignin-derived phenolics: Mechanism, kinetics, and descriptors. *Catal Sci Technol* **11**, 7047–7059 (2021).
74. Stephens, K. J. *et al.* A Mechanistic Study of Polyol Hydrodeoxygenation over a Bifunctional Pt-WOx/TiO2Catalyst. *ACS Catal* **10**, 12996–13007 (2020).
75. Fu, J. *et al.* Modulating the dynamics of Brønsted acid sites on PtWOx inverse catalyst. *Nat Catal* **5**, 144–153 (2022).
76. Wu, Y. *et al.* Dynamic Formation of Brønsted Acid Sites over Supported WOx/Pt on SiO2 Inverse Catalysts─Spectroscopy, Probe Chemistry, and Calculations. *ACS Catal* **13**, 7371–7382 (2023).

Chapter 2: Structure Sensitivity of Pt in HDO

Reproduced in part from:

Marlowe, J., Ford, P., Abu-Omar, M. M., Christopher, P. Structure sensitivity in Pt-catalyzed hydrodeoxygenation of multi-oxygenated lignol model compounds. *Cat. Sci. Tech*., **2023**, 13, 5662-5678.

With permission from the Royal Society of Chemistry.

2.1 Introduction

2.1.1 Background

In determining the structure of the "active site" of WO_x/Pt catalysts in the HDO of phenolics, it is first necessary to consider the landscape of active sites that might feasibly exist on the surface of these catalysts. The materials that have been reported to date present what might be considered a limitless number of structurally unique sites for reaction, comprised of any combination of W, Pt, Si, and O atoms. Importantly, however, the site moiety responsible for the observed reactivity may ostensibly be a rare structural motif relative to the entire catalyst surface, and as such it is not sufficient to simply describe the composition of the catalyst as nanoparticles of Pt on a SiO_2 support.

This concept of structural domains which constitute a minority of the surface but represent the motif responsible for the bulk of the reactivity was first proposed by Hugh Stott Taylor in 1925[1]. Taylor built upon the growing breadth of materials science and chemical knowledge at the turn of the 20th century to propose the importance of atomic-scale structure on reactivity. An appreciation for the composition of the catalytic surface developed beginning in 1913 with the work of the Bragg family on x-ray diffraction in crystals[2,3], identifying that

solid materials such as catalysts were composed of structurally organized atoms arranged in repeating lattices. In 1918, Irving Langmuir first described the theory of monolayer adsorption of molecules onto the surfaces of solids, introducing the concept of "sites" as we know them today, though without specific comments towards catalysis or the action of these sites outside of their capacity to adsorb molecules[4]. However, it was only a short time later in 1926 that Cyril Hinshelwood extended these concepts to the ideas of catalysis, framing the phenomenon of heterogenous catalysis as the co-adsorption of two molecule species on catalytic sites which thus enables reactivity, which is known today as the Langmuir-Hinshelwood mechanism of catalysis and remains the most widely utilized model for kinetics[5,6].

Taylor pointed out, however, that a number of phenomena that had been observed could not be fully rationalized by Langmuir's effective, but coarse, model. One of these was the observation by Taylor and coworkers at Princeton that quartz, regardless of how finely ground, would adsorb only a minuscule amount of carbon monoxide despite a relatively high surface area, leading to the conclusion that not all gases adsorb on all "sites". Studies on other materials had also shown at this time a disconnect between chemical reactivity and adsorption of gases, with chemical reactivity typically being much more sensitive to change than adsorption, which remains relatively more constant regardless of treatment. Combining the concepts of both Langmuir-Hinshelwood kinetics and crystalline atomic solids with these observations, Taylor postulated that the surface of catalysts was composed of both "active" and "inactive" sites, present in various quantities, with the active sites being those that contributed to adsorption and reactivity. Taylor's report on this hypothesis contains a figure describing his proposal of the arrangement of a catalytically active Ni surface, shown below in Figure 2.1 in as close to its original format as possible for the sake of underscoring the remarkable accuracy of this

hypothesis despite the technological limitation of the time. The wide range of modern, atomic-scale characterization techniques available today all confirm Taylor's hypothesis. It is fitting,

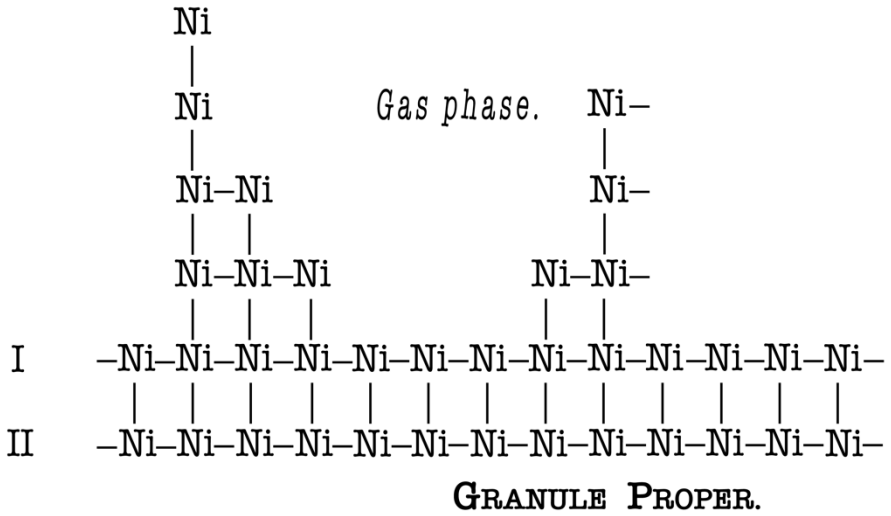

Figure 2.1: Taylor's proposed structure of a Ni surface relevant to hydrogenation catalysis, indicating that some Ni sites (above layers I and II) exhibit decreased connectivity due to their spatial arrangement. Taylor hypothesized that these defective regions were the "active site" for catalysis. Image adapted from Ref. 1.

if not of much technical importance, that the content of this dissertation is conducted in what can be considered Taylor's direct academic lineage (Taylor → Boudart → Madix → Linic → Christopher).

Taylor's report developing the concept of the active site in heterogeneous catalysis shows a Ni surface that contains Ni atoms existing out of plane of the bulk Ni crystal. These sites, Taylor proposed, may have greater activity stemming from their decreased connectivity to neighboring Ni atoms, with activity increasing in proportion to the degree of under-connectivity, or coordination, of these atoms, thus being larger for Ni atoms in the top-most layer, followed by the second layer, and finally the crystalline surface. Once again, in this regard, Taylor was entirely correct. The development of molecular orbital theory for molecules in 1931 by Mulliken set in motion the gradual development in the understanding of how atomic

orbitals, even in solids such as Ni, dictate reactivity through electronic interactions[7]. Altering the degree of coordination of Ni atoms through geometric constraints as shown in the figure above in turn alters the orbital characteristics of Ni atoms, particularly those in the outermost layer of Taylor's proposed surface, enabling greater reactivity.

While Taylor's proposed surface is an exaggerated perspective, decades of surface science research following this model of active sites have again validated his proposal. These lesser or under-coordinated sites are both a fundamental consequence of metal catalysts comprised of atoms and a result of the electronic differences between sites in the presence of adsorbates. Metal catalysts are very often utilized in the form of metal salts which are dispersed upon supporting materials in order to increase the effective surface area per given number of metal atoms, as will be discussed in more detail in the introduction to Chapter 3. A consequence of this dispersion is that metal species exist as semi-crystalline particles formed by truncation of the idealized crystal bulk consistent with the findings of the Bragg family. This act of truncation of a repeating lattice structure necessarily introduces interfaces between different lattice structures, analogous to the edges of three-dimensional polyhedra at the interface of the polyhedra's faces. Atoms at this interface, or edge, are under-coordinated relative to the atoms on the faces of particles. This analogy can be extended further to include a range of under-coordinated features, including corners and edges internal to a face, or step, sites. A decidedly more modern representation of the atomic arrangements of these sites for metal catalyst particles is shown below in Figure 2.2.

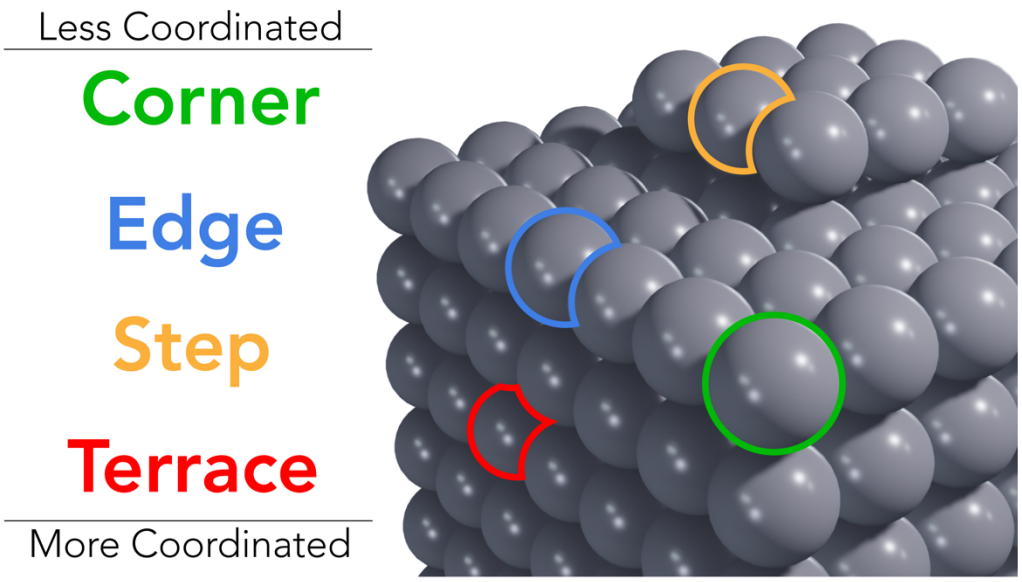

Figure 2.2: Atomic-scale representation of the different spatial relationships of corner, step, edge, and terrace sites on a metal nanoparticle. The cubic shape shown here is selected for simplicity, as realistic nanoparticle shapes exhibit a range of complex and dynamic structures which are broadly composed of these structural sites.

The truncations along which ideal crystals are split to produce metal particle shapes are not random but rather occur preferentially along specific directions to reduce the overall surface energy of the resulting particle. Once again, an analogy can be drawn between this preferential shape for metal particles and the shape of water droplets, which assume the classic tear-drop shape to reduce the surface energy of the droplets as first described by Joseph Willard Gibbs in 1878[8]. Drawing on this conclusion, George Wulff postulated that the same would be true for metal particles cut from a bulk structure[9,10], but mathematical proofs of the concept were not complete until the 1950s from the work of Laue and Herring[11]. Such well-defined truncations, today known for their original descriptor as Wulff constructions, result in characteristic shapes for particles depending on the element and enable the quantitative description of the number of each type of site, including faces (terrace), edges, steps, and corners for known geometries. Importantly, just as the relative surface area changes with the number of atoms, so too does the relative fraction of each site type for a given metal[12]. Thus,

the reactivity of metal particles is very frequently a function of the particle size, all other factors held constant. This can be quantitatively modeled for a given geometry and made tractable through the grouping of atoms into well-coordinated (8+ coordination) and under-coordinated (<8 coordination) atoms. One example is provided below in Figure 2.3, calculated for a variety of common Wulff construction shapes in metal nanoparticles.

This dependence on particle size experimentally manifests itself in so-called "structure sensitive" reactions, or reactions whose rates or selectivity depend greatly on the structure and/or size of the particles catalyzing the reaction[13,14]. The most famous example of this is the Haber-Bosch process over Fe catalysts for the production of ammonia from N_2 and H_2, where N_2 is a considerably challenging catalytic step due to its strong bond, step sites on metallic surfaces were found to be particularly active[15–17]. On a fundamental level, every reaction must

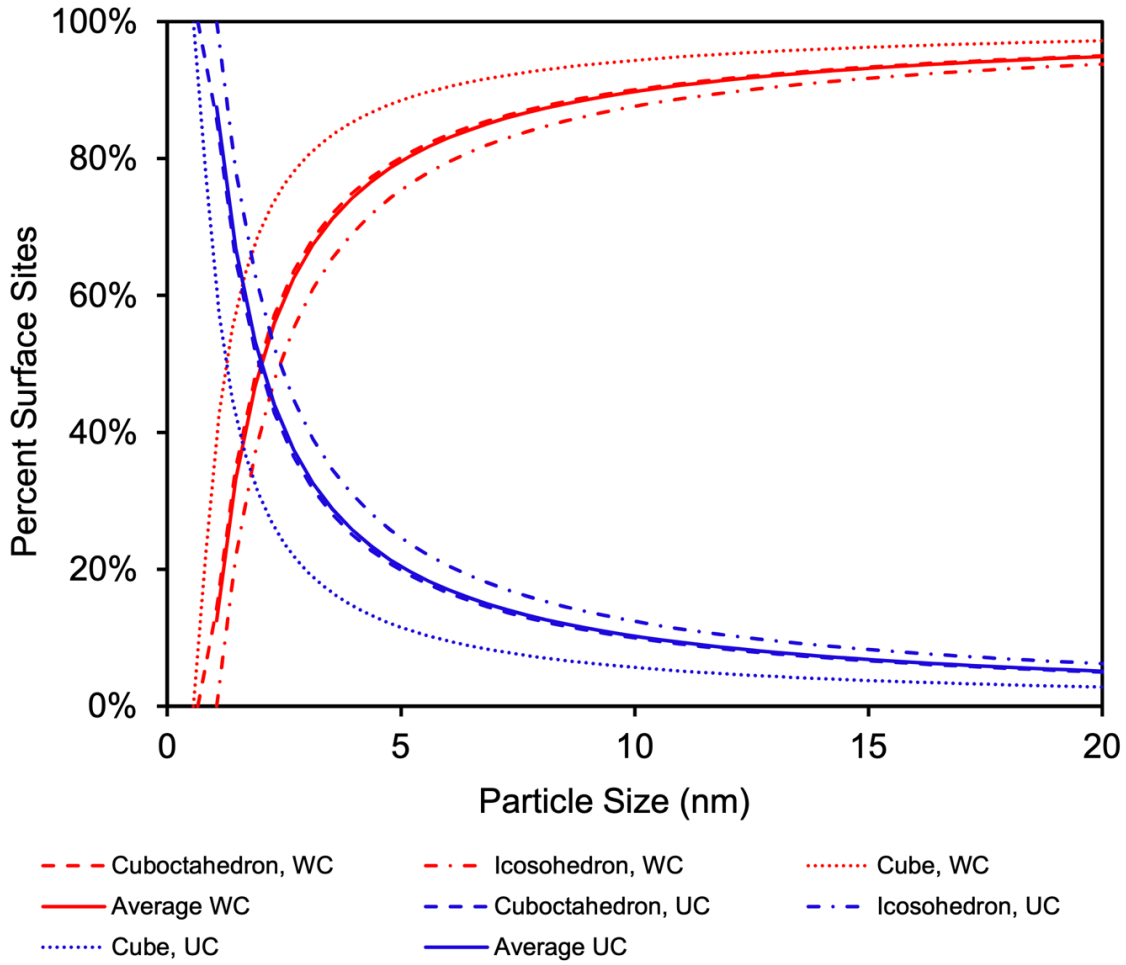

Figure 2.3: Distribution of surface sites on metal nanoparticles of various, thermodynamically-predicted shapes. Instead of describing sites based on individual identity, sites are grouped into two classes: well-coordinated (i.e. terraces, 8+ coordination) and under-coordinated (i.e. edges, <8 coordination). Broadly, well-coordinated site fraction (red lines) increases with increasing nanoparticle diameter.

necessarily exhibit some varying degree of structure sensitivity because of the electronic differences resulting from the changing coordination of metal sites with structure, which in turn modify the binding energies of adsorbates and, through linear free energy relationships, the activation energy for elementary steps[18].

2.1.2 Relevance of Structure Sensitivity in HDO

Despite the likelihood on a fundamental level that mechanistic steps in the HDO reaction, including deoxygenation or hydrogenation, exhibit structure sensitivity over Pt catalysts, there has been a lack of work that seeks to characterize the effect of Pt structure on HDO selectivity. Such structure-activity relationships represent an opportunity to tune HDO activity and selectivity, particularly towards undesired side reactions resulting in hydrogenation and coking, without the use of catalyst modifiers which introduce potential unnecessary complexity.

For instance, prior work unrelated to HDO has shown that aromatic ring hydrogenation requires a planar adsorption geometry that has a relatively large ensemble requirement (~6 Pt atoms[19–21]) compared to the activation of other moieties, a requirement that makes it sensitive to changes in particle size and shape. Metal particle size-dependent reactivity derives from the decreasing relative concentrations of extended metal terraces (well-coordinated, flat surfaces) with decreasing particle size and the concomitant increase in the relative concentration of under-coordinated metal sites (steps, edges, corners, etc.). The sensitivity of catalytic reactivity to particle size has been observed in benzene hydrogenation over Pt/SiO_2 catalysts, where smaller Pt nanoparticles exhibited lower turnover frequencies for hydrogenation to cyclohexane than larger particles, demonstrating the importance of extended flat metal surfaces for ring hydrogenation[22]. Therefore, our premise is that the use of small metal nanoparticles in HDO reactions might restrict planar aromatic ring adsorption, thus improving selectivity towards aromatic products.

Interestingly, the opposite trend has been observed for deoxygenation turnover frequency, which increases on smaller metal particles, stemming from facilitated C-O cleavage

at undercoordinated sites on metal nanoparticle surfaces[23–25], which increase in relative content with decreasing particle size. Thus, smaller metal particle sizes might suppress planar adsorption of phenolics, resulting in decreased rates of hydrogenation, but facilitate the cleavage of C-O bonds at under-coordinated sites with a high capacity for deoxygenation. Importantly, however, it has been shown that this trend in deoxygenation activity breaks down at the single atom limit[26], potentially due to insufficiently small ensemble size and accessible charge states for C-O bond cleavage. Thus, it is reasonable to expect that an optimum metal particle size may exist that maximizes HDO activity and selectivity.

Despite the evidenced influence of metal particle size (and active site structure) on reactions associated with HDO of lignin-derived monomers, limited work exists that tests this hypothesis. For example, it was found that in phenol HDO, turnover frequencies for hydrogenation increased and deoxygenation decreased with increasing particle sizes between 5 and 22 nm over Ni/SiO_2 catalysts[27]. Similarly, it was demonstrated for HDO of m-cresol over Ni/SiO_2 catalysts that smaller Ni particle sizes suppressed methanation via hydrogenolysis and increased rates of HDO towards toluene[28]. However, this work also reported the increase of aromatic ring hydrogenation rates with decreasing Ni particle size, in opposition to the report on phenol HDO. These reports generally support the expected influence of metal particle size described above with regard to deoxygenation, though questions remain as to the influence of particle size on aromatic HDO product selectivity, specifically regarding the structure sensitivity of aromatic ring hydrogenation. Additionally, no investigation into the influence of metal particle size has yet been made for Pt catalysts in HDO, despite their frequent use.

Importantly, prior reports that have examined metal particle size-dependent HDO reactivity have been limited to simple mono-oxygenated substrates, such as phenol or cresol.

Though these substrates provide insight into mechanistic details, realistic lignin-derived feedstocks contain a significant fraction of di- and tri-oxygenated phenolic species, consisting of both hydroxyl and alkoxyl functionalities[29,30]. As a result, there is little understanding of how metal nanoparticle size, and thus active site structure, influences HDO rates of various oxygenate functionalities (i.e. hydroxyl vs. alkoxyl group deoxygenation) and aromatic hydrogenation in multi-oxygenated phenolics.

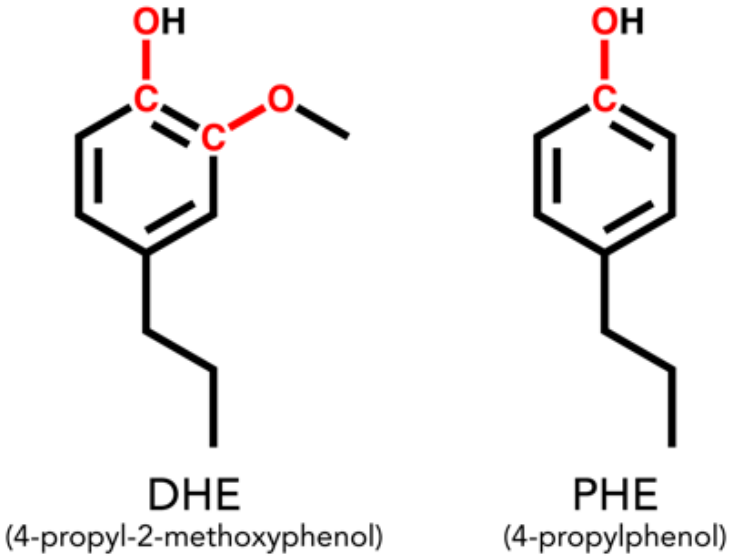

Figure 2.4: Structures of model lignols utilized this work as substrates for HDO reactions.

Here, we address these knowledge gaps and examine the influence of Pt particle size (2-12 nm) on the HDO of a multi-oxygenated phenolic substrate, dihydroeugenol (DHE). Pt particles were supported on SiO_2 supports to remove the influence of support acidity, and the Pt structure and exposed Pt site characteristics were characterized via transmission electron microscopy, volumetric chemisorption, and CO probe molecule FT-IR spectroscopy. Batch reactor DHE HDO studies were conducted to investigate the effects of Pt particle size on hydroxyl and methoxyl group deoxygenation, as well as aromatic hydrogenation. By measuring product concentrations as a function of substrate conversion, starting from both DHE and 4-propylphenol (Figure 2.4), the influence of Pt size, and thus active site structure,

on specific steps within the HDO network was elucidated. We also explore the competing roles of kinetics and thermodynamics on the product evolution in batch reactors as a function of time, driven in part by the lower hydrogen availability in liquid-phase systems compared to studies reported in the vapor phase. The findings presented here demonstrate the importance of controlling the structure of metal active sites to dictate desired product selectivity in the HDO of multi-oxygenated phenolics.

2.2 Results

2.2.1 Catalyst Characterization

To elucidate the sensitivity of phenolic HDO chemistry to the structure of active sites on metal nanoparticle surfaces, catalysts containing varying distributions of Pt particle sizes were synthesized on high surface area SiO_2 supports (170+ m^2/g) by altering Pt weight loading and calcination treatment conditions. Focus was placed on varying Pt particle sizes between an average of 1 and 10 nm in diameter, as the fraction of under-coordinated sites (steps, edges, etc.) and well-coordinated sites (planar terraces such as (111) and (100) planes) exposed on metal nanoparticle surfaces change most significantly in this size range (Figure 2.3). SiO_2 was chosen as the support because of its inactivity in HDO[31,32], which isolates the influence of Pt size and active site structure on HDO chemistry. However, the synthesis of late transition metal catalysts with controlled metal particle size distributions on SiO_2 is a known challenge. Both metal precursors and the metallic particles themselves bind weakly to the SiO_2 surface[33,34], resulting in aggregation and sintering upon elevated thermal treatment, such as those found during calcination, reduction, or HDO reactions[35,36]. This behavior has led researchers to deem the SiO_2 surface an "ice skating rink"[37], aptly capturing the difficulty of immobilizing

supported materials on these surfaces, which can result in catalyst samples with a broad distribution of particle sizes.

Pt/SiO_2 catalysts were prepared using modified strong electrostatic adsorption[35,38] (SEA) with metal loadings ranging from 0.4 wt% to 6 wt%. These materials were then treated by different calcination conditions (0.4 wt% at 300 ˚C, 2 wt% at 325 ˚C, and 6 wt% at 600 ˚C) to produce catalysts with distinct Pt nanoparticle distributions, summarized in Table 2.1. The catalysts are named X-Pt, where X indicates the catalyst weight loading (i.e. 0.4-Pt for 0.4 wt% Pt). The catalysts were characterized by HAADF-STEM, CO DRIFTS, and CO chemisorption. Each technique provides a different estimate for average Pt particle size depending on the size distribution, particle shape, and sample pretreatment[39–41].

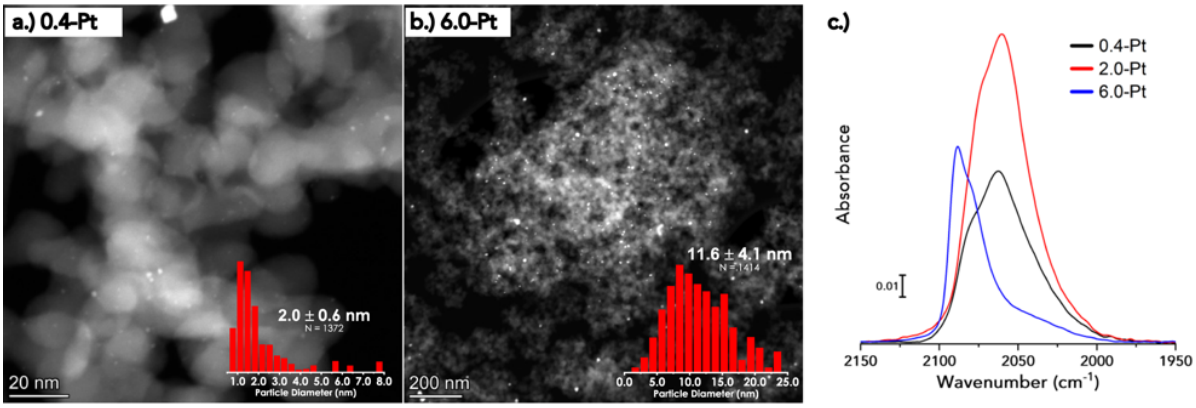

Figure 2.5: HAADF-STEM images of a.) 0.4-Pt and b.) 6.0-Pt catalysts. Corresponding particle size distributions on a surface area normalized basis are shown as inset images. c.) CO DRIFTS spectra of Pt/SiO_2 catalysts after adsorption of CO at 25˚C following *in situ* reduction under 10%

Volumetric CO chemisorption following *in situ* H_2 reduction showed Pt dispersions ranging from 26% for 0.4-Pt to 2% for 6.0-Pt. Based on assumptions of hemispherical particles[42], average Pt particle sizes were estimated to be 3.8 nm (0.4-Pt) to 44 nm (6.0-Pt), as shown in Table 2.1. The estimated average Pt particle size increases with Pt loading and calcination temperature, consistent with particle aggregation caused by greater Pt surface density and sintering.

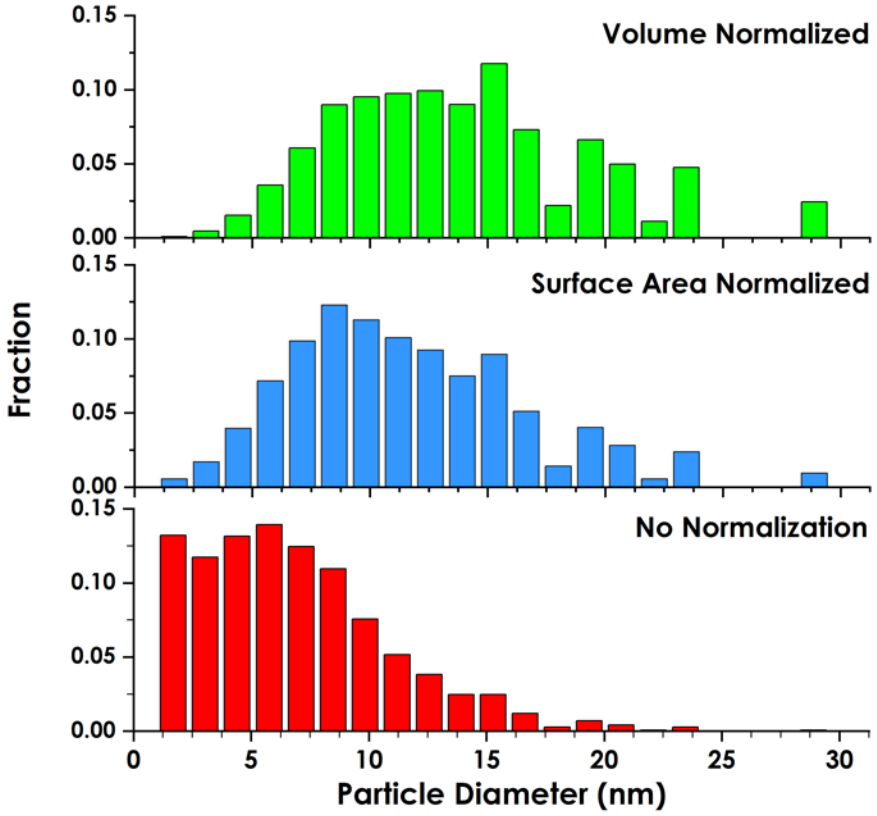

Figure 2.6: Histograms representing the contribution of binned particle diameters to the overall sample as measured by HAADF-STEM. Histograms are normalized by three different means: no normalization (red), surface area-normalized (blue), and volume-normalized (green). As can be seen, histogram density shifts towards larger diameters for normalized calculations, highlighting the greater contribution of large particles to both total surface area and volume of metal sites imaged on the catalyst.

To provide more insight into the Pt particle size distributions, HAADF-STEM images were collected. Particle size averages and distributions are presented using counts, surface-area-normalization, and volume-normalization. These three data presentations result in distinct averages and distributions due to changing surface area:volume ratio as a function of particle size, which is demonstrated in Figure 2.6. Typical images of the 0.4-Pt and 6.0-Pt catalysts are shown in Figures 2.5a and 2.5b, along with the surface area-normalized particle size distributions. The surface area-normalized average particle sizes and distributions are used since nanoparticle surface properties directly influence the reactivity of heterogeneous

catalysts. The average Pt particle size increases with Pt weight loading, from 2.0 ± 0.6 nm for 0.4-Pt to 3.0 ± 0.9 nm for 2.0-Pt, and to 11.6 ± 4.6 nm for 6.0-Pt, highlighting a consistent trend with the CO chemisorption results.

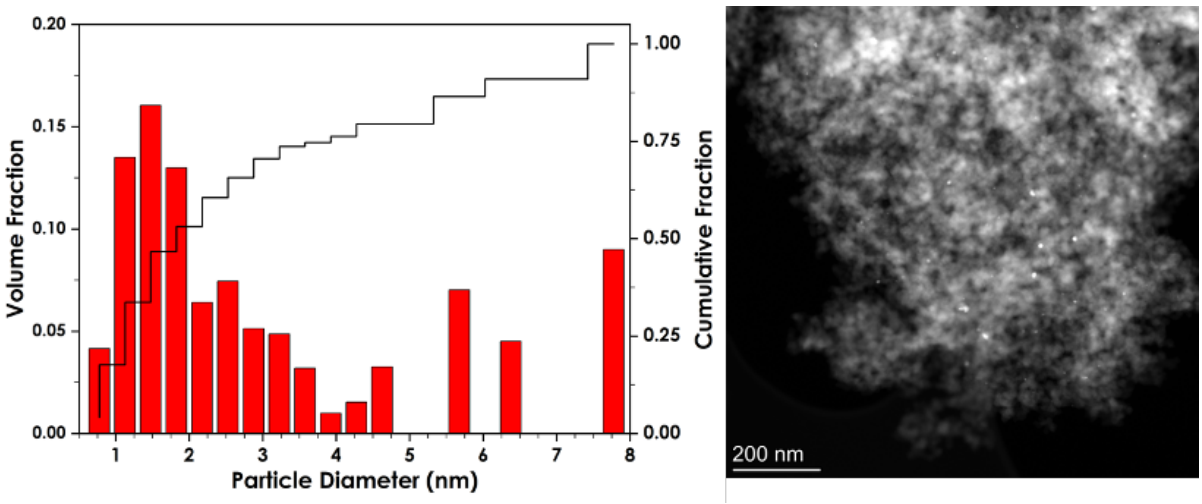

Figure 2.7: Another representation of the effects of volume-normalization for the case of 0.4-Pt. The volume-normalized histogram on the left clearly shows that a large portion of the Pt volume in 0.4-Pt is ascribed to small (<2 nm) Pt particles. However, nearly 25% of the total Pt atoms imaged (captured by volume-normalization) are contained in the 2% of imaged particles >5 nm, explaining the discrepancy in CO chemisorption and DRIFTS/TEM results for measured particle size.

As shown in Table 2.1, STEM-based particle size estimates are lower than chemisorption-based values. This is attributed to outliers in the particle size distributions. Using 0.4-Pt as an example, particle size distributions from HAADF-STEM images show that although there are only 22 out of 1372 (~2%) counted particles greater than 3 nm in size, these outlier particles contain ~40% of the total imaged Pt volume (Figure 2.7). These outlier particles contribute to the measured CO chemisorption values (a volume-normalized analysis), but less so to surface area-normalized analysis (e.g. reactivity and surface area normalized TEM). This can be seen in the better agreement in average particle sizes obtained via CO chemisorption and volume-normalized STEM images.

HAADF-STEM and chemisorption measurements were complemented by CO DRIFTS (Figure 2.5c), which benefits from being a sample-averaged, bulk measurement, similar to CO

chemisorption, yet provides particle size estimates based on only metal surface properties, analogous to surface-normalized HAADF-STEM. The vibrational frequency of CO adsorbed on Pt is sensitive to the Pt coordination number, allowing for the identification of CO adsorbed to well-coordinated (WC, 8+ coordinate) Pt sites, located at the surface of flat, low-index terraces, and under-coordinated (UC, 7 or fewer coordinate) sites, which are found at steps, edges, corners, and other structural defect sites[43,44]. The ratio of these sites on Pt surfaces is known to be a function of particle size[45–47].

Table 2.1

	Calcination Treatment	Mean Particle Size (nm)				
		TEM				
		Counts[a]	S.A. Normalized[b]	Volume Normalized[c]	CO DRIFTS[d]	CO Chemisorption[e]
0.4-Pt	300˚C, 2 hours	1.3 ± 0.6	2.0 ± 0.6	3.1 ± 0.6	<1.1	3.8 ± 0.3
2.0-Pt	325˚C, 3 hours	1.4 ± 0.9	3.0 ± 0.9	4.6 ± 0.9	1.6	4.9 ± 1.2
6.0-Pt	600˚C, 6 hours	6.8 ± 4.1	11.6 ± 4.1	13.8 ± 4.1	2.9-7.1	44 ± 17

Figure 2.5c shows CO DRIFTS spectra at saturation CO coverage and room temperature for the Pt catalysts following *in situ* reduction in H_2. Each spectrum consists of a complex feature centered between 2097 and 2050 cm^{-1}, consistent with the C-O stretching frequency of CO bound linearly atop Pt atoms with varying coordination numbers[45–49]. The change in position of the observed CO stretching frequency stems from both the convolution of the individual features associated with CO adsorbed to WC and UC Pt sites at ~2090-2080 and ~2070-2050 cm^{-1}, respectively[41,43], as well as shifts related to CO dipole-dipole interactions[50–52]. Deconvolution of the CO DRIFTS spectra using 3 Gaussian features, as described in more detail in Figure 2.8, results in estimated average particle sizes of ~1 nm to 7 nm for the 0.4-Pt and 6.0-Pt catalysts, respectively. Overall, CO DRIFTS estimates follow the

same trend in average particle size as observed from both HAADF-STEM and CO chemisorption measurements. CO DRIFTS provided the smallest average Pt particle size estimate from the three techniques, likely due to CO-induced roughening of Pt surfaces, which causes an overestimation of the UC relative site concentration[41]. Despite small discrepancies, the particle size estimates from CO-DRIFTS are in better agreement with surface-normalized HAADF-STEM distributions than estimates from CO chemisorption, suggesting that the CO DRIFTS analysis is less skewed by the presence of outlier particles in broad particle size distributions. Regardless of the technique used, the results consistently demonstrate that the

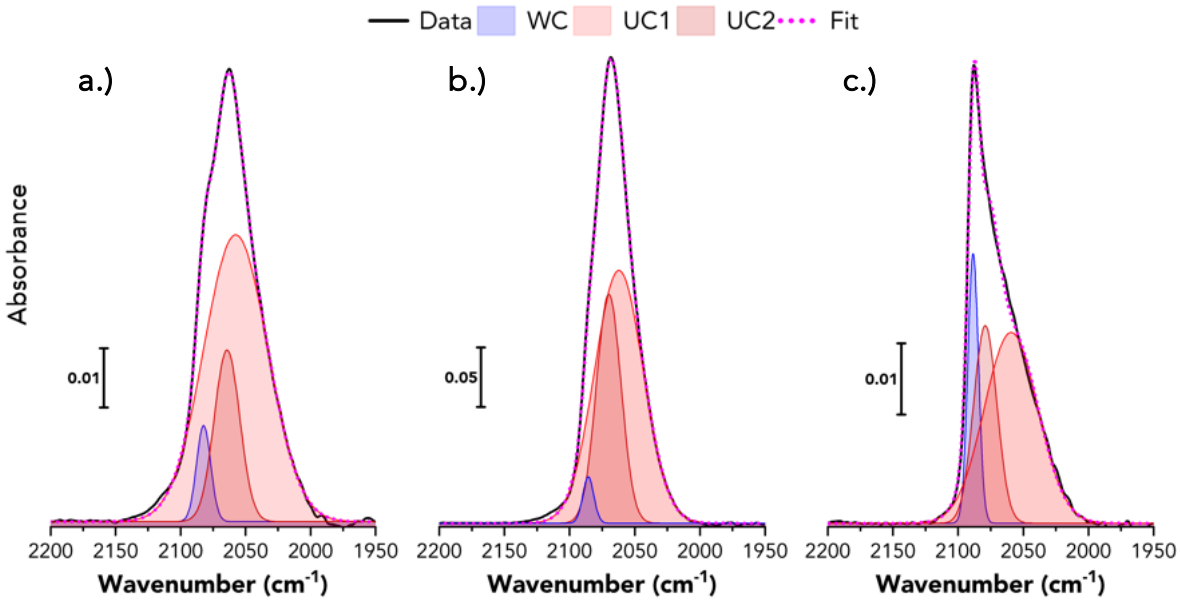

Figure 2.8: Spectral deconvolution of CO DRIFTS spectra shown in Figure 2c. Deconvolution uses 3 Gaussian features to best represent the experimentally obtained spectra, with specifically 2 Gaussian features (UC1 and UC2) used to describe the UC site peak shape, which has been frequently observed to be asymmetric. For fitting, peak maxima and intensity were set as free parameters, while peak FWHM was constrained between the same limits for all catalysts. Allowing peak maxima to change freely captures the changing spectral signature of geometrically identical CO features with increasing dipole-dipole coupling, most noticeably observed for CO linearly bound to WC Pt terraces. Increased dipole-dipole coupling with increasing terrace size (and Pt particle size) results in a blue-shift and narrowing of the feature, despite the peak corresponding to the same structural motif (i.e. WC sites).

Pt/SiO_2 catalysts prepared exhibit distinct average particle size distributions and provide sufficient variation of surface composition to determine the structure sensitivity of HDO.

2.2.2 HDO Reactivity

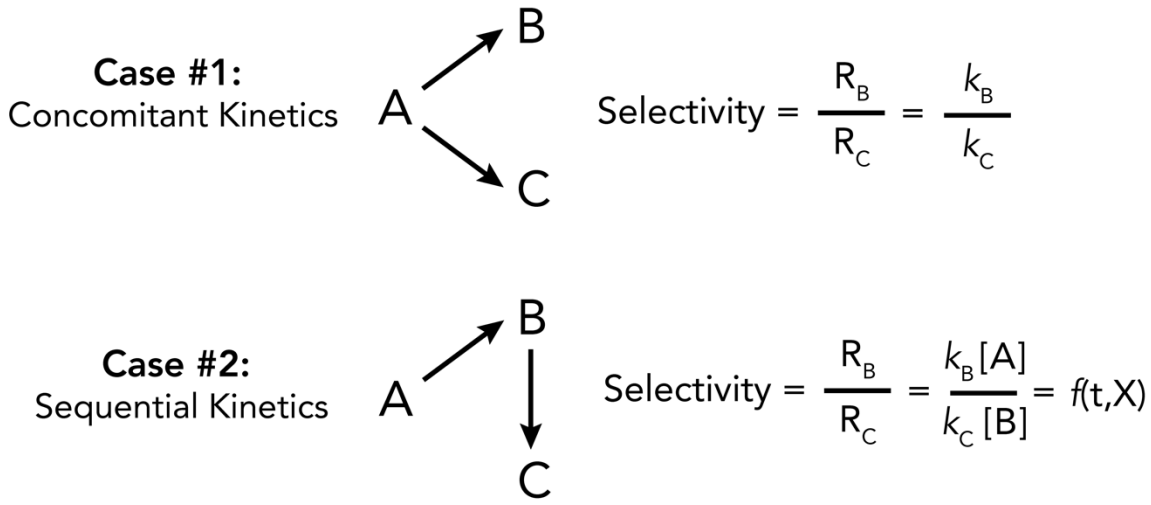

Scheme 2.1: Brief kinetics representation of the importance of isoconversion measurements in the case of sequential reaction pathways. Case #2 (sequential) shows that the measured selectivity is a function of time and conversion, compared to the case of concomitant kinetics (Case #1) where selectivity is defined by the relative rate constants.

The Pt/SiO_2 materials described above were used to catalyze HDO of the multi-oxygenated lignin model compound dihydroeugenol (DHE). Liquid-phase batch reactions were conducted in a high-pressure reactor at 275˚C using cyclohexane as a solvent. To ensure comparability between Pt/SiO_2 catalysts, reactions were initially conducted at isoconversion, moderated by changing catalyst loading into the reactor, and reaction performance was analyzed by quantifying DHE conversion and product yield using GC-FID. The analysis of reactions at isoconversion is essential for complex reaction networks in which substrate conversion and product selectivity are intrinsically linked (Scheme 2.1)[53]. The investigation of low DHE conversions (<15%) and short reaction times (under 2 hours) ensured that the studies of HDO structure sensitivity were made in the absence of catalyst deactivation effects (*vide*

infra), which is a known challenge for HDO of oxygenates[54–56]. For all Pt/SiO_2 catalysts studied, product analysis of the liquid phase resulted in the quantification of 7 major products, shown in Scheme 2.1, which include both partially and fully deoxygenated species. Mass balances calculated on the basis of C_6 ring products for the isoconversion experiments in Table 2.2 and Figure 2.9 were above 87% for all catalysts, indicating that the products shown here capture the primary reactivity. The remaining mass not quantified by GC-FID is attributed to the formation of strongly bound adsorbates and oligomers which cannot be measured by GC-FID and are ubiquitously observed under comparable reaction conditions[57–59]. Analysis of the gas phase products in the headspace of the reactor indicates the formation of CH_4, CO, and methanol likely stemming from demethoxylation and demethylation, with no evidence of light hydrocarbons stemming from cracking reactions. Thus, gaseous products do not need to be accounted for in the mass balance.

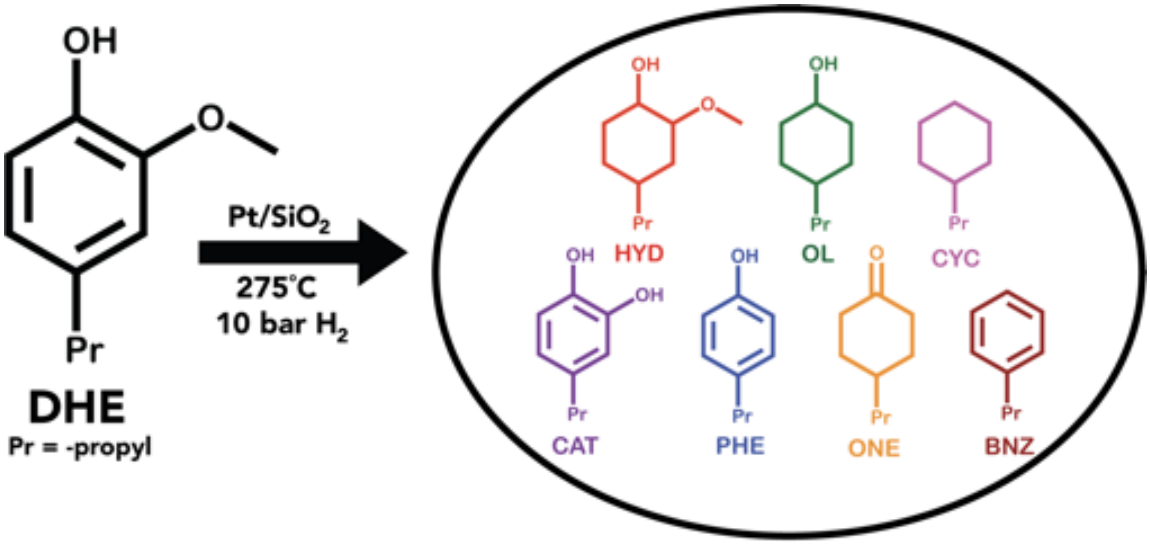

Scheme 2.2: Structures and naming convention used in discussion for DHE and its products identified by GC-FID. Products (left to right): 4-propyl-2-methoxycyclohexanol (HYD), 4-propylcyclohexanol (OL), 4-propylcyclohexane (CYC), 4-propylcatechol (CAT), 4-propylphenol (PHE), 4-propylcyclohexanone (ONE), 4-propylbenzene (BNZ).

Table 2.2 shows rates of DHE consumption estimated using the measured conversion at 2 hours, normalized by the amount of Pt loaded into the reactor. A DHE conversion of 14% was observed after 2 hours under reaction conditions for 50 mg of 0.4-Pt, while 20 mg of the 6.0-Pt catalyst reached 8% DHE conversion in a 2-hour reaction. The DHE consumption rates calculated on a Pt weight basis are 10-fold higher for 0.4-Pt as compared to 6.0-Pt. However, after normalizing the DHE consumption rates by the active Pt site density measured by CO chemisorption, the turnover frequencies (TOF) for DHE are comparable for all 3 catalysts. It is important to note that due to the complexity of the reaction network, these estimates do not capture differences in estimated rates for individual reactions, such as hydrogenation and deoxygenation, but rather capture the similar per-site rates of DHE consumption. Still, the comparable TOFs across the three catalysts are indicative of a shared rate-limiting step prior to the structure-sensitive steps discussed below. One explanation may be the saturation of the Pt surface by adsorbates, causing adsorption to be kinetically relevant for all catalysts, while product selectivity is dictated by the subsequent reaction steps. Another possibility is that

Table 2.2

Sample	Catalyst Loaded (mg)	Conversion (%)	Rate ($\frac{mmol_{DHE}}{hr*g_{Pt}}$)	TOF (hr^{-1})
0.4-Pt	50	14	1053	790
2.0-Pt	15	15	752	712
6.0-Pt	20	8	100	848

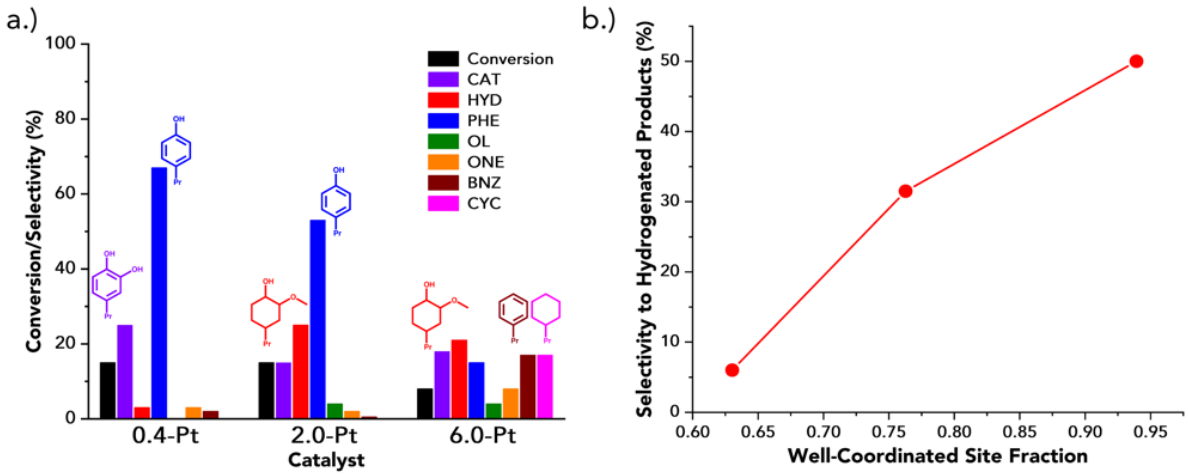

Figure 2.9: Results of DHE HDO reactions at isoconversion (~15%) over various-sized Pt catalysts. a.) Selectivity breakdown of all species detected by GC-FID for DHE HDO. b.) Grouping of hydrogenated products (HYD, OL, ONE, CYC) from DHE HDO shows clear trend with increasing particle size. *Conditions*: 500 mg DHE, 275˚C, 2 hours, 20 mL cyclohexane, 10 bar H_2

structure-insensitive deactivation through site blocking by oligomeric species is occurring, leading to inaccurate TOF estimations due to transient changes in site availability.

Analysis of the product selectivity (Figure 2.9) reveals that there are differences in the observed products with variation of the Pt particle size distribution. The most apparent trend is the significant drop in 4-propylphenol (PHE) selectivity with increasing average Pt particle size. PHE is presumably the product of direct demethoxylation of DHE (partial HDO), though this will be discussed later. PHE is the primary product over 0.4-Pt at 68% selectivity, as well as over 2.0-Pt, albeit at a lower selectivity of 53% due to increasing selectivity to off-target products such as 4-propyl-2-methoxycyclohexanol (HYD), the product of DHE ring hydrogenation. This trend continues with 6.0-Pt, which exhibits the lowest selectivity to PHE after 2 hours of reaction at 15%. It is worth noting that there is no evidence of initial attack on the hydroxyl group of DHE to yield anisole derivatives or the HDO products of anisole derivatives. Initial deoxygenation occurs through the methoxy functionality of DHE, consistent with the weaker bond strength of the C-OCH_3 bond[60].

In addition to PHE formation, the production of 4-propylcatechol (CAT) via DHE demethylation is also observed. CAT is the only other major product formed by 0.4-Pt, with a selectivity of 25%. However, unlike the monotonic trend observed for PHE formation with increasing Pt particle size across the catalyst series, there is no discernible trend of CAT selectivity as a function of particle size distribution. 2.0-Pt and 6.0-Pt have CAT selectivities of 15% and 18%, respectively, similar to what was observed for 0.4-Pt despite the marked differences in PHE productivity, Pt loading, and average Pt particle size.

Another clear trend exists between average Pt particle size and selectivity to the hydrogenated products (4-propyl-2-methoxycyclohexanol, HYD; 4-propylcyclohexanol, OL; 4-propylcyclohexanone, ONE; 4-propylcyclohexane, CYC), which are the result of ring hydrogenation of DHE, PHE, or 4-propylbenzene (BNZ), respectively. The production of these species is summarized in Figure 2.9b, showing the collective selectivity towards these 4 products as a function of well-coordinated (WC) Pt site fraction, estimated from average particle size using the cuboctahedron model geometry[41,61]. As discussed above, 0.4-Pt demonstrates negligible formation of these products, indicating a low rate of aromatic ring hydrogenation despite the occurrence of partial HDO of DHE to PHE and CAT. Activity towards aromatic hydrogenation increases with increasing Pt particle size, with 2.0-Pt producing 32% hydrogenated ring products and 6.0-Pt increasing to 50%. For 2.0-Pt, the increase is primarily driven by an increased selectivity to HYD, which constitutes 23% of the overall products, although PHE remains the dominant product. HYD selectivity does not increase in the case of 6.0-Pt, and instead, the increase in total hydrogenated products is driven primarily by increased selectivity to CYC at 17%. In contrast, 0.4-Pt and 2.0-Pt did not produce detectable quantities of CYC.

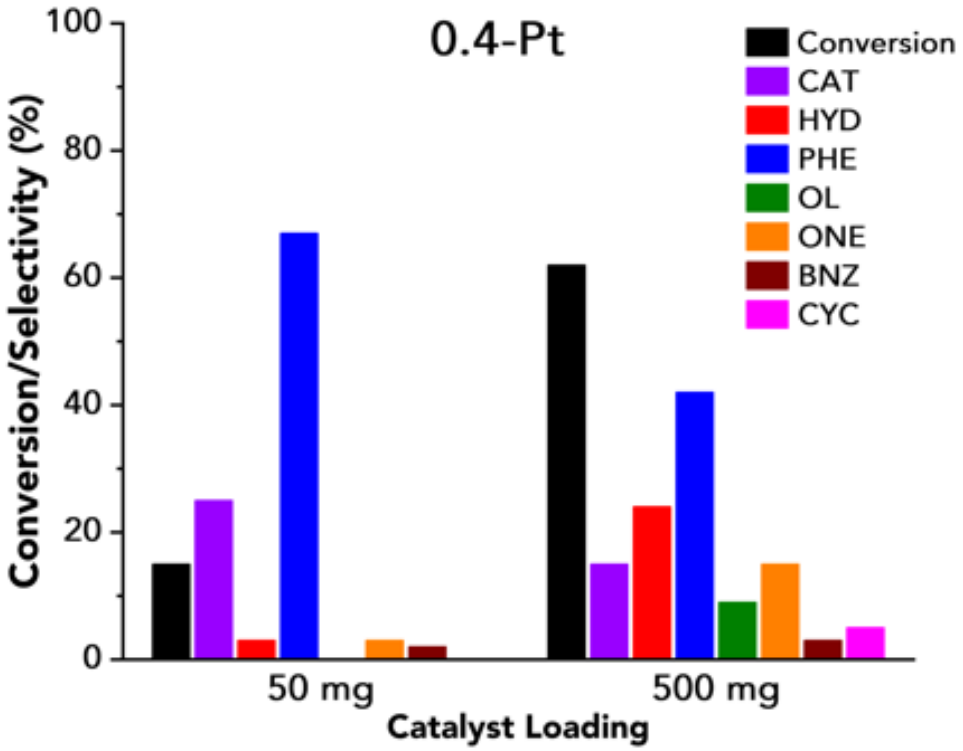

Figure 2.10: HDO reactions of DHE investigating the influence of 0.4-Pt catalyst loading on product selectivity. Results demonstrate that the selective formation of PHE by 0.4-Pt persists at significantly higher conversions than shown in Figure 2, underscoring that this behavior stems from the structure sensitivity of HDO over Pt/SiO_2 catalysts. *Conditions*: 500 mg DHE, 275˚C, 2 hours, 20 mL cyclohexane, 10 bar H_2.

The increased activity of 6.0-Pt to CYC production is accompanied by increased production of BNZ at 17% selectivity of the overall products. Thus, 6.0-Pt provides the highest activity for complete HDO to fully-deoxygenated products, in addition to exhibiting the highest rates of ring hydrogenation. It is worth noting the nearly equal selectivity of BNZ and CYC in the case of 6.0-Pt, despite the observed ability of 6.0-Pt to effectively perform aromatic ring hydrogenation. This is analogous to the results of 0.4-Pt and 2.0-Pt reactions, where BNZ is observed in small quantities (<2% selectivity), but CYC is not observed. Additionally, the production of BNZ and CYC is expected to be unrelated to the hydrogenation activity of 6.0-Pt, as previous work has shown Pt/SiO_2 catalysts do not facilitate the HDO of saturated oxygenates[31].

Deactivation due to strong adsorption of substrates and intermediates is a known issue for HDO catalysts, particularly for small nanoparticles and clusters exhibiting a large fraction of UC sites which bind oxygenates more strongly than WC sites[25]. To ensure that differences in the isoconversion experiments were not a result of deactivation of Pt/SiO_2 catalysts, HDO of DHE over 0.4-Pt was carried out in the presence of 500 mg catalyst to reach a higher DHE conversion of 62%, as shown in Figure 2.10. Exhibiting the smallest average particle size and thus the highest fraction of UC sites, the 0.4-Pt catalyst is expected to be most affected by deactivation. However, Figure 2.10 shows that the product selectivity trends are comparable at both 15% and 62% conversion of DHE. PHE remains the dominant product at 42% of the products, indicating that the 0.4-Pt catalyst is effective for DHE demethoxylation over hydrogenation even at high conversions. In the high conversion experiment, HYD, OL, and ONE selectivities are all higher than in the isoconversion experiment but remain minor products relative to PHE. This contrasts experiments performed over 6.0-Pt, over which HYD was the dominant product. Therefore, the structure sensitivity observed in the isoconversion experiments is not a result of catalyst deactivation, but rather differences in the intrinsic reactivity of DHE over different Pt sites.

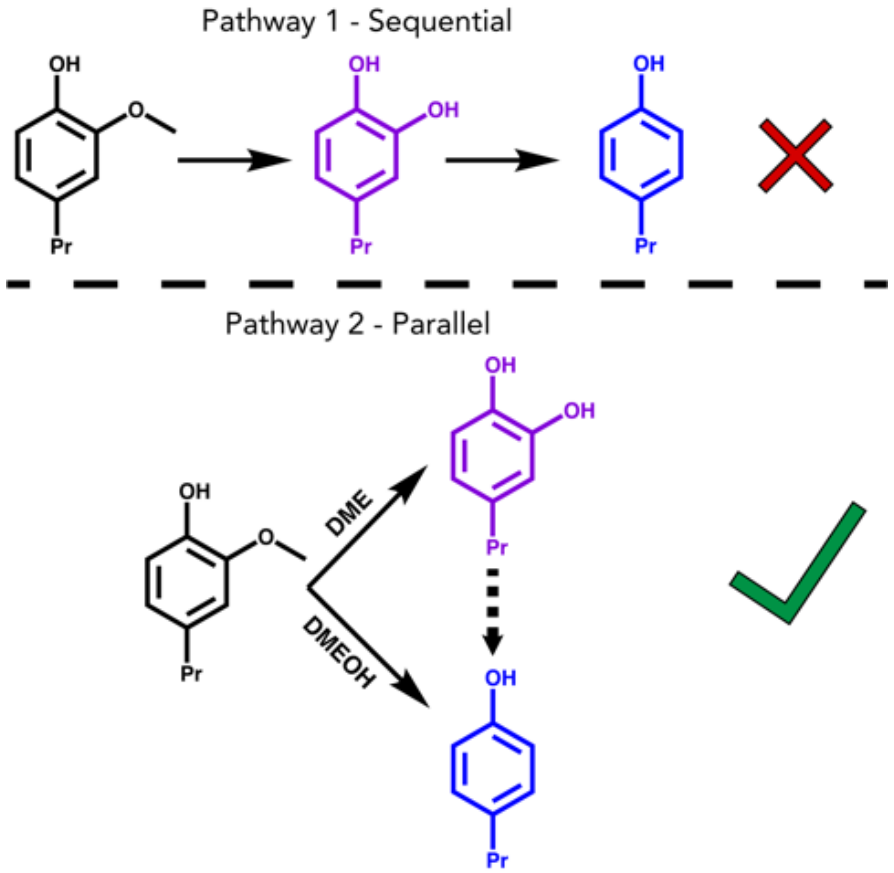

Scheme 2.3: Proposed pathways for initial deoxygenation of DHE via either sequential or parallel schemes. Time profile reactions evidence the parallel formation of CAT and PHE via independent routes (Pathway 2)

The isoconversion results demonstrate that the product distribution of DHE HDO is sensitive to the average particle size of Pt/SiO_2 catalysts and thus the geometry of the exposed active Pt sites. However, single time-point experiments alone cannot determine the reaction pathways by which final products are formed, which contain vital information as to the specific reactions exhibiting structure sensitivity. For example, it is unclear whether PHE is produced directly from DHE via demethoxylation or if PHE is formed from CAT via dehydroxylation, as shown in Scheme 2.3. To explore this and identify the transience of product formation in DHE HDO, time profile experiments were conducted between 0 and 2 hours at 275˚C under 10 bar of H_2, shown in Figure 2.11. Focus was placed on the 0.4-Pt and 6.0-Pt catalysts, as

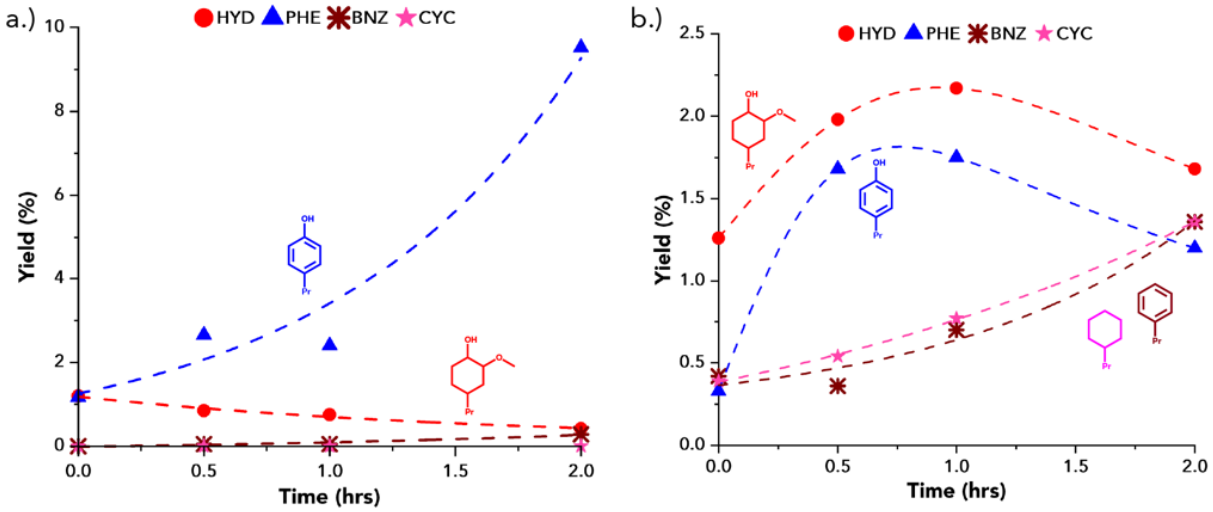

Figure 2.11: Selected product yield as a function of reaction time for a.) 0.4-Pt and b.) 6.0-Pt. Lines are included to guide the eye only and do not represent kinetic fits. Product distributions are expressed in yield rather than selectivity to clarify changes in time due to changing conversion as well as selectivity. Black circles (o) and the corresponding black dotted line (- - -) represent conversion levels with time. *Conditions*: 500 mg DHE, 50 mg cat., 275˚C, 10 bar H_2, 20 mL cyclohexane.

these exhibited the greatest differences in product selectivity in the isoconversion experiments. Catalyst loadings were identical to those described in Table 2.2.

A notable feature of the batch reactor set-up is the introduction of catalyst and substrate to the reactor at room temperature, resulting in measurable activity during the thermal ramping stage to reaction temperature. To account for this, the data profile for 0 hours represents reactions that were set up and allowed to ramp to 275˚C before immediately quenching the reaction. Figure 2.11a shows the time profile experiments for 0.4-Pt, which exhibits the aforementioned reactivity during the thermal ramp, resulting in 1.5% conversion at 0 hours. Interestingly, it can be seen that a major reaction during the thermal ramp is aromatic ring hydrogenation of DHE to form HYD, which was only a minor product over 0.4-Pt during 2-hour reactions at 275˚C. This is consistent with the lower apparent activation barriers reported for aromatic ring hydrogenation over Pt catalysts (50-100 kJ/mol[62]) compared to apparent

barriers for HDO (100-200 kJ/mol[63–65]); thus, at temperatures below 275˚C, hydrogenation is facilitated relative to HDO over 0.4-Pt.

At 275˚C, DHE conversion increases from 3% at 0 hours to 14% at 2 hours. During this period, PHE and CAT are produced and become the dominant products, as seen in the isoconversion experiments. At the same time, overall HYD yield falls, indicating HYD consumption in the reaction. Considering the inability of Pt/SiO_2 catalysts to perform deoxygenation on saturated species[31], we attribute this consumption to dehydrogenation to reform the original DHE substrate, which can then undergo deoxygenation at reaction temperatures to form PHE and CAT. This points to an interesting role of hydrogenation and dehydrogenation over 0.4-Pt which will later be discussed. As noted in the isoconversion experiments, production of other deoxygenated species such as OL, ONE, BNZ, and CYC is minimal over 0.4-Pt. One notable trend is the monotonic loss of OL yield paired with increasing ONE and BNZ yields. The greatest OL yield occurring during the thermal ramp is consistent with the hydrogenation activity of 0.4-Pt below reaction temperature, as seen in the behavior of HYD formation.

The production of PHE and CAT occurs at similar rates over the reaction period, increasing in yield from their original values of 1.2% and 0.4%, respectively, to 9.5% and 3.5%, corresponding to final selectivities of 54% and 35%. However, what is not observed is the increase of PHE yield at the expense of CAT yield, which is what would be expected in a sequential reaction scheme (Scheme 2.3). Instead, the simultaneous formation of PHE and CAT supports the parallel formation of both products through distinct pathways of demethylation and demethoxylation of DHE. Though the interconversion of CAT and PHE cannot be entirely excluded, it is apparently not the dominant pathway of PHE formation under the conditions

studied here. This also suggests that the structure-sensitive reaction in the formation of PHE from DHE is indeed demethoxylation and not the conversion of CAT to PHE. Similarly, the demethylation of DHE to CAT is not apparently structure sensitive, as evidenced by the nearly constant selectivity to CAT across all Pt/SiO_2 catalysts studied.

Time profile experiments over 6.0-Pt (Figure 2.11b) show different trends. As with 0.4-Pt, HYD formation is dominant during the thermal ramp. However, unlike 0.4-Pt, HYD yield continues to increase up to 1 hour before decreasing slightly at 2 hours. This contrasts with 0.4-Pt reactions, where HYD concentration decreases monotonically during the time profile

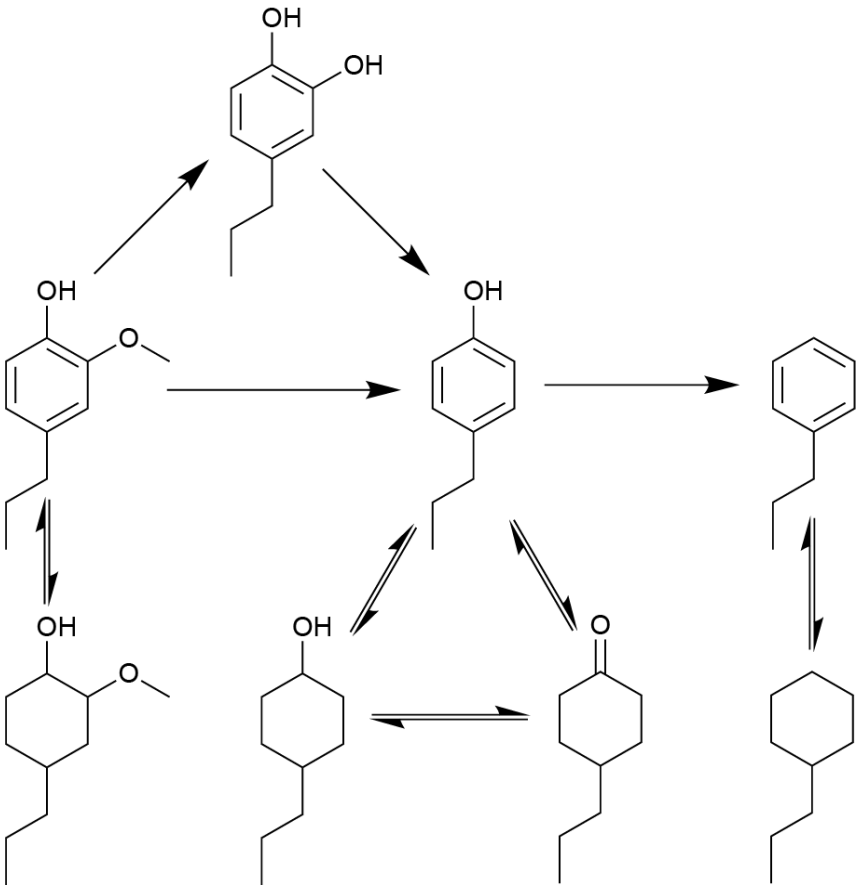

Scheme 2.4: Overall proposed scheme of DHE HDO over Pt/SiO_2. Single arrows represent steps which are observed to be irreversible under the reaction conditions studied. Double arrows indicate reactions which show evidence of being reversible, though not necessarily at equilibrium or quasi-equilibrated.

experiments due to dehydrogenation to DHE. This is consistent with the reported structure sensitivity of dehydrogenation[66], which has pointed towards smaller nanoparticles being more effective catalysts for dehydrogenation. Thus, the larger nanoparticles present in the 6.0-Pt catalyst perform dehydrogenation less effectively than 0.4-Pt, but more effectively catalyze hydrogenation of DHE to HYD.

The most striking difference in 6.0-Pt performance over the 2-hour time profile compared to 0.4-Pt reactions is the production and consumption of PHE. PHE yield rises from 0.3% to 1.8% over 1 hour, before falling to 1.2% at 2 hours. Concomitant with the consumption of PHE between 1 and 2 hours is the rise of BNZ and CYC yields to 1.4% each at the end of the 2-hour reaction period. Clearly, PHE is an intermediate to form CYC and BNZ, but this pathway was not facilitated over 0.4-Pt. CAT formation over 6.0-Pt follows a similar trend as was observed over 0.4-Pt and additionally does not undergo any obvious consumption during the reaction period. It follows that CAT is not an intermediate towards the formation of CYC and BNZ, which apparently form only from PHE.

The time profiles highlight two trends that were not apparent in the isoconversion experiments (Figure 2.9). First, 0.4-Pt performs dehydrogenation at the reaction temperature, as shown in the loss of HYD yield with time, resulting in higher yields of aromatic products. On the other hand, 6.0-Pt does not facilitate dehydrogenation, thus leading toward off-target hydrogenated products such as HYD. Second is the greater ability of 6.0-Pt to form deeper deoxygenated products such as BNZ and CYC from DHE, specifically through the conversion of PHE. This supports the conclusions from the isoconversion experiments over 6.0-Pt and contrasts the inability of 0.4-Pt to facilitate the HDO of PHE. Clearly, deoxygenation of PHE

is distinct between the 0.4-Pt and 6.0-Pt catalysts and causes the discrepancy in fully-deoxygenated BNZ and CYC formation (Scheme 2.4).

As evidenced from the time profiles, although 0.4-Pt catalyzes the dehydrogenation of HYD back to DHE prior to HDO to deoxygenated species, hydrogenation to HYD clearly occurs during the thermal ramp. Since both reactions appear to be kinetically accessible over this catalyst, what was not immediately clear was the high yield of PHE over 0.4-Pt over a range of conversions (Figure 2.10) and time (Figure 2.11a) without significant hydrogenation of PHE to OL and ONE. One potential explanation of this is the ability of 0.4-Pt, through facile hydrogenation and dehydrogenation, to approach the equilibrium composition of saturated and unsaturated products. To explore this further, the HDO of DHE was studied over 0.4-Pt with varying initial H_2 pressures between 5 and 20 bar. A higher isoconversion level of 50% was targeted for each pressure, in comparison to the 10% isoconversion studied initially in Figure 2, to allow comparison of the product distribution at an advanced state in the reaction network after multiple potential reactions such as deoxygenation and hydrogenation.

Figure 2.12 shows that reactions over 0.4-Pt at 5 bar initial H_2 result in high selectivity to PHE of 66%, even at 54% conversion of DHE, which is almost identical to the PHE selectivity seen in Figure 2 at ~15% DHE conversion. Increasing H_2 pressure to 10 bar results in an increase of HYD selectivity to 24% at the expense of PHE, which drops to 42%, as well as an increase in OL and ONE selectivities to 9% and 15% respectively, though PHE remains the dominant product. Further increasing pressure to 20 bar results in a continuation of this trend, with HYD becoming the dominant product at 50% selectivity, with OL and PHE selectivities becoming approximately equal at 21% and 22%. These results show that the extent

of hydrogenation over 0.4-Pt is not inhibited by the catalyst structure, but rather is dictated by the pressure of H_2.

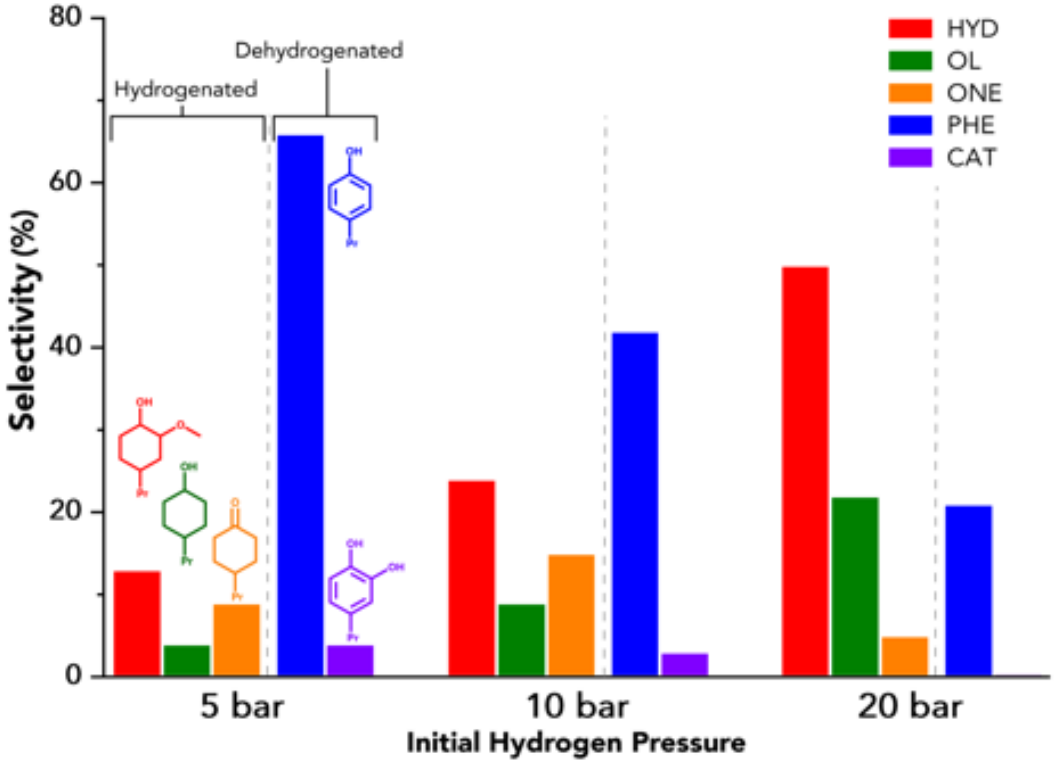

Figure 2.12: HDO reactions of DHE conducted under varying initial H_2 pressure using the 0.4-Pt catalyst. Conducted at isoconversion of ~50% by adjusting catalyst loading. Conditions: 500 mg DHE, 275˚C, 2 hours, 20 mL cyclohexane

Also, HYD selectivity increases to a greater extent with increasing H_2 pressure than OL and ONE selectivity. The increase in HYD selectivity represents decreasing HDO activity, as HYD is not the product of any deoxygenation. This supports the observation that non-acidic catalysts such as Pt/SiO_2 studied here are not active for the conversion of saturated species such as HYD, which act as dead ends in the HDO pathway unless they are able to undergo dehydrogenation back to aromatic species. This is also supported by pressure-dependent studies carried out over 6.0-Pt (Figure 2.13), which showed decreasing BNZ and CYC yield with H_2 pressure with increasing HYD yield. Thus, increasing H_2 pressure decreases yield for Pt/SiO_2 catalysts by facilitating dead-end product formation.

To understand the mechanistic differences between 0.4-Pt and 6.0-Pt in PHE dehydroxylation, HDO reactions starting from PHE as the substrate were conducted at 275˚C for 2 hours under 10 bar H_2, shown in Figure 6. Isoconversion conditions were achieved at approximately 25% conversion, moderated by different catalyst loading for each reaction. The product distributions demonstrate that there are again differences caused by Pt particle size distribution. Consistent with the observations of reactions using DHE as a substrate, 0.4-Pt and 2.0-Pt both catalyze relatively little conversion to BNZ and CYC, despite starting from PHE, a less oxygenated substrate than DHE. This is also consistent with the time profile results of 0.4-Pt, wherein PHE was effectively produced from DHE but did not appreciably react further. There is also a shift in the dominant product from OL to ONE in PHE HDO between 0.4-Pt

and 2.0-Pt, respectively, suggesting that there is some difference in the hydrogenation chemoselectivity of these two catalysts.

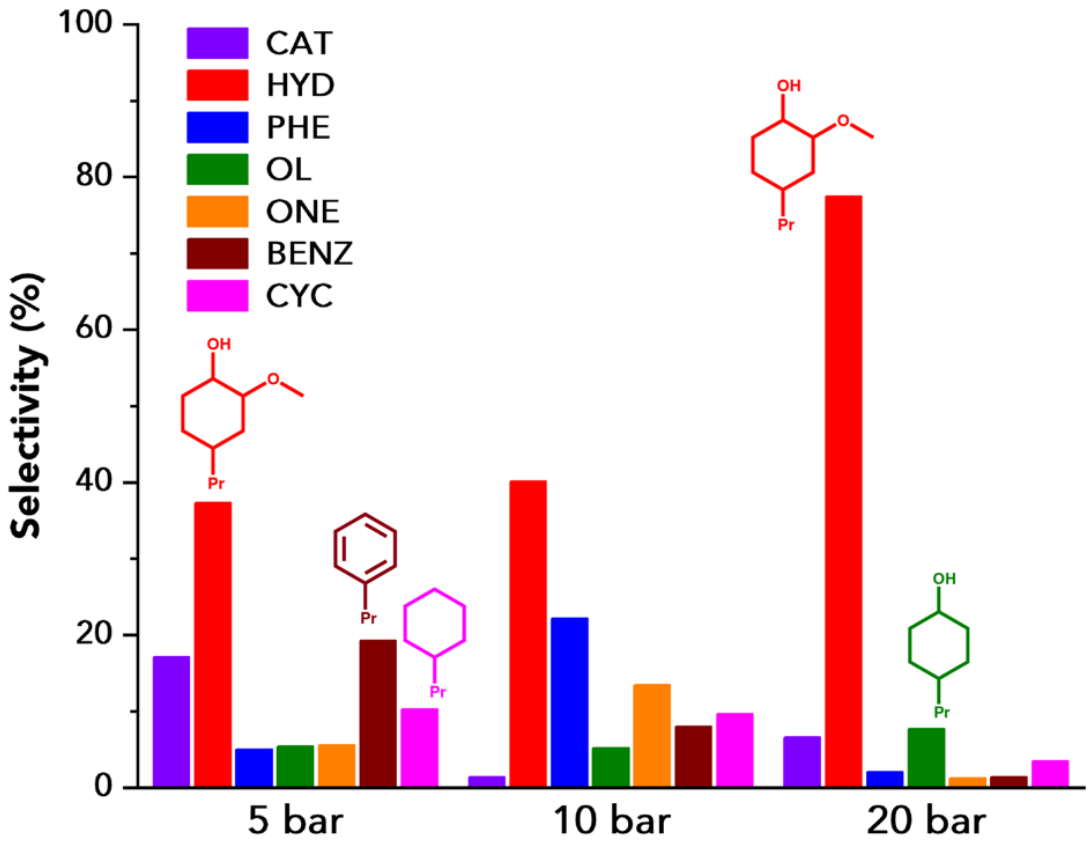

Figure 2.13: Pressure-dependent HDO reactions of DHE over 6.0-Pt. Isoconversion of ~30% was obtained by altering the catalyst loading. *Conditions*: 275˚C, 2 hours, 500 mg DHE, 20 mL cyclohexane. For all pressures studied, HYD is the dominant product, in line with the observation of favored aromatic ring hydrogenation over 6.0-Pt in all other experiments conducted. Additionally, BNZ and CYC are formed in significant quantities at all pressures, in stark contrast to the 0.4-Pt catalyst which does not yield fully deoxygenated species, regardless of H_2 pressure. BNZ and CYC selectivity drops with increasing H_2 pressure, likely due to the increasing selectivity to HYD. As discussed in the main text, HYD is considered a dead end intermediate due to the inactivity of saturated ring species in the HDO pathway over non-acidic catalyst.

PHE HDO results over 6.0-Pt are consistent with prior reactions starting from DHE, as 6.0-Pt is highly active to the formation of BNZ, demonstrating once again the ability of 6.0-Pt to facilitate complete deoxygenation. Interestingly for the HDO of PHE in Figure 2.14, BNZ selectivity is greater than CYC at 45% for BNZ compared to 4% for CYC, perhaps due to the greater conversions reached in these experiments compared to the isoconversion experiments previously at ~10%. Once again, this can be explained by a reaction pathway wherein BNZ forms directly from PHE, and only then undergoes subsequent hydrogenation of BNZ to form CYC. Overall, these results demonstrate that the 6.0-Pt catalyst is uniquely capable of facilitating HDO of both mono- and multi-oxygenated phenolics.

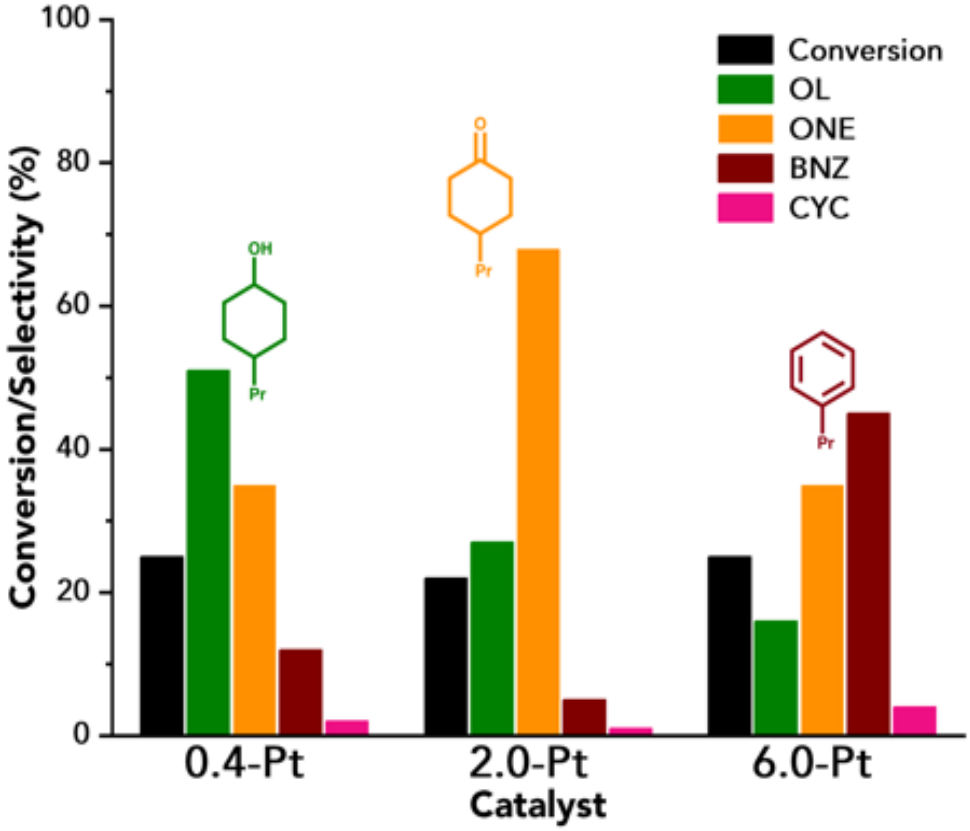

Figure 2.14: HDO reactions at isoconversion of PHE over various sized Pt catalysts. Conditions: 500 mg DHE, 275˚C, 2 hours, 10 bar H_2, 20 mL cyclohexane. Catalyst loading was varied to achieve isoconversion of 25% across all catalysts.

2.3 Discussion

The results shown above demonstrate a clear effect of Pt nanoparticle size distribution (and thus exposed Pt site structure) on activity and selectivity in the HDO of multifunctional oxygenated substrates, highlighting that these trends have broad effects for HDO of aromatic phenols derived from lignin outside of model systems. However, it is important to consider how the Pt particle size effect is manifested in these complex networks, as numerous steps in the HDO reaction scheme may be individually responsible for the observed behavior. In order to concisely interpret these results in the context of the HDO reaction network, we summarize our findings as follows:

1. Hydrogenation of the aromatic ring in lignin model phenolics is structure-sensitive over Pt/SiO_2 catalysts. Catalysts with larger Pt particle sizes increase the selectivity to hydrogenated products (HYD, OL, ONE, CYC), thus indicating that well-coordinated sites on low-index planes of metal nanoparticles are responsible for planar aromatic adsorption, which facilitates aromatic hydrogenation.
2. Demethoxylation also exhibits structure sensitivity, with increased selectivity to demethoxylated products over smaller Pt particle sizes. In contrast to ring hydrogenation, under-coordinated sites of Pt nanoparticles at steps, edges, and other defects are active indicating that planar adsorption is not necessary for demethoxylation.
3. Hydrogenated and dehydrogenated products exist in an equilibrium in the liquid phase batch reactions and are dictated in part by the H_2 pressure.

4. Dehydroxylation, HDO of phenolic hydroxyl group, is structure sensitive over Pt/SiO_2 catalysts. Surprisingly, and in contrast to suggestions made previously in the literature[24–26], increased selectivity to fully deoxygenated hydrocarbons is observed for larger Pt particle sizes, suggesting that WC sites on Pt terraces are the active site for dehydroxylation of phenolics under the conditions studied here.

The contextualization of these results lends further insight into the fundamental nature of structure sensitivity over Pt/SiO_2 catalysts shown here. Considering first the structure sensitivity of aromatic ring hydrogenation, we identify through increased selectivity to hydrogenated products that WC sites present on low-index, planar Pt terraces are the active sites for ring hydrogenation. This observation is consistent with findings from previous literature on hydrogenation of aromatic hydrocarbons such as benzene[22,66]. Phenolic ring hydrogenation pathways over Pt require planar adsorption of the substrate to the Pt surface, which leads to disruption of ring aromaticity and facilitates hydrogenation. Importantly, planar aromatic adsorption is not facilitated by stepped surfaces or over edges, as the ring requires a contiguous planar surface upon which to adsorb to maximize substrate-metal interaction[67].

Demethoxylation, on the other hand, is apparently less geometrically demanding and is facilitated over small nanoparticles with UC sites located at steps, edges, and other defect sites. Hence, demethoxylation does not require planar adsorption of the aromatic ring. Non-planar adsorption modes have previously been identified by spectroscopy on the surface of metal catalysts[68] and have been attributed to facilitating C-O cleavage as a result of specific interaction of the metal surface with the C_{Aryl}-OCH_3 bond. The occurrence of demethoxylation over UC sites is also consistent with the greater binding strength of methoxy fragments and

methanol to these sites, in turn creating a thermodynamic driving force for the reaction over these sites[69]. Our results also suggest that demethylation of DHE to CAT is a parallel reaction competing with demethoxylation, and not a sequential pathway from DHE to CAT to PHE. Interestingly, the demethylation of DHE to form CAT is not structure-sensitive over the Pt/SiO_2 catalysts studied here, resulting in similar selectivity of CAT across all catalysts.

Our results also highlight the influence of hydrogen pressure on product selectivity. At high conversions (60%), selectivity of the 0.4-Pt catalyst favored the aromatic compounds PHE and CAT over saturated hydrocarbon products for pressures at or below 10 bar of H_2. Importantly, the reactor contains at least 4.6 molar equivalents of H_2 relative to DHE when pressurized to 5 bar, indicating that for all reactions aromatic hydrogenation is not stoichiometrically limited. At 20 bar H_2, the saturated products HYD and OL became dominant. These results demonstrate that 0.4-Pt exhibits the sites necessary for hydrogenation, though these sites are scarce relative to 6.0-Pt as shown by the lower extents of ring hydrogenation during the thermal ramp over 0.4-Pt compared to 6.0-Pt. Therefore, the production of aromatic products over 0.4-Pt is not a result of a structurally limited capacity for ring hydrogenation. Instead, the kinetic accessibility of dehydrogenation over UC sites present on the 0.4-Pt catalyst enables the system to approach an equilibrium determined by the H_2 pressure.

To support this, equilibrium calculations were made for phenol hydrogenation as a simplified model system. HDO reaction of DHE over 0.4-Pt catalysts at low and high conversions under 10 bar (gauge) of H_2 indicated that unsaturated aromatic compounds such as PHE and CAT were favored over the analogous saturated compounds (i.e. cyclohexanol, cyclohexanone, cyclohexa-1,2-diol). However, pressure studies demonstrated that the 0.4-Pt

catalyst is capable of performing aromatic ring hydrogenation at reaction conditions. Thus, the preferential formation of unsaturated species over 0.4-Pt at under specific H_2 pressures, i.e. under 10 bar of H_2, is likely the result of equilibrium limitations on the extent of hydrogenation. To support this, the following estimates were made of the equilibrium position for a model reaction of phenol hydrogenation, which was chosen due to the availability of thermochemical data.

Table 2.3

Species	$\Delta H^0_{f,g}$ (kJ/mol)	$S^0_{f,g}$ (J/mol*K)
H_2	0	130 (Ref. [2])
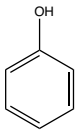	-91.8 (Ref. [4])	316 (Ref. [5])
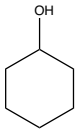	-290.8 (Ref. [1])	353.8 (Ref. [3])

Using these values, the standard changes in enthalpy and entropy of reaction can be calculated as:

$$\Delta H^0_{rxn} = \sum \nu_i \Delta H^0_f$$

$$S^0_{rxn} = \sum \nu_i S^0_f$$

Where υ_i is the stoichiometric factor of the reaction. From this, the equilibrium constant can be estimated assuming that ΔH^0_{rxn} and S^0_{rxn} are temperature independent via:

$$\ln K = -\frac{\Delta H^0_{rxn}}{RT} + \frac{S^0_{rxn}}{R}$$

At 275˚C, this gives a value of K = 3.74. This can be related to the composition of the reaction by representing the equilibrium constant as:

$$K = \frac{\left[\text{ 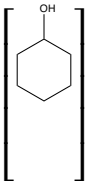 }\right]}{\left[\text{ 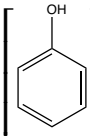 }\right][H_2]^3}$$

In the case of liquid phase reactions, as conducted here, the concentration of H_2 is not immediately obvious. To capture the availability of hydrogen in the reaction medium (the liquid-catalyst interface), gas solubility data was interpolated for the conditions of interest (275˚C, ~50 bar total pressure). This provided an estimated molar fraction of H_2 in the liquid phase of 0.047. This mole fraction can be represented as a molarity by:

$$[H_2] = \frac{x_{H_2,l} V_{M,Cyc}}{\left(1 - x_{H_2,l}\right)}$$

Where $x_{H2,l}$ is the mole fraction of H_2 in the liquid phase and V_M is the molar volume of cyclohexane, which is the overwhelmingly dominant component of the liquid phase as the solvent in mol/mL. This gives an H_2 molarity of 0.45. Substituting this into the equilibrium expression, the ratio of cyclohexanol to phenol can be solved for as:

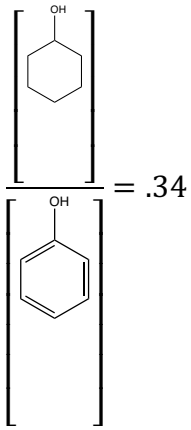

$= .34$

In a simple model reaction system, this would give a phenol selectivity of 74%. Though the direct comparison of this model system to the HDO reaction studied is limited due to the number of products and reactions occurring, it is highly supportive that the formation of unsaturated species is thermodynamically favorable for similarly structured oxygenates. Moreover, the obtained 2-hour selectivity towards PHE (4-propylphenol) over 0.4-Pt catalysts of 68% at low (14%) conversion aligns very well with the 74% estimated by this method. In the high (62%) conversion case, the agreement is lower at 42% selectivity to PHE, though this is likely impacted primarily by the favored formation of HYD from DHE, which prevents the formation of PHE and thus creates a significantly different system composition than estimated here via thermochemistry.

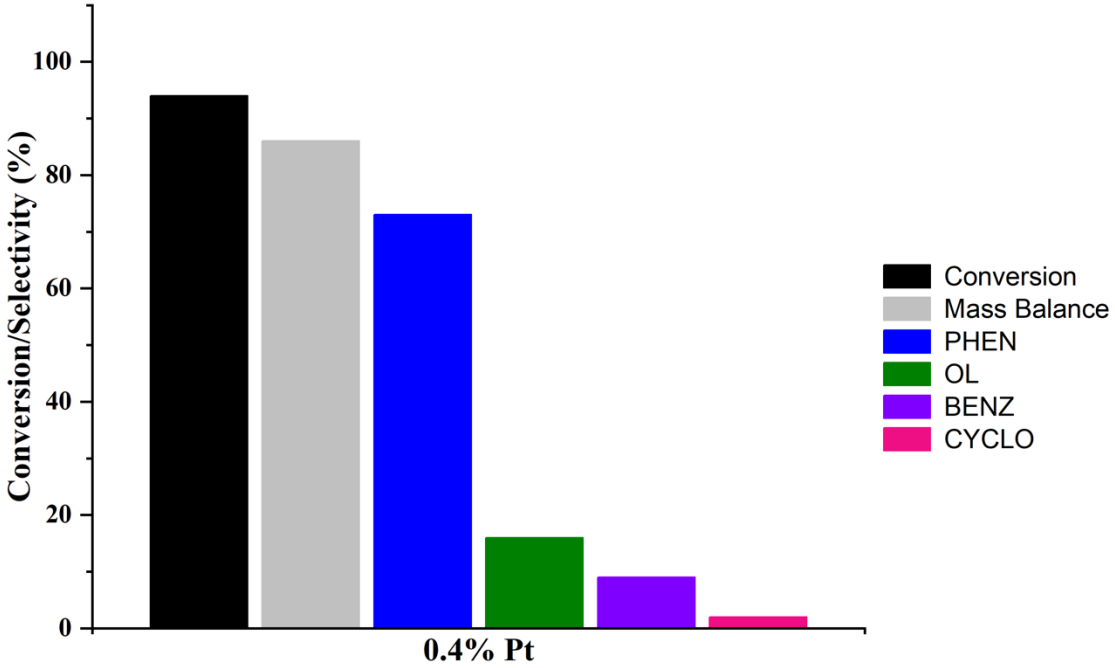

Figure 2.15: Control experiment performed over 0.4-Pt using ONE as the substrate under 10 bar of H_2. Results clearly show that ONE dehydrogenation to PHE is facile over 0.4-Pt, underscoring both the kinetic accessibility of dehydrogenation over 0.4-Pt due to the density of UC sites and the thermodynamic accessibility of dehydrogenation due to H_2 availability in the liquid phase. *Conditions*: 275˚C, 2 hours, 500 mg ONE, 20 mL cyclohexane, 50 mg 0.4-Pt, 10 bar H_2

To support these equilibrium calculations further, a reaction was conducted starting from a saturated substrate to observe the reactivity over 0.4-Pt. For this reaction, ONE was chosen as the substrate, exhibiting a saturated ring, to observe whether the content of H_2 at the reaction interface was sufficient to favor the maintenance of the hydrogenated structure or whether 0.4-Pt would perform dehydrogenation to obtain PHE. As can be seen in Figure 2.15, the reaction produces a dominant quantity of PHE from ONE over 0.4-Pt, highlighting that 0.4-Pt facilitates dehydrogenation despite the 10 bar H_2 pressure utilized in the headspace. Additionally, these results are consistent with the result of both PHE and DHE HDO, in which 0.4-Pt does not produce a significant quantity of deoxygenated species but rather selectively produces PHE.

These calculations and control experiments demonstrate that despite the stoichiometric excess of H_2 present at all pressures studied, equilibrium positions at 275˚C favor the formation of aromatic products such as phenol. Comparatively, over the 6.0-Pt catalyst, dehydrogenation is less favorable because of the dominant exposure of WC sites on the surface. Thus, despite exhibiting the same equilibrium position (dictated solely by the temperature and pressure of reaction) as the 0.4-Pt catalyst, product selectivity for the 6.0-Pt favors saturated ring species.

The most surprising conclusion resulting from the work described here is the structure sensitivity for dehydroxylation of phenolics facilitated by WC sites. This step is the most catalytically demanding, considering the C_{Aryl}-OH bond is the strongest C-O bond present in lignin-derived phenolics[60], and thus it is surprising that our work identifies WC sites as critical for the cleavage of these C-O bonds, especially since C_{Aryl}-OCH_3 bonds were cleaved by UC sites. In general, WC metal sites are regarded as less reactive than under-coordinated (UC) sites. Importantly, this trend holds over both DHE and PHE substrates at low and high conversions, supporting the conclusions discussed earlier that deactivation does not influence structure sensitivity and that this behavior holds for diverse substrates.

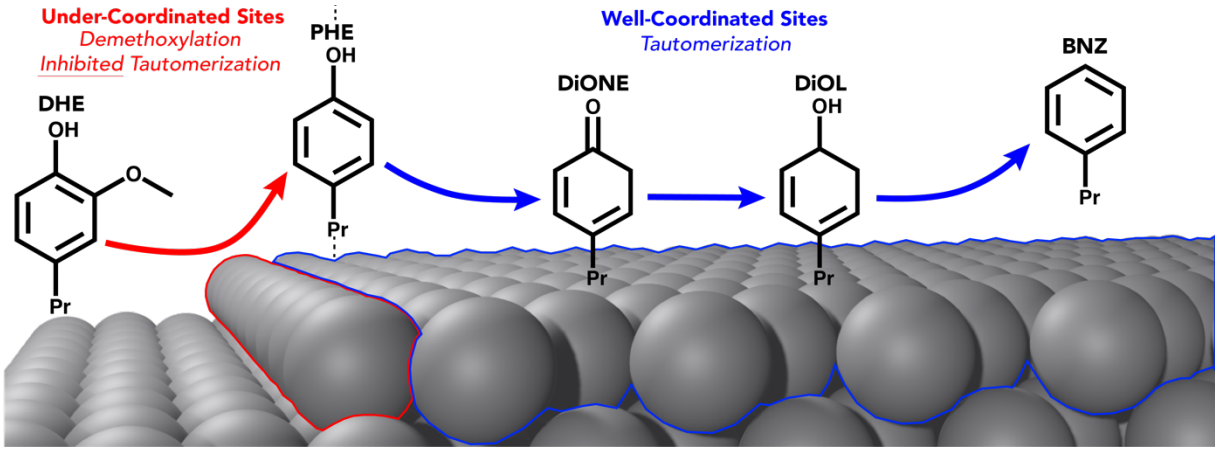

Scheme 2.5: Summary of the structure sensitivity of deoxygenation steps in the HDO of DHE over Pt/SiO_2 catalysts. PHE deoxygenation proceeds through tautomerization over WC sites, explaining the observed production of BNZ and CYC over 6.0-Pt but not 0.4-Pt. Aromatic ring hydrogenation and dehydrogenation reactions, which also exhibit structure sensitivity, have been omitted from this scheme since these do not contribute directly towards deoxygenation.

In catalytic HDO schemes, the following pathways have been suggested for the dehydroxylation of phenolics over metal catalysts: hydrogenation followed by dehydration[70–72], direct deoxygenation (DDO)[73–75], and tautomerization[31,76]. Complete hydrogenation to a cyclohexanol intermediate followed by dehydration has been rejected previously for Pt/SiO_2 catalysts because of the inherent lack of acidity of the silica support and will not be considered here further. DDO, or direct cleavage of the C_{Aryl}-OH bond without any other mechanistic steps, has also been proposed as a pathway for HDO of phenolics. Typically, the DDO mechanism is invoked in systems involving oxophilic components. For instance, NiFe surfaces have been predicted by DFT to proceed through DDO[77]. However, over weakly oxophilic monometallic catalysts such as Pt/SiO_2, DDO is considered kinetically unfavorable under the conditions studied here. Additionally, UC sites are predicted to facilitate DDO more effectively, opposite the structure sensitivity observed in our reactions. Thus, DDO is an unlikely mechanism for our system.

Instead, we propose that the structure sensitivity observed here for the dehydroxylation of PHE to BNZ is consistent with a pathway involving metal-facilitated aromatic tautomerization. Tautomerization-based mechanisms for HDO have gained increased attention for a range of metal catalysts, specifically for non-acidic catalysts. The proposed mechanistic steps are shown in Scheme 2.5. Briefly, PHE is adsorbed to Pt and tautomerized to the corresponding 4-propylcyclohexa-3,5-dien-1-one (DiONE). The C=O bond in DiONE is then hydrogenated to form the unstable 4-propylcyclohexa-3,5-dien-1-ol (DiOL), which readily undergoes dehydration to form BNZ. Importantly, these tautomerization events are proposed to occur while the substrate is adsorbed to the metal catalyst surface, as tautomerization of phenol to the keto form in free solvent environments is negligible due to the favorable stability of the aromatic ring[78]. Thus, it might be expected that metal surface characteristics change the favorability of tautomerization.

The greater selectivity of 6.0-Pt towards BNZ and CYC from HDO of both DHE and PHE substrates is indicative of WC sites promoting tautomerization. We attribute this behavior to an adsorption effect that can proceed more readily over WC sites wherein phenolics adsorb co-planar with the metal surface prior to tautomerization, analogous to the adsorption mode required for hydrogenation. The shared need for co-planar ring adsorption between both hydrogenation and tautomerization pathways is consistent with the need to disrupt ring aromaticity in both reactions. On the other hand, UC sites on stepped surfaces or at particle edges do not exhibit the contiguous ensembles necessary to achieve intermediate stabilization. This would explain the inability of 0.4-Pt to produce significant quantities of BNZ or CYC, even at conditions of high conversion and high H_2 pressure. This would also explain the differences in selectivity between 0.4-Pt and 2.0-Pt in the HDO of PHE, as the hydrogenation

of PHE is proposed to proceed through a tautomerization mechanism to produce ONE104[79]. Considering the inability of 0.4-Pt to facilitate this tautomerization, the favored product is instead OL. This is consistent with the larger particle size of 2.0-Pt exhibiting more WC sites. On the other hand, the similarity in performance between 0.4-Pt and 2.0-Pt in HDO of DHE is consistent with the initial demethoxylation step of DHE not involving tautomerization, but rather direct cleavage or demethylation to CAT.

Regarding the influence of the metal surface on tautomerization, there are few works that comment on the promotion or suppression of the tautomerization pathways for HDO. It is known that metal identity is critical in determining the dominant HDO pathway, with relatively oxophilic metals such as Ru favoring direct C-O cleavage, whereas Pt prefers tautomerization pathways. However, the tendency of a specific metal to facilitate tautomerization has been shown to be sensitive to the electronic and compositional characteristics of the catalyst. For instance, bimetallic PtMo alloy catalysts promote tautomerization compared to monometallic Pt catalysts in HDO of m-cresol[76]. DFT calculations supported the hypothesis that the oxophilicity of Mo sites promotes strong interactions with the keto tautomer, decreasing barriers of tautomerization. Similarly, alkali-modification of Fe catalysts for HDO resulted in the destabilization of tautomer intermediates depending on the degree of electron donation, demonstrating a relationship between metal electronics and tautomerization. Given the relative similarity in the electronic structure of Pt sites of varying coordination in our studies, we hypothesize that the reactant adsorption geometry on Pt sites is primarily responsible for the moderation of tautomerization of phenolic substrates such as DHE and PHE. However, we cannot rule out the potential contribution of electronic differences between UC and WC Pt sites in tautomerization reactions.

2.4 Conclusion

In conclusion, the directed synthesis of various-sized Pt catalysts supported on SiO_2 enabled the assessment of structure sensitivity in HDO reactions. Importantly, by employing both DHE and PHE as substrates, we have shown that observed structure sensitivity trends exist for both mono-oxygenated and multi-oxygenated phenolics. Analysis of the product distribution provided the surprising result that larger Pt nanoparticles, in this case 12 nm in size, were superior to Pt nanoparticles <3 nm in catalyzing complete HDO of DHE and PHE to BNZ. Though this runs counter to the observation that DDO is facilitated over smaller nanoparticles, our results suggest that an alternative pathway, namely surface-mediated tautomerization of phenol to dienone, is responsible for full deoxygenation. This conclusion underscores the potential of facilitating tautomerization HDO pathways to enhance overall deoxygenation activity. These results also highlight the balance that exists for monometallic catalysts in which large particles drive rapid deoxygenation but with broad product distributions, compared to the slower but more selective HDO found for smaller Pt particles.

2.5 Methods

2.6.1 Catalyst Preparation

Supported Pt/SiO_2 catalysts of varying average particle size were prepared by a modified strong electrostatic adsorption (SEA) procedure using tetraamine platinum nitrate (TAPN, Sigma)[48,49]. In the case of 0.4wt% and 2wt% Pt/SiO_2 catalysts, amorphous SiO_2 (20-30 nm, USNano) was introduced to HPLC-grade water (Sigma) under magnetic stirring. The pH of the solution was adjusted to 10.5 using an appropriate amount of aqueous NH_4OH (28%,

Sigma), determined by monitoring with a pH meter and probe. Once the desired pH was achieved, the solution was left stirring for 30 minutes for the SiO_2 surface to equilibrate with the solution. To this, 50 mL of TAPN in HPLC-grade water, also adjusted to a pH of 10.5, was added dropwise via a syringe pump at a rate of 2.5 mL/min. After the addition was complete, the solution was heated to 80˚C and allowed to evaporate under stirring. The obtained powder was then thoroughly dried overnight in an oven at 110˚C and removed.

Synthesis of the 6% Pt/SiO_2 followed a similar procedure. The SiO_2 used for this catalyst series was a non-porous SiO2 (15-20 nm, USNano) in order to avoid Pt deposition in small pores which might stabilize small particles even under harsh calcination conditions. This SiO_2 was added to pH-adjusted water at 10.5 in a similar approach to the other catalyst preparation. To this, 10 mL of TAPN solution of appropriate concentration was added dropwise by pipette. After addition, the solution was allowed to equilibrate for 30 minutes before evaporating the solution in an identical fashion to the other catalysts.

Calcination to decompose the Pt precursor was performed in a tube furnace under 50 sccm flow of dry air (Airgas). All temperature ramp steps were performed at 10˚C/min. 0.4% Pt/SiO_2 was calcined at 300˚C for 2 h, which is above the decomposition temperature of the TAPN precursor in air but minimizes particle sintering and mobility[50]. Likewise, to prepare larger Pt particles, 2% Pt/SiO_2 was calcined at 325˚C for 3 h, and 6% Pt/SiO_2 was calcined at 600˚C for 6 h.

2.5.2 Catalyst Characterization

CO probe molecule diffuse reflectance infrared spectroscopy (CO-DRIFTS) was performed by placing catalyst powder into a Harrick High-Temperature reaction cell equipped

with ZnSe windows. The prepared cell was then coupled with a Harrick Praying Mantis diffuse reflectance adapter set into a Nicolet iS10 FT-IR spectrometer equipped with a liquid nitrogen-cooled mercury-cadium-telluride (MCT) detector. Prior to characterization, catalysts were pretreated under 50 sccm of 10% H_2/Ar (Airgas) by ramping to 325˚C at a rate of 10˚C/min for 1 h and then cooled to 30˚C under 50 sccm Ar (UHP, Airgas), at which point a background scan was collected. All measurements were performed by averaging 32 scans at a resolution of 0.482 cm^{-1}. After the background scan, 10% CO/Ar (Airgas) was flowed at 50 sccm for 15 minutes to bind CO to the metallic Pt sites. Saturation coverage of CO on the Pt sites was monitored by observing bound CO peak intensity while under CO flow. After 15 minutes of exposure, gas phase CO was purged from the cell by 50 sccm Ar, at which point final spectra were collected showing only CO bound to Pt sites. Spectral deconvolution was performed using 3 Gaussian features, specifically using 2 Gaussians to capture the peak shape of under-coordinated (UC) sites, which typically exhibit an asymmetric shape due to the broad range of geometric and electronic environments (steps, edges, corners, kink, etc.) that these features represent. Site fraction estimates were performed assuming a relative extinction coefficient of 2.7:1 for UC:WC sites, as reported previously[51,52]. Particle size estimates were obtained by relating site fraction estimates to a model cuboctahedron geometry.

CO chemisorption was performed using a Micromeritics Autochem 2920 II chemisorption analyzer. In a typical experiment, 100 mg of catalyst was loaded into the sample U-tube atop quartz wool. Catalysts were pre-treated under 50 sccm of 10% H_2/Ar by ramping from room temperature to 325˚C at 10˚C/min and held for 1 h. After reduction, catalysts were cooled in Ar to 30˚C and purged for an additional 5 minutes. 10% CO/He was introduced from a sample loop of known volume using a 6-way valve at 3.5-minute intervals. The gas

atmosphere was analyzed by a thermal conductivity detector (TCD) to measure the amount of CO remaining after exposure to the catalyst sample. Dispersion estimates were made by calculating the CO bound to the Pt catalysts, assuming a CO:Pt_{surf} ratio of 1:1[53].

High-angle annular dark field scanning transmission electron microscopy (HAADF-STEM) images were taken using a Thermo Fisher Talos F200X G2 transmission electron microscope. STEM samples were prepared by adding ground catalysts to methanol (Sigma) and sonicating for 30 minutes, followed by drop casting onto lacey carbon on Cu grids (Ted Pella). The drop cast grids were then kept under vacuum to fully dry for at least 48 hours prior to imaging. Images were collected under an accelerating voltage of 200 kV, and at least 400 particles were imaged to represent the true particle size distributions of the samples.

2.5.3 HDO Reactions

HDO reactions using the prepared catalysts were performed in 75-mL stainless-steel pressure reactors (Parr Instrument Co., 5000 Series). In a typical reaction, 50 mg of catalyst was loaded into the reactor along with 500 mg of dihydroeugenol (DHE, Sigma) and 20 mL of cyclohexane (Sigma). Reactions were stirred magnetically at 700 rpm using glass-shielded stir bars. Once loaded, the reactor was sealed and purged 3 times with 5.0 grade H_2 (Airgas) before pressurizing to a final gauge pressure of 10 bar at room temperature. Then, the vessel was heated to 275 ˚C and held for 2 hours. After the allotted reaction time, the reactor vessel was quickly removed and quenched using a water bath. Once cooled to room temperature, the liquid products were collected by centrifugation and analyzed by GC-FID (Agilent) using *n*-decane (Sigma) as an internal standard. In some cases, the gas headspace was collected and analyzed by GC. Product identification was carried out using commercially-sourced standards where

possible (DHE, 4-propylbenzene, 4-propylphenol, 4-propylcyclohexanol, 4-propylcyclohexane). In instances where standards are not commercially available, FID responses were estimated using effective carbon number (ECN)[54–56]. Reaction performance metrics were defined as:

$$Conversion\ (\%) = \frac{N_{DHE}}{N_{DHE}^{0}}$$

$$Selectivity\ (\%) = \frac{N_{Product}}{\sum N_{Product}}$$

$$Yield\ (\%) = Conversion * Selectivity = \frac{N_{Product}}{\sum N_{Product}} * \frac{N_{DHE}}{N_{DHE}^{0}}$$

where N_i is the number of moles of species i measured by GC-FID and N_i^0 is the initial number of moles of *i* loaded into the batch reactor. For isoconversion experiments, the conversion of the substrate was altered by changing the catalyst loading into the reactor, thus moderating the catalyst:substrate mass ratio.

2.6 References

1. Taylor, H. S. A Theory of the Catalytic Surface. *Proceedings of the Royal Society of London* **108**, 105–111 (1925).
2. Robotti, N. The discovery of X-ray diffraction. in *Rendiconti Lincei* vol. 24 (2013).
3. Bragg, W. H. & Bragg, W. L. *X-Rays and Crystal Structure*. (G. Bell and Sons, Ltd., London, 1915).
4. Langmuir, I. ADSORPTION OF GASBS ON GLASS, MICA AND PLATINUM. THE ADSORPTION OF GASES ON PLANE SURFACES OF GLASS, MICA AND PLATINUM. *J Am Chem Soc* 1361–1403 (1918).
5. Thompson, H. Cyril Normal Hinshelwood, 1897-1967. *Biographical Memoirs of Fellows of the Royal Society* **19**, 375–431 (1973).
6. Hinshelwood, C. N. *The Kinetics of Chemical Change in Gaseous Systems*. (Claredon Press, Oxford, 1926).

7. Mulliken, R. S. Spectroscopy, Molecular Orbit: and Chemical Bond. *Science (1979)* **157**, 3784 (1967).
8. Elliott, J. A. W. Gibbsian Surface Thermodynamics. *Journal of Physical Chemistry B* **124**, 10859–10878 (2020).
9. Wulff, G. XXY. Zur Frage der Geschwindigkeit des Wachs-thums und der Auflösung der Krystallflächen. *Zeitschrift für Kristallographie* **34**, 1–6 (1901).
10. Barmparis, G. D., Lodziana, Z., Lopez, N. & Remediakis, I. N. Nanoparticle shapes by using Wulff constructions and first-principles calculations. *Beilstein Journal of Nanotechnology* **6**, 361–368 (2015).
11. Herring, C. Some Theorems on the Free Energies of Crystal Surfaces. *Physical Review* **82**, 87–93 (1951).
12. Van Hardeveld, R. & Hartog, F. *THE STATISTICS OF SURFACE QTOMS AND SURFACE SITES ON METAL CRYSTALS*. *SURFACE SCIENCE* vol. 15 (1969).
13. Boudart, M. *HETEROGENEOUS CATALYSIS BY METALS*. *Journal of Molecular Catalysis* vol. 30 (1985).
14. Boudart, M. & Mcdonald, M. A. *Structure Sensitivity of Hydrocarbon Synthesis from CO and H2*. *J. Phys. Chem* vol. 88 https://pubs.acs.org/sharingguidelines (1984).
15. Somorjai, G. A. & Materer, N. Surface structures in ammonia synthesis. *Top Catal* **1**, 215–231 (1994).
16. Spencer, N. D., Schoonnaker, R. C. & Somorjai, G. A. STRUCTURE SENSITIVITY IN THE IRON SINGLE CRYSTAL CATALYSED SYNTHESIS OF AMMONIA0r5qn Publication Date. *Nature* (1981).
17. Dumesic, J. A., Topsoe, H., Khammouma, S. & Boudart', M. Surface, Catalytic and Magnetic Properties of Small iron Particles II. Structure Sensitivity of Ammonia Synthesis. *J Catal* **37**, 503–508 (1975).
18. Nørskov, J. K. *et al.* Universality in heterogeneous catalysis. *J Catal* **209**, 275–278 (2002).
19. Jia, X. & An, W. Adsorption of Monocyclic Aromatics on Transition Metal Surfaces: Insight into Variation of Binding Strength from First-Principles. *Journal of Physical Chemistry C* **122**, 21897–21909 (2018).
20. Ihm, H., Ajo, H. M., Gottfried, J. M., Bera, P. & Campbell, C. T. Calorimetric measurement of the heat of adsorption of benzene on Pt(111). *Journal of Physical Chemistry B* **108**, 14627–14633 (2004).
21. Campbell, J. M., Seimanides, S. & Campbell, C. T. Probing Ensemble Effects In Surface Reactions. 2. Benzene Adsorption on Clean and Bismuth-Covered Pt(111). *J. Phys. Chem* **93**, 815–826 (1989).
22. Flores, A. F., Burwell, R. L. & Butt, J. 8. Structure Sensitivity of Benzene Hydrogenation on Supported Pt Catalysts. *Journal of the Chemical Society, Faraday Transactions* **88**, 1191–1196 (1992).
23. Liu, R. & An, W. Stepped M@Pt(211) (M = Co, Fe, Mo) single-atom alloys promote the deoxygenation of lignin-derived phenolics: Mechanism, kinetics, and descriptors. *Catal Sci Technol* **11**, 7047–7059 (2021).
24. Lu, J., Behtash, S., Mamun, O. & Heyden, A. Theoretical Investigation of the Reaction Mechanism of the Guaiacol Hydrogenation over a Pt(111) Catalyst. *ACS Catal* **5**, 2423–2435 (2015).

25. Chiu, C. C., Genest, A., Borgna, A. & Rösch, N. C-O cleavage of aromatic oxygenates over ruthenium catalysts. A computational study of reactions at step sites. *Physical Chemistry Chemical Physics* **17**, 15324–15330 (2015).
26. Resasco, J. *et al.* Relationship between Atomic Scale Structure and Reactivity of Pt Catalysts: Hydrodeoxygenation of m-Cresol over Isolated Pt Cations and Clusters. *ACS Catal* **10**, 595–603 (2020).
27. Mortensen, P. M., Grunwaldt, J. D., Jensen, P. A. & Jensen, A. D. Influence on nickel particle size on the hydrodeoxygenation of phenol over Ni/SiO2. *Catal Today* **259**, 277–284 (2016).
28. Yang, F. *et al.* Size Dependence of Vapor Phase Hydrodeoxygenation of m-Cresol on Ni/SiO2 Catalysts. *ACS Catal* **8**, 1672–1682 (2018).
29. Ma, Z., Troussard, E. & Van Bokhoven, J. A. Controlling the selectivity to chemicals from lignin via catalytic fast pyrolysis. *Appl Catal A Gen* **423–424**, 130–136 (2012).
30. Jiang, G., Nowakowski, D. J. & Bridgwater, A. V. Effect of the temperature on the composition of lignin pyrolysis products. *Energy and Fuels* **24**, 4470–4475 (2010).
31. Nie, L. & Resasco, D. E. Kinetics and mechanism of m-cresol hydrodeoxygenation on a Pt/SiO 2 catalyst. *J Catal* **317**, 22–29 (2014).
32. Zhang, X., Tang, W., Zhang, Q., Wang, T. & Ma, L. Hydrocarbons Production from Lignin-derived Phenolic Compounds over Ni/SiO2 Catalyst. *Energy Procedia* **105**, 518–523 (2017).
33. Ngandjong, A. C., Mottet, C. & Puibasset, J. Influence of the Silica Support on the Structure and the Morphology of Silver Nanoparticles: A Molecular Simulation Study. *Journal of Physical Chemistry C* **120**, 8323–8332 (2016).
34. Ma, Q., Klier, K., Cheng, H., Mitchell, J. W. & Hayes, K. S. Interaction between catalyst and support. 3: Metal agglomeration on the silica surface. *Journal of Physical Chemistry B* **105**, 9230–9238 (2001).
35. Miller, J. T., Schreier, M., Kropf, A. J. & Regalbuto, J. R. A fundamental study of platinum tetraammine impregnation of silica: 2. The effect of method of preparation, loading, and calcination temperature on (reduced) particle size. *J Catal* **225**, 203–212 (2004).
36. Ferreira-Aparicio, P., Rodriguez-Ramos, I. & Guerrero-Ruiz, A. *Methane Interaction with Silica and Alumina Supported Metal Catalysts*. *Applied Catalysis A: General* vol. 148 (1997).
37. Soled, S. Silica-supported catalysts get a new breath of life. *Science* vol. 350 1171–1172 Preprint at https://doi.org/10.1126/science.aad0267 (2015).
38. Zakem, G., Ro, I., Finzel, J. & Christopher, P. Support functionalization as an approach for modifying activation entropies of catalytic reactions on atomically dispersed metal sites. *J Catal* **404**, 883–896 (2021).
39. Agostini, G. *et al.* Determination of the particle size, available surface area, and nature of exposed sites for silica-alumina-supported Pd nanoparticles: A multitechnical approach. *Journal of Physical Chemistry C* **113**, 10485–10492 (2009).
40. Smith, J. S., Thrower, P. A. & Vannice, M. A. Characterization of Ni/TiO, Catalysts by TEM, X-Ray Diffraction, and Chemisorption Techniques. *J Catal* **68**, 270–285 (1981).
41. Kale, M. J. & Christopher, P. Utilizing Quantitative in Situ FTIR Spectroscopy to Identify Well-Coordinated Pt Atoms as the Active Site for CO Oxidation on Al2O3-Supported Pt Catalysts. *ACS Catal* **6**, 5599–5609 (2016).

42. Bergeret, G. & Gallezot, P. Particle Size and Dispersion Measurements. in *Handbook of Heterogeneous Catalysis* vol. 2 738–765 (Wiley-VCH, 2008).
43. Sangnier, A. *et al.* Thermokinetic and spectroscopic mapping of carbon monoxide adsorption on highly dispersed Pt/γ-Al2O3. *ACS Catal* **11**, 13280–13293 (2021).
44. Hayden, B. E., Bradshaw, A. M. & Greenler, R. G. AN INFRARED STUDY OF THE ADSORPTION OF CO ON A STEPPED PLATINUM SURFACE. *Surf Sci* **149**, 394–406 (1985).
45. Kappers, M. J. & Van Der Maas, J. H. Correlation between CO frequency and Pt coordination number. A DRIFT study on supported Pt catalysts. *Catal Letters* **10**, 365–374 (1991).
46. Becker, E., Skoglundh, M., Andersson, M. & Spetz, A. L. In situ DRIFT study of hydrogen and CO adsorption on Pt/SiO2 model sensors. *IEEE Sensors* 1028–1031 (2007).
47. Brieger, C., Melke, J., Kaghazchi, P. & Roth, C. CO Adsorption on Platinum Nanoparticles - the Importance of Size Distribution Studied with in-Situ DRIFTS and DFT Calculations. *ECS Trans* **69**, 249–253 (2015).
48. Rioux, R. M. *et al.* Adsorption and co-adsorption of ethylene and carbon monoxide on silica-supported monodisperse Pt nanoparticles: Volumetric adsorption and infrared spectroscopy studies. *Langmuir* **24**, 198–207 (2008).
49. Podkolzin, S. G., Shen, J., De Pablo, J. J. & Dumesic, J. A. Equilibrated Adsorption of CO on Silica-Supported Pt Catalysts. *Journal of Physical Chemistry B* **104**, 4169–4180 (2000).
50. Woodruff, D. P., Hayden, B. E., Prince, K. & Bradshaw, A. M. *DIPOLE COUPLING AND CHEMICAL SHIFTS IN IRAS OF CO ADSORBED ON Cu(Ll0)*. *Surface Science* vol. 123 (1982).
51. Kim, C. S., Tornquist, W. J. & Korzeniewski, C. Site-dependent vibrational coupling of CO adsorbates on well-defined step and terrace sites of monocrystalline platinum: Mixed-isotope studies at Pt(335) and Pt(111) in the aqueous electrochemical environment. *J Chem Phys* **101**, 9112–9121 (1994).
52. Curulla, D., Clotet, A. & Ricart, J. M. Adsorption of carbon monoxide on Pt{100} surfaces: dependence of the CO stretching vibrational frequency on surface coverage. *Surf Sci* **460**, 101–111 (2000).
53. Sun, K., Wilson, A. R., Thompson, S. T. & Lamb, H. H. Catalytic deoxygenation of octanoic acid over supported palladium: Effects of particle size and alloying with gold. *ACS Catal* **5**, 1939–1948 (2015).
54. De Souza, P. M. *et al.* Hydrodeoxygenation of Phenol over Pd Catalysts. Effect of Support on Reaction Mechanism and Catalyst Deactivation. *ACS Catal* **7**, 2058–2073 (2017).
55. Bykova, M. V., Zavarukhin, S. G., Trusov, L. I. & Yakovlev, V. A. Guaiacol hydrodeoxygenation kinetics with catalyst deactivation taken into consideration. *Kinetics and Catalysis* **54**, 40–48 (2013).
56. Lan, X., Hensen, E. J. M. & Weber, T. Hydrodeoxygenation of guaiacol over Ni2P/SiO2–reaction mechanism and catalyst deactivation. *Appl Catal A Gen* **550**, 57–66 (2018).
57. Huang, X., Korányi, T. I., Boot, M. D. & Hensen, E. J. M. Ethanol as capping agent and formaldehyde scavenger for efficient depolymerization of lignin to aromatics. *Green Chemistry* **17**, 4941–4950 (2015).
58. Lindfors, C. Hydrodeoxygenation of lignin-derived phenol compound isoeugenol over nickel-and cobalt-based catalysts. (Abo Akademi University, Turku, 2019).

59. Tieuli, S. *et al.* Hydrodeoxygenation of isoeugenol over Ni-SBA-15: Kinetics and modelling. *Appl Catal A Gen* **580**, 1–10 (2019).
60. Prasomsri, T., Shetty, M., Murugappan, K. & Román-Leshkov, Y. Insights into the catalytic activity and surface modification of MoO 3 during the hydrodeoxygenation of lignin-derived model compounds into aromatic hydrocarbons under low hydrogen pressures. *Energy Environ Sci* **7**, 2660–2669 (2014).
61. Le Valant, A. *et al.* Platinum supported catalysts: Predictive CO and H2 chemisorption by a statistical cuboctahedron cluster model. *Journal of Physical Chemistry C* **120**, 26374–26385 (2016).
62. Lin, S. D. & Vannice, M. A. Hydrogenation of Aromatic Hydrocarbons over Supported Pt Catalysts III. Reaction Models for Metal Surfaces and Acidic Sites on Oxide Supports. *J Catal* **143**, 563–572 (1993).
63. Gao, D., Xiao, Y. & Varma, A. Guaiacol Hydrodeoxygenation over Platinum Catalyst: Reaction Pathways and Kinetics. *Ind Eng Chem Res* **54**, 10638–10644 (2015).
64. Tan, Q. *et al.* Different Product Distributions and Mechanistic Aspects of the Hydrodeoxygenation of m-Cresol over Platinum and Ruthenium Catalysts. *ACS Catal* **5**, 6271–6283 (2015).
65. Cordero-Lanzac, T. *et al.* Revealing the pathways of catalyst deactivation by coke during the hydrodeoxygenation of raw bio-oil. *Appl Catal B* **239**, 513–524 (2018).
66. Rioux, R. M., Hsu, B. B., Grass, M. E., Song, H. & Somorjai, G. A. Influence of particle size on reaction selectivity in cyclohexene hydrogenation and dehydrogenation over silica-supported monodisperse pt particles. *Catal Letters* **126**, 10–19 (2008).
67. K G, L., Puthiyaparambath, M. F., S, A. & Chatanathodi, R. Adsorption of benzene on defective Pt surfaces: A DFT study. *Surf Sci* **716**, (2022).
68. Chen, T. & Vohs, J. M. Direct Hydrodeoxygenation of m-Cresol to Toluene over Bifunctional NbOx-Pt. *Journal of Physical Chemistry C* **124**, 14253–14261 (2020).
69. Gupta, S., Khan, T. S., Saha, B. & Haider, M. A. Synergistic Effect of Zn in a Bimetallic PdZn Catalyst: Elucidating the Role of Undercoordinated Sites in the Hydrodeoxygenation Reactions of Biorenewable Platforms. *Ind Eng Chem Res* **58**, 16153–16163 (2019).
70. Hočevar, B., Grilc, M. & Likozar, B. Aqueous dehydration, hydrogenation, and hydrodeoxygenation reactions of bio-based mucic acid over ni, nimo, pt, rh, and ru on neutral or acidic catalyst supports. *Catalysts* **9**, (2019).
71. Zhao, C., Song, W. & Lercher, J. A. Aqueous phase hydroalkylation and hydrodeoxygenation of phenol by dual functional catalysts comprised of Pd/C and H/La-BEA. *ACS Catal* **2**, 2714–2723 (2012).
72. Zhao, C., He, J., Lemonidou, A. A., Li, X. & Lercher, J. A. Aqueous-phase hydrodeoxygenation of bio-derived phenols to cycloalkanes. *J Catal* **280**, 8–16 (2011).
73. Nelson, R. C. *et al.* Experimental and Theoretical Insights into the Hydrogen-Efficient Direct Hydrodeoxygenation Mechanism of Phenol over Ru/TiO2. *ACS Catal* **5**, 6509–6523 (2015).
74. Bui, V. N., Laurenti, D., Afanasiev, P. & Geantet, C. Hydrodeoxygenation of guaiacol with CoMo catalysts. Part I: Promoting effect of cobalt on HDO selectivity and activity. *Appl Catal B* **101**, 239–245 (2011).
75. Wang, S. *et al.* Hydrodeoxygenation of anisole to benzene over an Fe2P catalyst by a direct deoxygenation pathway. *Catal Sci Technol* **10**, 3015–3023 (2020).

76. Robinson, A. *et al.* Enhanced Hydrodeoxygenation of m-Cresol over Bimetallic Pt-Mo Catalysts through an Oxophilic Metal-Induced Tautomerization Pathway. *ACS Catal* **6**, 4356–4368 (2016).
77. Liu, X., An, W., Turner, C. H. & Resasco, D. E. Hydrodeoxygenation of m-cresol over bimetallic NiFe alloys: Kinetics and thermodynamics insight into reaction mechanism. *J Catal* **359**, 272–286 (2018).
78. Capponi, M., Gut, I. G., Hellrung, B., Persy, G. & Wirz, J. Ketonization equilibria of phenol in aqueous solution 1. *Can. J. Chem.* **77**, 605–613 (1999).
79. Schutyser, W. *et al.* Selective nickel-catalyzed conversion of model and lignin-derived phenolic compounds to cyclohexanone-based polymer building blocks. *ChemSusChem* **8**, 1805–1818 (2015).

Chapter 3: Unravelling Preferential Decoration of Metal Sites by WO_x in WO_x/Pt Catalysts

Reproduced in part with permission from:

Marlowe, J., Deshpande, S., Vlachos, D. G., Abu-Omar, M. M., Christopher, P. Effect of Dynamic and Preferential Decoration of Pt Surfaces by WO_x on Hydrodeoxygenation Reactions. *J. Am. Chem. Soc.,* **2024,** 146, 20, 13862-13874.

3.1: Background

3.1.1 Multidimensional Roles of Supports in Catalysis

Though the work presented in Chapter 2 of this dissertation focuses exclusively on the ways in which atomic-scale changes to the metallic active site, moderated by particle size, influence HDO, the role of the support in catalysis, typically a transition metal oxide, cannot be ignored. While today a ubiquitous component in catalyst formulation, an appreciation for the role of the catalyst support in dictating properties and reactivity can be considered relatively new in the broad scheme of the history of catalysis and still evolving. The first use of a support for catalytic materials can likely be ascribed to Johann Wolfgang Dobereiner[1,2], a German chemist who in 1823, like many earlier contributors to the field of catalysis, studied platinum-catalyzed hydrogen combustion in air. While previous studies by notable chemists such as Edmund Davy had been made using a platinum wire[3], this platinum wire required heating prior to exposure to H_2 to manifest the notable catalytic activity. However, it was Dobereiner who first introduced a platinum salt, likely ammonium chloroplatinate, onto balls made from clay followed by subsequent calcination to arrive at an active material. This platinum-impregnated

material exhibited the capability to combust hydrogen under ambient conditions, even in the absence of prior heating, representing a notable step forward in the activity of platinum catalysts compared to bulk-like wires and filaments. Thus, the supported catalyst was born.

The concept of catalyst supports did not immediately take off, however, despite follow-up reports from other researchers at the time. William Henry in 1824 followed Dobereiner's method for additional studies of hydrogen oxidation (this is the first report that can be easily tracked down via modern means, and Henry includes the first detailed synthesis for a supported catalyst, noting ratios and pre-treatments, likely making it the first published catalyst synthesis procedure)[4]. Further popularization presumably stemmed from a process patented by Henry Deacon for the production of Cl_2 from HCl in the presence of O_2 over Cu catalysts impregnated on clay supports, deemed "Deacon's balls"[5].

Despite the consistent growth in the popularity of catalyst supports for the means of stabilizing catalytic materials without coalescence, it should be stressed that a true appreciation for the role of the support lay many decades of research ahead. Indeed, even once catalyst supports became commonplace in industrial and academic research, the supports themselves bore only marginal resemblance to the materials used today. Kieselguhr, or diatomaceous earth, was a naturally occurring, siliceous mineral exhibiting high surface area and small primary particle size stemming from its formation from fossilized diatoms, which are single-celled microalgae. Early catalysts explored by Fischer and Tropsch in the late 1920s for coal reforming into automotive fuel were promoted cobalt catalysts on kieselguhr[6,7]. Thus, it is worth considering that in the first 100 years after Dobereiner's initial work impregnating clay with platinum, there was very little progress in the field of catalyst supports past utilizing what

was essentially, inelegantly dirt as the catalyst support. Compare that to the progress made in the next 100 years, and the difference is striking.

An explosion in the utilization of heterogeneous catalysts in industrial processes during the early 1900s, attributable to the growth and maturation of the petroleum industry, brought along with it a revolution in the understanding of the roles of supporting materials in catalysis. Though naturally occurring acidic clays had been sparingly used as early as 1797[8], the Houdry process in 1936 utilized acid-activated clays in the fluidized catalytic cracking of crude oil into gasoline-grade molecules[9,10]. Such naturally occurring, treated acid catalysts were quickly replaced by synthetic acidic zeolites in the 1950's, which of course are not ubiquitous across the petroleum industry today for a number of hydrocarbon conversions[11,12]. Not long after the Houdry process in 1954 came the reports by Mars and van Krevelen on the ability of metal oxides to donate lattice oxygen species to reactions in a cycle of reduction and oxidation for vanadium oxide catalysts in SO_2 oxidation, giving rise to the so-called Mars-van Krevelen mechanism[13,14]. This research was utilized as the basis for the growing interest in CO oxidation reactions for automotive exhaust treatment during the 1970s and 1980s, culminating in the first CeO_2-based catalytic converter in 1981 relying heavily on Mars-van Krevelen-type activity for emissions abatement[15,16]. Early examples also exist of non-chemical support effects such as the alkylation of toluene to *p*-xylene, assisted by the facilitated diffusion of para-xylene relative to ortho- and meta-xylenes within the pores of ZSM zeolites[17–19]. Table 3.1 below summarizes some of the most industrially-relevant applications of support effects in heterogeneous catalysis today.

Table 3.1

Support Role	Classical Example	Common Usage
Acidity	Zeolite Y	Fluidized Catalytic Cracking
Redox Activity	$Pt/Rh/CeO_2/Al_2O_3$	Automotive Catalytic Converters
Transport Inhibition	H-ZSM-5	Toluene Alkylation to p-Xylene
Metal-Support Interaction	Pt/TiO_2	Photocatalysis

In the examples listed above, the supporting materials represent a structurally stable material that does not appreciably change during the course of reaction. For instance, in the absence of deactivation and coking, the acidic and porous properties of zeolites may be considered to be stable, although recent work has begun to investigate the ways in which process conditions can destabilize the zeolitic framework through heteroatom dissolution and segregation. In the case of CeO_2 and other Mar-van Krevelen-active supports, lattice oxygen diffusion is typically rapid enough such that oxygen consumption on the surface does not result in structural changes past the first few surface layers of the crystal. Innocent supports which play an even more minimal role in catalysis, such as SiO_2, Al_2O_3, and C, undergo even more negligible changes in structure and characteristics under all but the harshest reaction conditions.

However, the identification of dynamic catalysts that exhibit significant structural changes during reaction demands consideration for certain systems. It has been appreciated for some time now that metal nanoparticles themselves exhibit considerable dynamics under reaction conditions, assisted by the presence of adsorbates which facilitate the surface diffusion

of metal atoms. Gerhard Ertl's ground-breaking work observing the dynamic cycle of Pt(111) lattice structure in response to CO and O coverage during CO oxidation underscores that these changes are not just possible, but can effect measurable changes in reactivity[20]. More recently, studies into the Ni surface during CO_2 hydrogenation have identified the dynamics between NiO island formation and consumption, where NiO islands are not present during catalyst pre-treatment, but constitute the active site under reaction conditions[21]. Some work has also shown that these changes can affect more than just the metal surface through the dynamic diffusion of Ag single atoms into and out of the bulk in Pt nanoparticles depending on the adsorbate environment[22]. Thus, the dynamics for metal catalysts are known to be both long- and short-range in nature.

3.1.2 Strong Metal-Support Interaction (SMSI): Classical to Modern Applications

Dynamic changes to catalyst structure and properties are not isolated to active metal components but have also been observed for supports themselves, most famously represented in the response of Pt/TiO_2 catalysts to reduction. In what was to become perhaps a regrettable name in retrospect due to vagueness, the first report of the strong metal-support interaction (SMSI) was made by Tauster, Fung, and Garten in 1978[23]. The lack of specificity in the name stems directly from the initial uncertainty regarding the cause of the behavior identified to be SMSI, namely the suppressed chemisorption of CO and H_2 by Pt/TiO_2 that had been subjected to high-temperature (>500˚C) reducing treatments. A hallmark of the SMSI phenomenon is that the suppressed chemisorption capacity is reversible upon re-exposure of the catalyst to oxidative environments at high temperatures. This important distinction distinguishes the

phenomenon from other sources of suppressed chemisorption capacity, such as by sintering or poisoning, which are effectively irreversible processes, with the exception of various regeneration strategies.

Follow-up work employing transmission electron microscopy[24] (TEM) and x-ray photoelectron spectroscopy[25,26] (XPS) identified the reduction of the TiO_2 support into reduced states (originally assigned as Ti_4O_7) which mobilized onto the metal surface, forming a physical blockade against chemisorption. While of fundamental interest immediately from a materials science perspective, this over-coated or decorated state after reduction was also quickly identified to exhibit changes to reactivity. CO hydrogenation was an early probe reaction for these materials as improvements to methanation rates were observed despite the necessary loss of sites caused by the decoration itself[27,28]. Indeed, similar reactions such as CO_2 hydrogenation continue to garner interest in the study of catalysts under the SMSI state, exhibiting similarly improved rates of methanation as the original CO hydrogenation studies[29–31].

Though at this point a well-described phenomenon, a number of questions remain regarding the fundamentals of SMSI. Initially, it was believed that the driving force behind the overlayer formation was the overall reduction of surface energy of the system. This has been refined recently to pertain specifically to the Gibb's energy gained from the formation of crystalline domains on the metal surface by reduced phases. In the case of Rh/TiO_2, *in situ* TEM work demonstrated the formation of Ti_2O_3 and corroborated its formation against various other phases of TiO_x using thermodynamic calculations and TEM measurements made at different chemical potentials of O_2[32].

While these describe primarily the role of the oxide and conditions in the formation of the SMSI state, there is also a component contributed by the metal particles themselves. For instance, not all metal nanoparticles facilitate the formation of SMSI-like overlayers, and even those that do exhibit notable exceptions. For example, it has been shown that SMSI is unfavorable to form over Pt or Au nanoparticles smaller than approximately 1 nm[33,34]. Considering the argument in favor of crystalline domain formation being the primary driving force for decoration, one interpretation of these results is that nanoparticles that provide surfaces that strain or prevent crystalline oxide lattices might inhibit the SMSI state from forming.

This also has important consequences for the case of partially or incompletely oxide-decorated surfaces. Such partially decorated states have been of interest practically for their maintained availability of metal sites, which are frequently still considered to be the active sites even under the SMSI state. Such partially decorated systems may thus exhibit the benefits to selectivity that have frequently been observed in the SMSI state while also exhibiting diminished drawbacks in the form of less suppressed activity relative to completely decorated catalysts. Reports of partial decoration have been made for Pd/TiO_2 catalysts reduced at varying temperatures in what likely results in a kinetically-limited overlayer, but certain synthetic routes also exist, as will be discussed in the next section[35].

However, these partially decorated states raise important questions, as in the limit of low decoration the formation of organized, crystalline domains of oxide is not feasible due to the low density of oxide on the surface. Also, the incomplete decoration of the surface introduces additional degrees of freedom for the overlayer on both the atomic scale, in terms of whether the reduced oxide is present as monomers, oligomers, or crystalline domains on the

surface, and on more extended scales, regarding the spatial organization of the oxide domains relative to the metal nanoparticle surface and other oxide domains.

3.1.3 Inverse Catalysts for HDO

Recently, a new class of analogous materials deemed "inverse catalysts" have been reported[36–40]. These materials are composed of unsupported or irreducible (e.g. Al_2O_3, C, SiO_2) oxide-supported metal nanoparticles onto which reducible (Fe_3O_4, TiO_2, etc.) oxide domains are co-deposited, often through intentional, synthetic routes. The reducible oxide layers can overcoat the Pt group metal nanoparticles, akin to the overcoating seen in SMSI. An important feature of inverse catalysts in comparison to traditional SMSI catalysts (e.g. Pt/TiO_2), wherein the reducible support is present in a significant stoichiometric excess relative to the metal nanoparticles, is the tunable coverage of the reducible oxide on the metal based on the amount reducible metal oxide added, providing an additional dial to modify catalyst activity.

Inverse catalysts can exhibit significantly altered reaction kinetics as compared to the bare metal catalysts[29,41–43], with an important application being hydrodeoxygenation (HDO) of lignin-derived monomers towards biomass valorization[44–46]. For example, inverse catalysts such as $WO_x/Pt/C$ and $NbO_x/Pt/MgAl_2O_4$ achieve >98% selectivity to desirable deoxygenated aromatics, in stark contrast to their unmodified analogs that exhibit considerable aromatic hydrogenation activity to produce undesired products with saturated rings. Recently, we reported on the structure sensitivity of Pt catalysts for HDO of model lignin-derived phenolic monomers, identifying that low-index terraces, consisting of well-coordinated Pt (Pt_{WC}) atoms, are responsible for the undesired aromatic hydrogenation reaction[47]. Considering the likely co-existence of covered and uncovered metal sites on the surface of inverse catalysts for HDO, it

is thus essential to elucidate the extent to which specific surface Pt sites, such as Pt_{WC} sites, become decorated by reducible metal oxide domains in order to understand the role of oxide overcoating in altering catalyst performance. Thus, the goal of this work will be to develop a fundamental understanding of how atomic-scale WO_x/Pt structure alters catalyst reactivity in the HDO of phenolics, rather than push the limits of catalyst performance, which has been reported previously.

The organization of reducible oxide domains on the surfaces of metal nanoparticles, as seen in inverse catalysts, specifically with an appreciation of potential metal site-specificity (e.g. steps vs terraces), remains elusive, particularly under reaction conditions. Surface science studies of reducible oxide overcoating of metal single crystals have demonstrated the formation of oxide "trails" or dendrites, suggestive of facile surface diffusion of oxide species[48,49]. Further, it has been observed that oxide growth nucleates at metallic step sites, suggestive of energetic stabilization of oxide domains at specific locations on metal surfaces, shown in Figure 3.1 for NbO_x clusters on Au(111)[50–54]. However, these effects have not been resolved for nanoparticle surfaces under reaction conditions. Additionally, theoretical analyses have primarily focused on low-index metal surfaces, which have limited applicability to the

inherently defective surfaces of nanoparticles found in heterogeneous catalysts that expose steps, edges, and corners.

Herein, we theoretically assess the organization and stability of a model W_3O_7 trimer on various stepped Pt surfaces using density functional theory (DFT) and a new machine learning protocol. We combine these computational studies with electron microscopy, *in situ* and probe molecule spectroscopies, and HDO reactivity measurements to elucidate the dynamic, site-dependent organization of WO_x overcoating domains on Pt nanoparticle surfaces

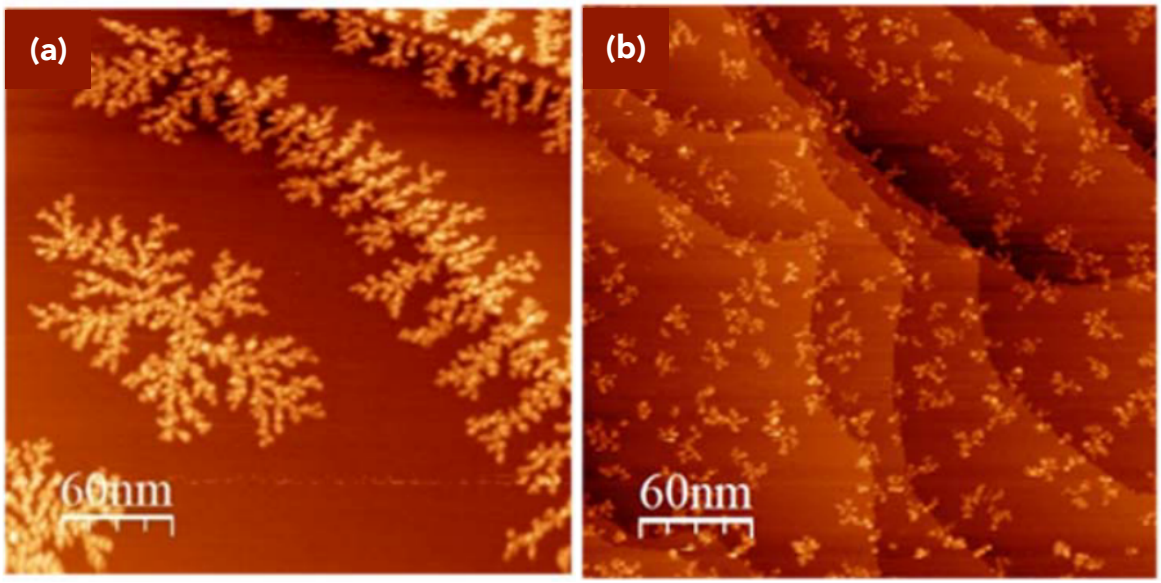

Figure 3.1: STM images of NbOx clusters on Au(111) surface showing dendritic structures which exist on terraces and step edges. Though surface science experiments under UHV conditions have suggested preferential growth, such behavior has been unreported for powder catalysts under reaction conditions. Reproduced from Ref. 50.

in heterogeneous inverse $WO_x/Pt/SiO_2$ catalysts. The computational and experimental results identify the preferential decoration of well-coordinated Pt sites (terraces) by WO_x as the primary contributor to suppressed hydrogenation of the aromatic ring in HDO of phenolics on inverse catalysts. The identification of preferential decoration of specific metal sites by reducible oxide domains extends the knowledge on inverse catalysts previously limited to model surfaces under ultra-high vacuum conditions to a broader understanding of high surface area metal nanoparticle catalysts under reaction conditions.

3.2 Results and Discussion

3.2.1 Computational WO_x/Pt Model and DFT Analysis

To theoretically assess the organization and structure of sub-monolayer domains of WO_x on Pt surfaces, a W_3O_7 trimer model was considered on a range of Pt surfaces, as shown in Figure 3.4a. The structure of W_3O_7 was studied on Pt(553), Pt(221), and kink-Pt(221) surfaces. These model surfaces exhibit two distinct classes of Pt sites across the step edge, as defined by their coordination to other Pt atoms, well-coordinated (WC, ≥8 nearest Pt neighbors) and under-coordinated sites (UC, <8 nearest Pt neighbors)[55]. The influence of different metal site coordination on W_3O_7 stability is of interest considering that the surface coordination of metal nanoparticles depends on factors such as nanoparticle shape and size. The two different step models, Pt(221) and Pt(553), are chosen to understand the effect of terrace width on WO_x stability. Based on a recent phase diagram analysis of WO_x domains on Pt(111)[56], W_3O_7 is considered a representative model structure for reduced WO_x growth on metal surfaces[43,57]. Additional WO_x models, including domains containing Brønsted acid sites (e.g., W_3O_xH), higher W oxidation states, and select W_4O_x structures were considered. These structures exhibited consistent trends in WO_x growth and organization as observed for W_3O_7, and thus, we focus on W_3O_7 on Pt surfaces for this model, though experimental systems likely

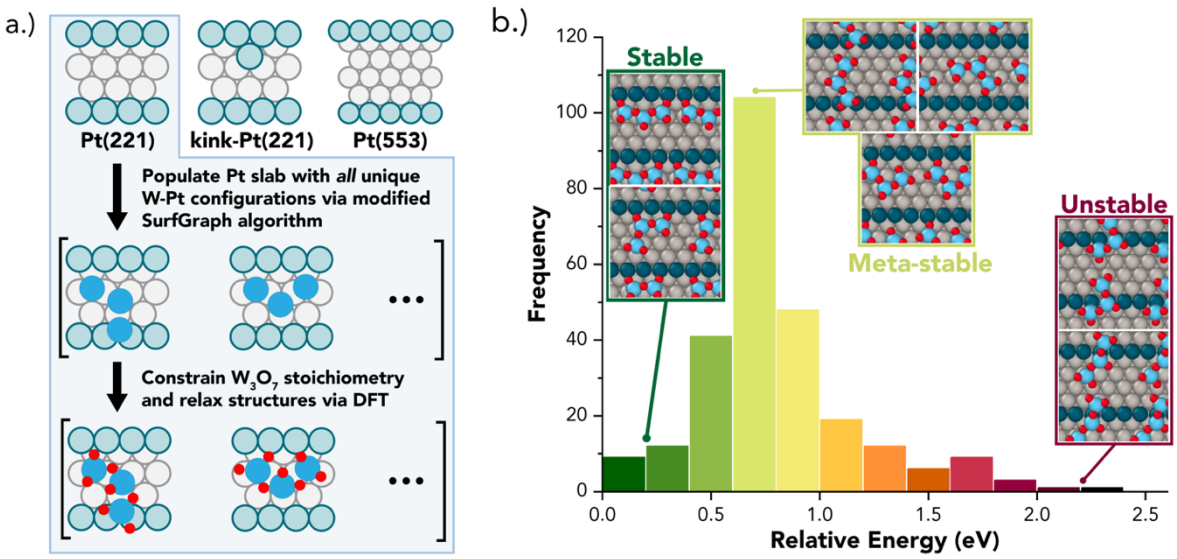

Figure 3.2: WO_x models on Pt step surfaces. a.) Summary of computational methods used to populate the W_3O_7 trimer model on Pt(221), kink-Pt(221), and Pt(553) surfaces, resulting in 340, 471, and 265 unique structures, respectively. b.) Histogram of DFT energies on Pt(553), with representative stable, meta-stable, and unstable structures (shown in insets). Legend: Pt_{WC} (grey), Pt_{UC} (dark blue), W (light blue), O (red)

exhibit a range of WO_x structures. A modified SurfGraph algorithm was utilized to estimate all possible (~1000) unique configurations of W_3O_7 on the Pt step model surfaces[58–60], as summarized in Figure 1a. The number of configurations is dictated by the different coordination numbers of the surface Pt atom(s) for a given surface model, and the orientation and structure of the adsorbed W_3O_7 trimer. The framework utilized to generate structures is discussed elsewhere[60,61], and its adaptation is detailed in the methods section.

DFT calculations were performed on the enumerated configurations to assess the stability of the SurfGraph-generated structures. As a representative case, the formation energy relative to the most stable W_3O_7/Pt structure is plotted as a histogram for various W_3O_7 structures on Pt(553) in Figure 3.2b. The most stable W_3O_7 structures (green bars in Figure 3.4b) preferentially adsorb on Pt_{WC} sites on the terrace adjacent to the Pt step edge, enabling a bond between O of WO_x and Pt_{UC} sites at the step edge. The distance between W in adjacent periodic images is at least 4.75 Å, suggesting minimal interaction and influence of computation

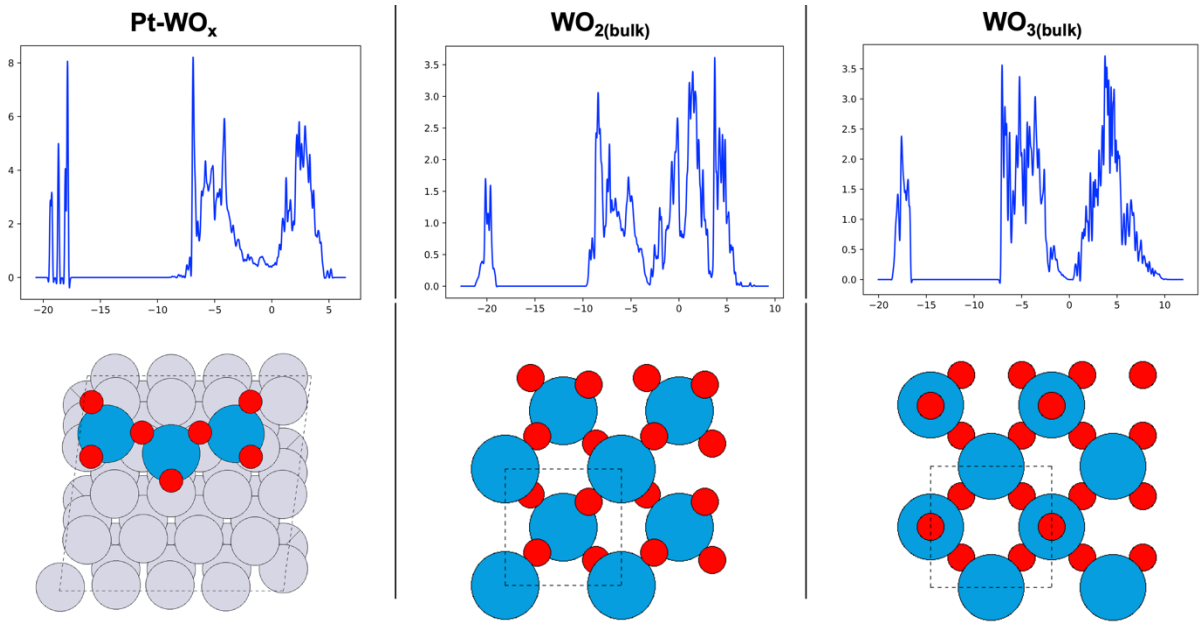

Figure 3.3: DOS simulations for W_3O_7/Pt(553), WO_2(bulk) and WO_3(bulk). The DOS for Pt-WO_x has features resembling both bulk WO_2 and WO_3, in line with an oxidation state between W^{4+} and W^{6+}.

cell size. Interaction between O and Pt_{UC} sites is typically more favorable than interaction with WC Pt sites by 0.2-0.3 eV, hence predicting WO_x growth on WC terraces adjacent to UC sites as well as on the extended terraces of large nanoparticles[62,63]. Projected DOS for W_3O_7/Pt(553) exhibits features between WO_3 and WO_2, suggesting W oxidation states including W^{4+} and W^{6+} (Figure 3.3). The meta-stable structures (yellow bars), which are 0.5–1 eV uphill compared to the most stable ones, contain W mostly on the terrace with fewer W-O-Pt_{UC} bonds. Further, structures with direct W-Pt_{UC} interactions are >0.6 eV higher in energy than the most stable structure. The most unstable structures (red bars), >1 eV higher in energy than the most stable structures, contain multiple W bonding directly to Pt_{UC} sites or WO_x oriented across the step edge.

Applying a Boltzmann distribution to the Pt(553) structure histogram in Figure 3.4, practically, only structures within 0.1 eV of the most stable structure will be accessible (Figure 3.2) under relevant conditions assuming the facile surface diffusion of oxide oligomers on

metals[48,64]. While Pt(553) provides insight into the structural motifs of WO_x organization on the Pt surface, machine learning modeling was also employed to identify the dominant features that dictate W_3O_7 stability.

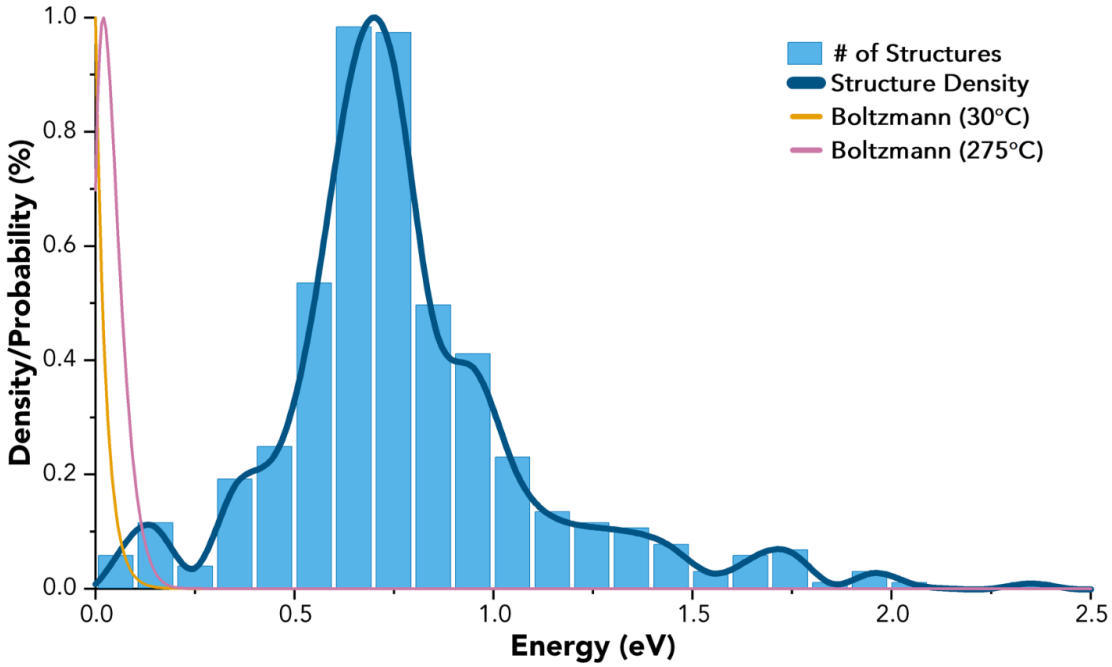

Figure 3.4: Boltzmann distribution applied to the relative energy histogram shown in Figure 1 at 30˚C and 275˚C. Narrow dispersion due to low kT suggests that only the stable states within ~0.25 eV of the most stable structure are expected on the WO_x/Pt surface.

3.2.2 Characteristic Features Via Machine-Learning

The DFT calculated energetics and structures for WO_x/Pt configurations on all three Pt model surfaces were combined into a single dataset. Ten geometric features, shown in Table 3.2 below, were calculated for each configuration to train a machine learning model (XGBoost) against the respective DFT energy[65,66].

These features include: (i) (3) Z-heights for each of the three W atoms of the trimer with respect to the last row of Pt-terrace atoms, (ii) (3) average coordination numbers of the Pt

atom(s) bound to each of the three W atoms, (iii) the number of O-Pt_{UC} bonds, (iv) (2) Z-heights of the W atoms in the W-O-W pair with the largest W-O-W angle, and (v) the largest W-O-W angle. These are intuitive geometric parameters and provide a basis for a model to understand W_3O_7 stability on Pt surfaces. W atoms were assigned an identifier (eg. W1, W2, W3), universal to all structures, based on their Z-height per feature (i) above. A 65:35 training:test split was utilized on the 1,023 configurations. Figure 3.5a-b shows the model training and testing. The black dashed lines represent the parity line and the red dashed lines

Table 3.2

	Name	Range	# of Values
Z-Height above Pt surface for each W atom in W_3O_7	$Z_{W\#}$	1-3 Å	3
Coordination number of Pt for each Pt-W bond	$CN_{W\#}$	7-10	3
Pt-O Bonds	Pt-O	0-2	1
Z-Height of W-O-W pairs grouped by bond angle	$\Delta Z_{\#}$	1-3 Å	2
W-O-W bond angles	θ_{WOW}	120˚-170˚	1
Total Features			**10**

Table 3.2: Features and parameter ranges used in the XGBoost modelling of WO_x/Pt(553) structures.

represent bounds of a width of 0.25 eV. A mean absolute error (MAE) of 0.14 eV was estimated, and the majority of the 358 testing points (81.6%) were inside the bounds. Utilizing the surrogate model, the gain metric was used to estimate the features contributing the most to the model fitting and were plotted in Figure 3.5c[67].

The three most important features are (i) the coordination number of the Pt sites onto which the W atoms with the lowest Z-height are adsorbed, (ii) the presence of O-Pt_{UC} bond(s), and (iii) the Z-height of the W atoms with the largest W-O-W bond angle. Features (i) and (ii),

together, showcase the stability of W atoms on Pt_{WC} sites in the concave region close to the Pt step edge that maximizes the interaction of O with Pt_{UC} sites while avoiding direct interaction of W with Pt_{UC}. Every O-Pt_{UC} bond stabilizes the W_3O_7 structure by ~0.2 eV compared to Pt(111), in agreement with the values of O bonding to Pt_{UC} sites in surface science[62,63]. However, the maximum number of Pt-O-W bonds formed by each W_3O_7 trimer is limited due to the lattice mismatch between Pt and WO_x. The Pt-Pt bonds have a bond distance of 2.8 Å[68,69], while the W-W bond length in WO_x is ~ 3.3 Å[70,71], resulting in a buckled garland-like W_3O_7 structure along the step edge (see most stable structure in Figure 3.4b). The importance of this "garland-like" structure toward the accessibility of undercoordinated Pt sites to adsorbates is discussed later. Feature (iii) highlights the role of strain in W-O-W bonds in stabilizing WO_x on Pt. Structures with large W-O-W angles, arising from one W atom present on top of a Pt_{UC} site and the other in the concave region (shown in Figure 3.4b as unstable structures), are less stable compared to ones with a smaller W-O-W bond angle (Figure 3.4b stable structures). However, the effect of W-O-W bond angle on the formation energy of WO_x is not intuitive and showcases the ability of ML-based methods to provide physical insights into complex configurational datasets.

The analysis highlights the importance of both step edges along with terrace sites in driving the stability of WO_x on Pt. The analysis predicts Pt_{WC} sites preferentially being decorated by WO_x on the terraces of Pt nanoparticles, with Pt_{UC} sites being only partially decorated by interacting with and anchoring the O of WO_x.

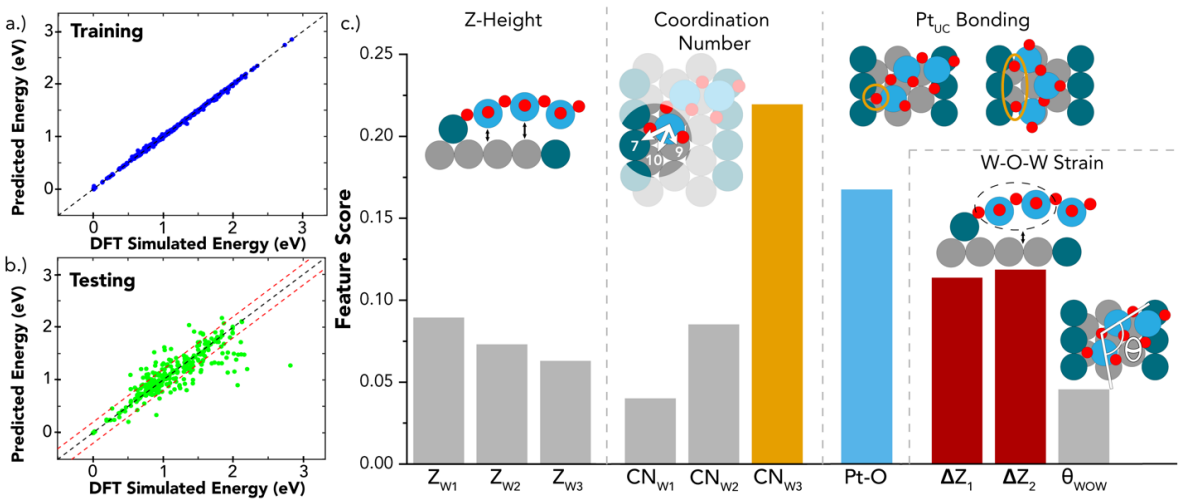

Figure 3.5: XGBoost model predicting dominant geometric features driving stability of WO_x on Pt(553) surfaces. a-b.) Training plot and parity plot of 65:35 split in model development. c.) XGBoost derived feature score for each feature trained in the ML model, with dominant features (CN_{W3}, Pt-O, and $\Delta Z_{1,2}$) highlighted in color.

3.2.3 Heterogeneous $WO_x/Pt/SiO_2$ Catalyst Characterization

To analyze the computationally predicted, site-dependent decoration of WO_x on stepped Pt surfaces, heterogeneous inverse $WO_x/Pt/SiO_2$ catalysts were synthesized. A Pt/SiO_2 catalyst was prepared via a modified strong electrostatic adsorption (SEA) procedure at 6% Pt weight loading[72–74]. SiO_2 was chosen as the catalyst support material due to its inactivity in HDO[75,76], low acidity, irreducibility, and amenability for spectroscopic characterization (e.g. compared to C supports which are often used in HDO but are black and thus are not conducive to UV-Vis-IR spectroscopy). Pt/SiO_2 catalysts exhibited an average Pt particle diameter of 11 ± 6 nm as measured by HAADF-STEM. This particle diameter was intentionally selected to align with the metal particle sizes of inverse oxide-on-metal materials previously studied in the literature that exhibited notable performance in HDO of phenolics[44,45]. Additionally, no clusters or single atom Pt species could be identified by HAADF-STEM, nor any other

characterization technique employed and discussed later, highlighting that all Pt-based reactivity can be attributed to nanoparticles.

WO_x was deposited via wet impregnation of the Pt/SiO_2 catalysts using an aqueous solution of ammonium metatungstate, $(NH_4)_6H_2W_{12}O_{40}$, with W weight loadings varied from 0.1-6 wt%. For simplicity, WO_x-loaded Pt/SiO_2 catalysts will be referred to as xW6Pt, where x is equal to the weight loading of W. Stepwise preparation of $WO_x/Pt/SiO_2$ catalysts enabled the development of catalysts with varying W loading and consistent Pt particle size distributions, which was essential to determine the role of WO_x overcoating of Pt on catalyst performance. HAADF-STEM images collected of 0.1W6Pt indicate that the average Pt particle size remains unchanged after WO_x deposition steps (Figure 3.6). This synthesis procedure

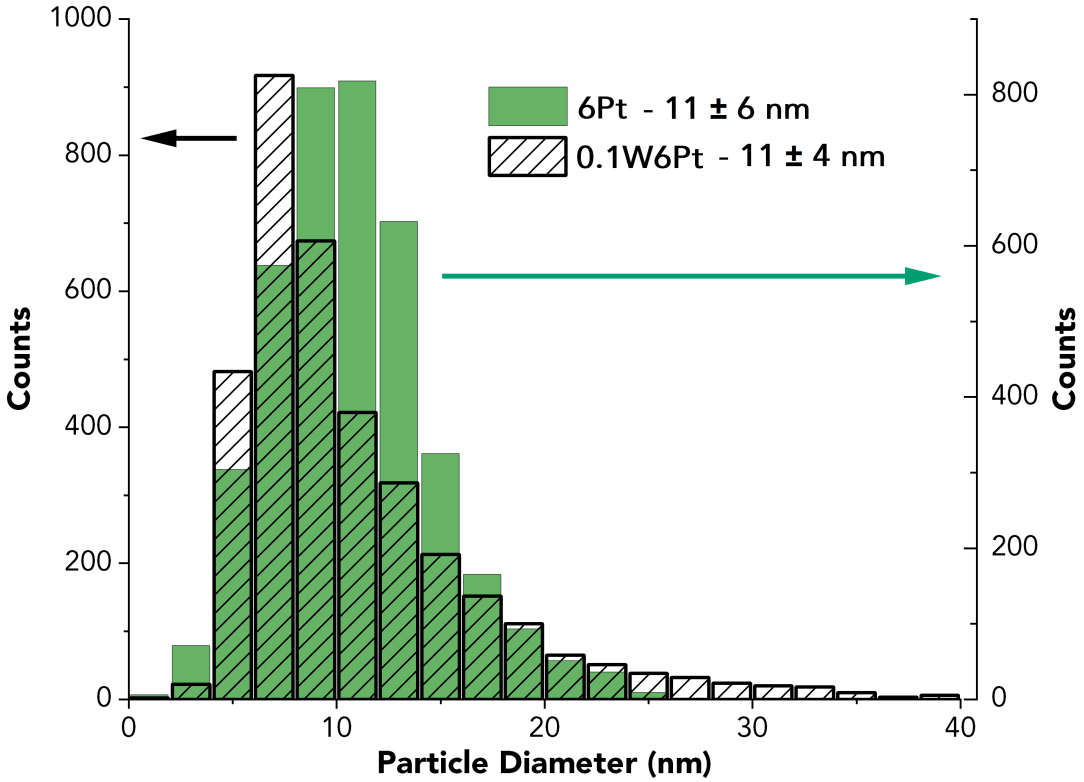

Figure 3.6: Comparison of the particle size distributions of 6Pt and 01W6Pt, showing that average particle size does not appreciably change as a result of the WO_x deposition synthetic steps. Differences in distribution breadth likely stem from batch-to-batch variation.

differs from inverse catalysts prepared via atomic layer deposition in that, here, WO_x is deposited uniformly over the surface of the SiO_2 catalyst, without preferential deposition on Pt nanoparticle surfaces. HAADF-STEM imaging of as-prepared 6W6Pt (Figure 3.7) shows that WO_x is observed both as isolated monomeric W species on SiO_2, as well as densely-packed WO_x oligomers that form 2D, film-like domains on the SiO_2 support. This is consistent with prior work that suggests that WO_x wets the surfaces of transition metal oxides and preferentially forms a monolayer-like structure before aggregation into well-ordered, 3D WO_3 particles[77,78]. The structures observed in HAADF-STEM are also consistent with UV-VIS measurements of the as-prepared $WO_x/Pt/SiO_2$, which exhibit edge energy consistent with the existence of monomeric and polymeric WO_x species.

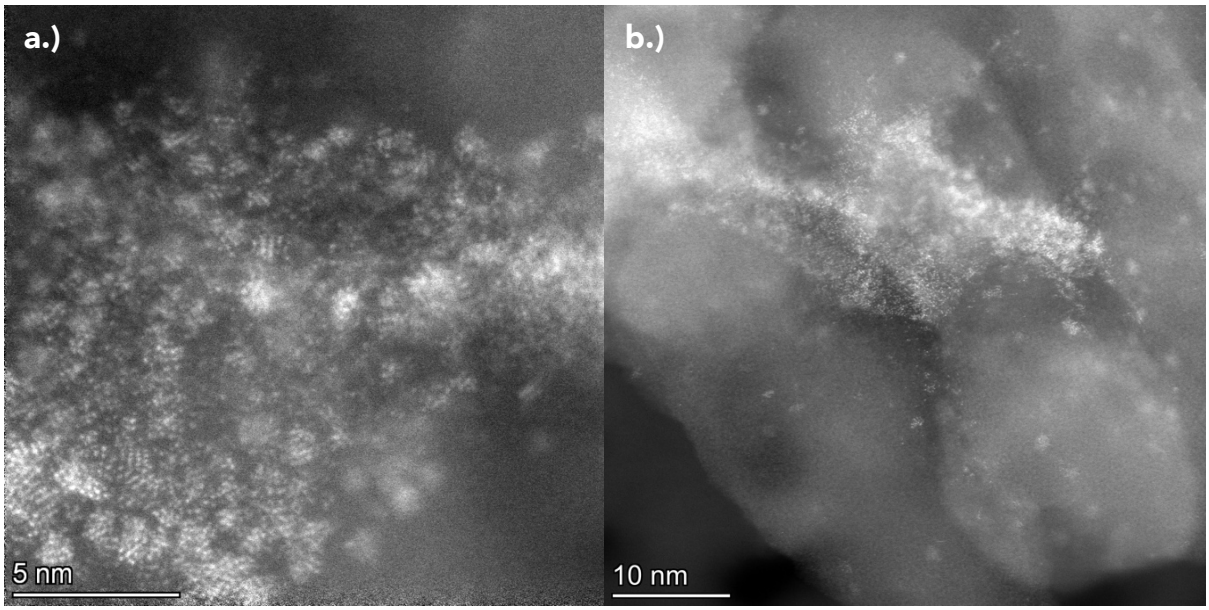

Figure 3.7: (a-b) HAADF-STEM images of 6W6Pt highlighting the morphology of WO_x domains on the SiO_2 surface.

HAADF-STEM imaging of 6W6Pt shows no evidence of WO_x decoration on Pt surfaces in the as-prepared materials following calcination in oxygen that is required to form WO_x from the precursor (Figure 3.8a). This demonstrates that under the oxidative conditions of catalyst synthesis (i.e. calcination), WO_x domains deposit on the SiO_2 support rather than

the Pt surface. This is either due to the significantly higher surface area of the SiO_2 support, or the instability of WO_x decoration on Pt when the Pt surface is oxidized and the WO_x is in its highest oxidation state (likely W^{6+}).

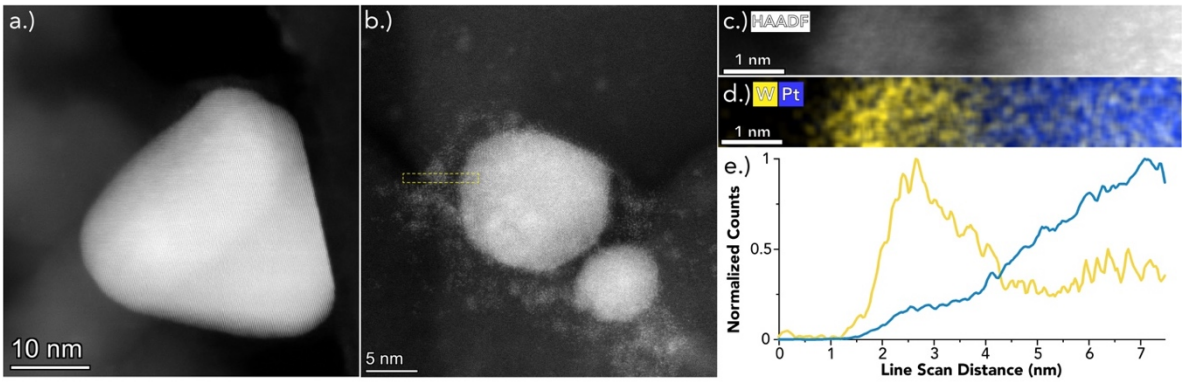

Figure 3.8: HAADF-STEM images of 6% W/6% Pt/SiO_2 catalyst a.) before and b.) after reduction at 325˚C for 1 hour in 10% H_2/Ar. c-e.) EDS map of the selected area in b.) shown by the yellow dashed box. EDS map evidences close spatial interaction between a W-rich layer (WO_x) and a Pt-rich area at the interface of a Pt nanoparticle seen in HAADF-STEM.

To explore the response of catalyst structure to reducing conditions, the as-prepared 6W6Pt was reduced in 10% H_2/Ar at 325˚C for 1 hour and then analyzed *ex-situ* by HAADF-STEM. Air contact between treatment and imaging was minimized by transporting the sample in an Ar-flushed vial. HAADF-STEM images, shown in Figure 3.8b, indicate noticeable changes to the surfaces of Pt nanoparticles induced by H_2 reduction, wherein visible overcoating exists on the surfaces of Pt nanoparticles. These overlayers both exist as disordered domains surrounding Pt nanoparticles and more ordered overlayers of uniform thickness. We attribute the differences in these two classes of overlayers to the degree of oxidation experienced in sample transfer between the reductive pre-treatment and the microscope. Beam effects have been excluded as the cause of these overcoating structures on Pt nanoparticles considering the absence of overlayers in as-prepared WO_x/Pt/SiO_2 materials following calcination, as well as the use of low beam currents during STEM imaging (<20 pA).

To confirm the composition of the overlayer observed in *ex-situ* imaging of reduced 6W6Pt, EDS was performed (Figure 3.8c-e). EDS demonstrates the presence of W and Pt in close proximity at the outer edge of the imaged particle (Figure 3.8d), suggesting that the W has decorated the Pt particle. The region imaged in EDS exists over a gap in the sample and substrate, supporting that W is bound to the Pt surface and not on the SiO_2 support existing below the edge of the Pt nanoparticle. Integration of the EDS results (Figure 3.8d) shows that the W signal increases along with the Pt signal, also supporting the close interaction of these two domains. The peak maximum of the W signal prior to the significant increase of the Pt signal, which remains high over the region of the nanoparticle itself, highlights that the overlayer is likely entirely composed of W, and not a combination of W and Pt, such as in an alloy phase which has been previously identified for W/Ni catalysts[79]. Thus, *ex situ* HAADF-STEM results identify that WO_x overlayers form on Pt particles during reductive pre-treatments via WO_x mobilization from the SiO_2 support to the Pt surface. However, further structural information as to the dynamics, extent, and structure of WO_x decoration cannot be assessed via STEM alone due to the use of *ex-situ* measurements and the lack of statistically relevant sampling.

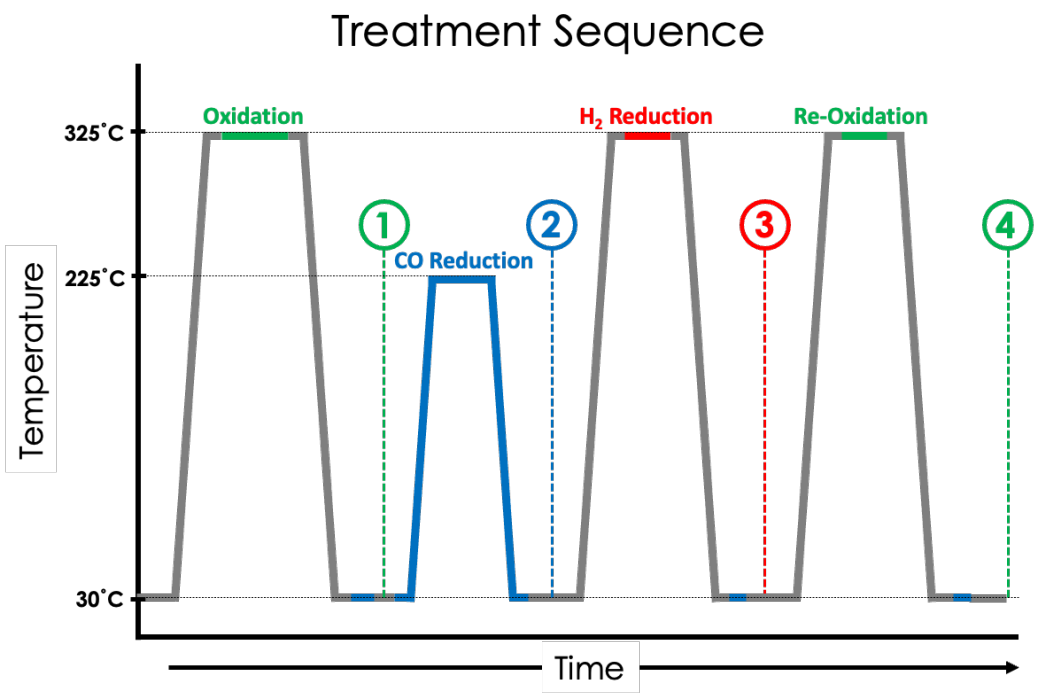

Scheme 3.1: Representation of the sequential pre-treatment used for the DRIFTS and UV-Vis characterization of 6W6Pt.

To explore the dynamic behavior of the catalyst structure and oxidation state under *in situ* conditions, UV-Vis and CO probe molecule diffuse reflectance infrared spectroscopy (DRIFTS) were performed. UV-Vis provides information on the oxidation state of W species and CO DRIFTS probes the nature and quantity of exposed Pt sites. Various pre-treatments were studied. 6W6Pt was first oxidized to investigate the dehydrated, as-prepared state of the catalyst. Then, 6W6Pt was reduced at 225 ˚C in the presence of 10% CO/Ar. CO is a mild reductant that does not reduce WO_x domains under the conditions studied here[80] (Figure 3.9). However, CO does facilely reduce PtO_x through CO oxidation to CO_2, thus allowing the characterization of the catalyst with Pt in the metallic state and WO_x in the fully oxidized +6 state[81]. This pre-treatment was important in the comparison of $WO_x/Pt/SiO_2$ catalysts with Pt/SiO_2, as the reductive H_2 pre-treatments typically used in the characterization of Pt/SiO_2 catalysts would have resulted in the formation of WO_x overlayers on Pt in $WO_x/Pt/SiO_2$. After

CO treatment, 6W6Pt was then reduced under 10% H_2/Ar, as in the HAADF-STEM experiments. Finally, the reversibility of observed changes was explored by conducting a second oxidation step. With the exception of the so-called oxidative SMSI state[82–84], wherein catalyst overlayers remain stable under O_2 atmospheres (typically at elevated temperatures), oxidation is expected to return the catalyst to the initial state exhibiting oxidized WO_x domains on SiO_2 and no WO_x coverage of Pt[23,85].

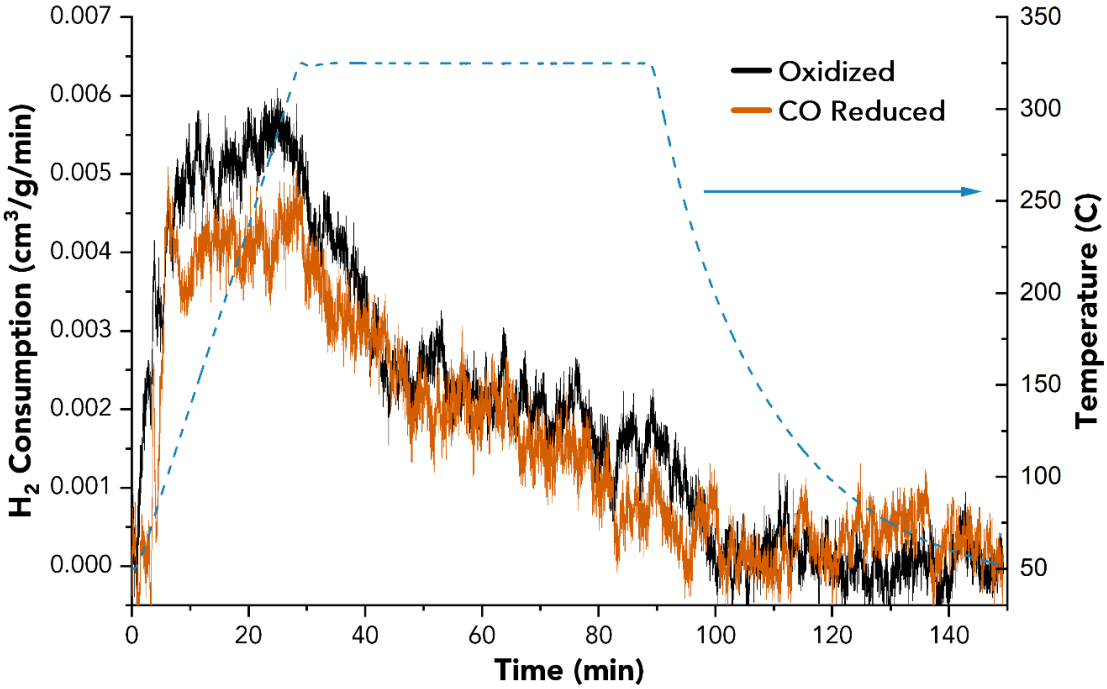

Figure 3.9: H_2-TPR of 6W6Pt taken after oxidation in UHP O_2 at 400˚C for 1 hour (black) and a sequential treatment of oxidation at 400˚C followed by CO reduction in 10% CO/Ar at 225˚C for 30 minutes (orange), mirroring treatments conducted in CO DRIFTS and UV-Vis experiments. Results show similar H_2 consumption trends, indicating that CO reduction does not cause significant WO_x reduction, as concluded from CO DRIFTS and UV-Vis.

Figure 3.10a shows the UV-Vis spectra of 6W6Pt collected under Ar at room temperature after the pre-treatment sequence described above. All spectra exhibit absorbance around 250 nm, which is related to the ligand-to-metal charge transfer (LMCT) between W and O associated with W^{6+} in WO_3 domains[77]. After the initial oxidation step, this is the only feature visible in the UV-Vis spectrum. The spectrum collected after CO pre-treatment shows

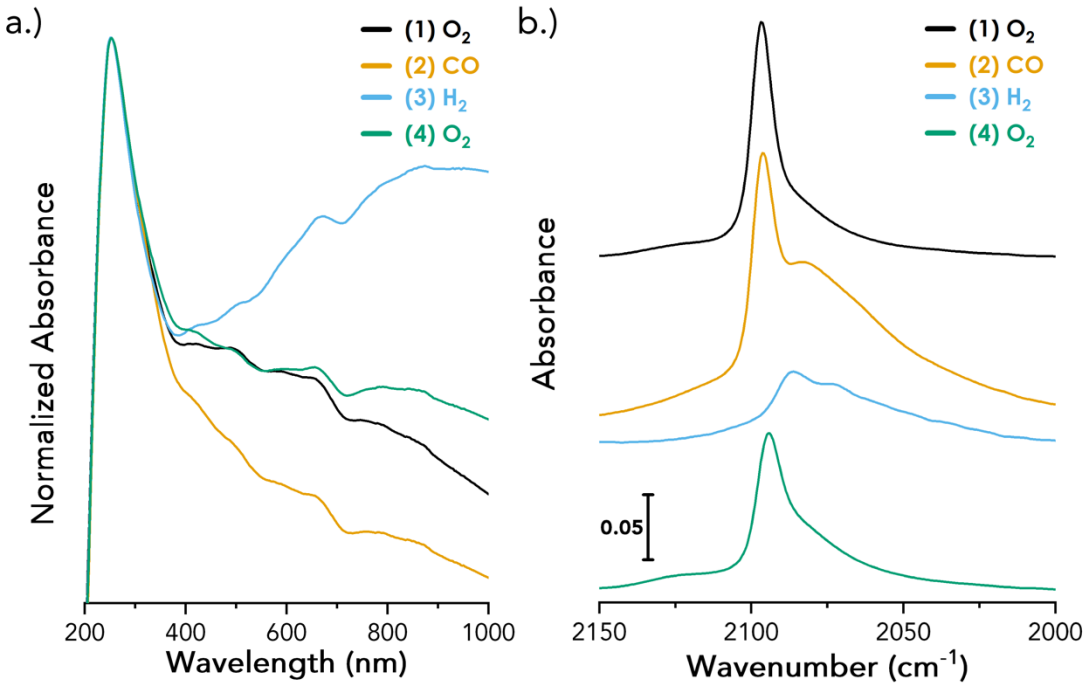

Figure 3.10: a.) UV-Vis and b.) CO DRIFTS spectra of 6W6Pt. Spectra collected under Ar flow at 30˚C after the pre-treatment step listed. Oxidations performed at 400˚C for 1 hour under UHP O_2. CO reduction conducted at 225˚C for 1 hour under 10% CO/Ar. H_2 reduction performed at 325˚C for 1 hour under 10% H_2/Ar.

no additional features other than a shift in the baseline at wavelengths between 400-1000 nm, which is related to changes in the overall optical properties of the material. This is likely caused by PtO_x reduction to a metallic Pt phase[86]. After H_2 treatment, a strong, broad feature is observed between 600-1000 nm, assigned to reduced W^{4+} and W^{5+} states, centered at ~500 nm and ~800 nm, respectively, that form from the WO_3 reduction[87,88]. Recent work has suggested that the absorption stems from intervalence charge transfer (IVCT) of mixed valent W-O-W pairs (e.g. W^{5+}-O-W^{6+})[89,90]. Deconvolution of this broad absorbance is suggestive of the presence of predominantly W^{5+} species after this step (Figure 3.11), though the relative cross-sections of these two absorption bands have not been reported, preventing confident quantification of the two species through UV-Vis. WO_x reduction can also be observed in the Raman spectrum collected of this material after reduction, showing the loss of the W=O vibrational feature at 930 cm^{-1} (Figure 3.12)[57]. The second oxidation step eliminates this

feature, and the sample absorption spectrum becomes essentially identical to the initial spectrum assigned to W^{6+}, highlighting the reversibility of oxidation state changes for W in this catalyst.

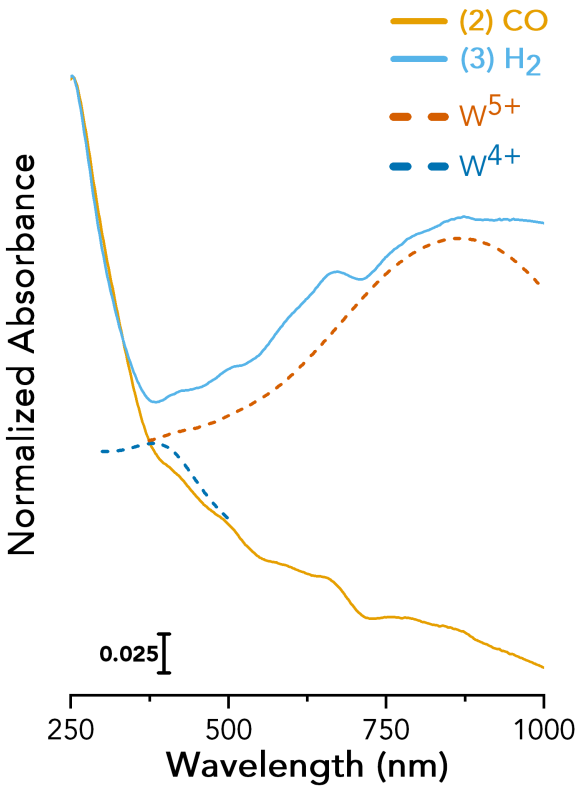

Figure 3.11: Deconvolution of UV-Vis spectrum for H_2-reduced 6W6Pt into components corresponding to W^{5+} and W^{4+} states. Assuming similar extinction coefficients between the states, W^{5+} predominates over W^{4+} after reduction.

To complement the HAADF-STEM results, which identified macroscopic changes to the organization and location of WO_x in response to reduction, and UV-Vis, which provided information into the oxidation state of W species, CO DRIFTS was performed. CO DRIFTS provides insights into the accessibility, geometric, and electronic state of Pt surface sites by probing the vibrational frequency of bound CO[91–94]. Considering the DFT calculations that identified preferential site decoration by WO_x on the terrace regions of Pt, insights into the

nature of exposed Pt sites are essential to understanding the location of WO_x overlayers on Pt surfaces, particularly for sub-monolayer coverages.

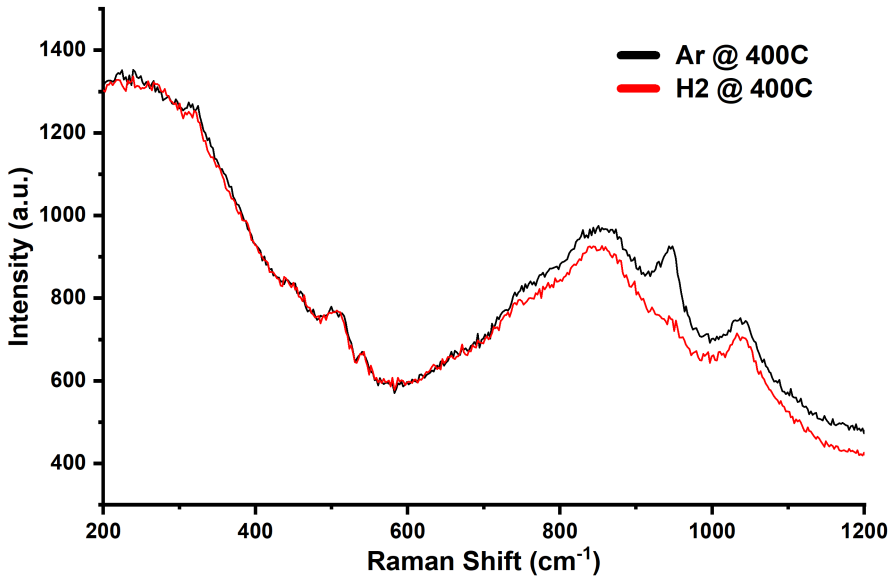

Figure 3.12: Raman spectra collected of 6W6Pt catalysts after inert and reductive pre-treatments showning the loss of W=O vibrations. Spectra were collected at 400˚C to mitigate the effects of fluorescence from the SiO_2 support, which entirely obscured Raman scattering at lower temperatures.

CO DRIFTS spectra were collected for 6W6Pt following each of the treatments previously discussed in the UV-Vis characterization. After each treatment, the sample was cooled to room temperature, exposed to CO until saturation coverage was reached, and then the cell was purged of CO by flowing Ar. Overall, the CO DRIFTS spectra (Figure 3.10b) show similar trends to the UV-Vis results in regard to the overall reversibility of WO_x decoration of Pt nanoparticles. After the initial oxidative pre-treatment, a single main feature is observed centered at 2096 cm^{-1}, corresponding to CO bound linearly to WC Pt sites located on low-index terraces such as Pt(111) and Pt(100) surfaces[55,95,96]. Additionally, a small, broad shoulder exists around 2120 cm^{-1}, assigned to CO bound to cationic Pt species, likely stemming from PtOx clusters or oxidized surface Pt species[94,97]. Since the catalyst has not been reduced prior to CO exposure in this step of the experiment, Pt surfaces are expected to exhibit high O

coverage, which can inhibit or co-exist with CO bound on the surface[98,99]. CO adsorption on WC metallic Pt sites is visible in this spectrum due to the CO oxidation reaction, which can consume surface oxygen (even at 30˚C) leaving metallic Pt sites available for CO adsorption[81,98]. This contrasts UC sites, found at steps, edges, and other defects on the Pt surface, which exhibit higher O binding energies[100,101] and are not considered active for CO oxidation under these conditions[102,103].

This conclusion is supported by the spectrum collected for 6W6Pt after reduction in a CO atmosphere at 225˚C in the following step. The resulting spectrum is characterized by two strong features, the same WC site feature at 2096 cm^{-1} as seen after oxidation and a second, newly exposed feature at 2080 cm^{-1}, assigned to CO bound to metallic UC Pt sites[55,104]. Exposing the catalyst to CO at 225˚C enables the CO oxidation reaction to occur on both WC and UC sites, consuming Pt-bound surface O species without reducing or otherwise mobilizing WO_x as shown in the UV-Vis results. The resulting spectrum, exhibiting the WC and UC features, is nearly identical to the CO-DRIFTS spectrum of the Pt/SiO_2 taken after reduction in H_2 (Figure 3.10b), supporting the conclusion that this spectrum is representative of a reduced Pt surface that is not overcoated by WO_x. Additionally, the similarity between CO-reduced 6W6Pt and H_2-reduced Pt/SiO_2 is further evidence that the WO_x deposition steps do not appreciably change the characteristics of the Pt nanoparticles, thus enabling direct comparison of the WO_x-modified catalysts with the unmodified catalyst. A small shoulder still persists at 2120 cm^{-1}, indicating that a small fraction of PtO_x domains present after oxidation were not reduced by the 10% CO/Ar atmosphere at 225˚C. Indeed, it has been previously shown that small PtO_x clusters can be difficult to reduce, even under H_2 atmosphere[105].

The CO DRIFT spectrum of 6W6Pt changes in shape and intensity after H_2 treatment and CO re-adsorption to saturation coverage at 30˚C. The loss of adsorbed CO intensity after H_2 treatment is consistent with the loss of Pt sites available to adsorb CO due to reduced WO_x overlayer formation, which was evidenced by UV-Vis based on W^{4+} and W^{5+} formation and seen in HAADF-STEM images. The CO stretching band is characterized by two convoluted features centered at 2085 and 2072 cm^{-1}, which are assigned to CO bound to WC and UC Pt sites, respectively, that remain after WO_x migration onto Pt. The relative intensities of the two features have changed after H_2 reduction, as compared to CO reduction, and the peak centers have shifted. These two observations provide important information about the state of WO_x decoration on the Pt surface and will be discussed in more detail below.

Following re-oxidation and re-adsorption of CO to saturation coverage at 30˚C, a similar spectrum is observed for 6W6Pt as compared to the initial oxidation, characterized by a single strong feature at 2095 cm^{-1} and a shoulder at 2120 cm^{-1}. These two features are assigned to CO bound linearly to WC Pt sites and CO bound to cationic Pt species in PtO_x domains, as previously discussed. The similarity of the CO DRIFTS spectrum following the first and last oxidation steps is evidence that in addition to the reversibility of WO_x reduction evidenced by UV-Vis spectroscopy, the decoration of the Pt surface by WO_x is reversible in response to the pre-treatment atmosphere used.

For 6W6Pt, the molar ratio of W:Pt is approximately 1, though there is a considerable excess of W compared to the number of surface Pt sites when accounting for the low dispersion of the ~10 nm Pt nanoparticles present in the Pt/SiO_2 catalyst. Thus, under reducing conditions, a large fraction of the Pt sites could be decorated by the reduced WO_x overlayer, as evidenced by the drop in the peak area associated with adsorbed CO species in the CO DRIFTS spectrum

after H_2 reduction (Figure 3.10b). As alluded to previously, however, the relative peak areas associated with CO adsorption on WC and UC sites changed between CO and H_2 pre-treatments. Specifically, the peak area associated with CO on WC Pt sites apparently decreased more than the peak area associated with CO adsorption on UC sites, suggesting that reduced WO_x species more effectively decorated WC sites than UC sites. This trend is opposite to what would be expected even when taking relative extinction coefficients of CO bound to WC and UC sites into account since perfectly non-preferential decoration would result in greater loss of UC site area relative to WC site area due to the higher extinction coefficient of UC sites[106].

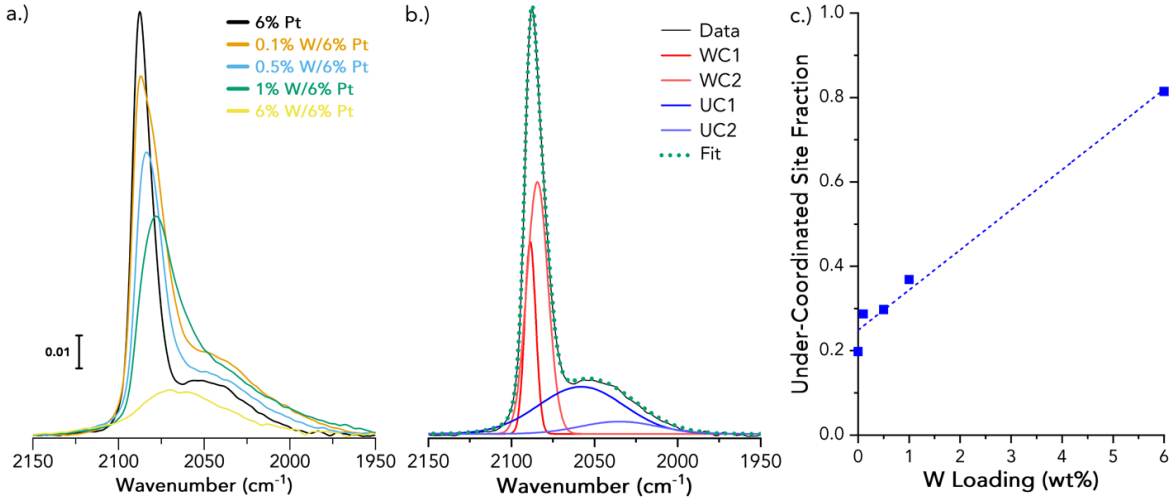

Figure 3.13: a.) CO DRIFTS spectra of various W loadings on 6% Pt/SiO_2. Spectra were collected at 30˚C. Catalysts were first oxidized at 400˚C for 1 hour in UHP O_2 before reduction in 10% H_2/Ar at 325˚C for 1 hour. CO adsorption conducted at 30˚C for 15 minutes before purging gas-phase CO from the cell with Ar. b.) Gaussian deconvolution of 6% Pt/SiO_2 using 4 features, 2 for each feature associated with CO on Pt_{WC} and Pt_{UC} sites. c.) UC site fraction determined by Gaussian fits of each $WO_x/Pt/SiO_2$ catalyst.

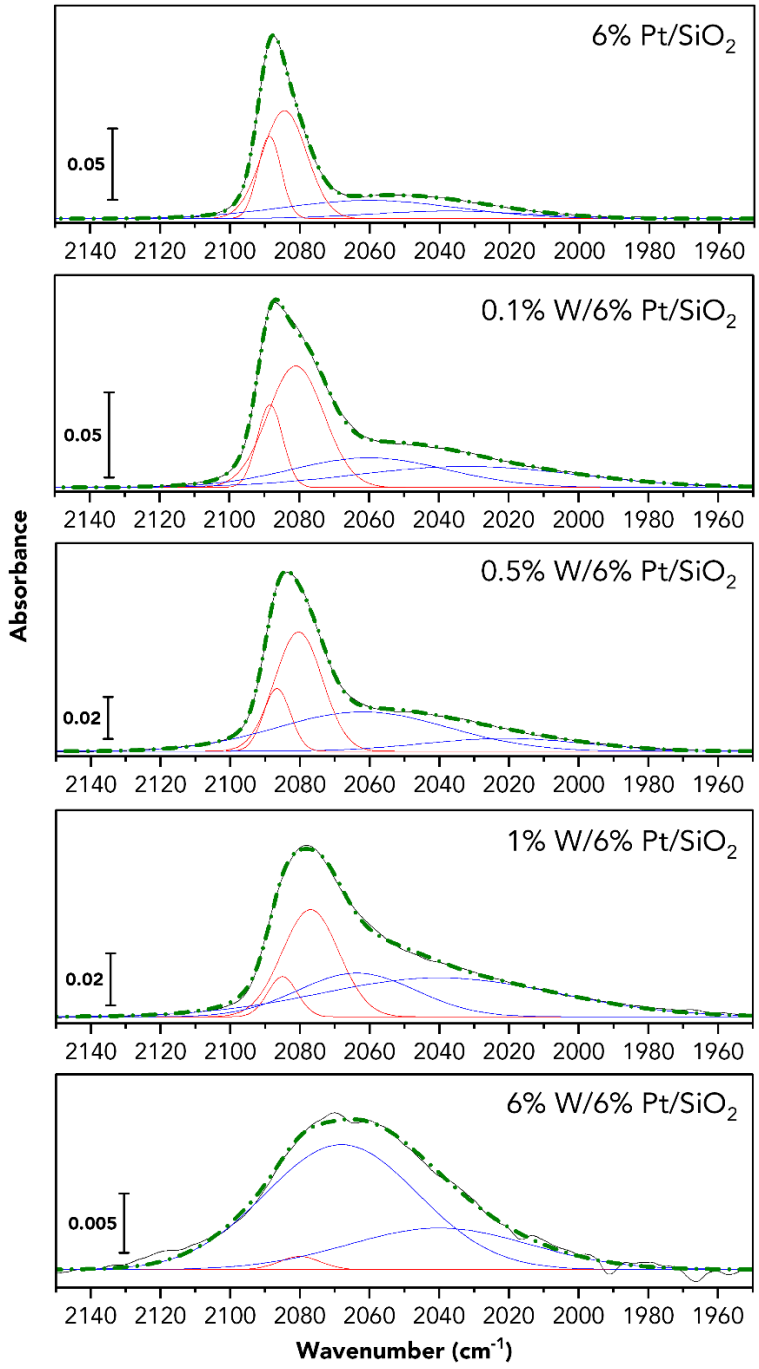

Figure 3.14: Deconvolution of $WO_x/Pt/SiO_2$ CO DRIFTS spectra into Gaussian features related to WC and UC sites. Two symmetric Gaussians were used for both WC and UC sites to capture asymmetry related to site heterogeneity.

To explore this in more depth, a series of WO_x-modified catalysts were synthesized from the same Pt/SiO_2 catalyst in the range of 0-6 wt% W. Moderation of W loading enabled

control over the amount of WO_x overlayer formation on the Pt surface after H_2 reduction. CO DRIFT spectra of the $WO_x/Pt/SiO_2$ materials with varying W loading following H_2 reduction are shown in Figure 3.13a. As discussed previously, the CO probe molecule DRIFT spectrum of the 6% Pt/SiO_2 catalyst without WO_x modification following H_2 reduction is qualitatively similar to the CO-reduced $WO_x/Pt/SiO_2$ shown in Figure 3.8b, exhibiting CO adsorption on both WC and UC features at 2087 and 2050 cm^{-1}, respectively. The relative peak areas and centers differ slightly for the spectrum shown in Figure 3.13a compared to that shown in Figure 3.8b due to differences in pre-treatment conditions between the two spectra.

Strikingly, CO DRIFT spectra of materials with increasing WO_x loadings following H_2 reduction exhibit a loss of intensity of the feature associated with CO adsorption on WC Pt sites, while the feature associated with CO adsorption on UC Pt sites exhibits comparatively less change. This is consistent with the preferential decoration of WC Pt sites by WO_x following H_2 reduction. Spectral deconvolution was performed using 4 Gaussian peaks, with 2 peaks being used for both the CO adsorption on WC and UC Pt sites to capture inherent peak asymmetry[91] and heterogeneity introduced by partial WO_x decoration on the Pt surface (Figure 3.13b). Deconvolution results for all materials and parameters can be found in Figure 3.14. As introduced briefly above, the molar extinction coefficient of CO bound to UC Pt sites has been reported to be 2.7 greater than the molar extinction coefficient of CO bound to WC Pt sites[92,106]. The relative molar extinction coefficient was used to determine the fraction of adsorbed CO residing on WC and UC Pt for each $WO_x/Pt/SiO_2$ catalyst following H_2 reduction. Figure 3.13c shows that there is a monotonic, linear loss in the fraction of WC sites relative to UC sites as a function of W loading, demonstrating the preferential decoration of WC sites on the Pt surface by WO_x after H_2 reduction.

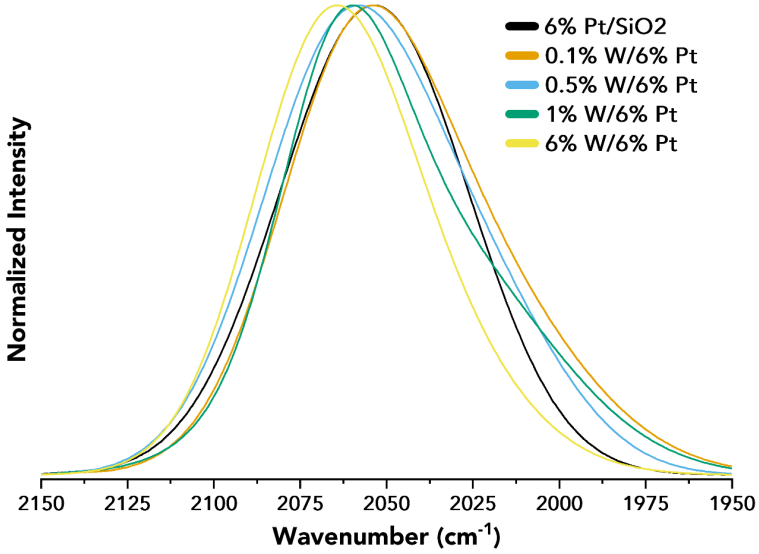

Figure 3.15: CO DRIFTS spectra for $WO_x/Pt/SiO_2$ catalysts showing blue-shift towards higher wavenumbers in the UC band center corresponding to increasing WO_x-Pt interactions with increasing decoration.

In addition to changes in the relative peak areas associated with the WC and UC Pt sites with increasing WO_x loading, there are also changes to peak centers in the CO DRIFTS spectra. The peak associated with CO bound linearly to WC Pt sites red-shifts to lower wavenumbers, whereas CO bound linearly to UC Pt sites blue-shifts to higher wavenumbers. The red-shifting of the WC feature is assigned to decreased dipole-dipole coupling on Pt terraces due to the presence of WO_x on these sites, consistent with WO_x localizing on WC Pt terraces. Dipole-dipole coupling for CO on extended metallic surfaces occurs when low energy modes transfer energy to higher energy states, resulting in the observed blue shift to CO vibrational frequency with increasing CO coverage on extended surfaces. When this coupling is disrupted, as we propose is the case in WO_x decoration, the CO stretch redshifts. Analogous shifts have been observed for both alloyed materials (CuPt) and isotopic exchange experiments between ^{12}CO and ^{13}CO, which don't vibrationally couple, highlighting that decreased effective CO coverage on WC sites caused by WO_x addition results in a red shift in the CO stretching frequency[107].

On the other hand, the blue shift of the feature associated with CO adsorption on Pt UC sites (Figure 3.15) cannot be ascribed to decreased CO coverage. In general, CO bound to UC sites exhibits less significant dipole-dipole coupling than on extended surfaces due to the spatial separation of adsorbates on stepped surfaces, reducing their ability to electronically couple[108]. Instead, the blue shift of the UC feature is attributed to electronic modification of UC Pt sites by proximal WO_x units. A Pt/WO_3 catalyst synthesized for comparison demonstrates that Pt sites near WO_x are blue-shifted compared to their Pt/SiO_2 analogs due to this electronic (charge transfer) effect (Figure 3.16).

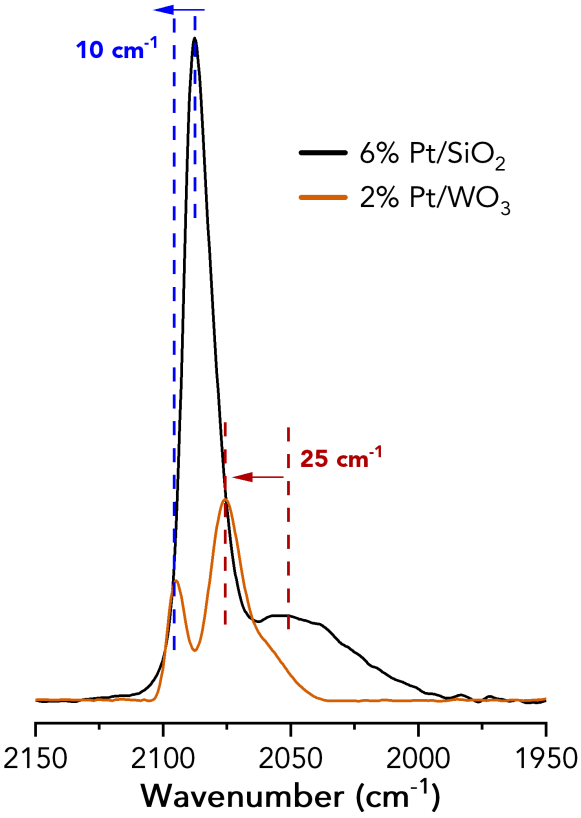

Figure 3.16: Comparison of CO DRIFTS spectra of neat Pt/SiO_2 and Pt/WO_3 catalysts. Pt/WO_3 clearly shows a strong blue shift to the CO feature corresponding to adsorption atop WC and UC sies peak centers.

The suspected electronic interaction of WO_x with UC Pt sites can be further understood by modeling CO adsorption for the most stable $W_3O_7/Pt(553)$ model and a pure Pt(553)

surface, as shown in Figure 3.15a. The SurfGraph algorithm was used to populate all unique configurations of CO in the presence and absence of W_3O_7, and UC Pt sites were predicted to be the most thermodynamically favorable CO adsorption sites for both surfaces, regardless of the presence of W_3O_7. In the case of the W_3O_7-modified Pt(553) surface, CO was most stable on the UC Pt sites between the W_3O_7 unit, essentially inside the so-called "garland" structure (Figure 3.15a, bottom image). CO binding on the UC Pt site involved in Pt-O-W bonding resulted in the breaking of the Pt-O-W bond and was less energetically favorable. As mentioned previously, the preferred garland-like structures enable UC Pt sites to continue to be accessible to adsorbates and may explain the ability of Pt-WO_x catalyst to adsorb CO on UC Pt sites at WO_x loadings greater than a monolayer equivalent, as seen for 30% W/6% Pt/SiO_2. Given that the formation energy of the most stable trimer W_3O_7 structure is energetically favorable, we believe that the key features stabilizing WO_x will be similar at high W coverage as well.

DFT calculations predict the most exothermic binding energy of CO* in the presence of W_3O_7 to be 0.2 eV weaker than on pure Pt, alluding to electronic modification of the Pt site due to the presence of WO_x. This electronic interaction also results in CO stretching frequencies of between 2041-2045 cm^{-1}, depending on CO coverage (Figures 3.17a), on the most stable adsorption site for WO_x/Pt(553), compared to 2030 cm^{-1} for the same site on bare Pt(553); thus, a blue shift in the CO frequency of ~15 cm^{-1} due to W_3O_7 addition was observed. Figure 3.17b shows the analysis of the deconvoluted CO DRIFTS spectra from Figure 3.13b, which evidence a blueshift of the UC feature of ~11 cm^{-1}, consistent with the shift calculated via DFT. The discrepancy in absolute peak positions for CO bound to the UC Pt site in experiment (~2060 cm^{-1}) and DFT (2045 cm^{-1}) is a common feature of DFT vibrational

calculations and stems from, among others, differences in adsorbate coverages and functional choice[81].

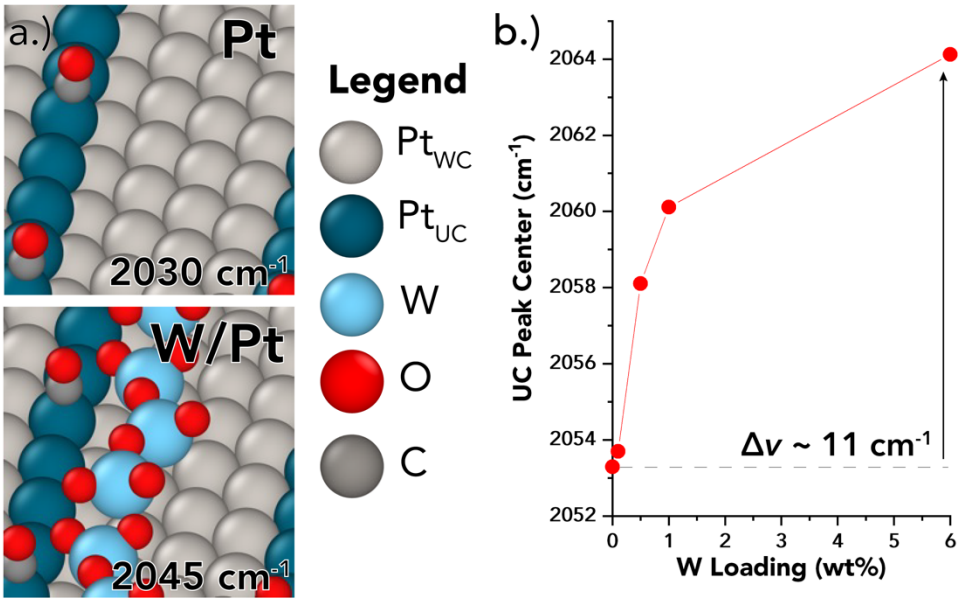

Figure 3.17: a.) DFT-predicted vibrational frequency shift of a single CO molecule bound to a Pt step on Pt and WO_x/Pt model surfaces. b.) Peak shift of the UC feature with increasing W loading in the CO DRIFTS spectrum determined from deconvolution. Strong agreement in the magnitude of the peak shift with experiments with increasing W loading indicates that experimental shifts are due to increasing WO_x interaction with UC Pt sites.

Collectively, the characterization of heterogeneous inverse WO_x/Pt/SiO_2 catalysts demonstrates that WO_x reduces and mobilizes under H_2 atmospheres to preferentially decorate WC sites on the surface of Pt nanoparticles. This is consistent with the DFT calculations, which concluded that WO_x growth on Pt terraces is energetically favored over WO_x growth across Pt steps. Further, the theoretical models identified the formation of Pt-O-W bonds at the Pt step as particularly stabilizing of the WO_x overlayer, which is consistent with observations made from UHV studies of oxide decoration on model metal surfaces[50–53].

3.2.4 HDO Reactions

The evidenced preferential growth of WO_x on WC Pt sites should result in modified catalytic performance, specifically for reactions that exhibit structure sensitivity. As mentioned in the introduction, we recently used unmodified Pt/SiO_2 catalysts of varying Pt nanoparticle size distributions to demonstrate that WC Pt sites are responsible for aromatic ring hydrogenation during HDO of phenolics such as dihydroeugenol (DHE)[47]. The results discussed above evidence that WO_x preferentially decorates these same WC Pt sites under reducing conditions similar to those experienced in HDO reactions (H_2 atmosphere, elevated temperatures). Thus, the ability of WO_x/Pt catalysts and other inverse catalyst compositions to suppress undesired hydrogenation during HDO reactions could be related to sub-monolayer WO_x overlayers blocking WC sites that are particularly active for aromatic ring hydrogenation.

To test this hypothesis, the HDO of DHE was performed using the series of $WO_x/Pt/SiO_2$ catalysts with varying W loading. Reactions were performed in a batch reactor under magnetic stirring in the absence of mass transport limitations. Reaction performance was normalized by loading a constant mass of Pt into the reactor for each catalyst. The products formed under reaction conditions include those related to ring hydrogenation, such as 2-methoxy-4-propylcyclohexanol (HYD), and deoxygenation, such as 4-propylphenol (PHE) and 4-propylbenzene (BNZ), as well as the combination of the two reactions, such as 4-propylcyclohexanol (OL), 4-propylcyclohexanone (ONE), 4-propylcyclohex-1-ene (CYE), and 4-propylcyclohexane (CYC)[19]. HDO products were grouped into two classes, hydrogenated products (HYD, OL, ONE, CYE, CYC) and fully deoxygenated products (CYC, CYE, BNZ).

Products and remaining substrate contributed to a mass balance after reaction of ~80%. The remaining mass is ascribed to the formation of small quantities of gas phase species, bound organics on the catalyst surface, and oligomerized products in solution[109–112]. However, control experiments indicate that oligomers and bound oxygenates are produced from DHE and not HDO products – thus, the mass balance closure does not influence the measured product yields. Moreover, oligomer formation is known to occur over acid sites, such as WO_x domains, which is evidenced here by the progressive coloration of the samples with increasing WO_x loading (Figure 3.18). This includes WO_x domains not on Pt nanoparticles, indicating that the sites not active for HDO (i.e. WO_x/SiO_2) may be the sites most responsible for oligomer formation and organics adsorption.

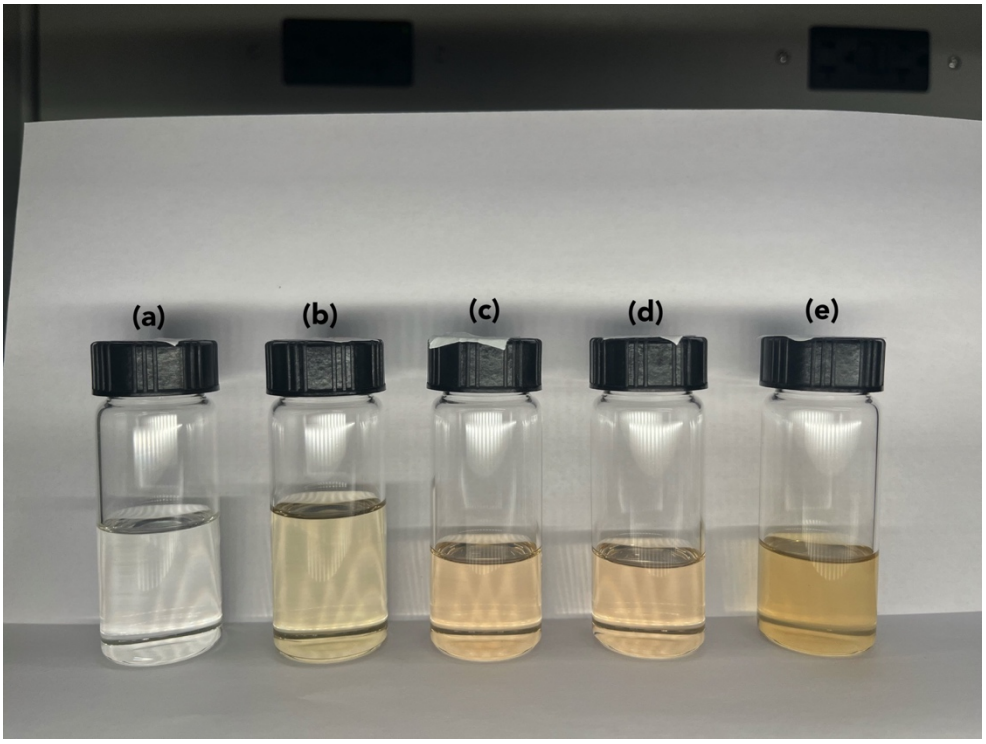

Figure 3.18: Final reaction mixtures obtained after HDO of DHE over $WO_x/Pt/SiO_2$ catalyst series. Increasing color from left to right indicates oligomer and other high-MW species unable to be detected by GC-FID, corresponding to the loss of mass balance. (a) 6Pt, (b) 0.1W6Pt, (c) 0.5W6Pt, (d) 1W6Pt, (e) 6W6Pt.

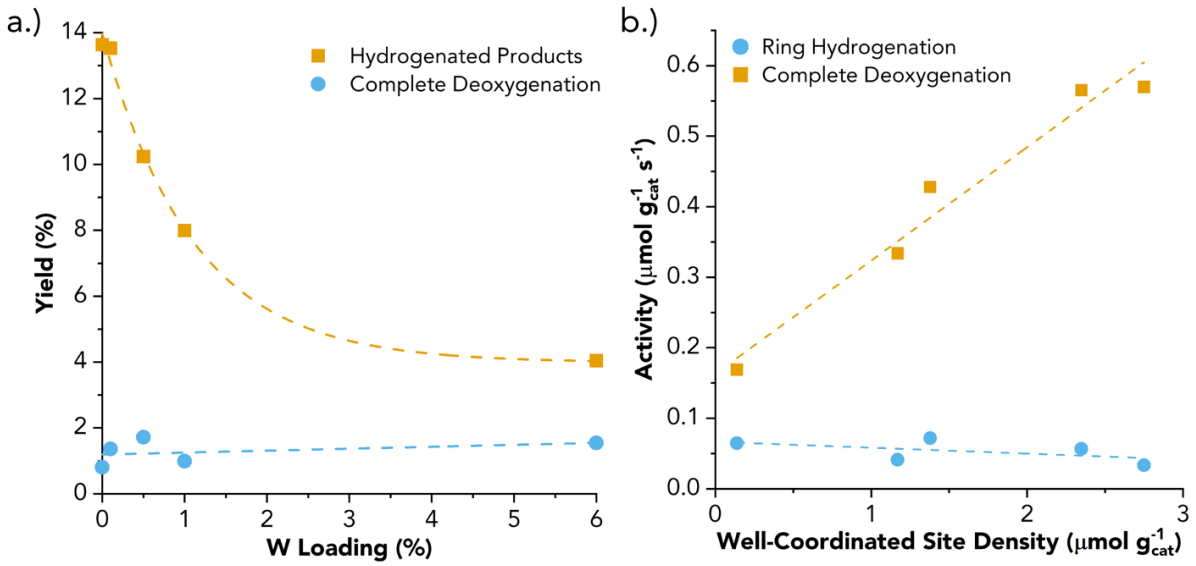

Figure 3.19: a.) Analysis of product yields in the HDO reaction of DHE over WO_x-modified Pt/SiO_2 catalysts. b.) Comparison of estimated hydrogenation and complete deoxygenation rates to well-coordinated site density highlights the effect of reduced well-coordinated site density on suppressed hydrogenation.

The results of reactions at 275˚C for 2 hours are shown in Figure 3.19. The yield of hydrogenated products decreases with increasing W loading. This is consistent with the blockage of well-coordinated sites by WO_x, as our prior work has demonstrated that well-coordinated sites are responsible for aromatic ring hydrogenation in unmodified Pt/SiO_2 catalysts under similar conditions[47]. However, there is no measurable change in the yield of fully deoxygenated products over this range of W loadings, including the case of 0% W, corresponding to the unmodified Pt/SiO_2 catalyst. It has been suggested that the role of reducible oxides modifiers, such as WO_x in HDO by Pt reactions may be to introduce oxygen vacancies that can facilitate a reverse Mars-van Krevelen-type reaction mechanism[44,113]. Others have pointed to the formation of oxide-metal interfaces as an essential component of the active site structure[88–90]. However, the minimal change in deoxygenation activity observed here as a function of W loading suggests that WO_x is not a strong promoter of deoxygenation activity under the conditions studied; in other words, it appears from our results that the active

site responsible for DHE HDO is not significantly promoted by the presence of WO_x. Instead, the trend in DHE HDO selectivity observed is suggestive of UC Pt sites, which are presumed to be accessible under reaction conditions stemming from the results of CO DRIFTS characterization, being the active site for deoxygenation. However, the influence of WO_x addition to Pt on catalyst stability and the exact identity of the active site for deoxygenation during HDO requires further analysis.

The impact of the preferential decoration of WC Pt sites by reduced WO_x species is further highlighted by correlating the measured rates of ring hydrogenation and complete deoxygenation against the concentration of WC sites on the catalyst surface, as shown in Figure 7b. Here, the concentration of WC sites is estimated based on the fraction of exposed Pt sites existing as WC Pt, as measured by CO DRIFTS, multiplied by the total quantity of exposed Pt sites, measured by CO chemisorption, both measured after *in situ* reduction at 325 ˚C in 10% H_2/Ar. It can be seen from the data spacing in Figure 3.19b that increasing W loading results in a consistent loss of Pt_{WC} site density. Moreover, there is no apparent relationship between the deoxygenation rate and this Pt_{WC} site density, suggesting that deoxygenation occurs on other sites on the catalyst surface, such as UC Pt sites or interfacial sites between Pt and WO_x. As discussed above, though, it is unlikely that deoxygenation occurs over sites only consisting of WO_x, as the Pt/SiO_2 catalyst exhibits deoxygenation activity comparable to WO_x-modified catalysts. On the other hand, a monotonic, linear relationship exists between the number of WC Pt sites exposed on Pt and WO_x-coated Pt surfaces and the rate of aromatic ring hydrogenation. Since Pt particle size is constant across all catalysts, this indicates that the preferential decoration of WC Pt sites by WO_x is the primary mechanism behind suppressed

aromatic hydrogenation during HDO of oxygenates common to lignin monomers for inverse WO_x/Pt catalysts.

3.3 Conclusions

The structural organization of WO_x on Pt in inverse WO_x/Pt/SiO_2 catalysts exhibiting sub-monolayer WOx overlayer coverage was investigated by theoretical and experimental approaches. DFT calculations were performed to understand the structural organization of WO_x on stepped Pt surfaces. Preferential decoration of WO_x oligomers on Pt_{WC} sites was observed with partial occupation of Pt_{UC} sites. A data-driven machine-learning algorithm identified the dominant features stabilizing WO_x as bonding between an O in WO_x and Pt_{UC} sites, the presence of W on Pt_{WC} sites adjacent to Pt_{UC} sites, and the growth of WO_x mainly on Pt_{WC} regions (terraces). An experimental system was developed using a Pt/SiO_2 catalyst modified by varying amounts of WO_x. *In situ* spectroscopic characterization and *ex-situ* electron microscopy uncovered the dynamic reversibility of WOx decoration of Pt surfaces, analogous to traditional SMSI catalysts, except here due to WO_x mobility to and from SiO_2. CO DRIFTS evidenced the preferential overcoating of Pt_{WC} sites with increasing WO_x loading, consistent with theoretical results. Reactivity studies in the HDO of DHE indicated that increasing WO_x loading primarily suppressed ring hydrogenation activity, with relatively little change in the yield of deoxygenated products. Considering that aromatic ring hydrogenation has been shown to occur over Pt_{WC} sites[114], our findings support that the preferential decoration of Pt_{WC} sites by WO_x identified in CO DRIFTS also occurs under reaction conditions. This work provides evidence that inverse catalysts can be designed and controlled to manipulate the

number and nature of exposed metal sites, which offers a unique lever for controlling activity and selectivity in a broad range of chemistries.

3.4 Methods

3.4.1 DFT Evaluation of Unique WO_x/Pt Structures

The DFT simulations were performed within the framework of periodic density functional theory with the Vienna Ab Initio Simulation Package (VASP)[115]. The energies and geometries of the identified configurations of WO_x on the Pt(553) surface were obtained through minimization of the total energy with respect to geometry by generalized gradient approximation calculations (GGA-PBE)[116]. The projected augmented wave (PAW) method was used to account for the effect of core electrons on the valence electron density[117]. A PBE-calculated lattice constant of 3.98 Å for Pt bulk was employed. The Pt(553) surface was represented by a 5×4 unit cell with four layers (56 total atoms per unit cell). The Pt(221) and kink-Pt(221) surfaces were represented by a 4×3 unit cell with four layers (33 and 34 total atoms, respectively). The top two layers were relaxed for all the cases and a vacuum equivalent to at least 13 Å was applied between any two successive slabs. A planewave energy cutoff of 400 eV was used for all the calculations. A minimum k-point grid sampling of 3x3x1 was employed. The electronic occupancies were determined according to a Methfessel−Paxton scheme with an energy smearing of 0.2 eV. The cutoff for the convergence of the electronic loop (EDIFF) was set to 10-4 eV. Structures were fully relaxed until the Hellmann− Feynman forces acting on the atoms were smaller than 0.05 eV/Å.

3.4.2 XGBoost Machine Learning

The XGBoost algorithm was used[66]. To assess its robustness, different seeds were used to split the data randomly into training and testing sets. Further, a 5-fold cross-validation was also performed to verify the results. The XGBoost model was fit using a mean squared error loss function. Default values were utilized for the other hyperparameters. The gain metric was utilized in the feature importance calculation to estimate the features contributing the most to the model fitting.

3.4.3 Catalyst Synthesis

Base 6 wt% Pt/SiO_2 catalysts were synthesized via a modified strong electrostatic adsorption methodology used previously. Briefly, 2 g of spherical, non-porous SiO_2 with an average particle size of 20-30 nm (USNano) was suspended in 100 mL of deionized water (Sigma) with magnetic stirring. The suspension was adjusted to pH 10 using an appropriate amount of NH_4OH (Sigma), monitored by an electronic pH meter. After reaching pH 10 and left stirring for 10 minutes, 10 mL of a solution of tetraamine platinum nitrate (TAPN, Sigma) was added dropwise under vigorous stirring. The resulting suspension was left to stir for 30 minutes before increasing the temperature to 70˚C until all the water was evaporated from the dish. The collected solids were further dried at 120˚C overnight prior to calcination in a tube furnace at 600˚C for 6 hours in 50 sccm dry air (Airgas).

WO_x-modified samples were prepared similarly using a wet impregnation of ammonium metatungstate (AMT, Sigma). Previously prepared 6 wt% Pt/SiO_2 was added to a dish with 20 mL of deionized water (Sigma) with magnetic stirring. To this, an appropriate amount of AMT was added to achieve the desired weight loading, in the range of 0.1 to 6 wt%

by W. After stirring for 30 minutes, the solution was heated to 70˚C to evaporate the water. The remaining solids were collected and dried overnight at 120˚C prior to calcination in a tube furnace at 350˚C for 3 hours.

3.4.4 Catalyst Characterization

High-annular angle dark field scanning transmission electron microscopy (HAADF-STEM) was performed on an aberration-corrected ThermoFisher Spectra 200 microscope. Typically, samples were prepared by drop casting onto a lacey carbon-coated Cu grid (400 mesh, Ted Pella). Briefly, samples were dispersed in methanol (Sigma) by physical mixing followed by sonication. 5 μL of the suspension was then dropped onto the carbon side of the grids via pipette and allowed to dry under flowing air before being placed in a vacuum oven at 100˚C using house vacuum for at least 24 hours to mitigate solvent-related contamination under the electron beam. Images were collected at 200 kV. Beam current was adjusted as needed to minimize sample charging and damage, particularly in the imaging of WO_x domains which exhibited mobility on the SiO_2 support under beam illumination. Energy dispersive x-ray spectroscopy (EDS) was utilized to identify the atomic identity of Pt and W in WO_x/Pt samples due to the two elements' similar contrast in the HAADF-STEM mode.

CO DRIFTS measurements were carried out on a Nicolet iS10 FT-IR spectrometer equipped with a Praying Mantis Diffuse Reflection Accessory (Harrick Scientific) and a High-Temperature Reaction Chamber (Harrick Scientific) fitted with a thermocouple in the catalyst bed. Ar (99.995%), He (99.995%), O_2 (99.50%), 10% CO/Ar, and 10% H_2/Ar were purchased from Airgas and used as received. In a typical DRIFTS experiment, catalyst was loaded into the Harrick cell and pre-treated under a desired gas environment and temperature. Temperature

set points were reached by ramping the catalyst at 10˚C/min in all experiments, except for cooling after pre-treatment steps which was allowed to happen passively. Gas flow rates across the catalyst bed in all cases were 50 sccm controlled by mass flow controllers (Teledyne Hastings). For CO DRIFTS experiments, catalysts were cooled to 30˚C prior to exposure to 10% CO/Ar. CO exposure was continued until saturation coverage of CO on the metal sites was achieved, determined by unchanging peak intensity in DRIFTS spectra. After metal surfaces were saturated by CO, the gas flow was switched to Ar to remove CO from the gas atmosphere. In sequential experiments, additional pre-treatments were conducted in the same manner. After each pre-treatment in the sequence, CO was re-adsorbed and purged at 30˚C in the same manner. UV-Vis spectra were recorded by following an identical *in situ* procedure to those performed during CO DRIFTS experiments, this time using a Thermo Scientific Evolution 300 spectrophotometer.

Pt site density measurements were made by performing CO pulse chemisorption using an Autochem 2920 II (Micromeritics). In a typical experiment, 50 mg of catalyst was loaded between two quartz wool plugs in a quartz cell. The catalyst was pre-treated at the desired temperature and gas atmosphere before cooling to 30˚C. Pulsed measurements were made by exposing the catalyst to 10 pulses of 50 sccm 10% CO/Ar separated by 3.5 minutes of Ar flow at 50 sccm. CO uptake was measured by integrating the difference of each peak area relative to the final peak, assuming a CO:Pt ratio of 1. H_2-temperature programmed reduction (H_2-TPR) was also performed using the same instrument. Catalyst loading procedures were the same, and catalysts were typically pre-treated at 400˚C for 1 hour in O_2 before being cooled to 50˚C to start the TPR.

3.4.5 HDO Reactions

HDO reactions using the prepared catalysts were performed in 75-mL stainless-steel pressure reactors (Parr Instrument Co., 5000 Series). In a typical reaction, catalyst was loaded into the reactor along with 500 mg of dihydroeugenol (DHE, Sigma) and 20 mL of cyclohexane (Sigma). Catalyst loading was determined such that a constant mass (6 mg) of Pt was loaded for each reaction. Reactions were stirred magnetically at 700 rpm using glass-shielded stir bars. Once loaded, the reactor was sealed and purged 3 times with 5.0 grade H_2 (Airgas) before pressurizing to a final gauge pressure of 20 bar at room temperature. Then, the vessel was heated to 275 ˚C and held for 2 hours. After the allotted reaction time, the reactor vessel was quickly removed and quenched using a water bath. Once cooled to room temperature, the liquid products were collected by centrifugation and analyzed by a gas chromatogram equipped with a flame ionization detector (GC-FID, Agilent) using *n*-decane (Sigma) as an internal standard. Product identification was carried out using commercially-sourced standards where possible (DHE, 4-propylbenzene (BNZ), 4-propylphenol (PHE), 4-propylcyclohexanol (OL), 4-propylcyclohexane (CYC)). In instances where standards are not commercially available, FID responses were estimated using effective carbon number (ECN)[118]. Reaction performance metrics were defined as:

$$Conversion\ (\%) = \frac{N_{DHE}}{N_{DHE}^{0}}$$

$$Selectivity\ (\%) = \frac{N_{Product}}{\sum N_{Product}}$$

$$Yield\ (\%) = Conversion * Selectivity = \frac{N_{Product}}{\sum N_{Product}} * \frac{N_{DHE}}{N_{DHE}^{0}}$$

where N_i is the moles of species *i* measured by GC-FID and N_i^0 is the initial moles of *i* loaded into the batch reactor.

3.5 References

1. Dobereiner, J. W. Ueber neu Entdeckte Höchst Merkwürdige Ei- genschaften des Platins und die Pneumatisch-Capillare Thä- tigkeit Gesprungener Gläser. *Ein Beitrag zur Corpuscular Philosophie* (1823).
2. Robertson, A. J. B. The Early History of Catalysis. *Platin Met Rev* **19**, 64–69 (1975).
3. Davy, E. On some Combinations of Platinum. *Phil. Trans.* 108 (1820).
4. Henry, W. XVI. On the action of finely divided Platinum on Gaseous Mixtures, and its Application to their Analysis. *Phil. Trans.* 266–289 (1824).
5. Moulijn, J. A., van Leeuwen, P. W. N. M. & van Santen, R. A. Chapter 1: History of Catalysis. in *Catalysis: An Integrated Approach to Homogeneous, Heterogeneous and Industrial Catalysis* 3–465 (1993).
6. Hofer, L. J. E. & Peebles, W. C. X-Ray Diffraction Studies of the Action of Carbon Monoxide on Cobalt-Thoria-Kieselguhr Catalysts. I. *J Am Chem Soc* **45**, 1 (1942).
7. Chakravarthy, K. M. & Sen, R. X-Ray Diffraction Studies of a Nickel-Thoria-Kieselguhr Catalyst For Fischer-Tropsch Synthesis. *Nature* 907–908 (1947).
8. Hettinger, W. P. *Contribution to Catalytic Cracking in the Petroleum Industry*. *Applied Clay Science* vol. 5 (1991).
9. Fletcher, R. P. The History of Fluidized Catalytic Cracking: A History of Innovation: 1942-2008. in *Innovations in Industrial and Engineering Chemistry* 189–249 (2009).
10. Ponder, E., Saslow, G., Warburg, E., Winge, K. & Woodard, H. Q. CATALYSIS BY METALLIZED BENTONITES. *Acta Med. Scand* **70**, 19 (1930).
11. Degnan, T. F. *Applications of Zeolites in Petroleum Refining*. *Topics in Catalysis* vol. 13 (2000).
12. Zimmermann, N. E. R. & Haranczyk, M. History and Utility of Zeolite Framework-Type Discovery from a Data-Science Perspective. *Crystal Growth and Design* vol. 16 3043–3048 Preprint at https://doi.org/10.1021/acs.cgd.6b00272 (2016).
13. Bhattacharyya, S. K. & Gulati, I. B. Catalytic Vapor-Phase Oxidation of Xylenes. *Ind Eng Chem* **50**, 1719–1726 (1958).
14. Mars, P. & Van Krevelen, D. W. Oxidations carried out by means of vanadium oxide catalysts. *Chem Eng Sci* **3**, 41–59 (1954).
15. Kummer Ford, J. T. CATALYSTS FOR AUTOMOBILE EMISSION CONTROL. *Prog. Energy Combust. Sci.* **99**, 177–199 (1980).
16. Su, E. C., Montreuil, C. N. & Rothschild, W. G. OXYGEN STORAGE CAPACITY OF MONOLITH THREE-WAY CATALYSTS. *Appl Catal* **17**, 75–86 (1985).
17. Van Vu, D., Miyamoto, M., Nishiyama, N., Egashira, Y. & Ueyama, K. Selective formation of para-xylene over H-ZSM-5 coated with polycrystalline silicalite crystals. *J Catal* **243**, 389–394 (2006).

18. Baertsch, C. D., Funke, H. H., Falconer, J. L. & Noble, R. D. Permeation of Aromatic Hydrocarbon Vapors through Silicalite-Zeolite Membranes. *Journal of Physical Chemistry* **100**, (1996).
19. Gobin, O. C., Reitmeier, S. J., Jentys, A. & Lercher, J. A. Diffusion pathways of benzene, toluene and p-xylene in MFI. *Microporous and Mesoporous Materials* **125**, 3–10 (2009).
20. Markus Eiswirth, R., Krischer, K. & Ertl, G. *Nonlinear Dynamics in the CO-Oxidation on Pt Single Crystal Surfaces*. *Appl. Phys. A* vol. 51 (1990).
21. Sandoval-Diaz, L. *et al.* Metastable nickel–oxygen species modulate rate oscillations during dry reforming of methane. *Nat Catal* **7**, 161–171 (2024).
22. Finzel, J. & Christopher, P. Dynamic Pt Coordination in Dilute AgPt Alloy Nanoparticle Catalysts Under Reactive Environments. *Top Catal* **65**, 1587–1603 (2022).
23. Tauster, S. J., Fung, S. C. & Garten, R. L. Strong Metal-Support Interactions. Group 8 Noble Metals Supported on TiO2. *J Am Chem Soc* **100**, 170–175 (1978).
24. Baker, R. T. K., Prestridge, E. B. & Garten, A. R. L. Electron Microscopy of Supported Metal Particles II. Further Studies of Pt/Ti02. *J Catal* **59**, 293–302 (1979).
25. Fung, S. C. XPS Studies of Strong Metal-Support Interactions (SMSI) - Pt/TiO2. *J Catal* **76**, 225–230 (1982).
26. Huizinga, T., Van, H., Blik, T., Vis, J. & Prins, R. XPS INVESTIGATIONS OF Pt AND Rh SUPPORTED ON g-Al2O3 and TiO2. *Surf Sci* **135**, 580–596 (1983).
27. Bracey, J. D. & Burch', R. Enhanced Activity of Pd/Ti02 Catalysts for the CO/H2 Reaction in the Absence of Strong Metal-Support Interactions (SMSI). *J Catal* **86**, 384–391 (1984).
28. Miessner, H., Orita, H., Naito, S. & Tamaru, K. CO HYDROGENATION ON A HIGHLY LOADED Rh/TiO 2 CATALYST AND THE INFLUENCE OF STRONG METAL-SUPPORT INTERACTION. *React. Kinet. Catal. Lett* **28**, 295–300 (1985).
29. Matsubu, J. C. *et al.* Adsorbate-mediated strong metal-support interactions in oxide-supported Rh catalysts. *Nat Chem* **9**, 120–127 (2017).
30. Vogt, C. *et al.* Unravelling structure sensitivity in CO2 hydrogenation over nickel. *Nat Catal* **1**, 127–134 (2018).
31. Monai, M. *et al.* Restructuring of titanium oxide overlayers over nickel nanoparticles during catalysis. *Science (1979)* **380**, 644–651 (2023).
32. Zhang, S. *et al.* Dynamical observation and detailed description of catalysts under strong metal-support interaction. *Nano Lett* **16**, 4528–4534 (2016).
33. Wu, Z., Li, Y. & Huang, W. Size-Dependent Pt-TiO2Strong Metal-Support Interaction. *Journal of Physical Chemistry Letters* **11**, 4603–4607 (2020).
34. Du, X. *et al.* Size-dependent strong metal-support interaction in TiO2 supported Au nanocatalysts. *Nat Commun* **11**, (2020).
35. Breckner, C. J. *et al.* Controlled site coverage of strong metal-support interaction (SMSI) on Pd NP catalysts. *Catal Sci Technol* **13**, 157–169 (2022).
36. Seo, H. O. *et al.* Carbon dioxide reforming of methane to synthesis gas over a TiO2-Ni inverse catalyst. *Appl Catal A Gen* **451**, 43–49 (2013).
37. Li, Y., Zhang, Y., Qian, K. & Huang, W. Metal-Support Interactions in Metal/Oxide Catalysts and Oxide-Metal Interactions in Oxide/Metal Inverse Catalysts. *ACS Catal* **12**, 1268–1287 (2022).

38. Yang, F. *et al.* CO oxidation on inverse CeOx/Cu(111) Catalysts: High catalytic activity and ceria-promoted dissociation of O2. *J Am Chem Soc* **133**, 3444–3451 (2011).
39. Zhao, G. *et al.* Metal/oxide interfacial effects on the selective oxidation of primary alcohols. *Nat Commun* **8**, 1–8 (2017).
40. Fu, J. *et al.* Modulating the dynamics of Brønsted acid sites on PtWOx inverse catalyst. *Nat Catal* **5**, 144–153 (2022).
41. Polo-Garzon, F. *et al.* In situ strong metal-support interaction (SMSI) affects catalytic alcohol conversion. *ACS Catal* **11**, 1938–1945 (2021).
42. Lin, Z. *et al.* Experimental and Theoretical Insights into the Active Sites on WO x/Pt(111) Surfaces for Dehydrogenation and Dehydration Reactions. *ACS Catal* **11**, 8023–8032 (2021).
43. Lin, Z. *et al.* Mechanistic Understanding of Ring-Opening of Tetrahydrofurfuryl Alcohol over WOx-Modified Pt Model Surfaces and Powder Catalysts. *ACS Catal* **13**, 8014–8024 (2023).
44. Wang, C. *et al.* Mechanistic Study of the Direct Hydrodeoxygenation of m -Cresol over WOx-Decorated Pt/C Catalysts. *ACS Catal* **8**, 7749–7759 (2018).
45. Wang, C. *et al.* Hydrodeoxygenation of m-Cresol Over Pt-WOx/C Using H2 Generated In Situ by n-Hexane Dehydrogenation. *Catal Letters* **150**, 913–921 (2020).
46. Huang, R., Kwon, O., Lin, C. & Gorte, R. J. The effects of SMSI on m-Cresol hydrodeoxygenation over Pt/Nb2O5 and Pt/TiO2. *J Catal* **398**, 102–108 (2021).
47. Marlowe, J., Ford, P. C., Abu-Omar, M. M. & Christopher, P. Structure sensitivity in Pt-catalyzed hydrodeoxygenation of multi-oxygenated lignol model compounds. *Catal Sci Technol* **13**, 5662–5678 (2023).
48. Lavroff, R. H., Wang, J., White, M. G., Sautet, P. & Alexandrova, A. N. Mechanism of Stoichiometrically Governed Titanium Oxide Brownian Tree Formation on Stepped Au(111). *Journal of Physical Chemistry C* **127**, 8030–8040 (2023).
49. Wang, J. *et al.* Surface structure of mass-selected niobium oxide nanoclusters on Au(111). *Nanotechnology* **32**, 1–12 (2021).
50. Li, F., Allegretti, F., Surnev, S. & Netzer, F. P. Atomic engineering of oxide nanostructure superlattices. *Surf Sci* **604**, L43–L47 (2010).
51. Kurzina, I. & Atrei, A. STEP REARRANGEMENT UPON LOW PRESSURE OXIDATION OF THE Pt3Ti(510) SURFACE: A STUDY BY SCANNING TUNNELING MICROSCOPY. *Surface Review and Letters* **10**, 861–866 (2003).
52. Lu, J. *et al.* First-principles predictions and in situ experimental validation of alumina atomic layer deposition on metal surfaces. *Chemistry of Materials* **26**, 6752–6761 (2014).
53. Yao, Y., Fu, Q., Wang, Z., Tan, D. & Bao, X. Growth and characterization of two-dimensional FeO nanoislands supported on Pt(111). *Journal of Physical Chemistry C* **114**, 17069–17079 (2010).
54. Surnev, S. *et al.* Growth and structure of ultrathin vanadium oxide layers on Pd"111…. *Phys Rev B* **61**, 13945–13954 (2000).
55. Kale, M. J. & Christopher, P. Utilizing Quantitative in Situ FTIR Spectroscopy to Identify Well-Coordinated Pt Atoms as the Active Site for CO Oxidation on Al2O3-Supported Pt Catalysts. *ACS Catal* **6**, 5599–5609 (2016).
56. Zhou, J. *et al.* The role of the metal core in the performance of WOx inverse catalysts. *Chem Catalysis* **3**, 1–17 (2023).

57. Wu, Y. *et al.* Dynamic Formation of Brønsted Acid Sites over Supported WOx/Pt on SiO2 Inverse Catalysts─Spectroscopy, Probe Chemistry, and Calculations. *ACS Catal* **13**, 7371–7382 (2023).
58. Sumaria, V. & Sautet, P. CO organization at ambient pressure on stepped Pt surfaces: First principles modeling accelerated by neural networks. *Chem Sci* **12**, 15543–15555 (2021).
59. Deshpande, S., Maxson, T. & Greeley, J. Graph theory approach to determine configurations of multidentate and high coverage adsorbates for heterogeneous catalysis. *NPJ Comput Mater* **6**, 1–6 (2020).
60. Ghanekar, P. G., Deshpande, S. & Greeley, J. Adsorbate chemical environment-based machine learning framework for heterogeneous catalysis. *Nat Commun* **13**, 1–12 (2022).
61. Deshpande, S. & Vlachos, D. G. A Data and DFT-Driven Framework for Predicting the Microstructure of Submonolayer Inverse Metal Oxide on Metal Catalysts. *J Phys Chem Lett* **15**, 2715–2722 (2024).
62. Wang, J. G. *et al.* One-dimensional PtO2 at Pt steps: Formation and reaction with CO. *Phys Rev Lett* **95**, 1–4 (2005).
63. Feibelman, P. J., Esch, S. & Michely, T. O Binding Sites on Stepped Pt(111) Surfaces. *Phys Rev Lett* **77**, 2257–2260 (1996).
64. Schoiswohl, J. *et al.* Metal supported oxide nanostructures: Model systems for advanced catalysis. *Top Catal* **46**, 137–149 (2007).
65. Kumar, R. & Singh, A. K. Chemical hardness-driven interpretable machine learning approach for rapid search of photocatalysts. *NPJ Comput Mater* **7**, 1–13 (2021).
66. Chen, T. & Guestrin, C. XGBoost: A scalable tree boosting system. in *Proceedings of the ACM SIGKDD International Conference on Knowledge Discovery and Data Mining* vols 13-17-August-2016 785–794 (Association for Computing Machinery, 2016).
67. Lei, Y. *et al.* Adsorbate-induced structural changes in 1-3 nm platinum nanoparticles. *J Am Chem Soc* **136**, 9320–9326 (2014).
68. Koningsberger, D. C. & Sayers, D. E. AN EXAFS STUDY OF PLATINUM-OXYGEN BONDS IN THE METAL-SUPPORT INTERFACE OF A HIGHLY Pt/A1203 CATALYST. DISPERSED. *Solid State Ion* **16**, 23–27 (1985).
69. Ramana, C. V., Utsunomiya, S., Ewing, R. C., Julien, C. M. & Becker, U. Structural stability and phase transitions in WO3 thin films. *Journal of Physical Chemistry B* **110**, 10430–10435 (2006).
70. Diehl, R., Brandt, G. & Salje, E. The Crystal Structure of Triclinic WO3. *Acta Crystallography* **34**, 1105–1111 (1978).
71. Huang, X., Zhai, H. J., Li, J. & Wang, L. S. On the structure and chemical bonding of tri-tungsten oxide clusters W3On- and W3On (n = 7-10): W3O8 as a potential molecular model for O-deficient defect sites in tungsten oxides. *Journal of Physical Chemistry A* **110**, 85–92 (2006).
72. Miller, J. T., Schreier, M., Kropf, A. J. & Regalbuto, J. R. A fundamental study of platinum tetraammine impregnation of silica: 2. The effect of method of preparation, loading, and calcination temperature on (reduced) particle size. *J Catal* **225**, 203–212 (2004).
73. Asokan, C., Xu, M., Dai, S., Pan, X. & Christopher, P. Synthesis of Atomically Dispersed Rh Catalysts on Oxide Supports via Strong Electrostatic Adsorption and Characterization by Cryogenic Infrared Spectroscopy. *The Journal of Physical Chemistry C* **126**, 18704–18715 (2022).

74. Zakem, G., Ro, I., Finzel, J. & Christopher, P. Support functionalization as an approach for modifying activation entropies of catalytic reactions on atomically dispersed metal sites. *J Catal* **404**, 883–896 (2021).
75. Nie, L. & Resasco, D. E. Kinetics and mechanism of m-cresol hydrodeoxygenation on a Pt/SiO 2 catalyst. *J Catal* **317**, 22–29 (2014).
76. Zhang, X., Tang, W., Zhang, Q., Wang, T. & Ma, L. Hydrocarbons Production from Lignin-derived Phenolic Compounds over Ni/SiO2 Catalyst. *Energy Procedia* **105**, 518–523 (2017).
77. Barton, D. G., Shtein, M., Wilson, R. D., Soled, S. L. & Iglesia, E. Structure and electronic properties of solid acids based on tungsten oxide nanostructures. *Journal of Physical Chemistry B* **103**, 630–640 (1999).
78. Ross-Medgaarden, E. I. & Wachs, I. E. Structural determination of bulk and surface tungsten oxides with UV-vis diffuse reflectance spectroscopy and raman spectroscopy. *Journal of Physical Chemistry C* **111**, 15089–15099 (2007).
79. Yang, F. *et al.* Elucidating the Structure of Bimetallic NiW/SiO2 Catalysts and Its Consequences on Selective Deoxygenation of m-Cresol to Toluene. *ACS Catal* **11**, 2935–2948 (2021).
80. Zaki, M. I., Hasan, M. A. & Pasupulety, L. Influence of CuOx additives on CO oxidation activity and related surface and bulk behaviours of Mn2O3 , Cr2O3 and WO3 catalysts. *Appl Catal A Gen* **198**, 247–259 (2000).
81. Meunier, F. C., Elgayyar, T., Dembélé, K. & Kaper, H. Stability of Pt-Adsorbed CO on Catalysts for Room Temperature-Oxidation of CO. *Catalysts* **12**, 1–12 (2022).
82. Tang, H. *et al.* Oxidative strong metal-support interactions (OMSI) of supported platinum-group metal catalysts. *Chem Sci* **9**, 6679–6684 (2018).
83. Song, T. *et al.* Oxidative strong metal-support interactions between metals and inert boron nitride. *Journal of Physical Chemistry Letters* **12**, 4187–4194 (2021).
84. Beck, A. *et al.* The dynamics of overlayer formation on catalyst nanoparticles and strong metal-support interaction. *Nat Commun* **11**, 1–8 (2020).
85. Tauster, S. J., Fung, S. C., Baker, R. T. K. & Horsley, J. A. Strong Interactions in Supported-Metal Catalysts. *Science (1979)* **211**, 1121–1125 (1981).
86. Kale, M. J., Avanesian, T., Xin, H., Yan, J. & Christopher, P. Controlling catalytic selectivity on metal nanoparticles by direct photoexcitation of adsorbate-metal bonds. *Nano Lett* **14**, 5405–5412 (2014).
87. Darmawi, S. *et al.* Correlation of electrochromic properties and oxidation states in nanocrystalline tungsten trioxide. *Physical Chemistry Chemical Physics* **17**, 15903–15911 (2015).
88. Hotchandani, S., Bedja, I., Fessenden, R. W. & Kamat, P. V. Articles Electrochromic and Photoelectrochromic Behavior of Thin WOs Films Prepared from Quantum Size Colloidal Particles. *Langmuir* **10**, 17–22 (1994).
89. Baucke, F. G. K., Duffy, J. A. & Smith, R. I. OPTICAL ABSORPTION OF TUNGSTEN BRONZE THIN FILMS FOR ELECTROCHROMIC APPLICATIONS. *Thin Solid Films* **186**, 47–51 (1990).
90. Yamazaki, S. & Isoyama, K. Kinetic Studies of WO3-Based Photochromism in Polyvinyl Alcohol Film. *Langmuir* **39**, 10240–10248 (2023).
91. Sangnier, A. *et al.* Thermokinetic and spectroscopic mapping of carbon monoxide adsorption on highly dispersed Pt/γ-Al2O3. *ACS Catal* **11**, 13280–13293 (2021).

92. Hayden, B. E., Bradshaw, A. M. & Greenler, R. G. AN INFRARED STUDY OF THE ADSORPTION OF CO ON A STEPPED PLATINUM SURFACE. *Surf Sci* **149**, 394–406 (1985).
93. DeRita, L. *et al.* Catalyst Architecture for Stable Single Atom Dispersion Enables Site-Specific Spectroscopic and Reactivity Measurements of CO Adsorbed to Pt Atoms, Oxidized Pt Clusters, and Metallic Pt Clusters on TiO2. *J Am Chem Soc* **139**, 14150–14165 (2017).
94. DeRita, L. *et al.* Structural evolution of atomically dispersed Pt catalysts dictates reactivity. *Nat Mater* **18**, 746–751 (2019).
95. Kappers, M. J. & Van Der Maas, J. H. Correlation between CO frequency and Pt coordination number. A DRIFT study on supported Pt catalysts. *Catal Letters* **10**, 365–374 (1991).
96. Lentz, C., Jand, S. P., Melke, J., Roth, C. & Kaghazchi, P. DRIFTS study of CO adsorption on Pt nanoparticles supported by DFT calculations. *J Mol Catal A Chem* **426**, 1–9 (2017).
97. Thang, H. V., Pacchioni, G., DeRita, L. & Christopher, P. Nature of stable single atom Pt catalysts dispersed on anatase TiO2. *J Catal* **367**, 104–114 (2018).
98. Newton, M. A., Ferri, D., Smolentsev, G., Marchionni, V. & Nachtegaal, M. Room-temperature carbon monoxide oxidation by oxygen over Pt/Al2O3 mediated by reactive platinum carbonates. *Nat Commun* **6**, 1–7 (2015).
99. Derry, G. N. & Ross, P. N. HIGH COVERAGE STATES OF OXYGEN ADSORBED ON Pt(100) AND Pt(111) SURFACES. *Surf Sci* **140**, 165–180 (1984).
100. Ogawa, T., Kuwabara, A., Fisher, C. A. J., Moriwake, H. & Miwa, T. Adsorption and diffusion of oxygen atoms on a Pt(211) stepped surface. *Journal of Physical Chemistry C* **117**, 9772–9778 (2013).
101. Yue, J., Du, Z. & Shao, M. Mechanisms of Enhanced Electrocatalytic Activity for Oxygen Reduction Reaction on High-Index Platinum n(111)-(111) Surfaces. *Journal of Physical Chemistry Letters* **6**, 3346–3351 (2015).
102. Xu, J. & Yates, J. T. Catalytic oxidation of CO on Pt(335): A study of the active site. *J Chem Phys* **99**, 725–732 (1993).
103. Szabó, A., Henderson, M. A. & Yates, J. T. Oxidation of CO by oxygen on a stepped platinum surface: Identification of the reaction site. *J Chem Phys* **96**, 6191–6202 (1992).
104. Creighan, S. C., Mukerji, R. J., Bolina, A. S., Lewis, D. W. & Brown, W. A. The adsorption of CO on the stepped Pt{211} surface: a comparison of theory and experiment. *Catal Letters* **88**, 39–45 (2003).
105. Slavinskaya, E. M. *et al.* States of Pt/CeO2 catalysts for CO oxidation below room temperature. *J Catal* **421**, 285–299 (2023).
106. Yoshinobu, J., Tsukahara, N., Yasui, F., Mukai, K. & Yamashita, Y. Lateral Displacement by Transient Mobility in Chemisorption of CO on Pt(997). *Phys Rev Lett* **90**, 1–4 (2003).
107. Toolenaar, F. J. C. M., Stoop, F. & Ponec, V. On Electronic and Geometric Effects of Alloying An Infrared Spectroscopic investigation of the Adsorption of Carbon Monoxide on Platinum-Copper Alloys. *J Catal* **82**, 1–12 (1983).
108. Kim, C. S., Tornquist, W. J. & Korzeniewski, C. Site-dependent vibrational coupling of CO adsorbates on well-defined step and terrace sites of monocrystalline platinum: Mixed-isotope studies at Pt(335) and Pt(111) in the aqueous electrochemical environment. *J Chem Phys* **101**, 9112–9121 (1994).

109. Lindfors, C. Hydrodeoxygenation of lignin-derived phenol compound isoeugenol over nickel-and cobalt-based catalysts. (Abo Akademi University, Turku, 2019).
110. Tieuli, S. *et al.* Hydrodeoxygenation of isoeugenol over Ni-SBA-15: Kinetics and modelling. *Appl Catal A Gen* **580**, 1–10 (2019).
111. Bartolomei, E. *et al.* Lignin Depolymerization: A Comparison of Methods to Analyze Monomers and Oligomers. *ChemSusChem* **13**, 4633–4648 (2020).
112. Xiao, X. *et al.* The role of oxygen vacancies in biomass deoxygenation by reducible zinc/zinc oxide catalysts. *Catal Sci Technol* **8**, 1819–1827 (2018).
113. Teles, C. A. *et al.* Role of the metal-support interface in the hydrodeoxygenation reaction of phenol. *Appl Catal B* **277**, 1–13 (2020).
114. Flores, A. F., Burwell, R. L. & Butt, J. 8. Structure Sensitivity of Benzene Hydrogenation on Supported Pt Catalysts. *Journal of the Chemical Society, Faraday Transactions* **88**, 1191–1196 (1992).
115. Kresse, G. & Furthmüller, J. Efficient iterative schemes for ab initio total-energy calculations using a plane-wave basis set. *Phys Rev B* **54**, 11169–11186 (1996).
116. Perdew, J. P., Burke, K. & Ernzerhof, M. Generalized Gradient Approximation Made Simple. *Phys Rev Lett* **77**, 3865–3868 (1996).
117. Kresse, G. & Joubert, D. From ultrasoft pseudopotentials to the projector augmented-wave method. *Phys Rev B* **59**, 1758–1775 (1999).
118. Scanlon, J. T. & Willis, D. E. Calculation of Flame Ionization Detector Relative Response Factors Using the Effective Carbon Number Concept. *J Chromatogr Sci* **23**, 333–340 (1985).

Chapter 4: Chemical Role of Reducible Oxides in MO_x/Pt Inverse Catalysts for HDO

4.1 Introduction

4.1.1 Background

The work presented in Chapters 2 and 3 of this dissertation seeks to fundamentally understand the structure-activity relationships in WO_x/Pt-catalyzed HDO of phenolics by virtue of their changes to reaction selectivity and stability, though the improvements to catalyst stability are outside of the scope of this dissertation. Initial studies using WO_x as the modifier were conducted as it is the most studied oxide modifier for these reactions for inverse catalysts[1–4], exhibiting the highest selectivity to deoxygenated aromatics out of the metal oxide modifiers. However, there are a number of reducible metal oxide promoters that have been employed in MO_x/Pt catalyst formulations which have demonstrated comparable activity in the HDO of phenolics, including MoO_x[5–9], NbO_x[10–12], TiO_x[11,13–15], among others.

This, of course, raises questions in regard to the role of the oxide modifier in promoting reactivity. Frustratingly, by virtue of their bifunctional acid-metal characteristics, MO_x/Pt catalysts find application in a number of distinct HDO reactions from various substrates derived from biomass with distinct reactivity and mechanisms of deoxygenation[16–19]. For example, $^{1}H/^{2}D$-labelling experiments over a WO_x/Pt/TiO_2 catalyst showed that the HDO of 1,2,6-hexanetriol to 1,6-hexanediol could not be explained by direct deoxygenation or Mars-van Krevelen mechanisms, thus pointing to the likely participating of acid-catalyzed dehydration in the oxygen removal mechanistic step[20]. While this work is extremely detailed, the results are of limited utility considering the substantial chemical differences between the

saturated alcohols studied in that work and the phenolic substrates of interest here. This has left quite a large gap in the understanding of phenol-specific deoxygenation mechanisms.

In Chapter 3 of this dissertation, the role of WO_x in improving the selectivity during MO_x/Pt-catalyzed HDO of phenolics was clarified through the identification of the preferential decoration of well-coordinated Pt sites, which serve as the active site for the undesired aromatic hydrogenation reaction. However, though the results of Chapter 3 pointed towards the potential role of under-coordinated Pt sites in the deoxygenation step during HDO catalysis, no conclusion could be reached as to the specific structure of the active site for deoxygenation. On the basis of the similar deoxygenation reactivity of unmodified and modified Pt catalysts shown in Chapter 3, it is possible that WO_x and other reducible metal oxide modifiers play only a spectatorial role in deoxygenation chemistries during HDO.

While the reactivity of modified and unmodified catalysts are comparable in HDO reactions, there have been reports of oxide modifiers that exhibit similar, but measurably different reactivity towards deoxygenation of phenolics. In the study of either NbO_x or TiO_x-modified $Pt/MgAl_2O_4$ catalysts, it was shown that NbO_x demonstrated a greater spike in activity between 300˚C and 350˚C than TiO_x, though the selectivity of TiO_x catalysts was comparable, suggesting their role in catalysis was the same[10]. The authors of this work suggested that the mobility of the two oxide species explained the difference in reactivity, with the more mobile NbO_x able to mobilize from the Pt sites more effectively to enable their reactivity in deoxygenation. This would be consistent with a non-chemical, spectatorial role of the oxide modifiers. The Huttig temperature, or ~$0.3T_m$, where Tm is the melting temperature of the material, is often used as a metric for quickly assessing when solid-state diffusion becomes rapid enough that mobility should be considered for solids restructuring[21–23]. The

Huttig temperature for Nb_2O_5 is ~504˚C while that of TiO2 is ~614˚C, in line with the general trends observed for higher Nb2O5 mobility. However, though these results implicate the importance of oxide mobility to potentially expose either metal sites or metal-oxide interfacial sites, there is insufficient evidence either in favor or against a chemical contribution of oxide modifiers in promoting HDO of phenolics.

Some have suggested that interfacial chemistries may play a role, but significant gaps exist for this explanation[24–26]. Unfortunately, there are few other reports that attempt to identify the chemical contribution of oxides and fewer that do so in a manner that enables conclusive determination either way. One challenge is that the measurement of these interfacial areas is in and of itself a technically challenging pursuit, especially in the case of materials that might undergo dynamic restructuring to either maximize or minimize the interfacial area between the two domains under reaction conditions. This chapter will provide direct evidence that such NbO_x/Pt systems undergo SMSI behaviors akin to WO_x/Pt, suggesting that measurements of interfacial area may not capture the true interfacial area unless the measurements are conducted *operando*, which has not been accessible to date. Additional technical challenges in making these measurements experimentally are the differences in metal-support interactions and surface areas between catalysts, potentially altering both the particle size distribution and shape of metal domains between different oxides. Many of these reports also co-deposit oxides with metals in the same synthetic step, though this leads to changes to the metal particle size that can obscure the influence of the oxide[26,27].

To consider the scope of the issue, the possible mechanisms that have been proposed for phenolic HDO over MO_x/Pt catalysts can be considered including hydrogenation followed by dehydration[28–30], direct deoxygenation (DDO)[31–33], and tautomerization[5,34]. While in

Chapter 2, the influence of dehydration could be ignored because of the use of non-acidic SiO_2 supports, the introduction of metal oxides with acidic functionalities may facilitate such a pathway. In all but tautomerization facilitated solely by metal sites, which has been demonstrated in Chapter 2, all of the proposed mechanisms might be expected to show a chemical dependence on the properties of the decorating oxides. However, as discussed below, the breadth of oxide properties reported to facilitate successful HDO with high aromatics yields is in direct disagreement with the relative comparable rates that these catalysts exhibit.

4.1.2 Chemical Properties of Reducible Metal Oxides Reported for MO_x/M' HDO

Such interfacial mechanisms also fail to explain the similarity in reactivity despite considerable differences in chemical properties between reported metal oxide promoters that would be expected to influence interfacial reactivity. Of particular interest is the potential role of oxygen vacancies formed *in situ* by reduction of the oxidized metal oxides in sequestering oxygen from phenolic species during reaction and the presence of Brønsted acid sites which may participate in acid-catalyzed dehydration at some point in the reaction cascade. However, there is uncertainty whether the reactivity reported to date for these materials substantiates any participation of the modifying oxides through these pathways, as relatively similar activities have been reported despite the large differences in properties between them.

Considering first the role of reducibility, the oxides discussed above which have been reported for the HDO of phenolics (TiO_x, MoO_x, WO_x, and NbO_x) exhibit a wide range of reducibilities. Though there is no strict definition of reducibility, in general, it pertains to the ease with which a given material transits between a high oxidation state and a low oxidation state in response to a reductant, often H_2. In the case of transition metal oxides, this shift in

oxidation state usually coincides with the formation of water via oxygen removal as a consequence of the reduction in oxidation state of the transition metal cation, though recent work has shown that this is not always the case as can occur with hydroxyl formation over CeO_2 and TiO_2.

Stemming from the absence of a strict definition for reducibility, a number of qualitative measurements have been utilized for the development of relative reducibilities in materials. These include theoretical metrics such as metal-oxygen bond strength, work functions for valence electrons, and band gaps, each of which has distinct applications where they may relate better or worse to observed behavior. More applicable to the work presented in this dissertation and reported in the literature for similar materials is the use of H_2-mediated temperature-programmed reduction (H_2-TPR). H_2-TPR is a technique wherein the reduction of a material, in this case a transition metal oxide, is measured directly using H_2 at increasing temperatures. By measuring H_2 consumption by the material using a variety of detector methods (TCD, MS, etc.), it is possible to measure the temperature at which H_2 is consumed to reduce the transition metal oxide and form water. As such, H_2-TPR offers some benefits compared to theoretical approaches as it captures the realistic behavior of as-prepared catalysts rather than relying on models often derived from bulk materials. However, at the same time, the reduction events are often difficult to deconvolute and materials may undergo a variety of H_2 consumption events, including the formation of H_2 bronzes in the case of WO_x and MoO_x, which are distinct materials from the base WO_x and MoO_x originally loaded into the reactor. However, in general, H_2-TPR finds the greatest application for assessing material reducibility in heterogeneous catalysis.

Considering the reported H_2-TPR profiles for TiO_2, MoO_3, WO_3, and Nb_2O_5 shown in Figure 4.1 below, we can see that in the absence of a promotional metal, which can kinetically facilitate reduction by activating H_2 and participating in spillover to the support, the oxides listed have significantly different reduction behaviors. The largest reduction features can be seen for both WO_3, exhibiting a reduction feature at around 600˚C, and MoO_3, which begins significantly reducing at around 700˚C. On the other hand, TiO2 shows only minor reduction at 600˚C which does not correspond to overall bulk reduction, but rather oxygen vacancy formation on the surface at defect sites around 600˚C. The least reducible oxide, Nb_2O_5, demonstrates no obvious reduction event in the surface or bulk in the temperature range studied. Importantly, these are transient experiments that do not reflect a "reduction limit" for

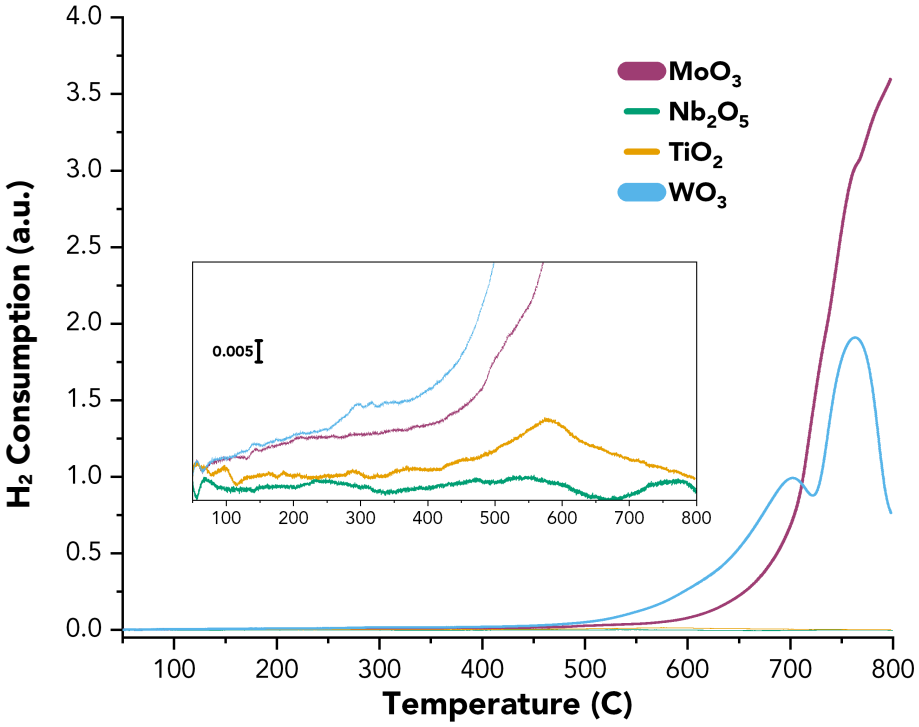

Figure 4.1: H_2-Temperature Programmed Reduction (TPR) profiles of bulk MoO_3, Nb_2O_5, TiO_2, and WO_3 showing the differences in reducibilities between the bulk oxide phases. WO_3 and MoO_3 show strong reduction features, while Nb_2O_5 and TiO_2 consume minimal H_2 over the same temperature range, as indicated by the inset.

these oxides – for example, it is known that WO_3 reduces under reaction conditions of only 250˚C, both due to the difference in reductant composition and the time-scales of reaction.

However, the ease of reduction may be linked to the activity of MO_x/Pt catalysts in HDO of phenolics, considering it is frequently cited that oxygen vacancies, formed via reduction, may become re-oxidized by interacting with oxygen atoms in phenolic substrates, stabilizing the transition state for deoxygenation and lowering the observed barriers for this step. In this sense, a moderate reducibility may actually be favorable, as the resulting re-oxidation must be favorable enough to energetically promote deoxygenation. It has been proposed that WO_x's high reducibility is potentially a shortcoming in this regard, as WO_x may stay in the reduced state under reaction conditions and not abstract oxygen from the substrate, though this has been primarily proposed as a retrospective rationalization of experimental results that may stem from any number of mechanisms.

As mentioned above, the acidities of the modifying oxide species also span a wide range. In the context of phenolic HDO, it has been proposed that specifically Brønsted acidity may play the greatest role in facilitating deoxygenation through Brønsted-acid catalyzed dehydration reactions as typically observed in organic chemistry. While aromatic oxygenates such as phenol itself are stable to Brønsted acid attack and do not undergo deoxygenation directly via this mechanism, it has been proposed that metallic components (M') in MO_x/M' catalysts, such as Pt, may either partially or fully hydrogenate the aromatic ring under reaction conditions, resulting in a C_{sp3}-OH functionality that is susceptible to Brønsted acid-catalyzed dehydration.

The comparison of Brønsted acidity is once again a challenging measurement to make experimentally because of the influence of environmental conditions on the acidity of a site

(i.e. hydration environment) and also the broad range of sites on the surface of heterogeneous catalysts, each exhibiting slightly different structural and physical characteristics which may influence acid strength. Arguably the most accurate measurement of Brønsted acid strengths is through calorimetry using a base to measure the heat released upon acid-base reactions for sites as a function of coverage, though measurement complexity means that relatively little data on the transition metal oxides exists for this method. More popular is another temperature-programmed desorption method, NH_3-TPD, where NH_3 is adsorbed to the acid sites of the catalyst at room temperature and transiently desorbed, providing information regarding the quantity of acid sites and their relative strength via the temperature at which desorption occurs. Though there are issues with this technique in regard to specificity, as NH_3 adsorbs to both Lewis and Brønsted sites and there is a lack of understanding of the relative ratio of the two

sites from NH_3-TPD alone, its broad utilization is useful in establishing a relative understanding of the acidities of transition metal oxides.

NH_3-TPD results indicate that Nb_2O_5 catalysts are by far the most acidic, explaining its utilization as a solid acid catalyst without modification in organic chemistry. Results in the literature point to the formation of primary Brønsted acid sites capable of reactions such as acid-catalyzed ether hydrolysis. Next are WO_x and MoO_x, exhibiting moderate acidity, followed by TiO_x, which exhibits essentially negligible acidity in its bulk form.

Recently, however, there has been a growing appreciation for the changes to acidity that can occur during catalysis. For instance, it has been shown that TiO_2 acidity depends strongly on the crystalline phase it is present as, increasing in the order of rutile, anatasae, and brookite, indicating that the surface composition and structure influence acidity[35].

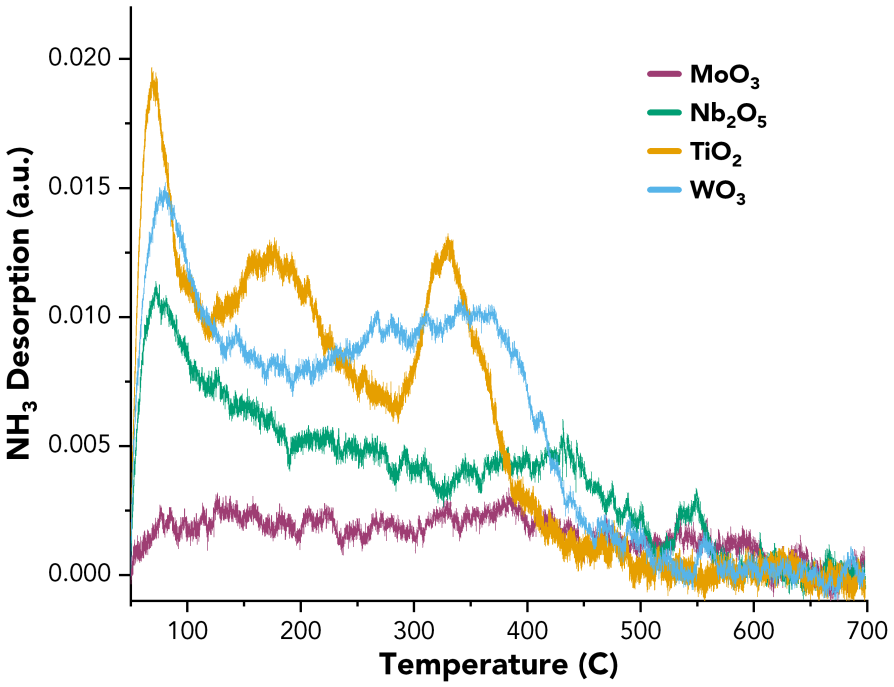

Figure 4.2: NH_3-Temperature Programmed Desorption (TPD) profiles of bulk MoO_3, Nb_2O_5, TiO_2, and WO_3 showing the differences in acidic properties, particularly to the Brønsted acid strength and site density. Brønsted acid sites correspond to NH_3 desorption greater than ~300˚C, where increasing temperature indicates stronger acid strength.

Additionally, the introduction of Pt interacting with TiO_2 has been shown to introduce new acid sites through H spillover during reduction[36], indicating that under reaction conditions, even TiO_x may exhibit *in situ* formed acid sites. Indeed, MoO_x and WO_x have been demonstrated to behave similarly during reaction. Combined experimental and theoretical work has shown that WO_x domains decorating metal nanoparticles such as Pt can become reduced to form hydroxyls rather than oxygen vacancies[37,38]. These hydroxyls have been shown to be dynamically formed in response to H_2 and thus facilitate acid-catalyzed reactions under H_2 environments.

Clearly, extensive work using a controlled system is necessary to elucidate the chemical role of oxide promoters in MO_x/Pt catalysts for the HDO of phenolics. Towards this end, the catalyst architecture reported in Chapter 3 utilizing base Pt/SiO_2 catalysts with controlled amounts of co-deposited oxides lends itself well to this investigation. Through this approach, Pt nanoparticle size distributions can be controlled and kept constant between oxide modifier series, eliminating effects related to structure-sensitivity of Pt itself. Moreover, oxide decoration on the active metal can be altered systematically to explore whether modifying oxides play an inhibitory, promotional, or spectatorial role in the deoxygenation of PHE. Thus, this chapter reports the exploration of MO_x/Pt/SiO_2 catalysts where M = W, Mo, Nb, and Ti to assess the potential roles of reducibility and acidity in dictating catalyst activity.

4.2 Results

Reducible metal oxide modified Pt/SiO_2 catalysts were synthesized analogously to previous chapters, with a step-wise preparation involving batch preparation of a base Pt/SiO_2 catalyst, followed by metal oxide deposition through aqueous precursors. This approach allows

for the conservation of the Pt particle size distribution across all catalysts studied, removing the influence of Pt structure sensitivity from all further analyses. Worth noting here is the difference in synthetic protocols used for the base Pt/SiO_2 catalyst discussed in this chapter and the base Pt/SiO_2 catalyst utilized in Chapter 3. Pt/SiO_2 catalysts in Chapter 3 were synthesized using aqueous impregnation of 15-20 nm, nonporous SiO_2 support using platinum tetraamine nitrate (TAPN) followed by calcination in air at 600˚C. The use of TAPN has a variety of benefits compared to other platinum precursors, including a net positive charge in solution that facilitates adsorption to negatively charged oxide surfaces and the formation of gaseous species upon decomposition that leave no residue on the catalyst surface.

However, at the time of the work conducted here, TAPN was not available for use so an alternative precursor and synthesis procedure were used, namely H_2PtCl_6. H_2PtCl_6, or chloroplatinic acid (CPA), is a common precursor for Pt, particularly in the synthesis of commercial catalysts due to its low cost and ease of preparation. However, CPA is typically undesirable for academic research due to the formation of anionic species ($PtCl_6^{2-}$) in solution during synthesis which may interact repulsively with negatively charged oxide surfaces, resulting in non-uniformities in deposition that may lead to higher rates of sintering, as well as the co-deposition of Cl^- during decomposition. Cl^- contamination has been shown in a number of studies to influence catalyst activity through a number of routes, including poisoning, electronic modification, and acid site formation[39,40]. Therefore, in academic studies, it is generally desirable to avoid Cl^--containing precursors, though the content of Cl^- contamination can be mitigated through the use of high-temperature reduction treatments. These reductive treatments, using H_2 as the reductant, react with Cl^- under high temperatures to liberate HCl, which volatilizes and removes Cl^- from the catalyst surface[41,42]. Thus, this synthesis route was

followed here, as opposed to the calcination in air at 600˚C used for TAPN-synthesized catalysts, to obtain a CPA-synthesized Pt/SiO_2 catalyst with minimal Cl^- contamination.

To ensure that the Pt nanoparticles in the same size regime as previously studied in Chapters 2 and 3 were obtained with the new synthetic route, HAADF-STEM images were collected of the 6Pt catalysts synthesized from CPA (Figure 4.3). The image clearly shows large Pt nanoparticles between 10 and 20 nm in size, broadly consistent with the materials used in Chapter 3. One difference of the TAPN catalyst synthesis discussed above is the use of an oxidation step forming volatile PtO_2 species at elevated temperatures[43]. In TAPN-synthesized catalysts, these species were intentionally targeted, in part, to increase the rate of sintering to provide Pt nanoparticles of approximately 10 nm in average diameter, informed by both previous literature reported for WO_x/Pt catalysts as well as the structure-sensitivity results described in Chapter 2 of this dissertation. However, the synthesis from CPA employing high-temperature reduction in H_2 to mitigate Cl content on the surface avoids this and may result in

Pt nanoparticles of a different size than previously studied, at worst limiting the consistency of results between the works reported in this dissertation.

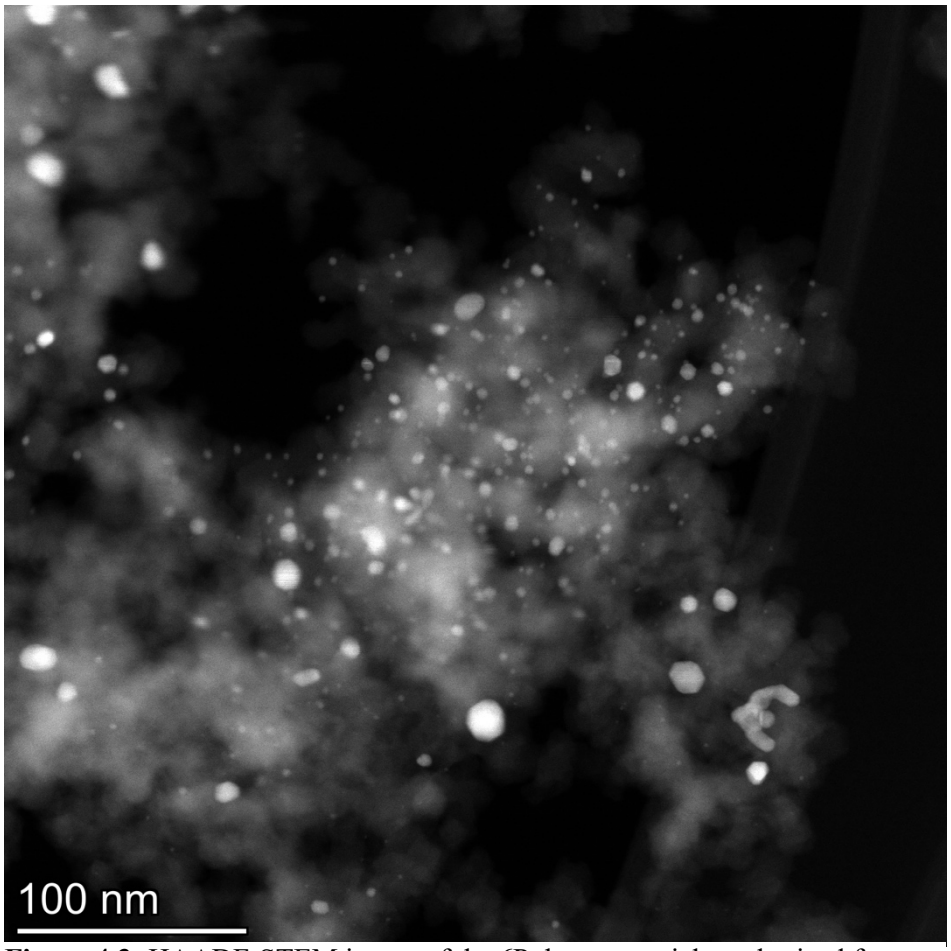

Figure 4.3: HAADF-STEM image of the 6Pt base material synthesized from CPA. Particle size distribuion analysis shows good agreement with Pt catalysts reported in Chapters 2 and 3 of this dissertation

The deposition of aqueous reducible oxide precursors was conducted in a manner similar to $WO_x/Pt/SiO_2$ and $WO_x/Pt/Al_2O_3$ catalysts presented in Chapters 3 and 4, though care was needed to select appropriate precursors for some species. W and Mo share significant chemical similarities, with both W and Mo forming polyoxometalate (POM) species with multiple metal species (i.e. Mo_7O_{24} and $H_2W_{12}O_{40}$). In terms of synthesis, these species may further decompose into more dispersed species (i.e. WO_4^{2-}) depending on conditions such as pH and concentration[44,45], though all forms are highly soluble and thus deposit facilely through

aqueous approaches. The TEM and UV-Vis results in Chapter 3 regarding the deposition of WO_x demonstrate typically uniform deposition across the SiO_2 surface, as opposed to significant segregation around specific moieties such as the Pt nanoparticles present during this synthetic step.

NbO_x and TiO_x precursors, however, demonstrate significantly different chemical properties that present challenges to this synthetic approach. Considering first titanium, typical precursors for the synthesis of TiO_2 are water sensitive, with the most common either being $TiCl_4$ or alkoxides such as $Ti(OPr)_4$, both of which fume in ambient air due to their reactivity towards humidity[46]. Niobium faces similar challenges in terms of a smaller library of monomeric or polymeric precursors which are stable in aqueous solution, with popular synthetic routes typically proceeding through $NbCl_5$, which is water sensitive, or $Nb_2O_5*xH_2O$, which is an insoluble solid. In both cases, it was desired to obtain a water-soluble form of the reducible oxide of interest such that deposition occurred homogeneously across the SiO_2 surface as was previously observed for $WO_x/Pt/SiO_2$ catalysts.

Fortunately, chelated forms of NbO_x and TiO_x are available, both in the form of oxalate salts. Ammonium niobium oxalate is an aqueously soluble, monomeric precursor to Nb_2O_5, and potassium titanium oxide oxalate is similarly soluble, monomeric precursor for TiO_2. These precursors were selected for the deposition of NbO_x and TiO_x and used in an identical fashion to WO_x and MoO_x precursors to obtain modified Pt/SiO2 catalysts. To control the amount of modifying oxide present in the catalyst despite large differences in molar masses across the spectrum of materials, loadings were maintained relative to the molar ratio of reducible metal oxide to Pt. In this manner, the moles of modifying oxide remain comparable despite large differences in weight loading across the materials. For this purpose, catalysts will

be referred to from here on out as *x*M6Pt, where *x* represents the molar ratio of M:Pt, which varies from 0.083 to 1.

In order to assess the influence of oxide modifier identity and characteristics on the HDO performance of $MO_x/Pt/SiO_2$ catalysts, where M = W, Nb, Mo, and Ti, batch reactions were conducted using 4-propylphenol (PHE) as the starting substrate. PHE was used in these reactions, instead of dihydroeugenol (DHE) as shown in Chapters 2 and 3, to reduce the number of possible intermediates and to clarify the formational pathways of deoxygenated products. Of particular interest in these experiments were the formation of 4-propylcylohex-1-ene (CYE), or the product of 4-propylcyclohexanol (OL) dehydration through Brønsted acid sites relative to the desired formation of 4-propylbenzene (BNZ). In Chapter 3, it was discussed that CYE production became significant over WO_x/Pt catalysts at the highest W loadings due to the participation of SiO_2-bound WO_x sites which are known to be acidic[47–49]. Considering that the reducible oxides selected here cover a wide range of acid strengths and densities, the objective was to deconvolute the participation of acid sites from other potential sites, such as the well-coordinated Pt sites which have been identified as possible active sites in Chapters 3 and 4, in the formation of BNZ.

HDO reactions were conducted using 20 mL of a stock solution of PHE in cyclohexane as a solvent, with a PHE concentration of 0.183 M. For quantification, *n*-decane was included as an internal standard at a concentration of 0.084 M. Control experiments confirmed that *n*-decane was not measurably reactive under these conditions for these catalysts.

The mass balance of liquid-phase species was typically >98%, in stark contrast to the HDO experiments conducted on DHE by $WO_x/Pt/SiO_2$ catalysts as presented in Chapter 3 for which mass balances were frequently as low as 80%. This is attributed to the functionally

simpler structure of PHE compared to DHE, as it exhibits the removal of the ortho methoxy functionality in the precursor. This methoxy species, specifically in the ortho position as present in DHE, is proposed to path a number of deleterious roles in the reduction of liquid-phase mass balances during HDO reactions. For one, it has previously been demonstrated that the presence of methanol during HDO reactions over metallic catalysts results in the reduction of liquid phase mass balance through the formation of oligomerized species[50]. This behavior is attributed to the participation of methanol and methanol derivatives on the metal surface in the radical polymerization of aromatic species into oligomers, in some ways analogous to the in vivo synthesis of lignin itself. Thus, these oligomeric species are highly recalcitrant to depolymerization and reaction, representing a dead-end in the reaction pathway that cannot be quantified by GC-FID due to the high boiling point of the oligomeric fractions. In using DHE under HDO conditions, methanol is formed *in situ* through the hydrogenolysis of DHE into PHE. Considering the PHE and its derivatives are present in high yield at the end of reaction, there is a stoichiometric amount of methanol present during reaction relative to the amount of demethoxylated products. Importantly, relatively little of the catechol-like species, or the product of demethylation of DHE, is ever observed, indicating that the primary pathway for DHE HDO in the presence of $WO_x/Pt/SiO_2$ catalysts proceeds through demethoxylation rather than demethylation. Additionally, it has been shown that the vicinal functionalities present in DHE lend themselves to strong interactions with the silica surface[51,52], resulting in a higher rate of strong adsorption to the catalyst surface for DHE compared to PHE. Conducting HDO of PHE, even over strongly acidic oxides such as NbO_x which present stronger acidity than the WO_x/Pt catalysts used in the HDO of DHE shown in Chapter 4, results in no noticeable

coloration of the solution after reaction, consistent with the high mass balances obtained in the liquid phase.

Figure 4.4 shows the HDO performances of the oxide-modified Pt/SiO_2 catalysts in the HDO of PHE, with performance represented by the yield of products grouped by their reaction, namely aromatic ring hydrogenation and deoxygenation. Hydrogenated products include 4-propylcyclohexanone (ONE), 4-propylcyclohexanol (OL), CYE, and 4-propylcyclohexane (CYC). Deoxygenated products are represented by 4-propylbenzene (BNZ), CYE, and CYC. The hydrogenated product yield in Figure 4.2a shows that that are only broad trends between the different oxide modifiers, with WO_x-modified catalysts exhibiting the highest yield of hydrogenated products across all M:Pt ratios, followed by NbO_x- and MoO_x-modified catalysts which perform similarly, and finally MoO_x-modified catalysts, which represent the lowest yields of hydrogenated products. Also included in Figure 4.4a is the performance of unmodified Pt/SiO_2 catalysts in the HDO of PHE, shown as the data point at M:Pt = 0. All modified catalysts produce lower hydrogenated product yields than the unmodified Pt catalyst, consistent with the results in Chapter 3 which demonstrated that WO_x modification was an effective strategy to reduce the formation of hydrogenated products in the HDO of DHE.

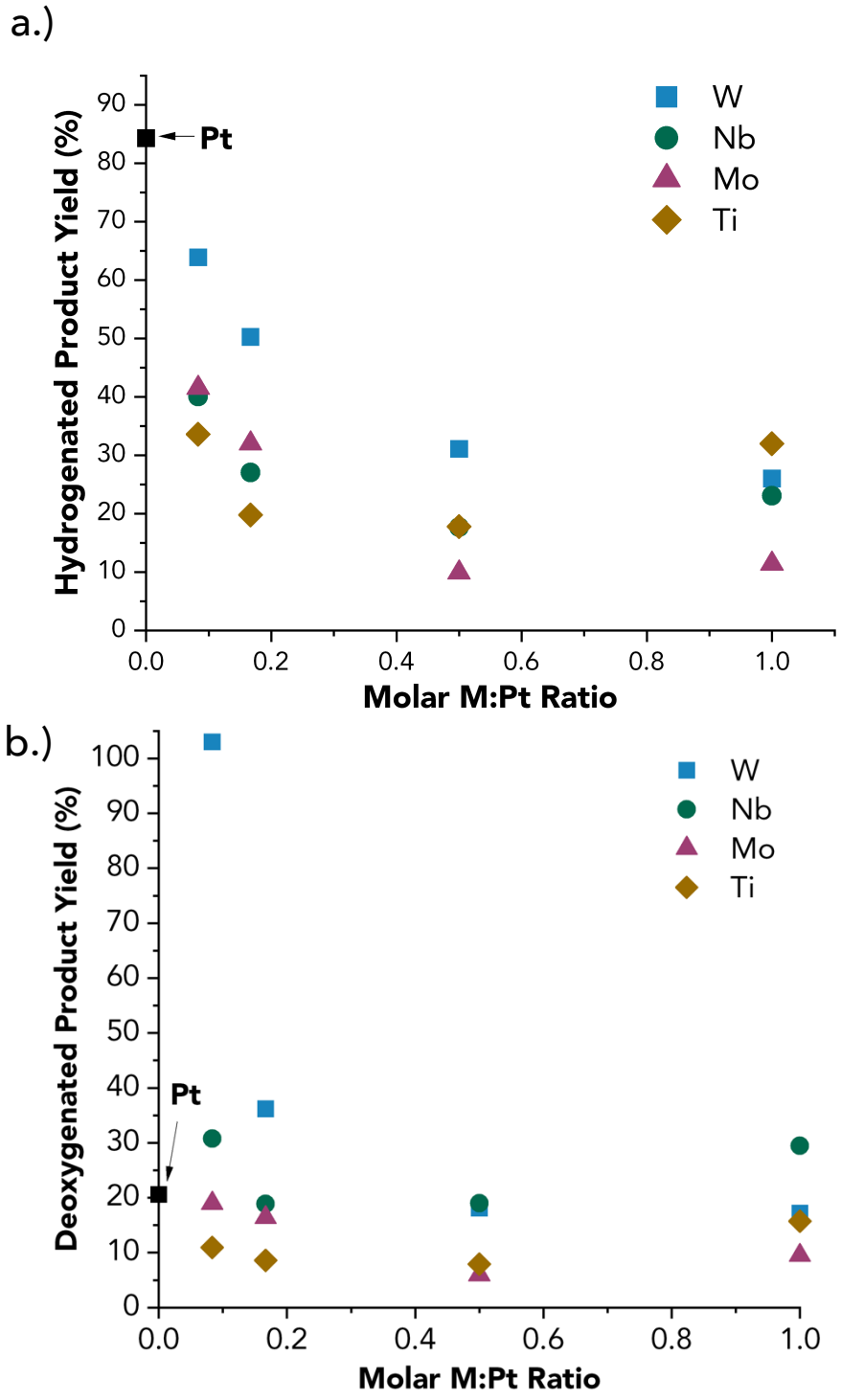

Figure 4.4: PHE HDO reaction results of oxide-modified Pt catalysts. (a) shows the hydrogenated product yield including OL, ONE, CYE, and CYC. (b) shows the yield of deoxygenated products including BNZ, CYE, and CYC. Catalyst loading was kept constant at 10 mg for each reaction to load a constant mass of Pt. *Conditions*: 275˚C, 2 hours, 20 mL of PHE in cyclohexane, 10 mg catalyst, 20 bar H_2.

Figure 4.4b also shows the performance of modified Pt catalysts in the HDO of PHE, this time representing the yields of deoxygenated products. In this case, there is a markedly less clear trend than what was observed in Figure 4.4a for the hydrogenated products. Unmodified Pt catalysts produce an intermediate yield of deoxygenated products from PHE with a total yield of approximately 21%. The performance of the modified catalysts in this perspective appears to be highly oxide-dependent, with some oxides performing both better and worse than unmodified Pt. For example, TiO_x-modified Pt exhibits lower yields of deoxygenated products across its entire range, whereas NbO_x-modified catalysts exhibit higher yields relative to unmodified Pt. Across all modified catalysts, however, there is no monotonic trend that links oxide modification with deoxygenation performance, in contrast to hydrogenation. This provides a murky picture of the role of the oxide in the deoxygenation of PHE at best, as unlike the WO_x/Pt catalysts shown in Chapter 3, it cannot be said that unmodified Pt performs equally to all modified catalysts in deoxygenation from the perspective of M:Pt ratio alone.

However, an important component of the catalyst formulation is ignored when representing reactivity based on the metal loading alone, which is the fractional quantity of modifying oxide present on the surface of metallic Pt nanoparticles in the SMSI state. There is sufficient basis to believe that the efficiency of Pt surface decoration may vary significantly with the oxide modifier identity, related to a convolution of energetics related to the stabilization of reduced species on the oxide surface, the reducibility of individual oxide modifiers, and the mobility of oxide species on the SiO_2 surface, among others.

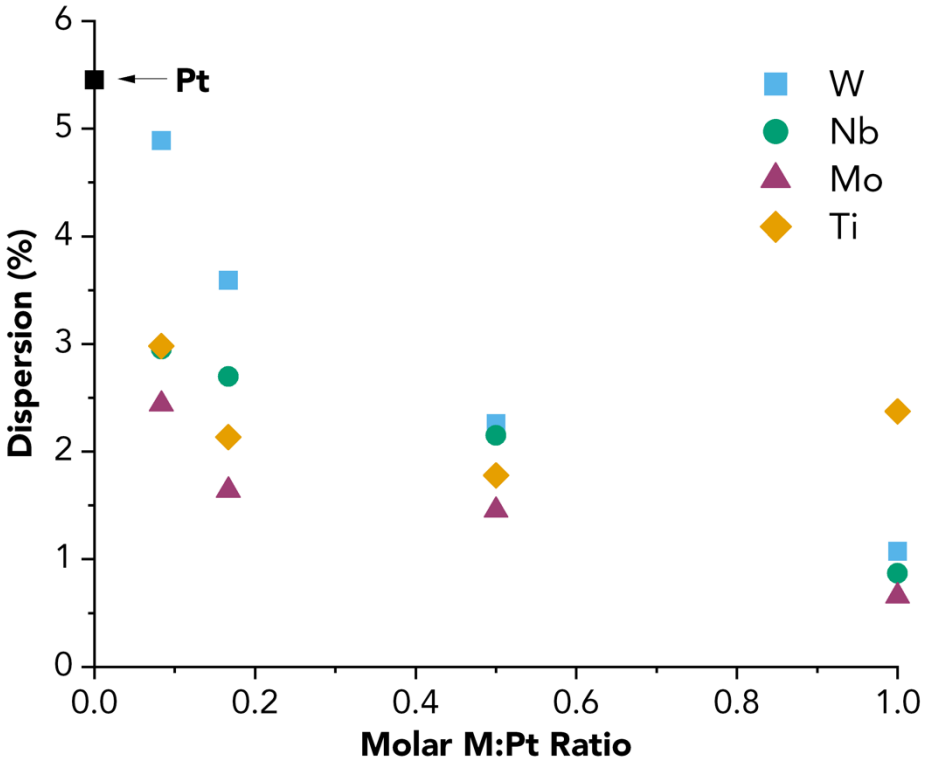

Figure 4.5: Measured dispersion of Pt in oxide-modified catalysts by pulsed CO chemisorption after reduction at 325˚C in 10% H_2/Ar for 1 hour.

To gain a greater insight into the contribution of oxide decoration on top of Pt surfaces to HDO performance, dispersion measurements were made for each oxide using CO chemisorption after a standard reduction at 325˚C under 10% H_2/Ar for 1 hour. These measurements are analogous to the ones made in Chapter 3 for WO_x/Pt/SiO_2 catalysts used in the HDO of DHE, which were critical in linking the preferential decoration of WO_x on well-coordinated Pt sites on nanoparticle surfaces to the suppression of hydrogenation activity. Figure 4.5 shows the measured dispersions for each modified catalyst, as well as the unmodified Pt/SiO_2 catalyst, across the range of M:Pt ratios explored here. Broadly, it can be seen that unmodified Pt/SiO_2 catalysts exhibit the highest dispersion at 5.5%, corresponding to an estimated particle size of ~17 nm. This is consistent with the TEM-measured particle size distribution of Pt catalysts used in Chapter 3 when considering that CO chemisorption is a

volume-normalized measurement that heavily weighs the presence of large nanoparticles. Thus, the Pt nanoparticles on the surface of unmodified and modified Pt catalysts used in this chapter represent comparable catalysts to those utilized previously, and thus the reactivity is likely comparable. HAADF-STEM images were also taken of the unmodified Pt/SiO_2 catalysts synthesized here and the images also corroborate the dominant presence of ~10 nm Pt nanoparticles on the surface of the SiO_2 support. However, unavoidably, a fraction of the volatile PtO_2 species formed during synthesis does not re-deposit, resulting in lower actual Pt loadings on the SiO_2 surface relative to what was nominally calculated. For the purposes of the reactions conducted in Chapter 3, the actual loading of Pt on the catalyst surface was not important, as all catalysts utilized the same base Pt/SiO_2 catalyst, and formation rates were calculated based on actual Pt sites measured by CO chemisorption.

The same can be said for the CPA-synthesized catalysts reported here, as the results of this work are not influenced or biased by the actual loading of Pt on the surface. However, dispersion represents the number of catalyst surface sites normalized by the total Pt loaded into the system, which is inherently a measurement that will be biased by inaccuracies in the expected nominal loading of Pt on the catalyst surface. This can be seen in a larger disagreement for TAPN-synthesized Pt/SiO_2 catalysts between average particle sizes measured directly by HAADF-STEM and those obtained by known relationships between dispersion and average particle size, namely[53]:

$$D_{est} = \frac{1.01}{\mathcal{D}}$$

Where D_{est} represents the estimated diameter of particles and $\mathcal{D}$ indicates the dispersion as measured by CO chemisorption. For TAPN-synthesized catalysts, the dispersion for base Pt/SiO_2 catalysts was measured at approximately 1.5%, resulting in particle size estimates of greater than 50 nm via this measurement alone. However, no particles of this size could be observed using HAADF-STEM to directly measure particles. The explanation for this discrepancy is as discussed above, with nominal Pt weight loadings of Pt/SiO_2 catalysts being lower than true values because of a loss of Pt by volatilization during 600˚C calcination.

Returning to the trends shown in modified catalysts in Figure 4.5, it can be seen that dispersion measured by CO chemisorption after H_2 reduction at 325˚C for all reducible oxides is lower than the value for unmodified Pt/SiO_2. These values are consistent with the reduction of the modifying oxides by H_2 spillover from the Pt support, followed by reduction of the oxide and mobilization of the oxide to the Pt surface. In decorating the surface, these reduced oxide species prevent the adsorption of CO to the Pt surface, thus lowering the measured dispersion. Importantly, this loss of dispersion is not caused by sintering, as was shown with post-reduction HAADF-STEM in Chapter 3 for $WO_x/Pt/SiO_2$ catalysts. The synthetic protocol for oxide modification, that is, the oxidative calcination of oxide precursors after deposition, was the same for these oxides as it was in Chapter 3, providing sufficient reason to believe that no Pt particle growth has occurred here. Also, the continual, monotonic loss in measured Pt dispersion with increasing M:Pt ratio is good evidence of this loss being related to oxide decoration on the Pt nanoparticle surfaces, as all catalysts, regardless of oxide loading, were treated the same and thus any sintering that might occur would be kept constant across all catalysts.

Despite all oxide modifiers exhibiting decreased measured Pt dispersion with increasing loading, there are notable differences in the magnitude of decoration across the modifying oxides. All modifying oxides except TiO_x reach minimum dispersions of ~1% at an M:Pt ratio equal to 1, with TiO_x reaching a minimum dispersion of ~2%. This indicates that for all catalysts, full coverage on the Pt surface is never reached and the reaction is conducted on a partially decorated metal surface. At low M:Pt ratios, there are differences in the degree of decoration for each oxide, with WO_x-modified catalysts being the least decorated for M:Pt

ratios between 0.083 and 0.16 and MoO_x-modified catalysts being the most decorated, though the reason for these trends in not immediately clear.

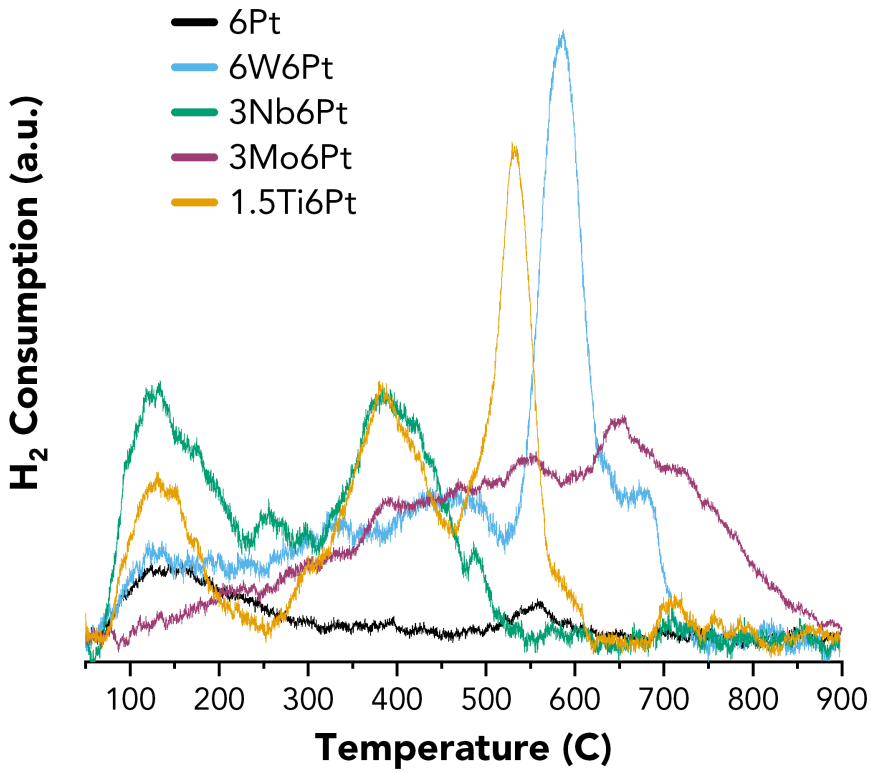

Figure 4.6: (a) H_2-TPR measurements of oxide-modified and unmodified Pt/SiO_2 catalysts. Clearly, the introduction of reducible metal oxide species on the surface results in measurable H_2 uptake related to reduction of the metal oxide component, resulting in varying decoration of the Pt nanoparticles through SMSI-like phenomena. (b) Integrated H_2 consumptions indicating a trend in reducibility of the oxide modifiers.

In order to assess whether or not the degree of reducibility trends with the extent of decoration, H_2-TPR was conducted on the highest loading of each oxide modifier to identify the ease of reduction for each species. Under the assumption that reduction is a prerequisite for mobilization and decoration, it might be expected that the trends in H_2 TPR might explain the results of CO chemisorption at low metal oxide loadings. However, as shown in Figure 4.6, this is not apparently the case. Over the temperature range investigated, all modifying oxides

were shown to reduce when subjected to a ramp to 900˚C at 10˚C/min under 10% H_2/Ar. The first reduction peak, at approximately 100˚C, is shared between all modified catalysts and the unmodified Pt/SiO_2 catalyst, indicating that this feature represents the PtO_x reduction event. The magnitude of the reduction feature, however, is different for each material. This may correspond to the co-reduction of oxide species in close proximity to the PtO_x phase. This close proximity may be related to the different synthesis precursors used, which may deposit the modifying oxides in more or less homogenous distribution across the SiO_2 surface. TiO_x and NbO_x, the two oxides with complex, chelated precursors, show the highest H_2 consumption feature at 100˚C, suggesting that these precursors may deposit oxide closer to the PtO_x phase. This close proximity in turn facilitates the spillover of H_2 to the reducible oxides, thus presenting as a shared reduction feature in the H_2 TPR profiles shown. This is supported by the clear TiO_x reduction feature for TiO_x-modified catalysts at ~500˚C, before even WO_x reduction at ~600˚C. In their bulk forms, it is known that WO_3 is more easily reduced than TiO_2, and thus one might expect that another phenomenon might explain the opposite trends shown here in the TPR experiments. One such explanation would be the closer proximity of TiO_x domains to Pt, resulting in more facile transport of H spillover species to the TiO_x as compared to the WO_x domains. Typically, SiO_2 is considered an irreducible oxide incapable of facilitating H spillover in its pristine state. However, the presence of defects, water, and hydroxylated regimes present chemically different surfaces and thus different H spillover behaviors from pristine materials typically studied under UHV conditions. Thus, these results and reports in the literature support the idea that H spillover is possible over SiO_2, though with higher barriers than what would be observed for traditional reducible supports, which are the modifying species here.

The total quantity of H_2 used in the reduction of the reducible oxide domains, along with PtO_x domains, can be measured using the H_2 TPR profiles shown in Figure 4.6. Surprisingly, though MoO_x shows the highest reduction temperature in H_2 TPR, the total quantity of H_2 consumed per gram is the highest. Interestingly, the values for total H_2 consumed up to 900˚C are more consistent with the trends in dispersion as measured by CO chemisorption. This suggests that the extent of decoration is a function of how much oxide can become reduced, as might be expected, but less a function of the ease of reducibility of the oxide itself, which is perhaps a less obvious result. This points to the mobility of reduced oxide species being potentially different amongst the modifying oxides, and this mobility being a driving factor in the extent of decoration possible for these catalyst formulations.

With these dispersion values, it is possible to normalize the reactivity for each catalyst against its dispersion value, which correlates with the extent of decoration by the modifying oxide on the Pt nanoparticle surfaces. Considering that the deoxygenation active site has been shown in Chapters 2 and 3 to be related to a site involving Pt and potentially the contribution of reduced oxide species adjacent to Pt, dispersion is thus a good measure of the total number of active sites present for each catalyst. This is also true in regards to aromatic ring hydrogenation, which is known to occur over the well-coordinated sites of Pt, thus making dispersion a good metric for the active sites of hydrogenation as well. However, the dispersion value shown here cannot be taken as the true number of active Pt sites available under reaction conditions. The CO chemisorption experiments used to measure dispersion here were conducted at 50˚C and flushes of inert gas after an *in situ* reduction. While it is expected that the *in situ* reduction has formed a decorated catalyst state that is present under reaction conditions, there is a growing body of evidence building that these overlayers are dynamic and

mobile under a range of conditions[10,54,55]. However, CO chemisorption measurements cannot be conducted under these conditions due to the desorption of the probe CO species from sites at elevated temperatures. Indeed, there is a glaring lack of characterization techniques that enable the measurement of active site density under conditions identical to reaction. For the analysis here, however, it is implicitly assumed that although the exact number of sites that are available under reaction conditions will not be captured by CO chemisorption dispersion measurements made at 50˚C, the trends in site availability as a function of modifying oxide loading and modifying oxide identity will. This assumption is consistent with the results of Figure 4.4a-b, which show broad trends in reactivity that align with the dispersion measurements of Figure 4.5, though this is discussed in more detail below.

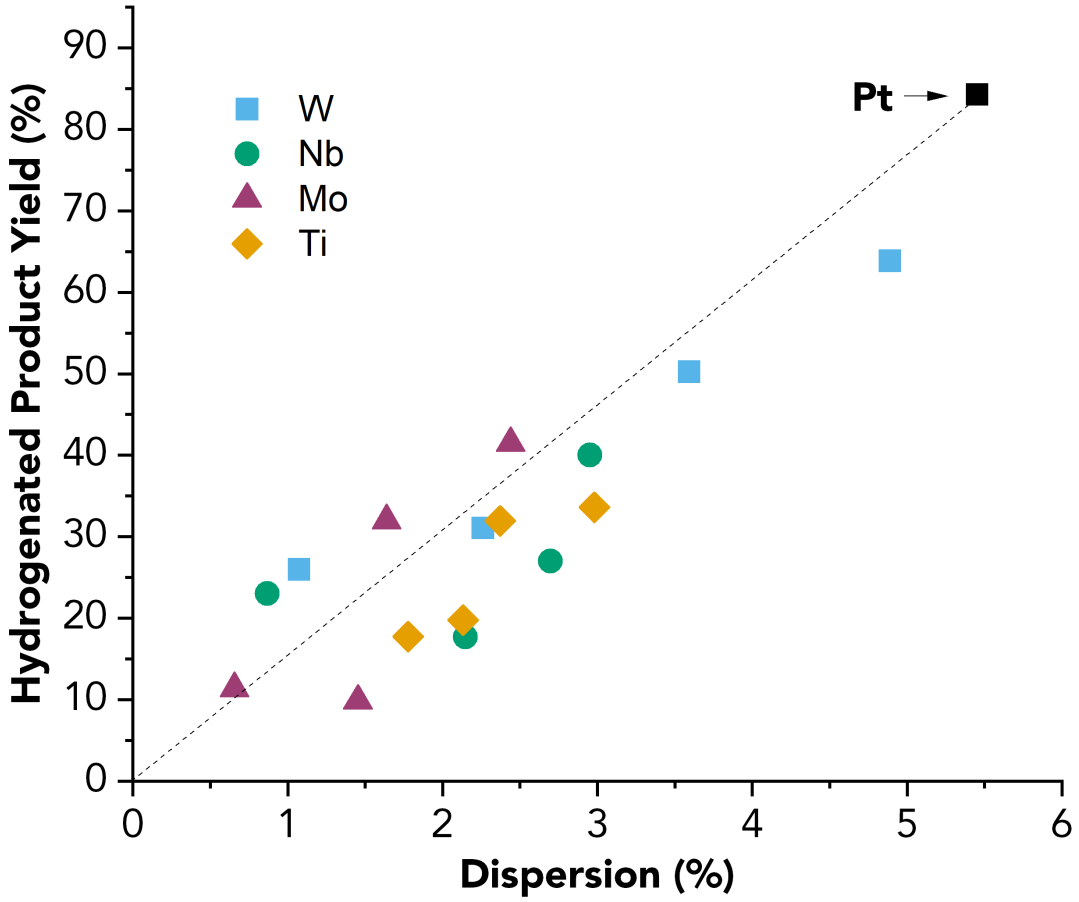

Figure 4.7: PHE HDO results towards hydrogenated products as originally shown in Figure 4.2a, re-plotted against the measured dispersion of Pt as measured by CO chemisorption instead of the global oxide:metal ratio during synthesis. The resulting trend clearly demonstrates that the reduction of hydrogenation activity is a physical phenomenon that depends solely on the extent of metal site decoration, rather than the chemical identity of the decorating species.

Figure 4.7 shows the overall hydrogenation activity of modified Pt/SiO_2 catalysts in the HDO of PHE, represented in terms of the dispersions measured by CO chemisorption instead of M:Pt ratio. Whereas Figure 4.4a showed a series of lines that were independent for each oxide, it can be seen that Figure 4.7 shows a monotonic trend consistent between different modifying oxides, as represented by the black dotted line. Importantly, a large fraction of the oxide-modified Pt/SiO_2 catalysts fall on the black line which relates the undecorated Pt/SiO_2 catalyst, which exhibits the highest dispersion and the highest hydrogenated product yield, to

the imaginary case of 0% dispersion, which would be expected to yield no hydrogenated products due to a lack of metal sites capable of hydrogenation.

The results of Figure 4.7 strongly support that the primary role of modifying oxides in the HDO of phenolic substrates, broadly, is to suppress aromatic hydrogenation, regardless of oxide identity. This relationship clearly demonstrates that the inhibitory effect of oxide decoration on metal nanoparticle surfaces is physical, rather than chemical, as the oxides utilized here demonstrate significantly different chemical properties to one another, and yet fall on the same general trend. Thus, it can be concluded that the results of Chapter 3, which identifies oxide decoration physically inhibiting the planar adsorption of phenolic species atop well-coordinated Pt sites leading to hydrogenation, is broadly applicable to a range of modifying oxides, so long as those oxides are capable of mobilizing to the metal nanoparticle surface.

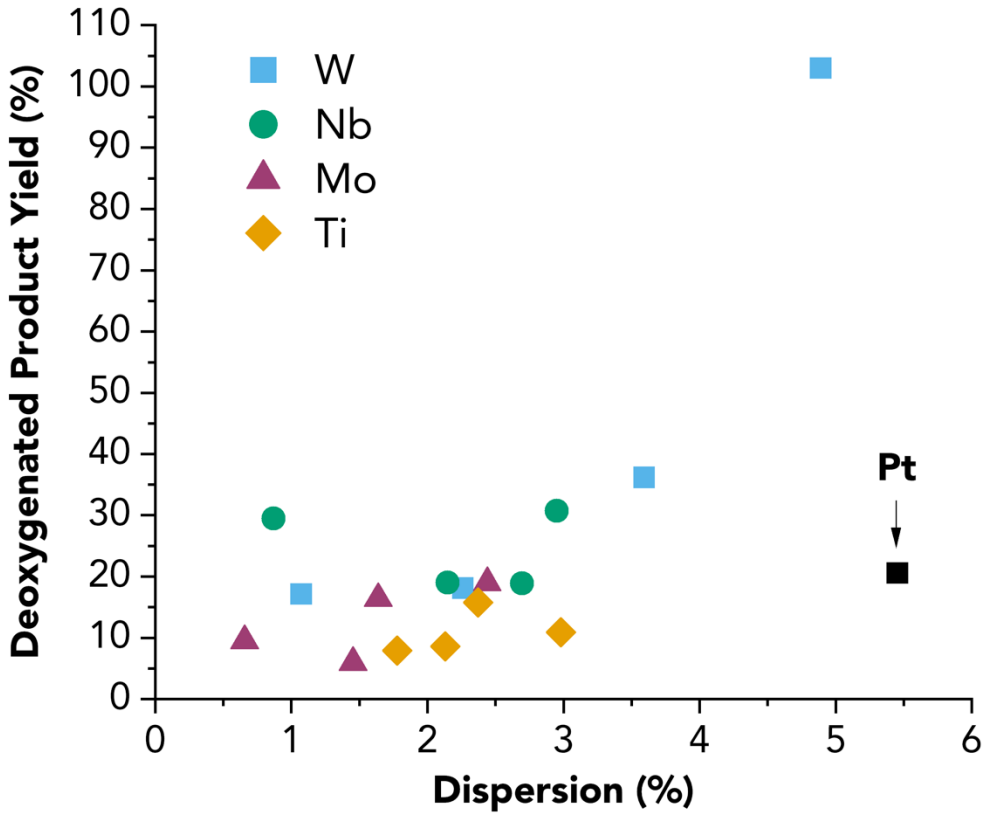

Figure 4.8: PHE HDO results as originally shown in Figure 4.2b, re-plotted against measured Pt dispersion as measured by CO chemisorption. The resulting plot shows no clear trend, counter to what was observed in Figure 4.4, suggesting that there is a chemical component to the total production of deoxygenated species.

The deoxygenation activity of modified Pt/SiO_2 catalysts can be represented in a similar manner, as shown in Figure 4.8. It is immediately clear that the overall deoxygenation activity of modified Pt catalysts during HDO does not follow the same trend as hydrogenation, indicating that there are likely distinct sites responsible for overall deoxygenation activity. A clue for the explanation behind this behavior lies in the relative positions of NbO_x and TiO_x modified catalysts as the highest deoxygenation yielding catalyst and lowest, respectively. NbO_x and TiO_x are the strongest and weakest acid catalysts studied here, respectively, with MoO_x and WO_x falling intermediate to these two materials. Thus, the lack of trend in assessing overall deoxygenation activity corresponds to the ability of strongly acidic catalysts, such as

NbO_x-modified Pt, to achieve deoxygenation through acid-catalyzed dehydration of OL to CYE, rather than direct deoxygenation, presumably through tautomerization, of PHE to BNZ as is the case over unmodified Pt catalysts. This behavior was also observed in the highest WO_x-loaded samples of $WO_x/Pt/SiO_2$ catalysts in the HDO of DHE discussed in Chapter 3, which presumably exhibited the highest acidities due to the buildup of WO_x on the SiO_2 support.

Similarly, the behavior shown in Figure 4.8 is partly assigned to the dehydration of OL to CYE through oxide domains present on the SiO_2 support rather than the Pt surface. While it is known that reduced oxide species on the surface of metal nanoparticles exhibit Brønsted acid sites under H_2 atmosphere, it is expected that the sites on the catalyst surface far outnumber those on the metal surface. For instance, a back-of-the-envelope estimate for how much of each oxide remains on the surface of the catalyst under reaction conditions can be conducted. Assuming an accurate nominal loading of Pt and modifying oxide species, which is reasonable for the case of CPA-synthesized catalysts as discussed above, the modifying oxide is present in a nearly 20-fold excess relative to surface Pt sites, even if all sites were decorated which is not the case, as discussed above. Thus, the catalyst at the highest weight loading of modifying oxide might be considered a convolution of both decorated Pt catalysts and supported oxide catalysts, capable of conducting its own reactivity depending on the oxide identity. In the absence of Pt, the activity of these supported oxides is relatively low as has been shown in the literature[1] because of the inactivity of phenolic species to Brønsted acid sites without prior hydrogenation and the difficulty oxidic domains have in directly activating H_2 without Pt promotion[56]. However, in the presence of Pt, which may both spillover H or

hydrogenate phenolics directly to species reactive to Brønsted acids, these surface-bound sites cannot be ignored.

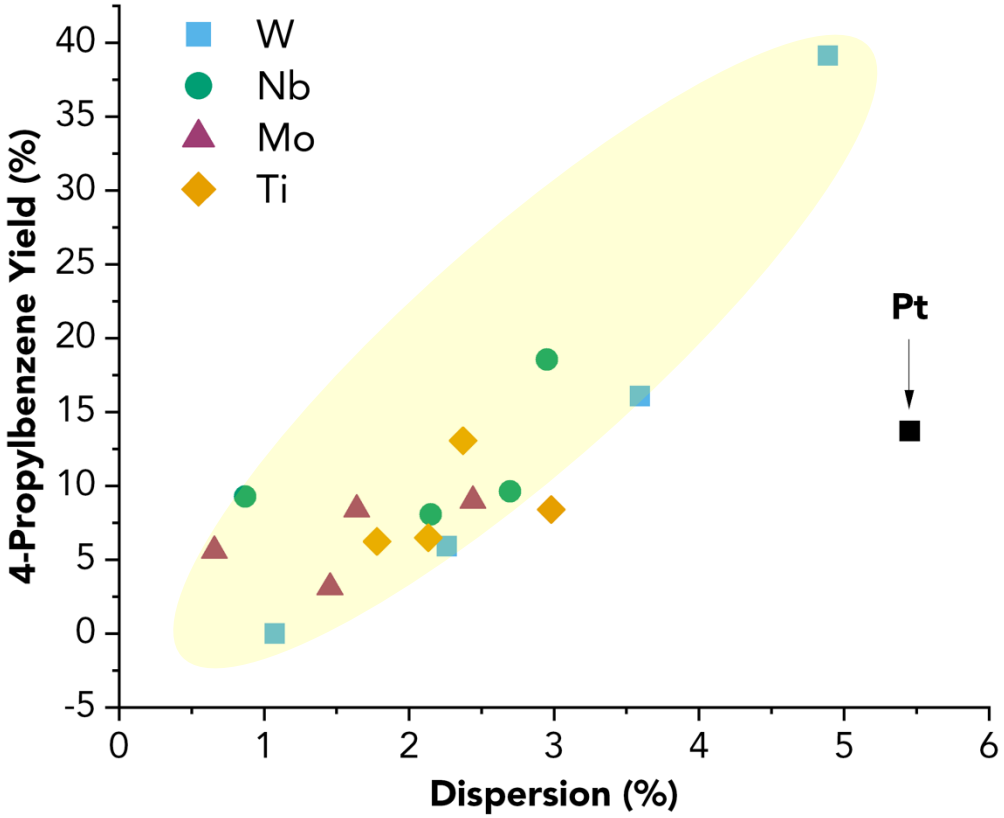

Figure 4.9: PHE HDO results over modified and unmodified Pt catalysts shown only as the yield of BNZ, considered the product most of interest for direct deoxygenation pathways which occur over oxide-decorated metal sites. A trend arises which demonstrates a moderate impact of chemical identity on BNZ yield, but an overall dependence on the extent of decoration of metal sites, pointing to the importance of Pt sites in the production of BNZ from PHE.

This also likely explains the non-linearity of deoxygenation yield when plotted in terms of dispersion as shown in Figure 4.8. The relative contribution of acid-catalyzed OL dehydration to CYE is a convolution of available acid site density, which increases with modifying oxide loading, and the concentration of OL, which presumably decreases with modifying oxide loading due to the loss of sites responsible for PHE hydrogenation to OL. This relationship is unsurprisingly complex and non-linear, explaining the confusing trends shown in Figure 4.8.

Instead of representing deoxygenation activity as a combination of all deoxygenated products, deoxygenation activity correlated to the active Pt site can be tracked solely by BNZ yield, as BNZ is assumed to form solely from direct deoxygenation of PHE over Pt sites, whether in the absence or presence of a modifying oxide. While the possibility for dehydrogenation was discussed in Chapter 2, it is reasonable to believe that neither CYE nor CYC will dehydrogenate to form BNZ here, thus minimizing their contribution to the BNZ yield. For one, dehydrogenation was observed in that case over the 0.4-Pt catalyst, exhibiting small Pt nanoparticles under 2 nm with an abundance of under-coordinated sites. Dehydrogenation reactions are known to be structure-sensitive, occurring preferentially over these under-coordinated sites. The industrial catalyst for dehydrogenation is typically Pt/Al_2O_3 exhibiting average Pt particle sizes near 1 nm in size. The catalysts used here are substantially larger, exhibiting primarily well-coordinated sites, thus dehydrogenation might be expected to be kinetically limited. In this work, as in Chapter 3, a higher H_2 pressure of 20 bar was chosen to facilitate the reduction of modifying oxides and ensure decoration took place analogous to characterization performed in the vapor phase. This results in a substantially higher availability of H_2 and an equilibrium position favoring hydrogenation rather than dehydrogenation from the perspective of thermodynamics as well. Thus, BNZ is an effective species to track for direct deoxygenation of PHE here.

Figure 4.9 shows the contrasting case to Figure 4.8, where a clearer trend has appeared as highlighted by the yellow area. Though not a perfectly linear trend, it appears that the yield of BNZ increases with increasing dispersion or increasing availability of metal sites. This is consistent with the picture that the metallic Pt site is intrinsic to the ability of modified Pt catalysts to perform direct HDO to aromatics in high yield. However, the resolution capable

here using PHE HDO as the probe reaction is different than that concluded in Chapter 3, where HDO of DHE suggested that there was no trend of deoxygenation with Pt site availability. This is primarily due to the dominant product in HDO of DHE being 4-propyl-2-methoxycyclohexanol (HYD), with fewer secondary deoxygenation products able to be discerned. It is also possible that HDO of DHE resulted in the production of PHE, which forms stoichiometric quantities of methoxy fragments on the catalyst surface that may otherwise detract from the analysis. In using PHE as the substrate here, reactivity is focused on the fundamentally more interesting dehydroxylation step in the absence of potential complications arising from methoxy fragments.

4.3 Discussion

There is similarity between the BNZ formation yields of modified Pt catalysts and the structure sensitivity discussed in Chapter 2, where BNZ formation trends with the number of well-coordinated sites that are available for reaction. Once again, as was seen in some form in Chapter 2 using $WO_x/Pt/SiO_2$ catalysts for DHE HDO, unmodified Pt exhibits notable BNZ formation activity by itself, with most of the catalysts falling under this performance. This is again consistent with the proposal that Pt facilitates the reactivity necessary for deoxygenation, whether in the presence of a modifying oxide or not. Additionally, the role of Pt in facilitating deoxygenation can be seen in the general positive correlation between the accessibility of Pt sites (dispersion) in oxide-modified catalysts and BNZ yield, indicating that these Pt sites are essential for the deoxygenation step.

This is reminiscent of the data shown in Chapter 2 of this thesis, where BNZ yield was maximized when specifically well-coordinated sites were exposed for the largest Pt

nanoparticles, which was assigned to the structure-sensitivity of a tautomerization pathway. In a similar fashion, these results suggest that minimally decorated surfaces are the ideal catalysts for deoxygenation, presumably exposing a balance of well-coordinated Pt sites and metal-oxide interfaces. Thus, it follows that the mechanism of deoxygenation for oxide-modified Pt catalysts in HDO may very well be through a tautomerization pathway analogous to the unmodified Pt catalysts discussed in Chapter 2. Such similarity in deoxygenation pathway would be entirely consistent with the seemingly similar reactivity of both unmodified and oxide-modified Pt catalysts reported both here and in the literature, where enhancement of HDO rates are relatively modest as discussed previously. While this has always pointed towards a shared mechanistic pathway, these results clarify that this shared pathway is likely tautomerization to the active keto-enol tautomer which may then undergo dehydration to yield BNZ over well-coordinated Pt sites[34,57].

Does this mean that the oxide modifiers play only a spectatorial role in deoxygenation

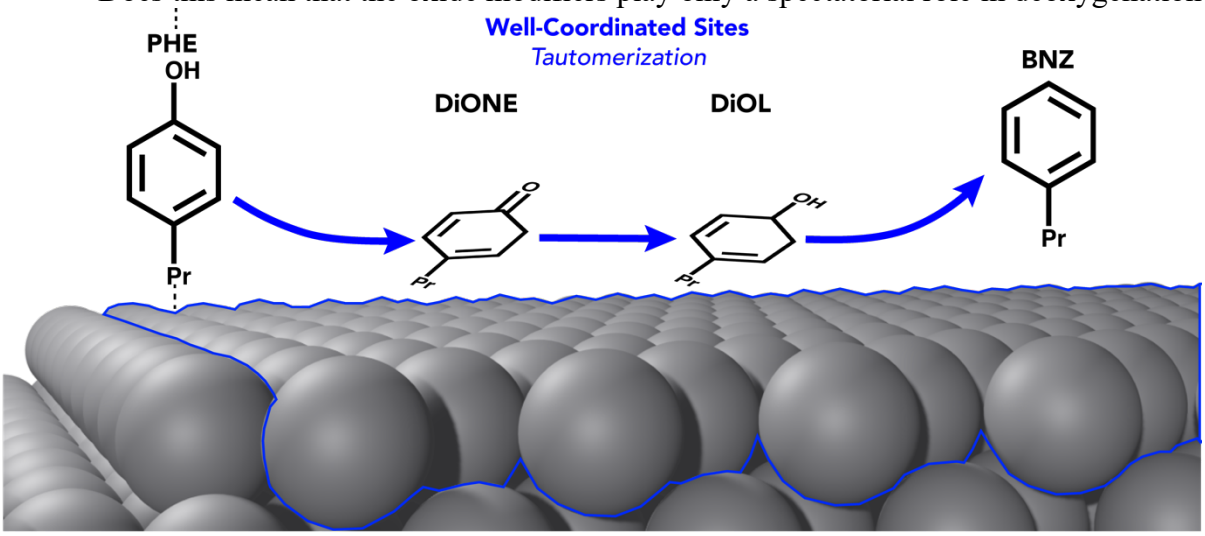

Scheme 4.1: Summary of proposed tautomerization mechanism for both unmodified and oxide-modified Pt/SiO_2 catalysts on the basis of the results above. PHE deoxygenation proceeds through tautomerization over WC sites, rationalizing the decreased BNZ yield with increasing oxide decoration shown in Figure 4.9.

during HDO of phenolics? As was discussed in the motivation for this work, the oxide utilized in this chapter exhibit acidities and reducibilities that differ vastly. Considering this, the

identity of the oxide appears to play a minimal role in the overall trend observed in Figure 4.9 showing BNZ yields, indicating that neither acidity nor reducibility play a very direct role in the HDO mechanism, again supporting that some other mechanism, namely tautomerization, is the kinetically-relevant step for deoxygenation. However, there are some weak trends within BNZ productivity that are worth discussing and may point to some chemical influence for deoxygenation. For instance, NbO_x-modified catalysts represent the highest BNZ yields of all the catalysts at comparable metal coverages. On the other hand, TiO_x-modified catalysts fall on the lower end of BNZ performance, almost perfectly in line between unmodified Pt and the origin. However, MoO_x and WO_x both fall intermediate between these two bounds for intermediate dispersions, whereas the 0.5W6Pt catalyst exhibits the highest BNZ yields overall, though there are no other comparable oxides at this specific oxide coverage. Overall, it appears from a first pass that neither acidity nor reducibility can describe the small trends in BNZ yield for oxide-modified catalysts.

To gain a further understanding of the BNZ yields for each catalyst, the BNZ rate enhancement relative to Pt on a per-site basis can be calculated, as shown in Figure 4.10. In this representation, it can be seen that there are overall BNZ rate enhancements for all of the oxides per-site, indicative of the fact that there is a promotional effect of oxide modifiers on the HDO activity of Pt catalysts. Interestingly, there are non-monotonic trends in rate enhancement for each oxide modifier that cannot be immediately explained by this work. WO_x-modified catalysts exhibit rate enhancements that decline with increasing WO_x loading, indicating that a minimally-decorated Pt surface by WO_x exhibits the highest activity towards deoxygenation. On the other hand, TiO_x-modified catalysts show monotonically increasing BNZ rate enhancements with increasing TiO_x. It is likely that these differences find some basis

in the distinct structural arrangements that each oxide assumes under reaction conditions, influenced by the different oxidation states and crystalline structures that each oxide might assume on the surface of the Pt nanoparticles. Based on the suppression of hydrogenation activity shown in Figure 4.7, despite these atomic-scale structural differences, the strong, linear trend across all oxides between hydrogenation suppression and dispersion is good evidence that decoration still occurs preferentially on well-coordinated Pt sites, analogous to the work shown for WO_x in Chapter 3.

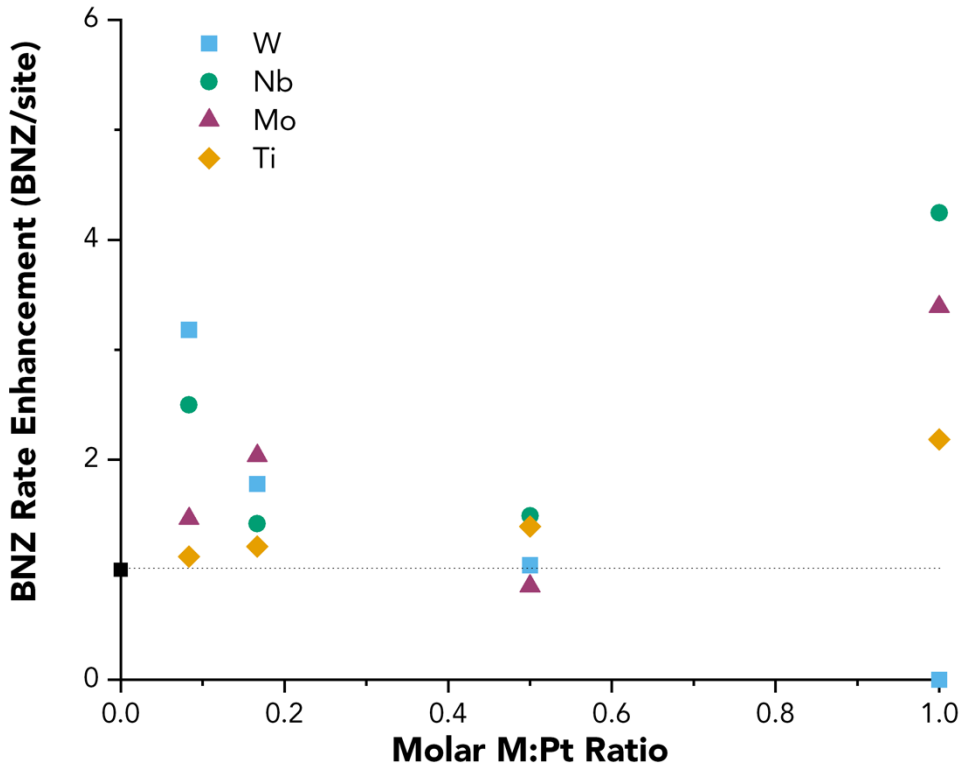

Figure 4.10: Rate enhancement of BNZ formation normalized by BNZ formation over Pt on a per-site basis. Results show that oxide-modified Pt catalysts exhibit enhanced BNZ formation on a per-site basis, though the extent of enhancement changes with M:Pt ratio.

Considering that the totality of these results indicate that oxide-modified catalysts exhibit some oxide-specific promotion to the tautomerization mechanism, the question remains as to the precise mechanistic step that the oxide-on-metal structure might feasibly promote.

Considering again the tautomerization mechanism proposed previously in Chapter 2, deoxygenation of PHE is proposed to proceed through Pt-facilitated tautomerization of PHE to DiONE, a cyclohexadieneone intermediate, followed by hydrogenation to an unstable DiOL product which is facilely dehydrated to BNZ. Considering that it has already been established that no clear trend exists with regard to acidity, oxide-promotion of the dehydration of DiOL can be ruled out as to the mechanistic step of interest for oxide-modified catalysts. However, oxide-modified catalysts may potentially interact with the DiONE intermediate stabilized by the Pt surface, enabling more facile hydrogenation to form the unstable DiOL which is assumed to be a short-lived intermediate on the surface.

The interaction of oxide-decorated metal catalysts with carbonyl-containing substrates such as the DiONE intermediate has fundamental interest in previous literature stemming from the rate enhancements observed for SMSI-state catalysts for both CO and CO_2 hydrogenation. Whereas the SMSI state, or oxide-decorated state, is typically associated with the suppression of reactivity due to the coverage of the active metal sites by oxide domains, both CO and CO_2 hydrogenation proceed more rapidly over these catalysts. The enhancement of reactivity in this case has been assigned to the interaction of CO bound to the metal surface, the kinetically relevant intermediate for both CO and CO_2 hydrogenation after initial O removal in the latter case, with unsaturated oxide cations present on the surface exhibiting Lewis acidity[63]. These unsaturated cations were proposed to accept electrons from the O of CO, removing electron density from the C-O sigma bond and thus weakening it, facilitating the addition of H to the C atom of CO. Importantly, it was shown that there was a linear relationship between the enhancement of both CO and CO2 hydrogenation rate with the Lewis acidities of the oxide modifiers, as measured by electronegativity of the cations (reproduced in Figure 4.11a below).

While there is no direct analogy between this mechanistic enhancement of CO hydrogenation and PHE HDO, there is a direct chemical analogy once PHE tautomerizes on the Pt surface to the DiONE intermediate. This DiONE intermediate, exhibiting a C=O functionality which is chemically similar to the C-O bonds of CO adsorbed to the surface, may presumably electronically interact with oxide modifiers on the Pt surface. To explore whether the oxide-interaction present in PHE HDO for oxide-modified Pt catalysts exhibited similar behavior, the maximum per-site rate enhancement of BNZ formation in PHE HDO was plotted against the likely electronegativities of the reducible oxide modifiers under PHE HDO reaction conditions. Electronegativities were calculated through the relationship:

$$\chi_i = (1 + 2Z)\chi_0$$

Where χ_i is the effective electronegativity of the metal cation, Z is the oxidation state of the metal cation in the reducible oxide under reaction conditions, and χ_0 is the electronegativity of the elemental metal on the Pauling scale. Since the direct measurement of oxide-modifier oxidation state was outside of the scope of this dissertation, complicated by the presence of oxide domains on both the metal surface (presumably reduced) and the support (presumably fully oxidized), reasonable assumptions were made regarding the likely state of the metal cation. NbO_x was shown to be essentially irreducible in the H_2-TPR's shown in Figure 4.1, and thus was assumed to decorate the Pt surface in the Nb^{5+} state. TiO_x, which was moderately reducible, has been shown to decorate Pt surfaces in the Ti^{3+} state. For both MoO_x and WO_x catalysts, which were shown to be significantly reducible in the H_2-TPR profiles shown in Figure 4.1, the oxidation state was assumed to be 4+. This is also consistent with

DFT results from Chapter 3 investigating WO_x-modified Pt catalysts, wherein the DFT-relaxed structures were found to exhibit oxidation states between WO_2 and WO_3, or 4+ and 6+.

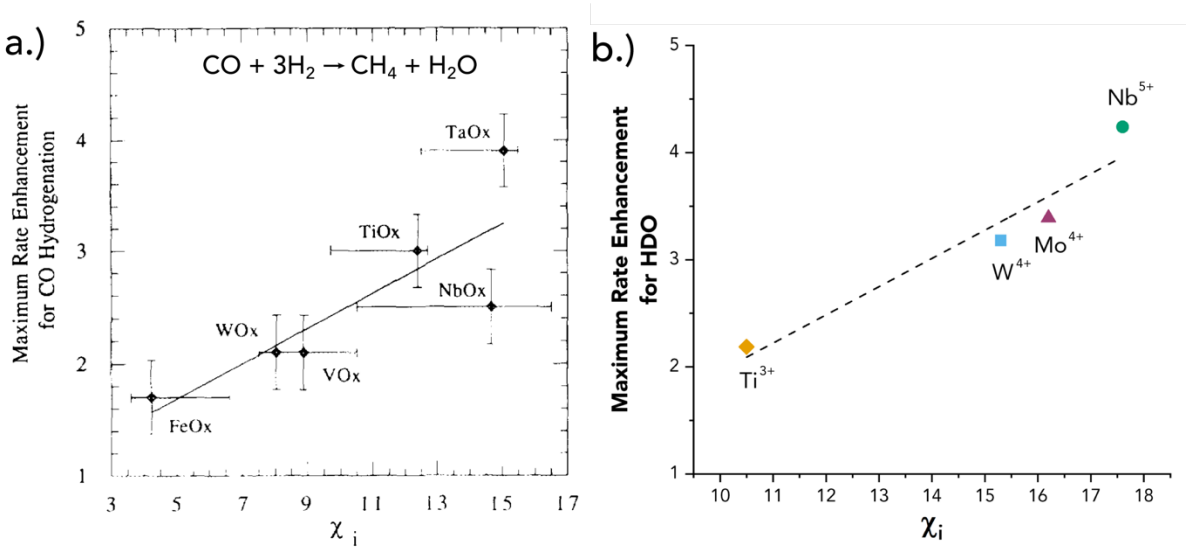

Figure 4.11: Rate enhancement of oxide-modified catalysts for carbonyl hydrogenation. a.) Enhancement of various oxide-modified Rh(111) surfaces in CO hydrogenation under UHV conditions, showing a linear correlation between maximum rate enhancement and electronegativity. Reproduced from Ref. 63. b.) Enhancement of BNZ activity on a per-site basis for oxide-modified Pt catalysts in PHE HDO as described in this chapter. Linear correlation between enhancement and electronegativity suggests a similar electronic interaction describes PHE HDO enhancement by reducible oxides as was suggested for CO hydrogenation.

Representing the per-site BNZ enhancements against these χ_i values in Figure 4.11b shows that there is a linear relationship between BNZ enhancement and electronegativity. The trend, which is notably similar to that reported for oxide-modified Rh surfaces for CO and CO2 hydrogenation, suggests that the HDO of phenolics is facilitated by surface tautomerization of PHE followed by interaction with the metal cations of oxide modifiers present at the metal-oxide interface. This interaction in turn weakens the C-O bond of the DiONE tautomer intermediate to a degree consistent with the electronegativity of the metal cation at the metal-oxide interface. Subsequent H addition steps lead to the cleavage of the C-O bond of tautomerized intermediate, forming the desired BNZ product directly. This direct formation of BNZ is consistent with the reports in the literature which proposed that BNZ forms directly

from PHE with no detectable intermediates, contrasting the sequential hydrogenation-dehydration-dehydrogenation pathway that was originally reported for oxide-modified catalysts.

4.4 Conclusions

The results in this Chapter expand the behavior observed in Chapters 2 and 3 to a number of other reducible transition metal oxides. Through the use of a conserved Pt/SiO_2 base catalyst, the contribution of the metal nanoparticles to HDO reactivity was kept constant across the different catalyst series, enabling the development of shared relationships based on catalyst descriptors such as dispersion and oxide identity. The result is a rationalization of the paradox present in the literature for inverse catalysts in HDO, wherein oxide-modified catalysts were shown to exhibit only moderate changes to activity and stability despite large changes in selectivity. The reasoning for this has been clarified as a shared mechanism between modified and unmodified catalysts for the deoxygenation of phenolic species, transiting through a surface-stabilized tautomerization pathway. The enhancement of tautomerization-facilitated deoxygenation trends linearly with the electronegativity or Lewis acidity of the metal oxide cation, suggesting that direct interaction of the tautomerized intermediate with the oxide component is responsible for facilitated deoxygenation. Thus, reducible oxide modifiers on Pt/SiO_2 catalysts are shown to play a complimentary role in HDO reactivity, both inhibiting undesired hydrogenation activity and promoting deoxygenation activity.

4.4 Methods

4.4.1 Catalyst Synthesis

Synthesis of a bulk Pt/SiO_2 catalyst was carried out using aqueous impregnation of a silica support with chloroplatinic acid. Briefly, 5 grams of 15-20 nm nonporous, spherical SiO_2 (USNano) was added to 20 mL of deionized H_2O (Sigma) under vigorous stirring. To this, 5 mL of a chloroplatinic acid (H_2PtCl_6, Sigma) solution with the appropriate amount of Pt to reach a final weight loading of 6% was added. The solution was left to stir for another 30 minutes before increasing the temperature to 80˚C and allowing the water to evaporate. The obtained powder was then dried in an oven overnight at 110˚C. A final catalyst was obtained by reducing the dried powder in 10% H_2/Ar at 650˚C for 6 hours.

Oxide-modified catalysts were synthesized by aqueous impregnation of the base 6% Pt/SiO_2 catalyst obtained in the steps above with soluble metal oxide precursors. For WO_x-modified catalysts, an appropriate amount of ammonium metatungstate hydrate (Sigma) was dissolved in 10 mL of water under vigorous stirring. To this, the desired amount of 6% Pt/SiO_2 catalyst was added and left to stir for 30 minutes. After this period, the temperature was increased to 80˚C and the water was evaporated. The obtained catalyst was dried overnight in an oven at 110˚C before being calcined in flowing air at 350˚C for 3 hours. An identical procedure was followed for all oxide-modified catalysts by substituting in the appropriate metal oxide precursor. For MoO_x-modified catalysts, ammonium heptamolybdate (Sigma) was used. For TiO_x-modified catalysts, potassium titanium oxide oxalate (Sigma) was used. Finally, for NbO_x-modified catalysts, ammonium niobate oxalate hydrate (Sigma) was used.

4.4.2 Catalyst characterization

Dispersion measurements were made using pulsed CO chemisorption on an Autochem 2920 II instrument. The outlet gas composition was measured using a thermal conductivity detector (TCD). In a typical measurement, 30 mg of catalyst was placed in a quartz U-tube between two packed regions of quartz wool. The catalyst was then reduced under 50 sccm of 10% H_2/Ar (Airgas) at 325˚C for 1 hour before cooling to 50˚C. Once at 50˚C, the sample was purged with 50 sccm UHP Ar (Airgas) and held until the baseline was measured to be stable by the TCD. At this point, 10 pulses of 10% CO/Ar were conducted at 3.5-minute intervals. The uptake of CO to the catalyst surface was measured by subtracting each peak area from the maximum peak area, indicating the quantity of CO adsorbed to the catalyst surface which did not pass over the TCD. A CO:Pt ratio of 1 was assumed.

H_2-TPR measurements were also taken on the Autochem 2920 II using the same sample preparation in the U-tube. For these measurements, catalysts were pretreated at 300˚C for 1 hour in UHP O_2 (Airgas) and purged in Ar while cooling from 300˚C to 50˚C. Once at 50˚C, gas flow was changed to 10% H_2/Ar and passed through a drying tube containing a combination of zeolite and 3A molecular sieves to trap any moisture that formed during reduction. Once the signal measured by the TCD was stabilized at 50˚C under 10% H_2/Ar, the samples were ramped to 900˚C at 10˚C/min under H_2/Ar.

HAADF-STEM images of the 6Pt catalyst were taken on a Thermo Fisher Spectra F200X aberration-corrected transmission electron microscope in the scanning mode (STEM) using a high-angle annular dark field (HAADF) detector. Images were collected at an accelerating voltage of 200 kV. Samples were prepared by dipping 300 mesh Cu grids coated with lacey carbon into the loose powder a number of times. After approximately 5 dips of the

grids into the loose powder, the grids were shaken to remove any macroscopic particles that had become stuck to the grid.

CO DRIFTS measurements were carried out on either a Nicolet iS10 or Nicolet iS50R FT-IR spectrometer equipped with a Praying Mantis Diffuse Reflection Accessory (Harrick Scientific) and a High-Temperature Reaction Chamber (Harrick Scientific) fitted with a thermocouple in the catalyst bed. Ar (99.995%), He (99.995%), O_2 (99.50%), 10% CO/Ar, and 10% H_2/Ar were purchased from Airgas and used as received. In a typical DRIFTS experiment, catalyst was loaded into the Harrick cell and pre-treated under a desired gas environment and temperature. Temperature set points were reached by ramping the catalyst at 10˚C/min in all experiments, except for cooling after pre-treatment steps which was allowed to happen passively. Gas flow rates across the catalyst bed in all cases were 50 sccm controlled by mass flow controllers (Teledyne Hastings). For CO DRIFTS experiments, catalysts were cooled to 30˚C prior to exposure to 10% CO/Ar. CO exposure was continued until saturation coverage of CO on the metal sites was achieved, determined by unchanging peak intensity in DRIFTS spectra. After metal surfaces were saturated by CO, gas flow was switched to Ar to remove CO from the gas atmosphere.

4.4.3 HDO Reactions

HDO reactions using the prepared catalysts were performed in 75-mL stainless-steel pressure reactors (Parr Instrument Co., 5000 Series). In a typical reaction, catalyst was loaded into the reactor along with 20 mL of a prepared stock solution. The stock solution consisted of 10.7335 g of 4-propylphenol (TCI Chemicals) and 5.16 g of *n*-decane (Sigma) dissolved in 430 mL of cyclohexane (Sigma). Catalyst loading was kept constant between catalysts for

constant Pt mass. Reactions were stirred magnetically at 700 rpm using glass-shielded stir bars. Once loaded, the reactor was sealed and purged 3 times with 5.0 grade H_2 (Airgas) before pressurizing to a final gauge pressure of 20 bar at room temperature. Then, the vessel was heated to 275 ˚C and held for 2 hours. After the allotted reaction time, the reactor vessel was quickly removed and quenched using a water bath. Once cooled to room temperature, the liquid products were collected by centrifugation and analyzed by a gas chromatogram equipped with a flame ionization detector (GC-FID, Agilent). Product identification was carried out using commercially-sourced standards where possible (4-propylbenzene (BNZ), 4-propylphenol (PHE), 4-propylcyclohexanol (OL), 4-propylcyclohexane (CYC)). In instances where standards are not commercially available (4-propylcyclohex-1-ene (CYE)), FID responses were estimated using effective carbon number (ECN)[95]. Reaction performance metrics were defined as:

$$Conversion\ (\%) = \frac{N_{DHE}}{N_{DHE}^0}$$

$$Selectivity\ (\%) = \frac{N_{Product}}{\sum N_{Product}}$$

$$Yield\ (\%) = Conversion * Selectivity = \frac{N_{Product}}{\sum N_{Product}} * \frac{N_{DHE}}{N_{DHE}^0}$$

where N_i is the moles of species *i* measured by GC-FID and N_i^0 is the initial moles of *i* loaded into the batch reactor.

4.5 References

1. Wang, C. *et al.* Mechanistic Study of the Direct Hydrodeoxygenation of m -Cresol over WOx-Decorated Pt/C Catalysts. *ACS Catal* **8**, 7749–7759 (2018).

2. Wang, C. *et al.* Hydrodeoxygenation of m-Cresol Over Pt-WOx/C Using H2 Generated In Situ by n-Hexane Dehydrogenation. *Catal Letters* **150**, 913–921 (2020).
3. Zhou, J. *et al.* The role of the metal core in the performance of WOx inverse catalysts. *Chem Catalysis* **3**, 1–17 (2023).
4. Shi, G. *et al.* Effect of WOx Doping into Pt/SiO2 Catalysts for Glycerol Hydrogenolysis to 1,3-Propanediol in Liquid Phase. *Catal Letters* **148**, 2304–2314 (2018).
5. Robinson, A. *et al.* Enhanced Hydrodeoxygenation of m-Cresol over Bimetallic Pt-Mo Catalysts through an Oxophilic Metal-Induced Tautomerization Pathway. *ACS Catal* **6**, 4356–4368 (2016).
6. Ballesteros-Plata, D., Infantes-Molina, A. & Rodríguez-Castellón, E. Study of bifunctionality of Pt/SBA-15 catalysts for HDO of Dibenzofuran reaction: Addition of Mo or use of an acidic support. *APPLIED CATALYSIS A-GENERAL* **580**, 93–101 (2019).
7. Ballesteros-Plata, D. *et al.* Incorporation of molybdenum into Pd and Pt catalysts supported on commercial silica for hydrodeoxygenation reaction of dibenzofuran. *APPLIED CATALYSIS A-GENERAL* **547**, 86–95 (2017).
8. Lai, Q. H., Zhang, C. & Holles, J. H. Mo@Pt overlayers as efficient catalysts for hydrodeoxygenation of guaiacol and anisole. *Catal Sci Technol* **7**, 3220–3233 (2017).
9. Ballesteros-Plata, D. *et al.* Zirconium Phosphate Heterostructures as Catalyst Support in Hydrodeoxygenation Reactions. *CATALYSTS* **7**, (2017).
10. Huang, R., Kwon, O., Lin, C. & Gorte, R. J. The effects of SMSI on m-Cresol hydrodeoxygenation over Pt/Nb2O5 and Pt/TiO2. *J Catal* **398**, 102–108 (2021).
11. Mäkelä, E. *et al.* Liquid-phase Hydrodeoxygenation of 4-Propylphenol to Propylbenzene: Reducible Supports for Pt Catalysts. *ChemCatChem* **12**, 4090–4104 (2020).
12. Chen, T. & Vohs, J. M. Direct Hydrodeoxygenation of m-Cresol to Toluene over Bifunctional NbOx-Pt. *Journal of Physical Chemistry C* **124**, 14253–14261 (2020).
13. Wu, X., Liu, C. jun, Wang, H., Ge, Q. & Zhu, X. Origin of strong metal-support interactions between Pt and anatase TiO2 facets for hydrodeoxygenation of m-cresol on Pt/TiO2 catalysts. *J Catal* **418**, 203–215 (2023).
14. He, Z., Hu, M. C. & Wang, X. Q. Highly effective hydrodeoxygenation of guaiacol on Pt/TiO_2: Promoter effects. *Catal Today* **302**, 136–145 (2018).
15. Zhao, X. Y. *et al.* Effect of Strong Metal-Support Interaction of Pt/TiO_2 on Hydrodeoxygenation of m-Cresol. *ChemistrySelect* **3**, 10364–10370 (2018).
16. Lin, Z. *et al.* Mechanistic Understanding of Ring-Opening of Tetrahydrofurfuryl Alcohol over WOx-Modified Pt Model Surfaces and Powder Catalysts. *ACS Catal* **13**, 8014–8024 (2023).
17. Lin, Z. *et al.* Experimental and Theoretical Insights into the Active Sites on WO x/Pt(111) Surfaces for Dehydrogenation and Dehydration Reactions. *ACS Catal* **11**, 8023–8032 (2021).
18. Wang, C. *et al.* A Study of Tetrahydrofurfuryl Alcohol to 1,5-Pentanediol Over Pt-WO_x/C. *Catal Letters* **148**, 1047–1054 (2018).
19. Liu, L. J. *et al.* Hydrodeoxygenation of C4-C6 sugar alcohols to diols or mono-alcohols with the retention of the carbon chain over a silica-supported tungsten oxide-modified platinum catalyst. *GREEN CHEMISTRY* **23**, 5665–5679 (2021).
20. Stephens, K. J. *et al.* A Mechanistic Study of Polyol Hydrodeoxygenation over a Bifunctional Pt-WOx/TiO2Catalyst. *ACS Catal* **10**, 12996–13007 (2020).

21. Cheng, S. Q. *et al.* Defect-rich BN-supported Cu with superior dispersion for ethanol conversion to aldehyde and hydrogen. *CHINESE JOURNAL OF CATALYSIS* **43**, 1092–1100 (2022).
22. Samsonov, V. M., Talyzin, I. V, Puitov, V. V & Vasilyev, S. A. TO THE PROBLEM OF APPLICABILITY OF THE TAMMAN TEMPERATURE CONCEPT TO NANOSIZED OBJECTS: TO THE 160TH ANNIVERSARY OF GUSTAV TAMMAN. *PHYSICAL AND CHEMICAL ASPECTS OF THE STUDY OF CLUSTERS NANOSTRUCTURES AND NANOMATERIALS* 503–512 (2021) doi:10.26456/pcascnn/2021.13.503.
23. Bonvicini, S. N., Fu, B., Fulton, A. J., Jia, Z. T. & Shi, Y. J. Formation of Au, Pt, and bimetallic Au-Pt nanostructures from thermal dewetting of single-layer or bilayer thin films. *Nanotechnology* **33**, (2022).
24. Teles, C. A., Duong, N., Rabelo-Neto, R. C., Resasco, D. & Noronha, F. B. Evidence of dependence between the deoxygenation activity and metal-support interface. *Catal Sci Technol* **12**, 5961–5969 (2022).
25. Deo, S., Medlin, W., Nikolla, E. & Janik, M. J. Reaction paths for hydrodeoxygenation of furfuryl alcohol at TiO_2/Pd interfaces. *J Catal* **377**, 28–40 (2019).
26. Teles, C. A. *et al.* Role of the metal-support interface in the hydrodeoxygenation reaction of phenol. *APPLIED CATALYSIS B-ENVIRONMENTAL* **277**, (2020).
27. Yang, F. *et al.* Elucidating the Structure of Bimetallic NiW/SiO2 Catalysts and Its Consequences on Selective Deoxygenation of m-Cresol to Toluene. *ACS Catal* **11**, 2935–2948 (2021).
28. Hočevar, B., Grilc, M. & Likozar, B. Aqueous dehydration, hydrogenation, and hydrodeoxygenation reactions of bio-based mucic acid over ni, nimo, pt, rh, and ru on neutral or acidic catalyst supports. *Catalysts* **9**, (2019).
29. Zhao, C., Song, W. & Lercher, J. A. Aqueous phase hydroalkylation and hydrodeoxygenation of phenol by dual functional catalysts comprised of Pd/C and H/La-BEA. *ACS Catal* **2**, 2714–2723 (2012).
30. Zhao, C., He, J., Lemonidou, A. A., Li, X. & Lercher, J. A. Aqueous-phase hydrodeoxygenation of bio-derived phenols to cycloalkanes. *J Catal* **280**, 8–16 (2011).
31. Nelson, R. C. *et al.* Experimental and Theoretical Insights into the Hydrogen-Efficient Direct Hydrodeoxygenation Mechanism of Phenol over Ru/TiO2. *ACS Catal* **5**, 6509–6523 (2015).
32. Bui, V. N., Laurenti, D., Afanasiev, P. & Geantet, C. Hydrodeoxygenation of guaiacol with CoMo catalysts. Part I: Promoting effect of cobalt on HDO selectivity and activity. *Appl Catal B* **101**, 239–245 (2011).
33. Wang, S. *et al.* Hydrodeoxygenation of anisole to benzene over an Fe2P catalyst by a direct deoxygenation pathway. *Catal Sci Technol* **10**, 3015–3023 (2020).
34. Nie, L. & Resasco, D. E. Kinetics and mechanism of m-cresol hydrodeoxygenation on a Pt/SiO 2 catalyst. *J Catal* **317**, 22–29 (2014).
35. Li, H. *et al.* Hydrothermal synthesis and acidity characterization of TiO2 polymorphs. *Mater Res Bull* **48**, 3374–3382 (2013).
36. Meng, F. C. *et al.* Tailoring the Brønsted acidity of Ti-OH species by regulating Pt-TiO_2 interaction. *ChemSusChem* **17**, (2024).
37. Fu, J. *et al.* Modulating the dynamics of Brønsted acid sites on PtWOx inverse catalyst. *Nat Catal* **5**, 144–153 (2022).

38. Wu, Y. *et al.* Dynamic Formation of Brønsted Acid Sites over Supported WOx/Pt on SiO2 Inverse Catalysts─Spectroscopy, Probe Chemistry, and Calculations. *ACS Catal* **13**, 7371–7382 (2023).
39. Muddada, N. B. *et al.* The role of chlorine and additives on the density and strength of Lewis and Brønsted acidic sites of γ-Al2O3 support used in oxychlorination catalysis: A FTIR study. *J Catal* **284**, 236–246 (2011).
40. Li, M. *et al.* Effect of Residual Chlorine on the Catalytic Performance of Co3O4 for CO Oxidation. *ACS Catal* **9**, 11676–11684 (2019).
41. Roth, D., Gélin, P., Primet, M. & Tena, E. *Catalytic Behaviour of Cl-Free and Cl-Containing Pd/Al 2 O 3 Catalysts in the Total Oxidation of Methane at Low Temperature*. *Applied Catalysis A: General* (2000).
42. Murata, S. & Aika, K.-I. Removal of chlorine ions from Ru/MgO catalysts for ammonia synthesis. *Applied Catalysis A* **82**, 1–12 (1992).
43. Kale, M. J. & Christopher, P. Utilizing Quantitative in Situ FTIR Spectroscopy to Identify Well-Coordinated Pt Atoms as the Active Site for CO Oxidation on Al2O3-Supported Pt Catalysts. *ACS Catal* **6**, 5599–5609 (2016).
44. Carocci, E., Truche, L., Cathelineau, M., Caumon, M. C. & Bazarkina, E. F. Tungsten (VI) speciation in hydrothermal solutions up to 400°C as revealed by in-situ Raman spectroscopy. *Geochim Cosmochim Acta* **317**, 306–324 (2022).
45. Wang, X. S., Timofeev, A., Williams-Jones, A. E., Shang, L. B. & Bi, X. W. An experimental study of the solubility and speciation of tungsten in NaCl-bearing aqueous solutions at 250, 300, and 350 °C. *Geochim Cosmochim Acta* **265**, 313–329 (2019).
46. Rigo, M., Canu, P., Angelin, L. & Della Valle, G. Kinetics of TiCl4 Hydrolysis in a Moist Atmosphere. *Ind. Eng. Chem. Res.* **37**, 1189–1195 (1998).
47. Scheithauer, M., Grasselli, R. K. & Knozinger, H. Genesis and structure of WO_x/ZrO_2 solid acid catalysts. *LANGMUIR* **14**, 3019–3029 (1998).
48. Chen, K. D., Bell, A. T. & Iglesia, E. Kinetics and mechanism of oxidative dehydrogenation of propane on vanadium, molybdenum, and tungsten oxides. *JOURNAL OF PHYSICAL CHEMISTRY B* **104**, 1292–1299 (2000).
49. Baertsch, C. D., Komala, K. T., Chua, Y. H. & Iglesia, E. Genesis of Brønsted acid sites during dehydration of 2-butanol on tungsten oxide catalysts. *J Catal* **205**, 44–57 (2002).
50. Huang, X., Korányi, T. I., Boot, M. D. & Hensen, E. J. M. Ethanol as capping agent and formaldehyde scavenger for efficient depolymerization of lignin to aromatics. *Green Chemistry* **17**, 4941–4950 (2015).
51. Mian, S. A. *et al.* A fundamental understanding of catechol and water adsorption on a hydrophilic silica surface: Exploring the underwater adhesion mechanism of mussels on an atomic scale. *Langmuir* **30**, 6906–6914 (2014).
52. Mian, S. A. *et al.* Density functional theory study of catechol adhesion on silica surfaces. *Journal of Physical Chemistry C* **114**, 20793–20800 (2010).
53. Bergeret, G. & Gallezot, P. Particle Size and Dispersion Measurements. in *Handbook of Heterogeneous Catalysis* vol. 2 738–765 (Wiley-VCH, 2008).
54. Monai, M. *et al.* Restructuring of titanium oxide overlayers over nickel nanoparticles during catalysis. *Science (1979)* **380**, 644–651 (2023).
55. Serrer, M. A. *et al.* Structural dynamics in Ni-Fe catalysts during CO2methanation-role of iron oxide clusters. *Catal Sci Technol* **10**, 7542–7554 (2020).

56. Gomez, L. A. *et al.* Selective Reduction of Carboxylic Acids to Aldehydes with Promoted MoO3Catalysts. *ACS Catal* **12**, 6313–6324 (2022).
57. Marlowe, J., Ford, P. C., Abu-Omar, M. M. & Christopher, P. Structure sensitivity in Pt-catalyzed hydrodeoxygenation of multi-oxygenated lignol model compounds. *Catal Sci Technol* **13**, 5662–5678 (2023).
58. SIMPSON, M. C., PORTEOUS, K., MACDOUGALL, J. K. & COLEHAMILTON, D. J. HYDROCARBONYLATION OF 2-PROPEN-1-OL CATALYZED BY TRIETHYLPHOSPHINE RHODIUM COMPLEXES - FORMATION OF 1,4-BUTANEDIOL AND MECHANISTIC STUDIES. *Polyhedron* **12**, 2883–2886 (1993).
59. Kovacs, D. G., Jackson, J. E. & Miller, D. J. MECHANISTIC INVESTIGATION OF GLYCEROL HYDROGENOLYSIS. *REVUE ROUMAINE DE CHIMIE* **60**, 735–742 (2015).
60. He, J. Y. *et al.* New catalytic strategies for α,ω-diols production from lignocellulosic biomass. *Faraday Discuss* **202**, 247–267 (2017).
61. Brentzel, Z. J. *et al.* Chemicals from Biomass: Combining Ring-Opening Tautomerization and Hydrogenation Reactions to Produce 1,5-Pentanediol from Furfural. *ChemSusChem* **10**, 1351–1355 (2017).
62. Campbell, C. T. The Degree of Rate Control: A Powerful Tool for Catalysis Research. *ACS Catalysis* vol. 7 2770–2779 Preprint at https://doi.org/10.1021/acscatal.7b00115 (2017).
63. Boffa, A., Lin, C., Bell, A. T. & Somorjai, G. A. Promotion of CO and CO2 Hydrogenation over Rh by Metal Oxides: The Influence of Oxide Lewis Acidity and Reducibility. *J Catal* **149**, 149–158 (1994).

Chapter 5: Assessing the Role of Oxide-Support Interactions in MO_x/Pt Catalysts for HDO

5.1 Introduction

As described in Chapter 3.1, the role of the support is multifaceted, providing mechanical stabilization and separation to dispersed phases, introducing unique active sites through hydroxyls[1,2], vacancies[3,4], interfaces[5–8], and other defect sites[9,10], and even altering the thermal and electrical conductivity of catalysts which may also influence catalysis[11,12]. Though the ideal in fundamental studies on heterogeneous catalysts is to identify and utilize supports that are entirely innocent in the reactions of interest[13,14], the reality is that completely innocent supports do not exist. Even if not participating directly in catalysis through the introduction of active sites which may influence observed reaction rates and selectivities, the support may play an indirect role in modifying many catalyst properties.

For example, SiO_2 was chosen here as the inactive support due to its irreducibility and negligible acidity, leading to negligible activity for HDO by itself[13,15]. Thus, in studies performed over Pt/SiO_2 catalysts, any reactivity could be ascribed to the Pt nanoparticles, allowing deeper fundamental insight into the role of Pt in HDO. However, for a number of reasons, it is worth considering the role that other traditionally "innocent" supports play in the observed reactivity during HDO. While SiO_2 is beloved in the academic heterogeneous catalysis community for providing such an inert surface, the reality is that SiO_2 finds little application in modern industrial catalysis. This unpopularity on the commercial scale is essentially due to the same reasons for SiO_2's popularity for fundamental research – that is, its inertness. The pristine SiO_2 surface forms very weak bonds with most species due to the high covalency of the Si-O bond and low acidity of the Si-OH proton. While this is a boon for

reactivity, the tradeoff is that supported species also form very weak bonds with the silica surface[16]. In an industrial setting, this can lead to the sintering of metal domains resulting in loss of active sites and the need for catalyst removal[17]. The problem is so bad, in fact, that some researchers have deemed SiO_2 "an ice-skating rink"[18].

On an industrial scale, Al_2O_3 finds far more application, both as a neat support itself as in hydrotreating catalysts[19–22] (CoMo or NiMo/Al_2O_3) and reforming catalysts[23–25] (Pt/Al_2O_3) and as a binder material for fluidized catalytic cracking[26–28] (FCC; Zeolite-Al_2O_3 extrudate). Al_2O_3 may be considered reasonably irreducible under typical conditions, thus not participating in redox reactions itself[29,30]. Additionally, though Al_2O_3 boasts higher acidity, particularly Lewis acidity, than SiO_2 due to the presence of stabilized Al^{3+} defects on the surface[31,32], the acidity is still far lower in both strength and density than typically observed for what are traditionally considered "acid" catalysts, such as zeolites. Thus, for the purposes of this work on HDO, wherein we consider that support acidity and reducibility are not expected to play a role due to the conditions and mechanism at play, Al_2O_3 may be similarly innocent to SiO_2 as a supporting material for catalysis – which is to say, not entirely innocent, but reasonably so. Additionally, Al_2O_3 has been previously reported as a support with WO_x for HDO (albeit with Pd at the catalytic metal).[33,34]

However, support alteration plays a further role than participating directly in catalysis. For example, altering support identity, even for unreactive supports, can alter metal nanoparticle geometry due to the strength of the interactions between the metal and the support at the interface[32]. Strong metal-support interactions (not SMSI) lead to hydrophilic-like interactions at the interface where the metal nanoparticles can truncate more significantly or even take on entirely new shapes in order to maximize metal-support interfacial area[35–37]. Such

behavior has been observed for small Pt nanoparticles supported on Al_2O_3, wherein the Pt restructures to form raft-like, two-dimensional shapes that maximize Pt-Al_2O_3 interactions. Conversely, the opposite is true of weak metal-support interactions, which analogously mimic hydrophobic interactions.

Such strong interactions are not reserved for just metal-support pairs but can also influence the stability and structure of supported oxides such as WO_x. On the surface of supporting oxides, WO_x is known to assume a variety of structures ranging from monomers to oligomers to more crystalline WO_3 domains[38,39]. These structural forms in turn influence the chemical characteristics of WO_x as well, moderating acidity and reducibility. Considering that reduction is considered to be a prerequisite to oxide mobilization atop the surfaces of metal nanoparticles during HDO, it might be expected that strong support interactions and the domain structure of WO_x might strongly influence the decoration state of WO_x on Pt nanoparticles.

Clearly, the intersection of oxide-metal, metal-support, and oxide-support interactions in the catalyst architecture explored throughout this work demands further clarification when considering supporting materials outside of SiO_2. Considering specifically the case of Al_2O_3, which is the most frequently used refractory support material for industrial settings, there is both a practical inspiration behind investigating the nature of WO_x/Pt catalysts supported on Al_2O_3 as well as a fundamental inspiration. As described in the conclusion of Chapter 3, the work conducted on WO_x/Pt/SiO_2 catalyst demonstrated that WO_x's primary role in driving the selectivity of HDO reactions of phenolics was as an inhibitor of off-target hydrogenation through the preferential decoration of well-coordinated Pt sites. However, inhibited mobility

of WO_x or the alteration of Pt nanoparticle geometry through support interactions may change the structure-activity relationships for $WO_x/Pt/Al_2O_3$ catalysts.

Towards this end, Al_2O_3-supported catalysts featuring both large (~10 nm) Pt nanoparticles were synthesized and then modified with WO_x in an identical, step-wise fashion to the approach taken with SiO_2. The large (~10 nm) Pt/Al_2O_3 catalyst acted as a control catalyst with SiO_2 to understand how Pt domains of similar size behaved in the HDO of phenolics. The influence of WO_x upon the reactivity of Pt is then clarified, complemented by CO DRIFTS characterization to understand the support-dependent behavior of WO_x decoration on $WO_x/Pt/Al_2O_3$ support. The culmination of these results reveals the importance of considering support-oxide interactions in inverse catalyst design and supports the structure-sensitivity described for Pt-catalyzed HDO of phenolics as discussed throughout this dissertation.

5.2 Results and Discussion

WO_x-modified Pt catalysts supported on 20 nm g-Al_2O_3 were synthesized in an analogous way to WO_x-modified Pt catalysts supported on SiO2, through a stepwise approach first synthesizing Pt/Al_2O_3 catalysts with subsequent WO_x deposition at desired weight loadings. Pt weight loading (4wt%), and calcination temperature was chosen to obtain large Pt nanoparticles to enable the direct comparison between Pt/SiO_2 and Pt/Al_2O_3 reaction results, as previous work in Chapter 2 has underscored the influence of Pt nanoparticle size distribution on the activity and selectivity of Pt catalysts in HDO.

HAADF-STEM was utilized to collect images of the as-prepared, unmodified catalysts to characterize the particle size distributions. Figure 5.1 shows representative images of the

4wt% Pt/Al_2O_3 catalyst, referred to from here on by 4Pt. HAADF-STEM indicates that the weight loading and high calcination temperature (650˚C) results in the facilitation of Pt nanoparticle sintering and growth, resulting in nanoparticles greater than 10 nm in size. Treatment of Pt catalysts under oxidative conditions greater than 600˚C is known to result in the formation of volatile PtO_2 species[40], which may overcome the strong metal-support interactions stabilizing Pt species at lower temperatures and facilitate the growth of Pt nanoparticles. The particle sizes here align well with the Pt particle sizes explored in Chapters 2-4, allowing the direct comparison of support effects in HDO of phenolics.

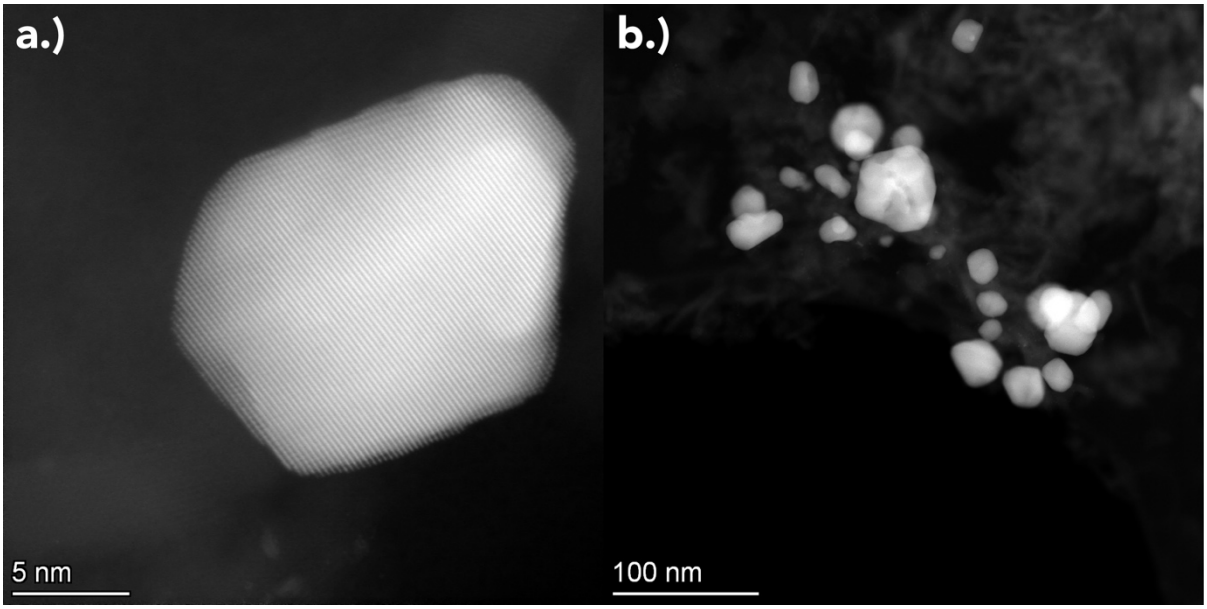

Figure 5.1: (a-b) HAADF-STEM images collected of 4Pt catalysts after calcination in air at 650˚C

To this base catalyst, WO_x was deposited to obtain modified catalysts. As was performed for WO_x-modified Pt/SiO_2 catalysts in Chapter 3 and MO_x-modified Pt/SiO_2 catalysts in Chapter 4, WO_x was deposited using a wet impregnation synthesis that results in WO_x deposition on the Al_2O_3 support. For brevity, WO_x-modified catalysts will be referred to as xW4Pt, where x is the weight loading of W added to the catalyst. To explore the effects of reduction on the catalysts, CO DRIFTS was utilized to assess the surface coverage of WO_x for

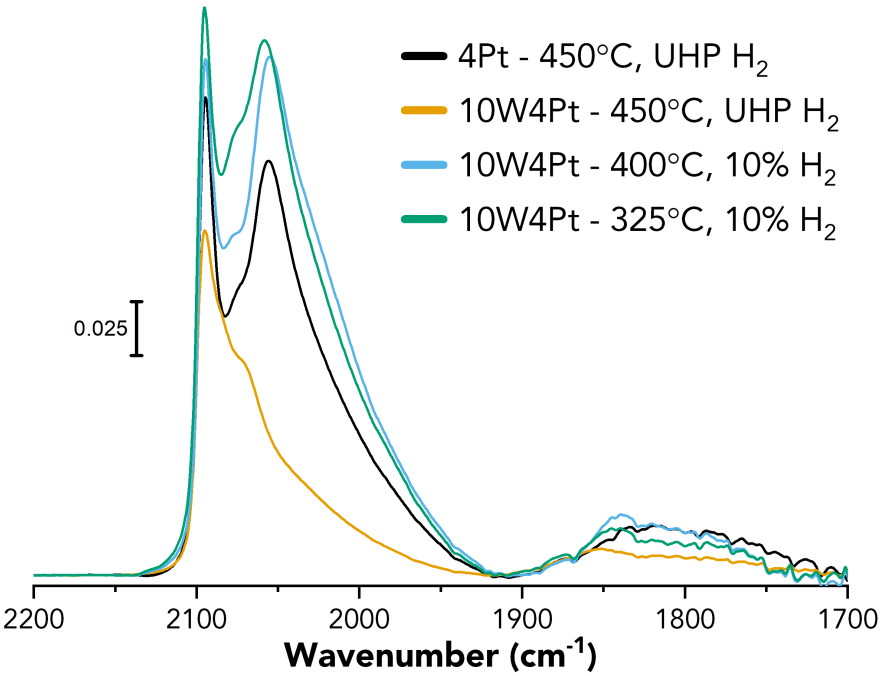

Figure 5.2: CO DRIFTS spectra of 10W4Pt catalysts summarizing the optimization of reduction temperature. The lack of changes to observable Pt structure under 10% H_2/Ar suggested that WO_x species were more stable on Al_2O_3 than on SiO_2. UHP H_2 at 450˚C successfully resulted in a measurably decorated Pt surface by WO_x.

10W4Pt after reduction at 325˚C for 1 hour using 10% H_2/Ar, shown in Figure 5.2. The spectrum exhibits two clear features at 2095 cm^{-1} and 2055 cm^{-1}, corresponding to the well-coordinated and under-coordinated sites of Pt nanoparticles, respectively[40]. However, the strength of the features observed was surprising considering that the weight loading of 10% W was expected to result in the near-complete decoration of Pt nanoparticles based on prior experience with similar materials in Chapters 3 and 4, where only 6wt% of metal oxide was typically enough to result in greatly suppressed CO adsorption as measured by CO DRIFTS and CO chemisorption.

One hypothesis for this behavior was the stability of WO_x on Al_2O_3 to reduction, thus inhibiting its mobility at the same conditions under which WO_x reduced and mobilized when

supported on SiO_2. To test this, 10W4Pt was subjected to additional reductions at 400˚C in 10% H_2/Ar and 450˚C in UHP H_2, both for one hour, and compared against the unmodified 4Pt catalyst reduced at the harshest condition of 450˚C in UHP H_2 (Figure 5.3). It can be seen that

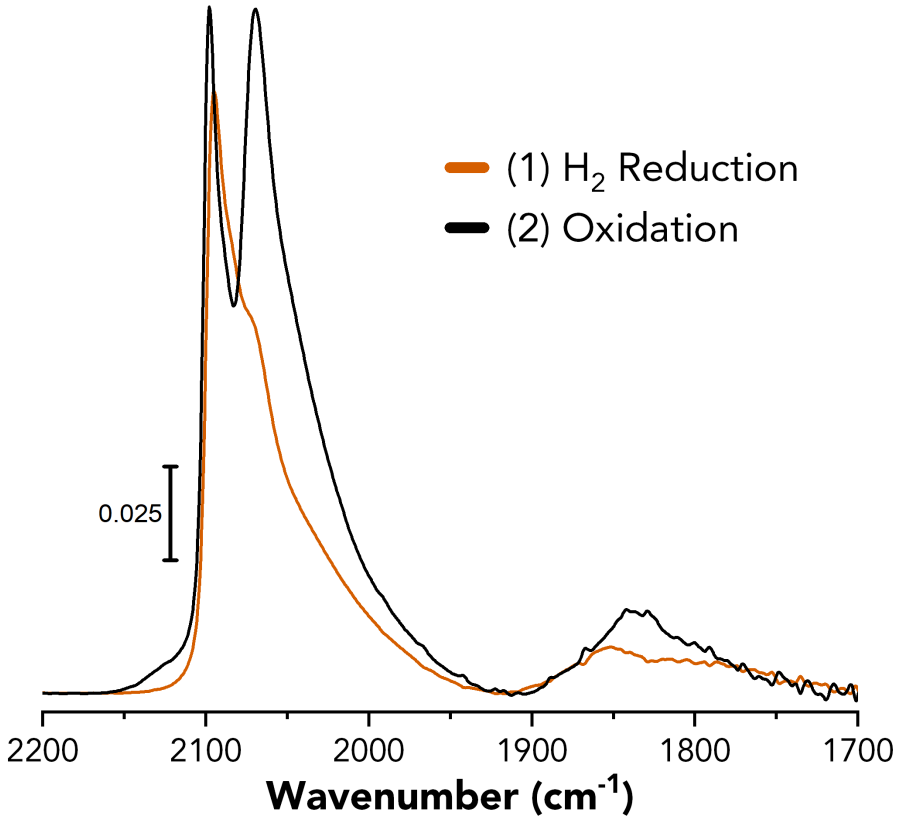

Figure 5.3: CO DRIFTS spectra of 10W4Pt catalysts (1) reduced in UHP H_2 at 450˚C and then (2) re-oxidized under UHP O_2 at 400˚C. Resulting spectra show the reversible decoration of Pt surfaces by WO_x.

only the harshest reduction at 450˚C for 1 hour in UHP H_2 results in a change to the CO DRIFTS spectral shape and intensity, as expected resulting from the decoration of reduced WO_x domains on Pt nanoparticles. To ensure that the changes to the spectral features were a result of WO_x decoration and not the result of irreversible processes such as sintering, 10W4Pt was reduced under UHP H_2 at 450˚C and then oxidized at 400˚C under UHP O_2, with CO DRIFTS collected after both pre-treatments. The resulting DRIFTS spectra are shown in Figure

5.3 and show that the decoration of Pt is reversible by oxidation to return a spectrum that is compared to the unmodified 4Pt catalyst. Thus, this treatment was selected going forward to assess the effects of WO_x decoration on the site availability and identity of Pt nanoparticles by CO DRIFTS.

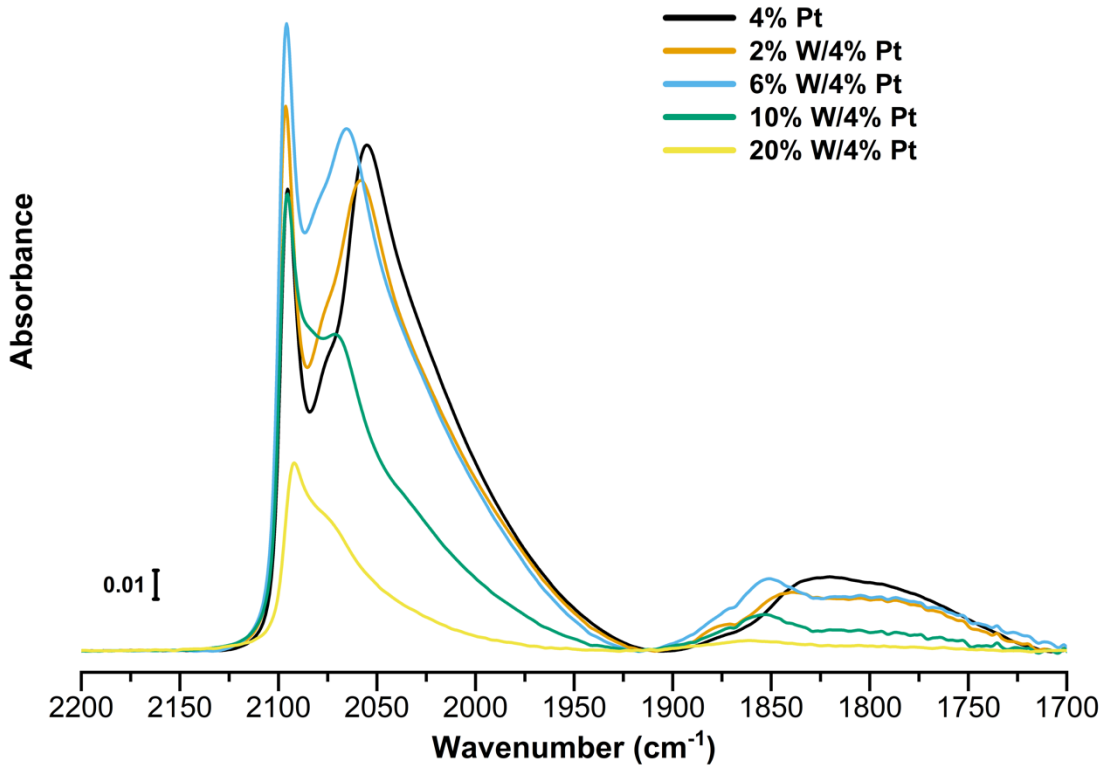

Figure 5.4: CO DRIFTS spectra of WO_x-modified Pt/Al_2O_3 catalysts taken after reduction in UHP H_2 at 450˚C.

Figure 5.4 demonstrates the effects of varied WO_x loading on Pt availability after 450˚C reduction in UHP H_2 for 4Pt catalysts supported on Al_2O_3. CO peak intensity exhibits little change between unmodified 4Pt and 6W4Pt, but decreases with W loading for 10W4Pt and 20W4Pt, though full decoration is never reached even in the case of 20W4Pt. However, the trend that is most apparent is the obvious decrease in UC peak intensity which appears to be more significant than the loss of WC site peak intensity. This behavior is the opposite of what was observed in the case of SiO_2-supported WO_x/Pt catalysts in Chapter 3 and is suggestive of

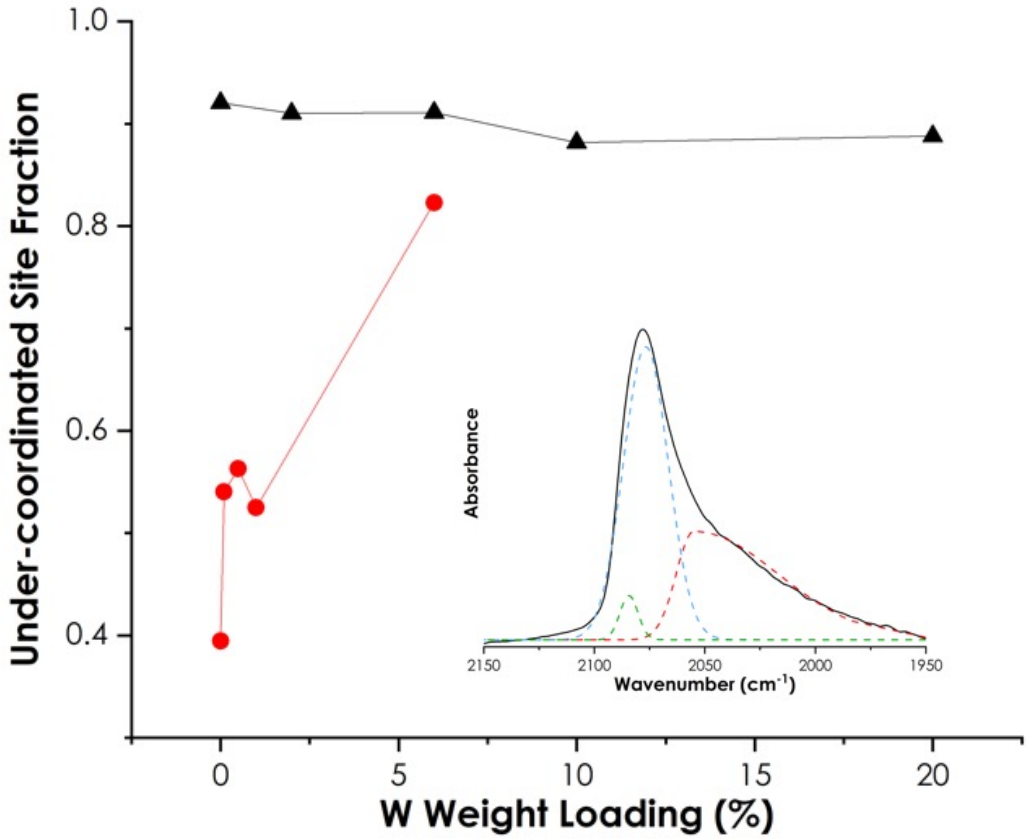

Figure 5.5: Quantification of surface sites, shown as the fraction of under-coordinated sites, for WO_x-modified Pt/SiO_2 catalysts (red) and Pt/Al_2O_3 catalysts (black). Anomalously, WO_x-modified Pt/Al_2O_3 catalysts show no preference towards either well-coordinated or under-coordinated sites, contrasting the behavior for SiO_2 supported catalysts described in Chapter 3.

the preferential decoration of undercoordinated sites on the Pt surface by WO_x. Based on the ML-DFT model developed in Chapter 3, WO_x decoration on top of step edges is energetically unfavorable, agnostic of the support. However, it was also shown that WO_x adsorption preferentially nucleated at step edges and grew inwards towards terraces, resulting in the partial destabilization of under-coordinated Pt sites for CO adsorption. While there is no clear explanation for the trends observed in Figure 5.4b, the only conclusion based on the totality of the data in this dissertation is that the support influence on Pt nanoparticle structure and WO_x mobility and structure results in the perceived decoration of under-coordinated Pt sites at a faster rate than well-coordinated sites. For instance, one might imagine the spiraled growth of

WO_x along the edges of a square in two-dimensional space, or the edges of a cube in three-dimensional space. In this case, where the under-coordinated sites (edges) are rare and spatially segregated by large domains of well-coordinated sites (faces), it may be possible for WO_x to nucleate around these edge sites entirely before significantly decorating the faces of the cube itself. However, the CO DRIFTS spectra shown cannot resolve such a proposal and it is left for now without conclusive explanation.

In order to gain quantitative insight into the decoration of sites, CO DRIFTS peak deconvolution is performed as was done for SiO_2-supported WO_x/Pt catalysts in Chapter 3 of this dissertation. The measured CO DRIFTS spectrum and feature intensities are not immediately quantitative, as different vibrational modes have a greater absorption cross-section for infrared light. This difference in cross-section manifests itself in a difference in sensitivity in the resulting spectrum, or molar extinction coefficient, where higher coefficients represent vibrational modes that adsorb infrared light more effectively and are thus stronger features in the collected spectrum. The molar extinction coefficient for CO bound linearly to under-coordinated Pt sites has been reported to be 2.7 times greater than CO bound linearly to well-coordinated sites[40,41], resulting in the over-representation of UC sites in the CO DRIFTS spectrum relative to the actual surface composition. Thus, to confirm the quantitative fraction of WC and UC Pt sites as a function of WO_x loading, the spectra are deconvoluted into 4 Gaussian features, 2 each for WC and UC sites, respectively. Peak centers are allowed to move for each deconvolution without constraint to capture blueshifts induced by WO_x decoration, but peak widths are constrained to provide comparable results between spectra.

The results of deconvolution are shown in Figure 5.5. It can be seen that SiO_2-supported WO_x/Pt shows an enrichment of the surface in UC sites with increasing WO_x loading due to

the preferential blockage of WC sites by WO_x domains, as discussed in Chapter 3. Interestingly, the decoration of Al_2O_3-supported 4Pt shows very little change in the site distribution, contextualizing the initial interpretation of the CO DRIFTS spectrum. While Al_2O_3-supported 4Pt exhibits distinct decoration behavior from SiO_2-supported WO_x/Pt catalysts, there appears to be no preferential decoration of either site until high W loadings where WC sites begin to become enriched

In order to understand the consequences of this distinct decoration behavior on Al_2O_3-supported WO_x/Pt catalysts, the 4Pt catalyst series was used in the HDO of PHE as a model reaction, shown in Figure 5.6. In all cases, regardless of conversion, the product selectivities remained nearly identical, producing only CYC and BNZ as the dominant products with minor amounts of CYE and ONE. With increasing WO_x loading and decoration as shown in CO DRIFTS, the conversion monotonically drops from 95% to 24%. The small change in product selectivity over this large range of reactivity is suggestive of the fact that the production of deoxygenated products forms directly from PHE without intermediate species, as would be expected for direct deoxygenation. As there is no clear pathway for the direct formation of CYC from PHE, this hypothesis needs further work. However, it is possible that in the pathway from PHE, the rate of BNZ hydrogenation is rapid and equilibrated relative to kinetically slower deoxygenation. Such equilibration between hydrogenated and dehydrogenated products has previously been shown for Pt/SiO_2 catalysts under similar conditions in Chapter 2 of this dissertation, related to the low solubility of H in the liquid phase reactions.

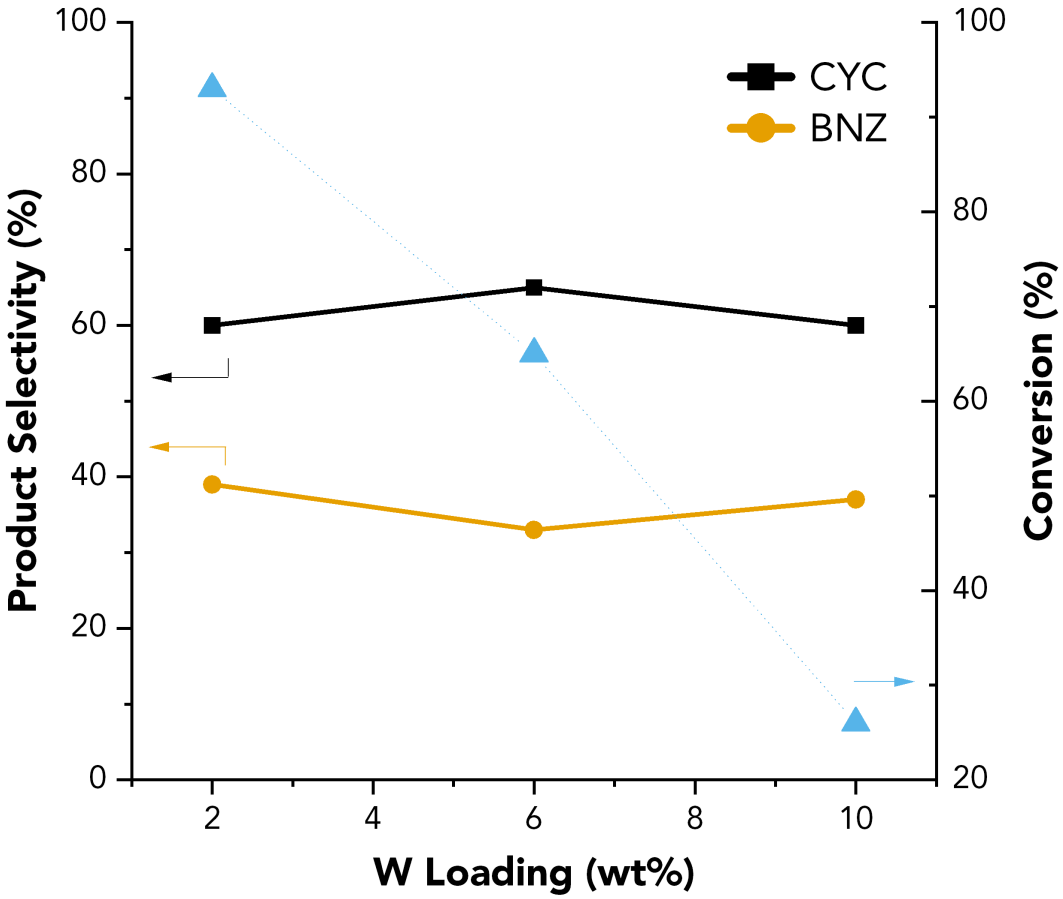

Figure 5.6: PHE HDO reactions conducted over $WO_x/Pt/Al_2O_3$ catalysts showing stable product selectivity with conversion changes between 95% and 24%. *Conditions:* 275˚C, 2 hours, 20 bar H_2, 10 mg catalyst, 20 mL 0.183 M PHE in cyclohexane,

These results are also consistent with the structure sensitivity of HDO described in Chapters 2 and 3 for unmodified and WO_x-modified Pt catalysts. The CO DRIFTS results shown in Figure 5.4 indicate that there is no change in the relative density of well-coordinated and under-coordinated sites on the surface of Pt nanoparticles as a function of WO_x decoration. Though in some ways surprising, this phenomenon is born out in unchanged product selectivity in PHE HDO with increasing WO_x fraction. This suggests once again that the characterization of metal surface sites available after decoration in MO_x/Pt catalysts is a strong predictor of reactivity.

One alternative interpretation of these results might be that WO_x decoration was not occurring over the course of the reaction, as Figure 5.2 demonstrated that harsher reducing conditions were necessary for the measurement of the decorated state for Al_2O_3-supported catalysts in CO DRIFTS. However, the decrease in PHE conversion with increasing WO_x loading is good evidence that WO_x is able to reduce and mobilize under reaction conditions to decorate the Pt surface. Considering the high-temperature calcination conditions the catalyst has been treated with previously, it is not believed that sintering or other irreversible routes of site loss could explain this reactivity. Additionally, sintering is known to alter the composition of the surface sites for metal nanoparticles, thus a change in selectivity would be expected.

5.3 Conclusions and Future Work

The results here identify that the support chosen for WO_x/Pt catalysts for HDO of phenolics may indirectly alter the structure-activity relationships for the active phase. CO DRIFTS identified that the decoration of WO_x atop Pt nanoparticles on Al_2O_3 supports is distinct from that observed for SiO_2-supported catalysts. Rather than exhibiting preferential decoration atop well-coordinated sites, as was observed in SiO_2-supported catalysts and validated through HDO reactivity measurements, the WO_x decoration of Al_2O_3-supported Pt nanoparticles appears to exhibit no site preference, as the ratio of well-coordinated to under-coordinated sites remained constant with decreasing coverage as measured by CO DRIFTS. The fundamental materials properties resulting in this support effect are not immediately clear but may be related to the geometry of Pt nanoparticles on the Al_2O_3 support, which is clearly different than over SiO_2 based on the CO DRIFTS spectra of unmodified Pt nanoparticles. Regardless of the fundamental material physics underpinning this behavior, HDO reactivity

results once again demonstrate that consideration of the atomic-scale structure of Pt in WO_x/Pt catalysts is predictive of catalyst performance. PHE HDO as a probe reaction over WO_x-modified 4% Pt/Al_2O_3 catalysts with an average particle size of 10 nm showed no change in product selectivity as a function of WO_x loading, consistent with the observed stability of well-coordinated to under-coordinated site ratios. Moreover, this behavior was consistent for small Pt nanoparticles (<2 nm) in a WO_x-modified 0.4% Pt/Al_2O_3 catalyst. Similarly low changes to both site fractions as measured by CO DRIFTS and HDO selectivity were observed over modified 0.4% Pt/Al_2O_3 catalysts. In conclusion, the importance of active site availability as discussed throughout this dissertation is confirmed using Al_2O_3 as support, but points to the importance of future work in determining the fundamentals behind the observed decoration behavior and the interplay of interactions in ternary metal-oxide-support systems, broadly.

5.4 Methods

5.4.1 Catalyst Synthesis

Catalysts were prepared on 20 nm g-Al_2O_3 support (USNano) by incipient wetness impregnation with tetraamineplatinum nitrate (TAPN, Sigma). In a typical procedure, 1 g of 20 nm g-Al_2O_3 was placed in a small crystallizing dish. Separately, the desired amount of TAPN was added to 1 mL of deionized H_2O (Sigma) to fill the pores of the g-Al_2O_3 and homogeneously deposit the Pt precursor on the support. Pt was introduced to the Al_2O_3 powder by dropwise addition until the full 1 mL solution had been deposited, resulting in a dry-looking powder. This was placed in the oven to dry fully overnight at 110˚C. Final catalysts were obtained by calcination in flowing air at 650˚C for 6 hours.

WO_x-modified catalysts were obtained using wet impregnation of Pt/Al_2O_3 catalysts synthesized above in a procedure identical to Chapter 3 of this dissertation for $WO_x/Pt/SiO_2$ catalysts. Briefly, Pt/Al_2O_3 base catalysts were suspended in 5 mL of water under stirring. To this, an additional 5 mL of solution containing the desired amount of ammonium metatungsate (Sigma) was added. The stirring solution was left for 30 minutes before the suspension was brought to 80˚C with heating to evaporate off water. Obtained powders were dried in an oven overnight at 110˚C before calcination under flowing air (Airgas) at 350˚C for 3 hours.

5.4.2 Catalyst Characterization

Dispersion measurements were made using pulsed CO chemisorption on an Autochem 2920 II instrument. The outlet gas composition was measured using a thermal conductivity detector (TCD). In a typical measurement, 30 mg of catalyst was placed in a quartz U-tube between two packed regions of quartz wool. The catalyst was then reduced under 50 sccm of 10% H_2/Ar (Airgas) at 325˚C for 1 hour before cooling to 50˚C. Once at 50˚C, the sample was purged with 50 sccm UHP Ar (Airgas) and held until the baseline was measured to be stable by the TCD. At this point, 10 pulses of 10% CO/Ar were conducted at 3.5-minute intervals. The uptake of CO to the catalyst surface was measured by subtracting each peak area from the maximum peak area, indicating the quantity of CO adsorbed to the catalyst surface which did not pass over the TCD. A CO:Pt ratio of 1 was assumed.

H_2-TPR measurements were also taken on the Autochem 2920 II using the same sample preparation in the U-tube. For these measurements, catalysts were pretreated at 300˚C for 1 hour in UHP O_2 (Airgas) and purged in Ar while cooling from 300˚C to 50˚C. Once at 50˚C, gas flow was changed to 10% H_2/Ar and passed through a drying tube containing a

combination of zeolite and 3A molecular sieves to trap any moisture that formed during reduction. Once the signal measured by the TCD was stabilized at 50˚C under 10% H_2/Ar, the samples were ramped to 900˚C at 10˚C/min under H_2/Ar.

HAADF-STEM images of the 6Pt catalyst were taken on a Thermo Fisher Spectra F200X aberration-corrected transmission electron microscope in the scanning mode (STEM) using a high-angle annular dark field (HAADF) detector. Images were collected at an accelerating voltage of 200 kV. Samples were prepared by dipping 300 mesh Cu grids coated with lacey carbon into the loose powder a number of times. After approximately 5 dips of the grids into the loose powder, the grids were shaken to remove any macroscopic particles that had become stuck to the grid.

CO DRIFTS measurements were carried out on either a Nicolet iS10 or Nicolet iS50R FT-IR spectrometer equipped with a Praying Mantis Diffuse Reflection Accessory (Harrick Scientific) and a High-Temperature Reaction Chamber (Harrick Scientific) fitted with a thermocouple in the catalyst bed. Ar (99.995%), He (99.995%), O_2 (99.50%), 10% CO/Ar, and 10% H_2/Ar were purchased from Airgas and used as received. In a typical DRIFTS experiment, catalyst was loaded into the Harrick cell and pre-treated under a desired gas environment and temperature. Temperature set points were reached by ramping the catalyst at 10˚C/min in all experiments, except for cooling after pre-treatment steps which was allowed to happen passively. Gas flow rates across the catalyst bed in all cases were 50 sccm controlled by mass flow controllers (Teledyne Hastings). For CO DRIFTS experiments, catalysts were cooled to 30˚C prior to exposure to 10% CO/Ar. CO exposure was continued until saturation coverage of CO on the metal sites was achieved, determined by unchanging peak intensity in DRIFTS

spectra. After metal surfaces were saturated by CO, gas flow was switched to Ar to remove CO from the gas atmosphere.

5.4.3 HDO Reactions

HDO reactions using the prepared catalysts were performed in 75-mL stainless-steel pressure reactors (Parr Instrument Co., 5000 Series). In a typical reaction, catalyst was loaded into the reactor along with 20 mL of a prepared stock solution. The stock solution consisted of 10.7335 g of 4-propylphenol (TCI Chemicals) and 5.16 g of *n*-decane (Sigma) dissolved in 430 mL of cyclohexane (Sigma). Catalyst loading was kept constant between catalysts for constant Pt mass. Reactions were stirred magnetically at 700 rpm using glass-shielded stir bars. Once loaded, the reactor was sealed and purged 3 times with 5.0 grade H_2 (Airgas) before pressurizing to a final gauge pressure of 20 bar at room temperature. Then, the vessel was heated to 275 ˚C and held for 2 hours. After the allotted reaction time, the reactor vessel was quickly removed and quenched using a water bath. Once cooled to room temperature, the liquid products were collected by centrifugation and analyzed by a gas chromatogram equipped with a flame ionization detector (GC-FID, Agilent). Product identification was carried out using commercially-sourced standards where possible (4-propylbenzene (BNZ), 4-propylphenol (PHE), 4-propylcyclohexanol (OL), 4-propylcyclohexane (CYC)). In instances where standards are not commercially available (4-propylcyclohex-1-ene (CYE)), FID responses were estimated using effective carbon number (ECN)[95]. Reaction performance metrics were defined as:

$$Conversion\ (\%) = \frac{N_{DHE}}{N_{DHE}^{0}}$$

$$Selectivity\ (\%) = \frac{N_{Product}}{\sum N_{Product}}$$

$$Yield\ (\%) = Conversion * Selectivity = \frac{N_{Product}}{\sum N_{Product}} * \frac{N_{DHE}}{N_{DHE}^{0}}$$

where N_i is the moles of species *i* measured by GC-FID and N_i^0 is the initial moles of *i* loaded into the batch reactor.

5.5 References

1. Meng, F. C. *et al.* Tailoring the Brønsted acidity of Ti-OH species by regulating Pt-TiO_2 interaction. *ChemSusChem* **17**, (2024).
2. Wu, Y. *et al.* Dynamic Formation of Brønsted Acid Sites over Supported WOx/Pt on SiO2 Inverse Catalysts─Spectroscopy, Probe Chemistry, and Calculations. *ACS Catal* **13**, 7371–7382 (2023).
3. Mars, P. & Van Krevelen, D. W. Oxidations carried out by means of vanadium oxide catalysts. *Chem Eng Sci* **3**, 41–59 (1954).
4. Xiao, X. *et al.* The role of oxygen vacancies in biomass deoxygenation by reducible zinc/zinc oxide catalysts. *Catal Sci Technol* **8**, 1819–1827 (2018).
5. Deo, S., Medlin, W., Nikolla, E. & Janik, M. J. Reaction paths for hydrodeoxygenation of furfuryl alcohol at TiO_2/Pd interfaces. *J Catal* **377**, 28–40 (2019).
6. Teles, C. A., Duong, N., Rabelo-Neto, R. C., Resasco, D. & Noronha, F. B. Evidence of dependence between the deoxygenation activity and metal-support interface. *Catal Sci Technol* **12**, 5961–5969 (2022).
7. Deng, L. *et al.* Strong metal-support interaction between Pt and SiO2 following high-temperature reduction: A catalytic interface for propane dehydrogenation. *Chemical Communications* **53**, 6937–6940 (2017).
8. Matsumoto, T., Batzill, M., Hsieh, S. & Koel, B. E. Fundamental studies of titanium oxide-Pt(100) interfaces II. Influence of oxidation and reduction reactions on the surface structure of TiO x films on Pt(100). *Surf Sci* **572**, 146–161 (2004).
9. Zhang, C. *et al.* Co-promoted few-layer and defect-rich MoS2 for enhanced hydrodeoxygenation of p-cresol. *Appl Catal A Gen* **621**, (2021).
10. Teles, C. A. *et al.* The role of defect sites and oxophilicity of the support on the phenol hydrodeoxygenation reaction. *Appl Catal B* **249**, 292–305 (2019).
11. Butt, J. B. Thermal Conductivity of Porous Catalysts. *AIChE Journal* **11**, 106–111 (1965).

12. Merino, D., Sanz, O. & Montes, M. Effect of the thermal conductivity and catalyst layer thickness on the Fischer-Tropsch synthesis selectivity using structured catalysts. *Chemical Engineering Journal* **327**, 1033–1042 (2017).
13. Nie, L. & Resasco, D. E. Kinetics and mechanism of m-cresol hydrodeoxygenation on a Pt/SiO 2 catalyst. *J Catal* **317**, 22–29 (2014).
14. Zheng, X. *et al.* Oxygen and CO adsorption on Au/SiO2 catalysts prepared by magnetron sputtering: The role of oxygen storage. in *Industrial and Engineering Chemistry Research* vol. 49 10428–10437 (2010).
15. Noh, G. *et al.* Lewis Acid Strength of Interfacial Metal Sites Drives CH3OH Selectivity and Formation Rates on Cu-Based CO2 Hydrogenation Catalysts. *Angewandte Chemie - International Edition* **60**, 9650–9659 (2021).
16. Zhu, Y. *et al.* Covalent-bonding to irreducible SiO2 leads to high-loading and atomically dispersed metal catalysts. *J Catal* **353**, 315–324 (2017).
17. Zou, W. & Gonzalez, R. D. *Stabilization and Sintering of Porous Pt/SiO,: A New Approach*. *Applied Catalysis A: General* vol. 102 (1993).
18. Soled, S. Silica-supported catalysts get a new breath of life. *Science* vol. 350 1171–1172 Preprint at https://doi.org/10.1126/science.aad0267 (2015).
19. SAJKOWSKI, D. J. *et al.* PHOSPHORUS PROMOTION OF MO-AL2O3 HYDROTREATING CATALYSTS. *Appl Catal* **62**, 205–220 (1990).
20. Sajkowski, D. J. & Oyama, S. T. Catalytic hydrotreating by molybdenum carbide and nitride: Unsupported Mo2N and Mo2C/Al2O3. *APPLIED CATALYSIS A-GENERAL* **134**, 339–349 (1996).
21. Tiwari, R. *et al.* Hydrotreating and hydrocracking catalysts for processing of waste soya-oil and refinery-oil mixtures. *Catal Commun* **12**, 559–562 (2011).
22. Xu, Y. M., Li, W. K., He, J. H. & Luo, X. H. Preparation and characterization of hydrotreating catalysts -: I.: Effect of preparation methods on properties of $MoNiP/Al_2O_3$ catalyst. *CHINESE JOURNAL OF CATALYSIS* **22**, 575–578 (2001).
23. XIAO, J. L. & PUDDEPHATT, R. J. PT-RE CLUSTERS AND BIMETALLIC CATALYSTS. *Coord Chem Rev* **143**, 457–500 (1995).
24. VANTRIMPONT, P. A., MARIN, G. B. & FROMENT, G. F. KINETICS OF THE REFORMING OF C-7 HYDROCARBONS ON A COMMERCIAL PTRE/AL2O3 CATALYST. *Appl Catal* **24**, 53–68 (1986).
25. CABALLERO, A., VILLAIN, F., DEXPERT, H., LEPELTIER, F. & LYNCH, J. CHARACTERIZATION BY IN-SITU EXAFS SPECTROSCOPY OF PT/AL2O3 AND PTRE/AL2O3 CATALYSTS UNDER REACTION CONDITIONS. *JAPANESE JOURNAL OF APPLIED PHYSICS PART 1-REGULAR PAPERS SHORT NOTES & REVIEW PAPERS* **32**, 439–441 (1993).
26. Verkleij, S. P. *et al.* Chemical Imaging of the Binder-Dependent Coke Formation in Zeolite-Based Catalyst Bodies During the Transalkylation of Aromatics. *ChemCatChem* **11**, 4788–4796 (2019).
27. Whiting, G. T., Chowdhury, A. D., Oord, R., Paalanen, P. & Weckhuysen, B. M. The curious case of zeolite-clay/binder interactions and their consequences for catalyst preparation. *Faraday Discuss* **188**, 369–386 (2016).
28. Zhou, S. L., Zhang, C. X., Li, Y. X., Luo, Y. B. & Shu, X. T. Effect of Particle Size of Al_2O_3 Binders on Acidity and Isobutane-Butene Alkylation Performance of Zeolite Y-Based Catalysts. *Ind Eng Chem Res* **59**, 5576–5582 (2020).

29. Wang, H. Y. & Ruckenstein, E. Carbon dioxide reforming of methane to synthesis gas over supported rhodium catalysts: the effect of support. *APPLIED CATALYSIS A-GENERAL* **204**, 143–152 (2000).
30. Doherty, F. & Goldsmith, B. R. Modeling plasma-induced surface charge effects on CO_2 activation by single atom catalysts supported on reducible and irreducible metal oxides. *Plasma Sources Sci Technol* **32**, (2023).
31. Shi, L. *et al.* Al_2O_3 Nanosheets Rich in Pentacoordinate Al³⁺ Ions Stabilize Pt-Sn Clusters for Propane Dehydrogenation. *ANGEWANDTE CHEMIE-INTERNATIONAL EDITION* **54**, 13994–13998 (2015).
32. Kwak, J. H. *et al.* Coordinatively Unsaturated Al³⁺ Centers as Binding Sites for Active Catalyst Phases of Platinum on γ-Al_2O_3. *Science (1979)* **325**, 1670–1673 (2009).
33. Hong, Y. K., Lee, D. W., Eom, H. J. & Lee, K. Y. The catalytic activity of Pd/WOx/γ-Al2O3 for hydrodeoxygenation of guaiacol. *Appl Catal B* **150–151**, 438–445 (2014).
34. Rasmussen, M. J. & Medlin, J. W. Role of tungsten modifiers in bimetallic catalysts for enhanced hydrodeoxygenation activity and selectivity. *Catal Sci Technol* **10**, 414–423 (2020).
35. Kasatkin, I., Kniep, B. & Ressler, T. Cu/ZnO and Cu/ZrO_2 interactions studied by contact angle measurement with TEM. *PHYSICAL CHEMISTRY CHEMICAL PHYSICS* **9**, 878–883 (2007).
36. Shibuta, Y. & Elliott, J. A. A molecular dynamics study of the carbon-catalyst interaction energy for multi-scale modelling of single wall carbon nanotube growth. *Chem Phys Lett* **427**, 365–370 (2006).
37. Zhao, K., Auerbach, D. J. & Campbell, C. T. Calorimetric Energies and Chemical Potentials of Metal Atoms in Catalytic Nanoparticles on Oxide and Carbon Supports: Improved Size Dependencies and Adhesion Energies. *ACS Catal* **13**, 13968–13981 (2023).
38. Lwin, S., Li, Y., Frenkel, A. I. & Wachs, I. E. Nature of WOx Sites on SiO2 and Their Molecular Structure-Reactivity/Selectivity Relationships for Propylene Metathesis. *ACS Catal* **6**, 3061–3071 (2016).
39. Barton, D. G., Shtein, M., Wilson, R. D., Soled, S. L. & Iglesia, E. Structure and electronic properties of solid acids based on tungsten oxide nanostructures. *Journal of Physical Chemistry B* **103**, 630–640 (1999).
40. Kale, M. J. & Christopher, P. Utilizing Quantitative in Situ FTIR Spectroscopy to Identify Well-Coordinated Pt Atoms as the Active Site for CO Oxidation on Al2O3-Supported Pt Catalysts. *ACS Catal* **6**, 5599–5609 (2016).
41. Yoshinobu, J., Tsukahara, N., Yasui, F., Mukai, K. & Yamashita, Y. Lateral Displacement by Transient Mobility in Chemisorption of CO on Pt(997). *Phys Rev Lett* **90**, 1–4 (2003).

Chapter 6: Conclusions and Outlook

6.1 Dissertation Summary

The work detailed in this dissertation has sought to fundamentally understand a highly complex system of materials, reactants, products, and conditions through the lens of a simplified, yet flexible, model system. Importantly, it was not the goal of this work to identify the most active, stable, and selective catalyst reported to date, nor has there been a material reported in the 5 years over which this work was conducted that exhibits desirable enough properties for immediate industrial implementation. However, this lack of progress underscores the need for additional studies developing a fundamental understanding of the structure-activity relationships underpinning these materials, lest progress continues to be made as a black box of randomized successes.

Overall, the work of this dissertation advances the understanding of both unmodified and modified MO_x/Pt catalysts for the HDO of phenolics. In the case of unmodified Pt catalysts, a significant structure sensitivity exists which dictates both the degree of saturation of product species and the degree of deoxygenation. Curiously, it has been found that there is a trade-off that exists for Pt catalysts: either deoxygenation can be achieved alongside the formation of saturated products through large Pt nanoparticles with ample well-coordinated sites, or the selective formation of demethoxylated, but still hydroxylated, species can be achieved through the application of small Pt nanoparticles exhibiting predominantly under-coordinated sites. This is not only counter to what would be expected intuitively through Hugh Stott Taylor's perspective of the active site[1] (those sites that are more under-coordinated are more active) but also counter to the results of prior computational research which had identified these under-coordinated sites as facilitating deoxygenation[2,3].

The lessons from this surprise result are three-fold. The first is that experimental results must always be employed to challenge and validate those obtained by theory and surface science, even with the expansion of computational techniques today with the development of increasingly accurate and specified functionals, the adoption of machine learning techniques, access to greater computational resources, etc. The second is that reaction performance is always a confluence of kinetics and thermodynamics, and that there is a need to consider both perspectives for every possible reaction when assessing likely mechanisms of activity for a catalyst. The results of Chapter 2 point towards the influence of a tautomerization pathway which had not been compared against direct deoxygenation in computational research prior; thus, there could be no assessment made without reactivity data of which pathway was more favorable. The theoretical results pointing towards the influence of under-coordinated sites in direct deoxygenation may still be true, but the kinetics of such a pathway may be negligible under the reaction conditions studied here compared to the kinetics of tautomerization-induced deoxygenation. Alternatively, there may be some mechanism of deactivation, such as the strong adsorption of oxygenates to these under-coordinated sites[4–7], that are similarly not captured by DFT models. The third lesson, and arguably most important, is that for the conditions studied in this dissertation, an optimal catalyst for HDO (high deoxygenation, low hydrogenation) cannot be achieved without modification using Pt nanoparticles alone because of the role of well-coordinated sites in both undesired (hydrogenation) and desired (deoxygenation) activity.

The results of Chapter 2 describing the structure sensitivity of Pt in unmodified catalysts lead directly into the role of oxide modifiers for MO_x/Pt catalysts in Chapter 3. The application of CO probe molecule DRIFTS enabled quantification of the atomic-scale state of the Pt surface after reaction-like reductive pre-treatments, a technique that has been utilized

previously in the Christopher group to identify structure sensitivity in CO oxidation reactions[8]. In this case, however, a fundamental behavior of reducible oxides on metal surfaces was uncovered that is at once surprising and entirely intuitive. The preferential decoration of reducible metal oxides like WO_x in the SMSI state on well-coordinated Pt nanoparticle surfaces suppresses the undesired hydrogenation reactions that would otherwise occur on these sites, while allowing the desired deoxygenation reaction to continue to occur, though seemingly without substantial promotion. Such preferential decoration is in line with reports from surface science where such behavior has been observed for decades on model oxide/metal systems but had never been observed for heterogeneous catalysts prior[9,10]. Presumably, this decoration of well-coordinated sites enables the structural organization of reduced oxide domains into crystalline or semi-crystalline structures with less strain than the decoration of under-coordinated sites, consistent with broader theories for SMSI in traditional systems[11–13]. Thus, the performance of modified MO_x/Pt catalysts can be seen as an amalgamation of phenomena including the inherent structure sensitivity of the underlying and active Pt surface and fundamental SMSI material science.

Indeed, the role of the reducible metal oxide is clarified to be primarily as an inhibitor of undesired reactivity and a moderate promoter, on a per-site basis, of deoxygenation activity. It is found that in the case of increasing catalyst complexity with the introduction of additional components, Occam's Razor dictating simplicity in explanation holds true. Even in the case of wildly varying chemical properties, only marginal changes to direct deoxygenation activity can be observed with changing oxide modifier, suggesting that in all cases, modified and unmodified, the underlying Pt sites are the predominantly active catalytic species. This clarifies the mechanism of deoxygenation under the conditions studied here as likely proceeding

through the tautomerization mechanism proposed in Chapter 2, with the influence of oxide modifiers acting through the facilitation of C-O cleavage of these tautomerized surface intermediates, similar to what has been observed for classical strong metal-support interaction (SMSI) systems in CO hydrogenation[14].

Overall, this dissertation underscores the importance of thorough characterization and model systems, employed here in the study of HDO. The structure-activity relationships developed herein may act as useful guides in the development of catalysts targeting specific products from phenolics, and as such may find broad application in a future where feedstock flexibility may prove to be essential rather than just desirable. However, as will be discussed in the following sections, a number of questions remain unanswered that may further clarify the precise mechanism and role of the oxide species under reaction conditions, and further open the landscape of products that biomass may ostensibly one day supply.

6.2 Outlook and Future Directions: Advanced Characterization Techniques

6.2.1 Overview

The work described in this dissertation leans heavily on the atomic-scale characterization of inverse catalysts in order to develop informed structure-activity relationships to build a fundamental understanding of material properties that should be targeted for future research to optimize overall catalyst performance. Typically, the atomic-scale characterization of inverse materials has fallen into two categories, either spectroscopy[15–19] or microscopy[20–24]. Much of the characterization done in this dissertation is in the form of *in situ* spectroscopy, enabling the study of catalysts in a near-active state on a bulk scale, though there has been much work recently detailing the use of ever-growing capabilities in *in situ* or

operando TEM offering similarly important insights[25,26]. While the information derived from electron microscopy often can be considered more direct (the age-old adage that "seeing is believing"), there are limitations as is the case with any other characterization technique. For one, there are concerns that beam effects may play a deleterious role in the accuracy of behaviors observed through electron microscopy, especially in the case of dynamic systems such as MO_x/Pt catalysts described here where the reducible oxides already exhibit appreciable mobility at only slightly elevated temperatures[27–30]. Additionally, there are growing concerns that the sample size of images from electron microscopy may never truly be large enough to capture the structure and characteristics of the bulk sample – that is, some bias in the image collection is always present[31–33]. Thus, spectroscopy is a preferred primary characterization technique in this dissertation and indeed shows good prospects for future work, though these measurements are technically challenging as will be discussed in more detail below.

6.2.2 Dynamics of Oxide Overlayers: Bridging the *In Situ*-*Operando* Gap

In the study of heterogeneous catalysts, the gold standard in developing structure-activity relationships is to perform a relevant characterization technique on the catalyst in its working state, in what has been defined as *operando* characterization. However, this gold standard or ideal is rarely actually achieved, even when authors use the term *operando*. Importantly, for truly *operando* characterization, the catalyst must not only be in its working state but strides must be made to quantify the activity of the catalyst, such that quantitative changes to catalyst structure and properties may be quantitatively assigned to reactivity metrics[34,35]. Understandably, the conduction of *operando* experiments represents a lofty goal

that requires careful planning, system selection, instrumentation, and quite frankly, in some cases, a good deal of luck.

Because of the challenges associated with *operando* characterization, *in situ* work is far more commonplace in the characterization of heterogeneous materials. *In situ*, or in place, work refers only to the fact that the catalyst is treated in the same place/setting that it is to be characterized in, avoiding the challenges associated with sample transfer from an *ex-situ*, or out-of-place, pre-treatment or change. If a sample is characterized in its as-prepared state, or one which is markedly different from the conditions that it is subjected to prior to pre-treatment, it cannot be considered an *in situ* characterization.

Pertaining to the challenges of conducting *operando* characterization, all of the characterization work performed here was done *in situ* – it would not be possible to perform DRIFTS spectroscopy, for example, on the catalyst in the working state under solvent and 20+ bar of H_2 pressure. While the pretreatment for the catalyst was considered to be representative of what the catalysts experience during reaction – high temperatures (275˚C vs. 325˚C), reducing atmospheres (0.1-1 bar of H_2 vs. 20 bar H_2), the catalyst system is by definition dynamic, that is, it is responsive to the conditions that it experiences. This is a central tenet of the work conducted herein. However, this necessarily begs the question of whether or not the catalyst during reaction maintains the same structure and properties as determined via the gamut of characterization techniques performed here.

The totality of the evidence reported here suggests that *in situ* characterization is, at the very least, a very good proxy for *operando* structure for the MO_x-Pt catalyst systems studied here. The linearity of hydrogenated product yields from DHE HDO over WO_x-Pt catalysts versus the CO chemisorption and DRIFTS measured well-coordinated Pt site density suggests

that a strong, linear relationship exists between quantifiable *in situ* and *operando* techniques. The same can be said for the results found over MO_x-Pt catalysts in Chapter 3.4 and WO_x-Pt catalysts for varied supports in Chapter 4. However, what cannot be determined via these comparisons alone is whether or not the slope of the linear trend between these results is sensible – that is, both *in situ* and *operando* results may trend linearly independently, but their magnitudes may be distinct. The most likely example of this is in the potential difference between measured CO chemisorption values at 30˚C and actual Pt availability at reaction conditions (275˚C, 20 bar H_2). Both of these values may trend linearly with WO_x loading, as might be expected, but it may be equally expected that their values are not identical, or that Pt availability at 275˚C would be greater due to the enhanced mobility of WO_x species and the Pt surface itself at elevated temperatures.

This is indeed something that the literature is beginning to embrace with more enthusiasm as the importance of *operando* measurements becomes more cemented, particularly in regard to dynamic systems. Frey *et al.* reported on the *operando* dynamics of Pt/TiO_2 catalysts under SMSI-forming conditions and noted that there were distinct behaviors between separate Pt nanoparticles on the TiO_2 surface, which they associated with a lattice plane-alignment argument[36]. Monai *et al*. conducted *operando* TEM of a Ni/TiO_2 catalyst under CO_2 hydrogenation conditions and found that the TiO_x overlayer receded during reaction to enable access of the reactants to the surface, relating this behavior to strain relaxation[26]. These results begin to point towards answers to long-standing questions in the community regarding how it is possible that catalysts in the SMSI or inverse state (oxide decorating the metal surface completely) can demonstrate activity for certain reactions that are importantly traditionally metal-catalyzed. Though in the absence of *operando* characterization there have

been a myriad of explanations proposed, such as reactivity atop the oxide layer itself[37], it seems far more likely through the lens of these results and others that the oxide layer experiences some degree of re-arrangement under reaction conditions. Critically, this re-arrangement may also be reversible such that *in situ* or *ex-situ* characterization techniques capture do not capture this state.

However, challenges abound for actually probing these re-arrangements under *operando* conditions! Take for instance the case of CO DRIFTS, wherein CO is the probe molecule that reports on the structure and availability of Pt sites on the metal surface. In this work, CO is used *in situ* to report on the accessibility of Pt sites not decorated by oxide domains. However, for truly *operando* work, probe molecules may not be able to be employed in this way. If reactivity can be maintained in the presence of probe molecules, it may be theoretically possible, but take for instance the example of CO – a common poison for reactions, including HDO[38–41]. In order to report spectroscopic information *operando* on every metal site available, CO would have to remain adsorbed to every metal site accessible, in turn likely suppressing all reactions through poisoning. One might imagine a reaction wherein CO is a reactant and operating this reaction in a non-CO poisoned regime, but for SMSI-like systems the conditions must also be strongly reducing to maintain the oxide-on-metal architecture – thus, CO oxidation or similar are not reasonable choices. Probe molecule desorption can also be a challenge in the case of *operando* characterization at elevated temperatures, requiring the presence of elevated pressures of probe molecule to maintain coverage on the catalyst. Of course, non-spectroscopic techniques are always an option, though these understandably present different, not fewer, challenges, such as the non-bulk information that microscopy provides[42].

Efforts can be made indirectly, however, to achieve information on the state of the catalyst under reaction conditions. A probe reaction that occurs under identical conditions to the reaction of interest might be used to count the number of sites available, assuming the probe reaction satisfies a number of assumptions. A good probe reaction for the accessibility of metal sites for inverse catalysts, for example, should be structure insensitive, such that the changes to site accessibility, which this work has shown to influence surface site distributions, do not affect the site-normalized probe reaction rate. It is likely that fundamentally structure-insensitive reactions do not actually exist in principle, but that reactions might be effectively assumed to be structure-insensitive under the correct operating conditions[43]. One example with some promise is alkene hydrogenation, for example, particularly for small alkenes that adsorb to a minimal amount of sites and utilize H_2, which has been shown to co-adsorb with a number of species on metal surfaces thanks in part to its small size.

Such reactions should also not be equilibrium limited or operated at maximum conversion in order to achieve relevant information from the probe reaction, though this can be adjusted by altering reactant concentration, catalyst loading, *etc*. Similarly, the probe reaction should proceed facilely under *identical* conditions to those of the reaction of interest (here, DHE or PHE HDO). In the case of alkene hydrogenation, for example, which proceeds very rapidly at high temperatures and pressures of H_2, careful consideration is needed to prevent equilibrium conversion from being achieved.

As has been alluded to, some of these techniques have been applied in a preliminary manner to the study of MO_x-Pt catalysts described in Chapter 3.3. Initial work was performed using CO DRIFTS in the presence of gas-phase CO during a TPD experiment (similar to the TPE experiments performed in Appendix A), with the goal of observing changes to Pt

availability at elevated temperature through the shape and area of the adsorbed CO feature. Analogous to standard CO DRIFTS analysis conducted throughout this dissertation, catalysts were pre-treated by reduction in 10% H_2/Ar at 325˚C for 1 hour prior to analysis.

Figure 6.1 below shows the spectrum of 6W6Pt catalysts exposed to 10% CO/Ar and ramped from 30˚C after saturation coverage was reached to 500˚C at 10˚C/min, followed by cooling to 30˚C at 10˚C/min. IR features associated with the gas-phase CO, which are quite

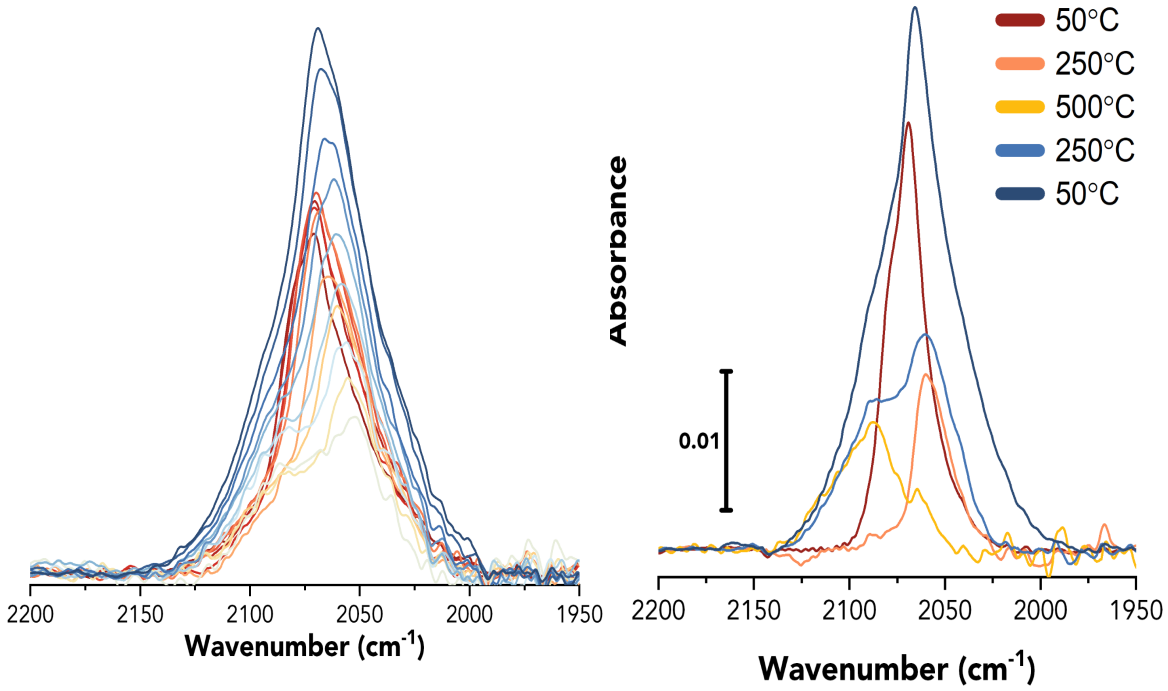

Figure 6.1: Preliminary results showing the response of 6W6Pt to a TPE procedure after reduction at 325˚C in 10% H_2, as was typically performed in Chapter 3. (b) shows selected temperatures for simplicity. Heating steps are shown in red and yellow, whereas cooling steps are shown in blue. Comparison of the spectra collected at the same temperature for either heating or cools shows that sites have been exposed by heating in 10% CO to 500˚C.

significant for 10% CO/Ar, have been subtracted by a reference spectrum obtained at the same temperature over a SiO_2-only bed. This methodology ensures that changes to the gas-phase CO signature, which tends to broaden and decrease in maximum intensity with increasing temperature due to the greater number of accessible vibrational states at elevated temperatures, are captured and do not introduce non-physical features into the resulting adsorbed CO spectra.

Lower concentrations of CO may be used for the gas-phase species, as these lower concentrations require less effort to deconvolute and remove from the adsorbed CO feature, though this results in significant desorption of the probe molecule from the catalyst surface at elevated temperature, thus limiting the amount of structural information that can be obtained. 1000 ppm CO in Ar was explored as a concentration for this purpose, as subtraction of the gas-phase signal is almost unnecessary, especially at elevated temperatures, but the resulting desorption provided incomplete information on the catalyst surface at temperatures relevant to the reactivity conducted here (275-325˚C).

A number of changes can be observed in the CO DRIFTS spectrum during the temperature ramp, shown in the selected spectra in Figure 6.1b. As temperature is increased up to 500˚C, CO peak area does decrease, indicating that some structural information is lost at these temperatures due to desorption. Higher CO concentrations or pressures would facilitate the suppression of desorption at these temperatures, but such conditions were not explored here, in part due to the potential hazards associated with high-pressure CO atmospheres in experiments conducted outside of specifically ventilated environments (i.e. not in a fume hood). Regardless, the loss in peak area is ~20%, suggesting that a majority of the structural information is retained even at the maximum temperatures studied here. Also, cooling steps ensure that whatever changes to the catalyst structure occur at elevated temperatures might be observed at identical coverage during the cooling step, presuming the oxide states are not metastable only at the highest temperatures.

Indeed, this comparison of heating and cooling steps at the same temperature, wherein CO coverage should be identical, demonstrates the ability to discern spectral changes. At 250˚C, for example, the cooling step shows greater adsorbed CO area and a general blue shift,

particularly to the well-coordinated (WC) Pt feature. One might consider that the blue shift of the WC feature might indicate sintering at elevated temperatures, as particle growth can result in blueshifts of this feature due to the increase of dipole-dipole coupling between CO molecules on larger extended surfaces for larger nanoparticles, but this is presumed not to be the case here. For one, the catalysts have been previously treated in O_2 at 600˚C for 6 hours during synthesis, under which conditions Pt is known to be extremely mobile, in part due to the transport of volatile PtO_2 species. The conditions of the TPE here are thus less prone to sintering from the standpoint of environmental conditions and Pt mobility. Additionally, it has been observed that the SMSI or inverse state is an effective method to suppress interparticle sintering due to either suppressed mobility of the metal nanoparticle on the support or the inhibition of coalescence by the oxide layer which might act as a "barrier" of sorts to metal-metal interactions preceding coalescence. Thus, from this perspective as well, sintering is perhaps not the most likely scenario. Additionally, it is also clear that the feature associated with adsorbed CO grows in strength after the thermal treatment in CO. This in itself is direct evidence against particle sintering, as it would be expected that particle sintering results in a loss of Pt surface area as particle sizes grow and total surface area diminishes.

Thus, the growth in adsorbed CO area and the blue shift of the adsorbed feature is likely due to WO_x rearrangement on the Pt surface. The blue shift of the adsorbed feature corresponds to the increased accessibility of WC Pt sites, either due to the migration of WO_x off of the Pt surface and back to the SiO_2 surface or through the aggregation of WO_x on the Pt surface. In the first case, it is possible that some extent of CO dissociation occurs at elevated temperatures that result in the oxidation of reduced WO_x species on the Pt surface, destabilizing their presence on the metal surface as was shown in environment-responsive studies in Chapter 3.2.

However, direct measurement of this is challenging considering that the CO peak area indicates that the extent of this change would be rather small as cited previously (~20% of the WO_x previously on Pt). Spectroscopic evidence of CO dissociation has been inconsistently observed for these catalysts previously after H_2 reduction, wherein saturation coverage for subsequent pulses of CO decreased. UV-Vis conducted for these samples showed no change to the absorption spectrum of these catalysts after high temperature CO exposure though, casting doubt on the structural explanation for these changes to saturation CO coverage. Thus, the exact causes of this behavior remain something of a mystery and underscores the interesting details available regarding WO_x reorganization should additional work be conducted in this direction.

6.2.3 Enhanced Structural Information via EXAFS

The drawback of utilizing probe molecule DRIFTS as a characterization technique in this work is that the information available gives only indirect information on the state of the reducible oxide domains themselves, essentially providing information about where the reducible oxides aren't, rather than where they actually are. While the work in this dissertation has underscored that the metal sites, in this case, Pt, are the sites responsible for a majority of the deoxygenation activity through metal-facilitated tautomerization, the results of Chapter 4 indicate that oxide decoration results in enhanced per-site deoxygenation rates compared to undecorated or unmodified catalysts. However, the trends of enhancement with increased coverage were not consistent between different oxide promoters, suggesting that the structures of the oxides evolved in different ways with increasing coverage on the metal surface. Thus,

identification of the manner in which these oxide structures evolve with coverage for oxide-modified catalysts is of interest.

Towards this end, there are a number of characterization techniques that may be attractive in identifying the structure of reduced oxide domains on the surface of metal nanoparticles. In Chapter 3, it was shown that Raman spectroscopy can provide insight into the W-O bonds of WO_x domains directly, indicating that W=O species were consumed during reduction, presumably into W-O species that were not apparently Raman active. In general, Raman might provide direct information regarding the chemical state of W bonding environments, which are often not accessible by infrared spectroscopies either due to overlapping absorptions in this structural regime (~1000 cm^{-1}) or due to selection rules that inhibit the interaction of these vibrational modes with infrared light. Some attempts were made, though not shown in this dissertation, to perform both *operando* and enhanced Raman spectroscopies, such as surface-enhanced Raman spectroscopy (SERS) through the use of SiO_2@Au nanoparticles for shell-isolated nanoparticle-enhanced Raman spectroscopy (SHINERS[44–47]), though both attempts proved outside the scope of this dissertation and likely represent individual dissertations of their own considering the experimental difficult of their collection.

Similarly, direct information can also be obtained via X-ray absorption (XAS) techniques. XAS, distinct from the more common X-ray diffraction technique (XRD), is typically performed at synchrotron radiation sources around the world for high-flux, broad-band X-ray sources. By conducting energy-resolved absorption experiments, information related to the oxidation state and coordination sphere can be obtained in x-ray absorption near-edge spectroscopy (XANES), as well as longer-range information about second- and third-

shell atomic neighbors through x-ray absorption fluorescence spectroscopy (EXAFS). Greater detail about the technical foundation and application of these techniques can be found elsewhere[48,49]. For the sake of this discussion, the structural information of atomic species such as W out to the second and third coordination shell could provide direct information as to the extent of W oligomerization on the surface, the presence or absence of direct Pt-W bonding, and confirmation regarding the decoration of WO_x adjacent to step edges.

One limitation of the EXAFS technique, however, is that it provides this elemental information for each W atom along the absorption length of the measurement, including those both associated with Pt and those associated with the support. In the case of $WO_x/Pt/SiO_2$ catalysts studied in this dissertation, a significant fraction of W can remain on the support, especially in the case of higher loading samples such as 6W6Pt or higher. However, at the same time, a high loading of W is favored to facilitate the formation of as much W-Pt interaction as possible, as the quality of the spectrum obtained is a function of the quantity of these domains that can be effectively formed. Thus, the synthesis procedure and materials utilized here failed to produce effective EXAFS information.

However, it is not difficult to imagine that materials synthesis approaches exist that enable the very specific decoration of Pt surfaces only with WO_x, thus maximizing the fraction of W atoms that are in contact with Pt surfaces at any given time. One of these approaches which has already been utilized by a number of different groups is atomic-layer deposition (ALD) of WO_x domains from WCl_6, which specifically decomposes over Pt surfaces but not the support, lending itself to higher selectivity towards these Pt-W interactions[50–52]. However, as this approach has been reported previously with some degree of success, despite somewhat

demanding apparatus and conditions for the synthesis itself, it will not be discussed further here.

One alternative synthetic approach that might lend itself equally as well to a higher fraction of W-Pt interaction than achieved through wet impregnation of WO_x alone is a stepwise colloidal approach to core-shell WO_x-Pt nanoparticles. Colloidal synthesis of nanoparticles lends itself well to the control of nanoparticle size and distribution through the direct tunability of a number of synthesis parameters. Pt nanoparticles have been synthesized in a range of shapes and sizes, both using protecting agents such as surfactants and without protecting agents[53]. Colloidal nanoparticles are also easily deposited onto the surfaces of supporting oxides, allowing the synthesis of well-defined heterogeneous catalysts[54,55].

One way that one might imagine to maximize W-Pt interactions through colloidal techniques is to grow WO_x shells directly onto Pt colloids prior to deposition on SiO_2 supports. Analogous approaches have previously been reported for the synthesis of FeO_x-decorated Pt nanoparticles as inverse catalysts[56]. Such a colloidal technique would offer similar control over the extent of decoration as achieved through wet impregnation catalysts and ALD, without the need for unconventional or specific equipment. After deposition, oxidation could be utilized to drive WO_x off of the Pt surface to the SiO_x support, but in close proximity to the Pt nanoparticles such that upon re-reduction, migration to the Pt surface occurs readily. Thus, colloidally synthesized catalysts would exhibit an identical structure to wet-impregnated catalysts, albeit with optimized W-Pt interactions.

The collection of XANES and EXAFS spectra for the colloidally-synthesized catalyst as a function of temperature would enable the determination of kinetics for oxide reduction and mobility, as well as information about the structure of WO_x on the Pt surface. Combining

this with measurements made via CO DRIFTS and CO chemisorption, relationships could be developed describing the structure of WO_x as a function of coverage. Stemming from this, a greater understanding of the extent of contiguous ensembles could be obtained, providing information as to the role of absorption geometry in HDO – i.e. does deoxygenation proceed through the planar adsorption of aromatics requiring larger contiguous ensembles as proposed in this work.

6.3 Outlook and Future Directions: Kinetic and Reactivity Measurements

6.3.1 Overview

The development of robust structure-activity relationships requires both the identification of atomically-accurate structures via advanced characterization techniques, as discussed above, as well as the measurement of kinetically-relevant reaction data. This can be challenging for dynamic catalysts, as the structure of the catalyst can be a function of both time and conditions, which can in turn manifest in transient behavior in catalyst activity, selectivity, and stability. In particular, the HDO of phenolics has proven difficult to understand precisely the mechanism of activity, in part due to the numerous potential reaction pathways that may ostensibly result in the formation of aromatics. Thus, careful reaction studies are still necessary, utilizing recent advances in the understanding of surface structure for MO_x/Pt catalysts both reported in the literature and this dissertation, which seek to identify the reactive pathway for phenolic deoxygenation in HDO. This will include reactions conducted over a wider range of conversions and contact times than currently available in the literature, particularly at the limit of low conversion to characterize the initial reactivity of the system, and further work towards understanding the predominant mechanism as a function of temperature and pressure.

Additionally, values for turnover frequency for HDO over MO_x/Pt catalysts remain only estimates at best because of uncertainty regarding the true number of sites at reaction conditions. Establishing reliable TOF measurements for these materials will facilitate the identification of oxide modification, either promotional or inhibitory, on the various reactions occurring during HDO on a per-site basis. Potential experimental approaches toward addressing these gaps in understanding are proposed below.

6.3.2 *Operando* Site Counting through Structure-Insensitive Probe Reactions

Though the CO TPE experiments over MO_x-Pt materials provide some information into the state of the catalyst at elevated temperatures, such as that additional sites may become accessible, it still presents a significant gap between *in situ* and *operando* characterization. To probe a more *operando* condition, a probe reaction, 1-decene hydrogenation, was conducted at the exact conditions under which DHE was performed, though in the absence of DHE. It was a concern that DHE adsorption would out-compete 1-decene for sites due to the relatively far stronger interactions of aromatics and oxygenates with the surface than aliphatic alkenes, though one might argue that this renders these probe reactions less than *operando* since the reaction of true interest is not concomitantly being performed. 1-decene hydrogenation was chosen as the probe reaction considering the small ensemble required for alkene adsorption, typically discussed for ethylene, though the use of a liquid reactant and product offered significant benefits for reaction workup. 1-decene was chosen over internal alkene isomers of decene to as closely mimic ethylene as possible and leave the terminal carbon unsubstituted, though some degree of isomerization to the more stable internal alkenes did occur during the reaction.

Figure 6.2 shows the reaction performance of 1-decene hydrogenation over WO_x-Pt catalysts with different WO_x loading at 275˚C and 20 bar of H_2, plotted alongside the hydrogenated product yield during DHE HDO over identical (same batch) catalysts. As shown previously in Chapter 3.2, the yield of hydrogenated ring products in the HDO of DHE decreases steeply with increasing WO_x loading, associated with the preferential decoration of WC Pt sites responsible for aromatic hydrogenation by reduced WO_x domains. However, comparing this to the yield of 1-decene hydrogenation, we observed marked changes. On its own scale, 1-decene hydrogenation follows a similar trend, decreasing with increasing WO_x loading as would be expected due to the loss of Pt sites for hydrogenation under reaction conditions. However, the total magnitude of the loss of sites is far lower, and the highest WO_x loading retains over 80% yield of decane. This suggests that the ensemble requirement for aromatic ring hydrogenation and alkene hydrogenation, which are known to be different, is the driving factor behind the differences in performance. These results point to the defective

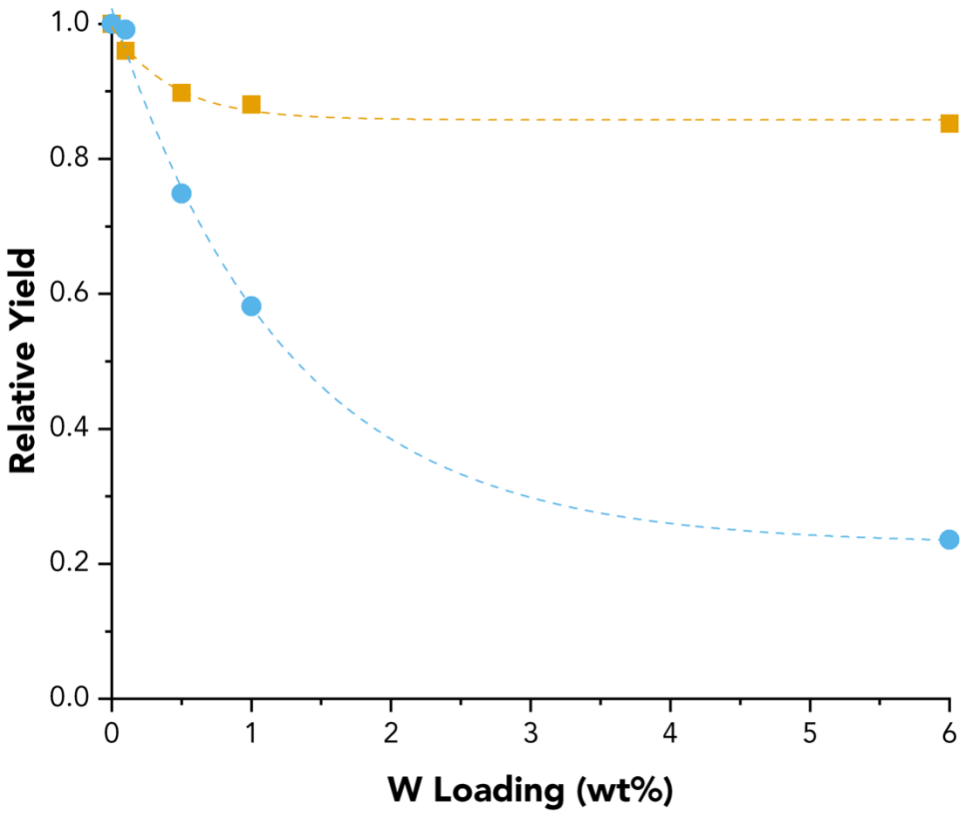

Figure 6.2: Reaction performance of DHE HDO (blue) and 1-decene hydrogenation (gold) over WO_x/Pt/SiO2 catalysts. While DHE HDO demonstrates a strong response to WO_x addition, 1-decene hydrogenation exhibits a more gradual loss of activity. This is in part attributed to the smaller ensemble requirement of 1-decene hydrogenation relative to DHE HDO.

decoration of the Pt surface by WO_x domains, leaving a sufficient number of small Pt ensembles available for alkene hydrogenation, while at the same time disallowing aromatic ring hydrogenation. Gorte et al. had previously proposed a similar mechanism to explain the HDO results of a NbO_x-Pt catalyst, wherein HDO activity suddenly increased above 300˚C. They proposed the mobility of NbO_x causing pinhole defects in the otherwise pristine oxide coating that enabled cresol access to underlying Pt sites, at which HDO occurred. In both cases, it seems oxide mobility and small ensembles may be the key to HDO activity over inverse, oxide-on-metal catalysts.

It is worth considering the driving forces behind such oxide rearrangement for decorated oxide-on-metal catalysts. The work presented in Chapter 3 demonstrates through ML-DFT that there is an enthalpic driving force behind the preferential decoration of WC Pt sites by reduced WO_x species and that meta-stable states with UC Pt occupation by WO_x are unlikely to form even at elevated temperatures. Thus, it is unlikely that enthalpy alone can explain the reorganization of WO_x, unless this reorganization occurs solely on WC Pt sites. For instance, ML-DFT models did not explore the effects of increased WO_x coverage in depth, which may result in the formation of extended agglomerates of WO_x which reorganize into 3D structures maximizing WO_x-WO_x interactions (pseudo-nanoparticles) compared to 2D WO_x-Pt interactions.

However, overall enthalpic drivers could be the explanation if we include the influence of adsorbates on the re-organization energetics. For instance, in the case of CO TPE experiments, the enthalpic penalty associated with removing WO_x from its preferred location on the Pt surface could be offset by the adsorption energy of CO to Pt, which is relatively high at ~140 kJ/mol, depending on coverage[57–59]. Similarly, under HDO conditions, the adsorption of aromatic species and oxygenates is known to occur strongly (~100 kJ/mol[60–62]) to the surface of metal nanoparticles, offering yet another source of enthalpic driving force to restructure oxide domains on metal surfaces, even under reducing conditions where decoration is predicted to be stable.

On the other hand, entropy might similarly influence the organization of WO_x at elevated temperatures, especially in the case of partial decoration where both undecorated and decorated sites exist. While the effects of enthalpic stabilization may overcome entropic considerations at low temperatures with respect to overall free energy, the temperature-

dependence of entropy may favor the disorganization of oxide domains at sub-monolayer coverages at higher temperatures, irrespective of the adsorbate environment.

2.3.3 Micro-TAP Reactors

While steady-state flow reactors exhibiting near-ideal plug flow are the workhorse of the kinetic experimentalist today due to their ease of operation and analysis through known models, such steady-state approaches exhibit limitations in the identification of mechanisms involving rapidly consumed intermediates, which are often invisible to these techniques. While operation at a range of conversions can often assist in elucidating these pathways for steady-state flow reactors, there are additional challenges operating at low conversions related to signal-to-noise in the analytic technique employed, typically either mass spectrometry or gas chromatography, or a combination of the two. In both cases, the presence of a steady-state flow of reactant and inert can obscure the signal associated with minority intermediate species. Additionally, the macroscopic scale of these reactors means that residence times are typically high enough that multiple gas-solid interactions may presumably take place throughout the length of the reactor, making it challenging to assign single-reaction events versus products of multiple reaction steps. Of course, in the context of HDO, this assignment of the reaction pathway continues to be a challenge. While a bulk of the mechanistic studies available point towards deoxygenation proceeding through a single, direct deoxygenation step over MO_x/Pt catalysts[50,52], conclusive evidence remains elusive. Additionally, a number of these studies investigate conversions much higher than 10%, meaning that discriminating between single and multiple reaction steps is challenging.

For the reasons above, non-steady-state or transient reaction techniques offer significant benefits in regard to complex kinetic networks. Examples of powerful transient techniques can also be observed in the field of characterization, where steady-state isotopic transient kinetic analysis (SSITKA[63–65]) and modulation excitation spectroscopy (MES[66,67]) techniques have been employed, albeit infrequently, to bring a new perspective to challenging problems in characterization such as the identification of spectator species in *operando* studies. However, typically, the analysis and modeling of transient reactions of heterogeneous catalysts is an intractable problem, limiting the application of such transient techniques to quantitative reaction kinetics.

Transient analysis of products (TAP) reactors, more frequently microreactors employing TAP fundamentals (micro-TAP), offer an operational reactor architecture facilitating both transient kinetic information and relatively facile quantitative analysis and modeling[68–71]. In TAP reactors, pulses of reactants are introduced to small catalyst beds such that the number of reactant molecules is typically smaller than the number of active sites present on the catalyst surface. In between pulses, no convective transport is provided, unlike in a flow system, meaning that molecule transport is primarily driven by Knudsen-like diffusion. This diffusional transport is easily modeled, and any deviations from the ideal Knudsen model can often be ascribed directly to reaction events. The exposure of such small quantities of reactant molecules also means that signal-to-noise ratios for TAP reactors are much higher than that of steady-state flow systems, enabling the confident identification of even minority intermediates. Essentially, micro-TAP reactors enable the sensitivity typically reserved for UHV and surface science experiments to be employed over realistic, powdered heterogeneous catalysts.

Recently, micro-TAP systems have been reported for the identification of structure sensitivity in the CO oxidation of Pt, identifying the oxidation of CO adsorbed atop well-coordinated Pt sites as the kinetically faster step compared to adsorbed O's reaction with CO bound to under-coordinated sites[72,73]. Interestingly, though only one catalyst was needed to achieve this information using this micro-TAP reactor (2 nm Pt/SiO_2), similar information could only be obtained in steady-state flow reactors through the use of multiple, size-varied Pt nanoparticles as has been previously reported.

A similar approach could be utilized to study MO_x/Pt catalysts for HDO in micro-TAP reactors to identify the reactivity occurring over well-coordinated and under-coordinated sites as a function of both oxide coverage and H_2 availability. Presumably, the use of low H_2 concentrations during pulses, or a pre-saturation with a known amount of H_2, could be used to modulate the activity towards hydrogenation, facilitating the deconvolution of deoxygenation away from hydrogenation, if the deoxygenation reaction pathway was not intrinsically connected through hydrogenated products. Additionally, the pulse broadening of products can be used to qualitatively assign products with more intermediates, as those with greater numbers of intermediate species typically exhibit longer surface residence times, leading to broader signals in analysis. Combining these approaches with the characterization techniques described in this dissertation would clarify on a kinetic basis the role of oxide modification on heterogenous MO_x/Pt catalysts.

2.4 Outlook and Future Direction: Impacts of this Work

A necessary step in the performance of fundamental research is the critical and honest assessment of the utility of the results. The work in this dissertation points towards the

influence of extended metal surfaces, exhibiting a high fraction of well-coordinated sites, facilitating the deoxygenation of phenolic substrates, moderated through the decoration of these surfaces with reducible metal oxides. While the catalysts achieve desirable activity, it must be noted that the catalyst architecture described throughout most of this dissertation, that is, $MO_x/Pt/SiO_2$, exhibits considerable shortcomings that will likely inhibit the commercial adoption of such a catalyst.

The zeitgeist of catalysis research today is atom efficiency[74]: in a global environment where catalytic metals are simultaneously exceedingly valuable and rare, a primary design rule should be that proposed catalysts utilize every atom to the maximum of its catalytic ability. Such design is both sustainable economically and environmentally, as the extraction of catalytically active metals is traditionally an environmentally ravaging process, occurring predominantly in regions with concerns about human rights violations and systemic exploitation. In considering this framework for proposed catalysts, it is perhaps not much of an exaggeration to state that the Pt wires explored by Humphrey Davies for hydrogen oxidation in 1823 would constitute only marginally worse atom efficiency than the catalysts employed in this dissertation. The importance of well-coordinated sites for reactivity described throughout this dissertation dictates that larger particle sizes must be employed in the absence of the stabilization of non-equilibrium shapes which may theoretically exhibit a higher fraction of these sites at smaller sizes. However, the movement towards atom efficiency in catalysis has propelled fundamental research in the opposite direction of large nanoparticles, instead focusing on the development and exploration of single atom catalysts, which in theory represent the maximal atom efficiency possible for a given catalyst structure. The Pt nanoparticles most frequently studied in this dissertation of ~10 nm in size contain only 10%

of their atoms on the surface for reactivity, representing a waste of 90% of the Pt atoms utilized in the system. This does not even take into account the additional Pt atoms decorated by reducible metal oxides in modified versions of this catalyst. It is likely accurate to estimate that upwards of 95% of the Pt atoms utilized in this research served no purpose for the sake of catalysis. Such waste of a costly component, with Pt prices reaching prices of over $USD 30,000/kg, is likely impractical in every application save for the most profitable catalyst utilization imaginable, of which biomass valorization to aromatics is not one. However, more careful evaluation of the economics of such a catalyst is required[75,76], considering that catalysts in industry are often leased, and the catalytic metal recovered and re-used at the end of each lease period.

While this does not in any way lessen the fundamental value of exploring this system, it does demand that this fundamental knowledge be employed in a different direction for future endeavors. Indeed, there have been some studies already that explore these modified catalysts formulated with earth-abundant substitutes for Pt such as Ni[77–79], Fe[80,81], and Cu[82–84]. Additional fundamental research will be needed to assess whether the conclusions reached for the Pt-catalyzed system can be translated to these burgeoning materials. If these materials cannot in their own right achieve comparable reactivity to the Pt-catalysts reported to date, then additional avenues must be explored for the reduction of Pt utilization. It has already been reported that Pt single atoms do not exhibit activity for HDO[85], and the bulk of the work in this dissertation seems to suggest that small nanoparticles are also ineffective for HDO, regardless of oxide modification. Other approaches could include bimetallic nanoparticles to dilute the concentration of Pt. Most ideally, one might imagine a core-shell nanoparticle utilizing an earth-abundant core that spontaneously enriches the surface with Pt due to surface energy and

adsorbate effects, both of which have some degree of support in current bimetallic literature. This would enable the use of large nanoparticles at significantly lower cost, though the waste of even earth-abundant metals in the core of large nanoparticles remains undesirable, if justifiable. In conclusion, continued research along the directions discussed here, building upon the work described throughout this dissertation, may realize sufficient catalytic activity, selectivity, and stability to justify the development of a biorefinery model utilizing lignin as a critical feedstock for the production of BTX aromatics.

2.5 References

1. Taylor, H. S. A Theory of the Catalytic Surface. *Proceedings of the Royal Society of London* **108**, 105–111 (1925).
2. Lee, K., Gu, G. H., Mullen, C. A., Boateng, A. A. & Vlachos, D. G. Guaiacol hydrodeoxygenation mechanism on Pt(111): Insights from density functional theory and linear free energy relations. *ChemSusChem* **8**, 315–322 (2015).
3. Lu, J., Behtash, S., Mamun, O. & Heyden, A. Theoretical Investigation of the Reaction Mechanism of the Guaiacol Hydrogenation over a Pt(111) Catalyst. *ACS Catal* **5**, 2423–2435 (2015).
4. Feibelman, P. J., Esch, S. & Michely, T. O Binding Sites on Stepped Pt(111) Surfaces. *Phys Rev Lett* **77**, 2257–2260 (1996).
5. Lan, X., Hensen, E. J. M. & Weber, T. Hydrodeoxygenation of guaiacol over Ni2P/SiO2–reaction mechanism and catalyst deactivation. *Appl Catal A Gen* **550**, 57–66 (2018).
6. Bykova, M. V., Zavarukhin, S. G., Trusov, L. I. & Yakovlev, V. A. Guaiacol hydrodeoxygenation kinetics with catalyst deactivation taken into consideration. *Kinetics and Catalysis* **54**, 40–48 (2013).
7. De Souza, P. M. *et al.* Hydrodeoxygenation of Phenol over Pd Catalysts. Effect of Support on Reaction Mechanism and Catalyst Deactivation. *ACS Catal* **7**, 2058–2073 (2017).
8. Kale, M. J. & Christopher, P. Utilizing Quantitative in Situ FTIR Spectroscopy to Identify Well-Coordinated Pt Atoms as the Active Site for CO Oxidation on Al2O3-Supported Pt Catalysts. *ACS Catal* **6**, 5599–5609 (2016).
9. Wang, J. *et al.* Surface structure of mass-selected niobium oxide nanoclusters on Au(111). *Nanotechnology* **32**, 1–12 (2021).
10. Lavroff, R. H., Wang, J., White, M. G., Sautet, P. & Alexandrova, A. N. Mechanism of Stoichiometrically Governed Titanium Oxide Brownian Tree Formation on Stepped Au(111). *Journal of Physical Chemistry C* **127**, 8030–8040 (2023).
11. Zhang, S. *et al.* Dynamical observation and detailed description of catalysts under strong metal-support interaction. *Nano Lett* **16**, 4528–4534 (2016).

12. Du, X. *et al.* Size-dependent strong metal-support interaction in TiO2 supported Au nanocatalysts. *Nat Commun* **11**, (2020).
13. Wu, Z., Li, Y. & Huang, W. Size-Dependent Pt-TiO2Strong Metal-Support Interaction. *Journal of Physical Chemistry Letters* **11**, 4603–4607 (2020).
14. Boffa, A., Lin, C., Bell, A. T. & Somorjai, G. A. Promotion of CO and CO2 Hydrogenation over Rh by Metal Oxides: The Influence of Oxide Lewis Acidity and Reducibility. *J Catal* **149**, 149–158 (1994).
15. Senanayake, S. D. *et al.* Hydrogenation of CO2 to Methanol on CeOx/Cu(111) and ZnO/Cu(111) Catalysts: Role of the Metal-Oxide Interface and Importance of Ce3+ Sites. *Journal of Physical Chemistry C* **120**, 1778–1784 (2016).
16. Cagnoli, M. V *et al.* Mossbauer and XPS spectroscopies studies of SMSI effect on Fe/Nb_2O_5 catalysts for the Fischer-Tropsch synthesis. *APPLIED CATALYSIS A-GENERAL* **326**, 113–119 (2007).
17. Liu, X. Y. *et al.* Strong Metal-Support Interactions between Gold Nanoparticles and ZnO Nanorods in CO Oxidation. *J Am Chem Soc* **134**, 10251–10258 (2012).
18. Figueiredo, W. T. *et al.* New insights on the electronic factor of the SMSI effect in Pd/TiO_2 nanoparticles. *Appl Surf Sci* **574**, (2022).
19. Breckner, C. J. *et al.* Controlled site coverage of strong metal-support interaction (SMSI) on Pd NP catalysts. *Catal Sci Technol* **13**, 157–169 (2022).
20. Zhu, Y. *et al.* Inverse iron oxide/metal catalysts from galvanic replacement. *Nat Commun* **11**, (2020).
21. Zhang, J. & Medlin, J. W. Catalyst design using an inverse strategy: From mechanistic studies on inverted model catalysts to applications of oxide-coated metal nanoparticles. *Surface Science Reports* vol. 73 117–152 Preprint at https://doi.org/10.1016/j.surfrep.2018.06.002 (2018).
22. Schoiswohl, J., Surnev, S. & Netzer, F. P. Reactions on inverse model catalyst surfaces: atomic views by STM. *Top Catal* **36**, 91–105 (2005).
23. Zhang, B. & Qin, Y. Interface Tailoring of Heterogeneous Catalysts by Atomic Layer Deposition. *ACS Catalysis* vol. 8 10064–10081 Preprint at https://doi.org/10.1021/acscatal.8b02659 (2018).
24. Kapiamba, K. F., Otor, H. O., Viamajala, S. & Alba-Rubio, A. C. Inverse Oxide/Metal Catalysts for CO2Hydrogenation to Methanol. *Energy and Fuels* vol. 36 11691–11711 Preprint at https://doi.org/10.1021/acs.energyfuels.2c02131 (2022).
25. Beck, A. *et al.* The dynamics of overlayer formation on catalyst nanoparticles and strong metal-support interaction. *Nat Commun* **11**, 1–8 (2020).
26. Monai, M. *et al.* Restructuring of titanium oxide overlayers over nickel nanoparticles during catalysis. *Science (1979)* **380**, 644–651 (2023).
27. Hansen, T. W., Wagner, J. B. & Dunin-Borkowski, R. E. Aberration corrected and monochromated environmental transmission electron microscopy: challenges and prospects for materials science. *MATERIALS SCIENCE AND TECHNOLOGY* **26**, 1338–1344 (2010).
28. Zhang, H. *et al.* In Situ Atomic-Scale Observation of Silver Oxidation Triggered by Electron Beam Irradiation. *NANOMATERIALS* **11**, (2021).
29. Song, K., Sauter, D. J., Wu, J. S., Dravid, V. P. & Stair, P. C. Evolution of High-Energy Electron Beam Irradiation Effects on Zeolite Supported Catalyst: Metal Nanoprecipitation. *ACS Catal* **2**, 384–390 (2012).

30. Wang, Y. Z., Niu, Y. M., Gao, T. T., Liu, S. Y. & Zhang, B. S. Assessing the Effect of the Electron-Beam Irradiation on Pd/Ga_2O_3 Catalyst under Ambient Pressure. *ChemCatChem* **12**, 4765–4769 (2020).
31. Su, D. S., Zhang, B. & Schlögl, R. Electron microscopy of solid catalysts - Transforming from a challenge to a toolbox. *Chem Rev* **115**, 2818–2882 (2015).
32. Datye, A. K. Electron microscopy of catalysts: Recent achievements and future prospects. in *Journal of Catalysis* vol. 216 144–154 (Academic Press Inc., 2003).
33. Mitchell, S. *et al.* Automated Image Analysis for Single-Atom Detection in Catalytic Materials by Transmission Electron Microscopy. *J Am Chem Soc* (2021) doi:10.1021/jacs.1c12466.
34. Chakrabarti, A. *et al.* A decade plus of operando spectroscopy studies. *Catal Today* **283**, 27–53 (2017).
35. Weckhuysen, B. M. Determining the active site in a catalytic process:: *Operando* spectroscopy is more than a buzzword. *PHYSICAL CHEMISTRY CHEMICAL PHYSICS* **5**, 4351–4360 (2003).
36. Frey, H., Beck, A., Huang, X., Van Bokhoven, J. A. & Willinger, M. G. *Dynamic Interplay between Metal Nanoparticles and Oxide Support under Redox Conditions*. https://www.science.org (2024).
37. Kim, D. *et al.* Metal Encapsulation-Driven Strong Metal-Support Interaction on Pt/Co3O4 during CO Oxidation. *ACS Catal* **13**, 5326–5335 (2023).
38. Liu, Z. M. *et al.* Poisoning and competitive adsorption effects during phenol hydrogenation on platinum in water-alcohol mixtures. *APPLIED CATALYSIS A-GENERAL* **585**, (2019).
39. Gopeesingh, J. *et al.* Kinetic and Mechanistic Analysis of the Hydrodeoxygenation of Propanoic Acid on Pt/SiO_2. *Ind Eng Chem Res* **60**, 16171–16187 (2021).
40. Murzin, D. Y. Catalyst deactivation and structure sensitivity. *Catal Sci Technol* **4**, 3340–3350 (2014).
41. Yu, X. W. & Pickup, P. G. Mechanistic study of the deactivation of carbon supported Pd during formic acid oxidation. *Electrochem commun* **11**, 2012–2014 (2009).
42. Chee, S. W., Lunkenbein, T., Schlögl, R. & Roldán Cuenya, B. Operando Electron Microscopy of Catalysts: The Missing Cornerstone in Heterogeneous Catalysis Research? *Chemical Reviews* vol. 123 13374–13418 Preprint at https://doi.org/10.1021/acs.chemrev.3c00352 (2023).
43. Crampton, A. S. *et al.* Assessing the concept of structure sensitivity or insensitivity for sub-nanometer catalyst materials. *Surf Sci* **652**, 7–19 (2016).
44. Zhang, H. *et al. In situ* dynamic tracking of heterogeneous nanocatalytic processes by shell-isolated nanoparticle-enhanced Raman spectroscopy. *Nat Commun* **8**, (2017).
45. Ballotin, F. C., Hartman, T., Koek, J., Geitenbeek, R. G. & Weckhuysen, B. M. Operando Shell-Isolated Nanoparticle-Enhanced Raman Spectroscopy of the NO Reduction Reaction over Rhodium-Based Catalysts. *CHEMPHYSCHEM* **22**, 1595–1602 (2021).
46. Kuruvinashetti, K., Zhang, Y. X., Li, J. N. & Kornienko, N. Shell isolated nanoparticle enhanced Raman spectroscopy for renewable energy electrocatalysis. *NEW JOURNAL OF CHEMISTRY* **44**, (2020).
47. Hartman, T. & Weckhuysen, B. M. Thermally Stable TiO_2- and SiO_2-Shell-Isolated Au Nanoparticles for In Situ Plasmon-Enhanced Raman Spectroscopy of Hydrogenation Catalysts. *CHEMISTRY-A EUROPEAN JOURNAL* **24**, 3733-+ (2018).

48. Finzel, J. *et al.* Limits of Detection for EXAFS Characterization of Heterogeneous Single-Atom Catalysts. *ACS Catal* **13**, 6462–6473 (2023).
49. Bare, S. R. & Ressler, T. Characterization of Catalysts in Reactive Atmospheres by X-ray Absorption Spectroscopy. in *ADVANCES IN CATALYSIS, VOL 52* (eds. Gates, B. C. & Knozinger, H.) vol. 52 339–465 (2009).
50. Wang, C. *et al.* Mechanistic Study of the Direct Hydrodeoxygenation of m -Cresol over WOx-Decorated Pt/C Catalysts. *ACS Catal* **8**, 7749–7759 (2018).
51. Wang, C. *et al.* A Study of Tetrahydrofurfuryl Alcohol to 1,5-Pentanediol Over Pt-WO_x/C. *Catal Letters* **148**, 1047–1054 (2018).
52. Huang, R., Kwon, O., Lin, C. & Gorte, R. J. The effects of SMSI on m-Cresol hydrodeoxygenation over Pt/Nb2O5 and Pt/TiO2. *J Catal* **398**, 102–108 (2021).
53. Peng, Z. & Yang, H. Designer platinum nanoparticles: Control of shape, composition in alloy, nanostructure and electrocatalytic property. *Nano Today* vol. 4 143–164 Preprint at https://doi.org/10.1016/j.nantod.2008.10.010 (2009).
54. Cargnello, M. *et al.* Control of metal nanocrystal size reveals metal-support interface role for ceria catalysts. *Science (1979)* **341**, 771–773 (2013).
55. Oh, J. *et al.* Colloidally Engineered Pd and Pt Catalysts Distinguish Surface- and Vapor-Mediated Deactivation Mechanisms. *ACS Catal* **13**, 1812–1822 (2023).
56. Wu, P. *et al.* Harnessing strong metal–support interactions via a reverse route. *Nat Commun* **11**, (2020).
57. Gunasooriya, G. T. K. K. & Saeys, M. CO Adsorption on Pt(111): From Isolated Molecules to Ordered High-Coverage Structures. *ACS Catal* **8**, 10225–10233 (2018).
58. Guo, C., Wang, Z., Wang, D., Wang, H. F. & Hu, P. First-Principles Determination of CO Adsorption and Desorption on Pt(111) in the Free Energy Landscape. *Journal of Physical Chemistry C* **122**, 21478–21483 (2018).
59. Abild-Pedersen, F. & Andersson, M. P. CO adsorption energies on metals with correction for high coordination adsorption sites - A density functional study. *Surf Sci* **601**, 1747–1753 (2007).
60. Singh, N. & Campbell, C. T. A Simple Bond-Additivity Model Explains Large Decreases in Heats of Adsorption in Solvents Versus Gas Phase: A Case Study with Phenol on Pt(111) in Water. *ACS Catal* 8116–8127 (2019) doi:10.1021/acscatal.9b01870.
61. Verma, A. M. & Kishore, N. Platinum catalyzed hydrodeoxygenation of guaiacol in illumination of cresol production: A density functional theory study. *R Soc Open Sci* **4**, (2017).
62. Chaudhary, N., Hensley, A., Collinge, G., Wang, Y. & McEwen, J. S. Coverage-Dependent Adsorption of Phenol on Pt(111) from First Principles. *Journal of Physical Chemistry C* **124**, 356–362 (2020).
63. Wang, X., Shi, H., Kwak, J. H. & Szanyi, J. Mechanism of CO2 Hydrogenation on Pd/Al2O3 Catalysts: Kinetics and Transient DRIFTS-MS Studies. *ACS Catal* **5**, 6337–6349 (2015).
64. Nelson, N. C., Nguyen, M. T., Glezakou, V. A., Rousseau, R. & Szanyi, J. Carboxyl intermediate formation via an in situ-generated metastable active site during water-gas shift catalysis. *Nat Catal* **2**, 916–924 (2019).
65. Janssens, P., Poissonnier, J., Chakkingal, A., Bos, R. & Thybaut, J. W. Recent advances in the use of Steady-State Isotopic Transient Kinetic Analysis data in (micro)kinetic modeling for catalyst and process design. *Catal Commun* **179**, (2023).

66. Shulda, S. & Richards, R. M. Modulation Excitation Spectroscopy with Phase-Sensitive Detection for Surface Analysis. in *New Materials for Catalytic Applications* 121–132 (Elsevier Inc., 2016). doi:10.1016/B978-0-444-63587-7.00005-6.
67. Müller, P. & Hermans, I. Applications of Modulation Excitation Spectroscopy in Heterogeneous Catalysis. *Industrial and Engineering Chemistry Research* vol. 56 1123–1136 Preprint at https://doi.org/10.1021/acs.iecr.6b04855 (2017).
68. Lobera, M. P., Téllez, C., Herguido, J., Schuurman, Y. & Menéndez, M. TAP studies of Pt-Sn-K/γ-Al_2O_3 catalyst for propane dehydrogenation. *CHEMICAL ENGINEERING JOURNAL* **171**, 1317–1323 (2011).
69. Engl, T., Langer, M., Freund, H., Rubin, M. & Dittmeyer, R. Tap Reactor for Temporally and Spatially Resolved Analysis of the CO_2 Methanation Reaction. *CHEMIE INGENIEUR TECHNIK* **95**, 658–667 (2023).
70. Shekhtman, S. O., Yablonsky, G. S., Gleaves, J. T. & Fushimi, R. R. Thin-zone TAP reactor as a basis of 'state-by-state transient screening'. *Chem Eng Sci* **59**, 5493–5500 (2004).
71. Gleaves, J. T., Yablonsky, G., Zheng, X. L., Fushimi, R. & Mills, P. L. Temporal analysis of products (TAP)-Recent advances in technology for kinetic analysis of multi-component catalysts. *JOURNAL OF MOLECULAR CATALYSIS A-CHEMICAL* **315**, 108–134 (2010).
72. Brandão, L., High, E. A., Kim, T. S. & Reece, C. Simplifying the Temporal Analysis of Products reactor. *Chemical Engineering Journal* **478**, (2023).
73. Kim, T. S., O'Connor, C. R. & Reece, C. Interrogating site dependent kinetics over SiO2-supported Pt nanoparticles. *Nat Commun* **15**, (2024).
74. Yang, X. F. *et al.* Single-atom catalysts: A new frontier in heterogeneous catalysis. *Acc Chem Res* **46**, 1740–1748 (2013).
75. Van Allsburg, K. M., Tan, E. C. D., Super, J. D., Schaidle, J. A. & Baddour, F. G. Early-stage evaluation of catalyst manufacturing cost and environmental impact using CatCost. *Nat Catal* **5**, 342–353 (2022).
76. Petel, B. E., Van Allsburg, K. M. & Baddour, F. G. Cost-Responsive Optimization of Nickel Nanoparticle Synthesis. *Adv Sustain Syst* (2023) doi:10.1002/adsu.202300030.
77. Yang, F. F., Wang, H., Han, J. Y., Ge, Q. F. & Zhu, X. L. In fluence of Re addition to Ni/SiO 2 catalyst on the reaction network and deactivation during hydrodeoxygenation of m - cresol. *Catal Today* **347**, 79–86 (2020).
78. Deplazes, R. *et al.* Melt infiltration for the preparation of finely dispersed Ni-FeO_x nanoparticles on SBA-15 for the hydrodeoxygenation of m-cresol. *Catal Today* **430**, (2024).
79. Lee, H., Cho, E. B., Jung, S. C., Kim, S. C. & Park, Y. K. Hydrocarbons Production from m-Cresol as a Lignin Model Compound Over Nickel Silicate Catalysts. *J Nanosci Nanotechnol* **20**, 5738–5741 (2020).
80. Hong, Y. C., Zhang, S. R., Tao, F. F. & Wang, Y. Stabilization of Iron-Based Catalysts against Oxidation: An *In Situ* Ambient-Pressure X-ray Photoelectron Spectroscopy (AP-XPS) Study. *ACS Catal* **7**, 3639–3643 (2017).
81. Hong, Y. C. & Wang, Y. Elucidation of reaction mechanism for *m*-cresol hydrodeoxygenation over Fe based catalysts: A kinetic study. *Catal Commun* **100**, 43–47 (2017).
82. Wang, X. F. *et al.* Synergistic effect for selective hydrodeoxygenation of anisole over Cu-ReOx/SiO2. *Catal Today* **365**, 223–234 (2021).

83. Sosa, L. F. *et al.* Study of the performance of SiO_2-supported Mo_2C and metal-promoted Mo_2C catalysts for the hydrodeoxygenation of m-cresol. *APPLIED CATALYSIS B-ENVIRONMENTAL* **331**, (2023).
84. Dickinson, J. G. & Savage, P. E. Development of NiCu Catalysts for Aqueous-Phase Hydrodeoxygenation. *ACS Catal* **4**, 2605–2615 (2014).
85. Resasco, J. *et al.* Relationship between Atomic Scale Structure and Reactivity of Pt Catalysts: Hydrodeoxygenation of m-Cresol over Isolated Pt Cations and Clusters. *ACS Catal* **10**, 595–603 (2020).

Appendix A: Evaluation of Penetration Depth for DRIFTS: Consequences for Quantification and Analysis

A.1 Introduction

Optical spectroscopies are essential tools for the characterization of solid-state materials[1–3]. In particular, infrared spectroscopy finds broad utilization due to its low cost, simple instrumentation, and ability to probe a broad range of chemically important functionalities in the near-IR, mid-IR, and far-IR regions[4–8]. Infrared spectroscopy, which almost ubiquitously indicates Fourier transform infrared spectroscopy (FT-IR) in modern instruments, can be broken down into a range of categories based on the means by which the infrared light is exposed to the sample of interest, including transmission, diffuse reflectance (DRIFTS), and attenuated total reflectance (ATR), though other techniques exist for unique sample requirements[9,10].

In addition to selecting the technique most compatible with the sample of interest, it is equally important to consider the information that is desired. For instance, ATR is typically employed for the study of samples that require *in situ* exposure to a liquid medium, such as electrochemical cells under operation or operation-like conditions, as other techniques are less equipped to facilitate light transmission through the liquid medium[11–14]. ATR circumvents this by operating on the fundamental of an evanescent wave through the sample of interest, allowing the spectrometer to measure the liquid-sample interface through the sample itself, allowing the sample to act as the barrier between the spectrometer and the liquid medium. On the other hand, the transmission mode enables the most direct application of the Beer-Lambert Law for the quantification of IR absorbance features[15–17]. Thus, the selection of the FT-IR technique is constrained by the sample, environment, and desired information.

In the study of heterogeneous catalysts, where the samples are often optically opaque or highly absorbing in the IR and visible regions, transmission becomes challenging, requiring sample preparation which provides sample wafers thin enough to be at least somewhat infrared transparent – this understandably comes with challenges. Dilution with an IR-transparent matrix is possible, such as KBr, though there is some indication that the presence of an additional matrix can influence spectral features, either through direct electronic interaction with the sample or the formation of electrical dipoles near the sample[18]. ATR is often not ideal for these samples either, as the infrared beam interacts with only a small fraction of the sample, providing low signal-to-noise ratio measurements[19].

For these optically non-transparent materials, the diffuse reflectance mode (DRIFTS) is preferable[6,18]. In this mode, loose powders are prepared into a bed and subjected to the infrared beam without further preparation. After undergoing a number of complex optical phenomena[20–22] such as transmission, absorption, and reflection at each particle interface, a fraction of the incident light is diffusely reflected back towards the detector after being captured by an ellipsoidal mirror. The optical design of DRIFTS scattering as well as the ability to probe optically opaque samples while still measuring an IR signal makes it particularly attractive for *in situ* or *operando* studies of these materials across a range of temperatures, pressures, and atmospheric compositions[23–25].

However, one challenge faced by DRIFTS as a direct result of the optical mode in which it is conducted is the uncertainty regarding the quantifiability of the information obtained directly from spectra[26]. Whereas transmission FT-IR is easily analyzed through the Beer-Lambert Law, the unknown nature of reflection and absorption events in the powdered beds of DRIFTS samples complicated such analysis, though there have been attempts to

employ the Beer-Lambert Law to DRIFTS[27]. Importantly, the light-matter interactions in the sample bed are both a function of the sample (absorptivity, index of reflection, particle size, etc.) as well as the sample preparation (dilution, void fraction, thickness, etc.). The broad scope of parameters affecting the resulting spectra thus makes reliable quantification a continued challenge in DRIFTS. Thus, the status quo has typically instructed that DRIFTS spectra not be used for inter-sample quantification, though intra-sample quantification by the comparison of two or more spectral features is accepted[28–30] and broadly used to estimate phenomena such as surface reaction kinetics.

One metric that is significantly impacted by the above sample characteristics is the depth of penetration of the infrared light. Generally, DRIFTS is not considered a surface-sensitive technique because the penetration depth of light has been estimated to be on the order of 50-100 μm into the sample itself[31–35]. Interestingly, this penetration depth estimate seems to be specifically for the case of mid-IR DRIFTS, which is the most common wavelength utilized for IR spectroscopy. However, other reports have been made in the near-IR regime, at a shorter wavelength than mid-IR, wherein experimental data pointed to DRIFTS penetrating only 1 or 2 particle diameters into the sample[36]. However, these estimates for the penetration depth of light have generally been made for systems with particle sizes greater than 10 μm. In this regime, the particle sizes are around the same order of magnitude as the incident infrared light (~5 μm), lending itself to unique scattering behaviors. The two-flux Kubelka-Munk theory, which is the most frequently employed theoretical approach to the scattering of light in DRIFTS and is thus frequently used for semi-quantitative DRIFTS[37–39], implicitly assumes that the powder is composed of particles much larger than the wavelength of light[20]. However, little is known about the light-matter interactions in the case of modern catalytic materials, which

exhibit particle sizes far smaller than the wavelength of light in DRIFTS[40], calling into question the applicability of Kubelka-Munk theory to these systems.

Considering that Kubelka-Munk theory likely cannot capture the scattering behavior of modern nanomaterials, it is reasonable to believe *a priori* that the penetration depth for these materials may be significantly different than original assumptions for DRIFTS which were built on studies of micron-scale pigments and crystallites. Moreover, there have been some analyses recently that have brought into question the penetration depth during DRIFTS analysis. Our lab has previously reported on the study of CO binding energy to Rh single atom species on Rh/Al_2O_3 catalysts and found that temperature-programmed desorption (TPD) during DRIFTS enabled CO binding energy estimations in good agreement with theory[41]. However, CO re-adsorption is a known challenge during TPD experimental methods which probe greater than ~20 micron sample beds[42]. These results consistently suggest that the penetration depth of DRIFTS for these samples is less than previously thought. Results from other authors have pointed to similar results. To date, though, the development of a material architecture that enables the measurement of DRIFTS penetration depth has been challenging, typically relying on pressed wafers akin to transmission measurements which clearly have experimental limitations in thickness. For instance, the study of $Ce_xZr_{1-x}O_2$ materials utilized a similar method to estimate penetration depth during DRIFTS analysis, resulting in a minimum wafer size of 500 nm[43]. Considering that this is still two orders of magnitude larger than the primary particle sizes employed in previous work on Rh/Al_2O_3 catalysts[41], a new method was required.

Herein, this work reports on the development of a drop-cast film methodology to carefully mediate the thickness of a particle-based film atop a standardized pressed powder

pellet. Pt/SiO_2 catalysts are pressed into a pellet and CO probe molecule DRIFTS is used to measure the penetration of DRIFTS light reaching the pellet. To simulate the penetration of DRIFTS light into a powder bed, powder films are drop-cast atop the pellet at varying thicknesses and the resulting DRIFTS intensity is measured. Since this technique does not rely on the processing of a wafer or other physically measured material, the film thicknesses accessible here are much thinner than previously considered. The results from the model system are then supplemented with additional application-based studies using TPD and equilibrium isobar experiments to demonstrate that TPD analysis corroborates more established equilibrium desorption measurements. Importantly, this can only be the case in the absence of readsorption for strongly binding molecules like CO, supporting a revised perspective in the penetration depth of DRIFTS analysis for certain systems. The results here also support the ability to utilize DRIFTS as a means to estimate inter-sample characteristics such as CO adsorption and explain the good agreement between adsorbed CO peak area and CO chemisorption for WO_x/Pt materials.

A.2 Results

A.2.1 Theory

At its most fundamental, DRIFTS utilizes the scattering behavior of light in powder beds to irradiate a representative portion of the sample and enable high enough adsorptions of the irradiant radiation to be measured by a detector. Typically, this scattering of light off of particles is a complex phenomenon depending on both the incidence direction and material properties, among other things. At a high level, the scattering behavior can be understood in terms of three categories which have distinct directional scattering properties relative to the

particle itself[44]. The dominant scattering regime for any particle can be broadly defined in terms of the ratio of particle size to incident light wavelength, or γ:

$$\gamma = \frac{D_p}{\lambda} \quad (1)$$

In the geometric regime, $\gamma >> 1$, and particles are far larger than the incident wavelength, causing light to scatter off of the particle in a direction highly dependent on the geometry of the particle itself. As particle size shrinks and γ approaches 1, the Mie scattering regime better describes scattering dependence. In Mie scattering, light is predominantly scattered forward for spherical particles, with a small component of omnidirectional scatter. Further decreasing particle size towards $\gamma << 1$ results in a special case of Mie scattering called Rayleigh scattering

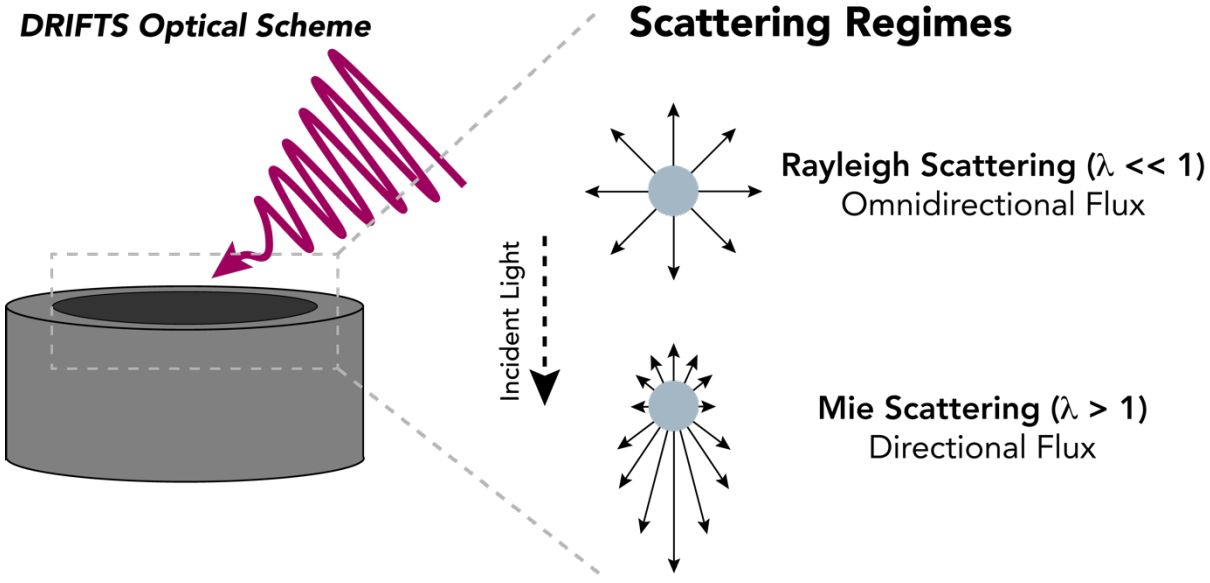

Scheme A.1: Schematic describing the magnitude and direction changes of scattering in different regimes determined by γ, or the ratio of particle size to incident wavelength. For particle sizes much smaller than the wavelength of light ($\gamma \ll 1$), Rayleigh scattering occurs where scattering is unidirectional. For particle sizes the same size or larger than incident light, Mie scattering predominates, where scattering occurs primarily in the forward direction. The magnitude of the scattering anisotropy increases consistently with the increase of γ.

where light is omnidirectionally scattered for spherical particles with no directional dependence on the incident light. A summary of the scattering behaviors for these two regimes is summarized in Scheme A.1.

While the exact scattering coefficient, which describes the magnitude of scattering for incident light, for the Mie regime is computationally intractable for heterogeneous scatterers such as the powders typically used in the diffuse reflectance experiments relevant to catalysis, the Rayleigh approximation provides a scattering cross-section for the Rayleigh regime as[44]:

$$\sigma_S = \frac{(2\pi)^5 D_p^6}{3\lambda^4} \frac{n^2 - 1}{n^2 + 2} \quad (2)$$

Where σ_S is the Rayleigh scattering cross-section, D_p is the particle diameter, λ is the wavelength of irradiant light, and n is the index of refraction of the scatterer. Considering an incident infrared wavelength of roughly 5 μm, corresponding to ~2000 cm^{-1} in DRIFTS, the limit to apply the Rayleigh approximation would be 1/16th the incident wavelength, or in this case ~300 nm. Importantly, the design of high surface area supports has driven the particle size of support particles in modern catalytic applications often far below this limit. Thus, one would expect that particles below ~300 nm in size will scatter light significantly differently in DRIFTS than particles larger than 300 nm in size, and importantly this scattering effect will

further depend on the particle size, among other properties such as particle shape and index of refraction.

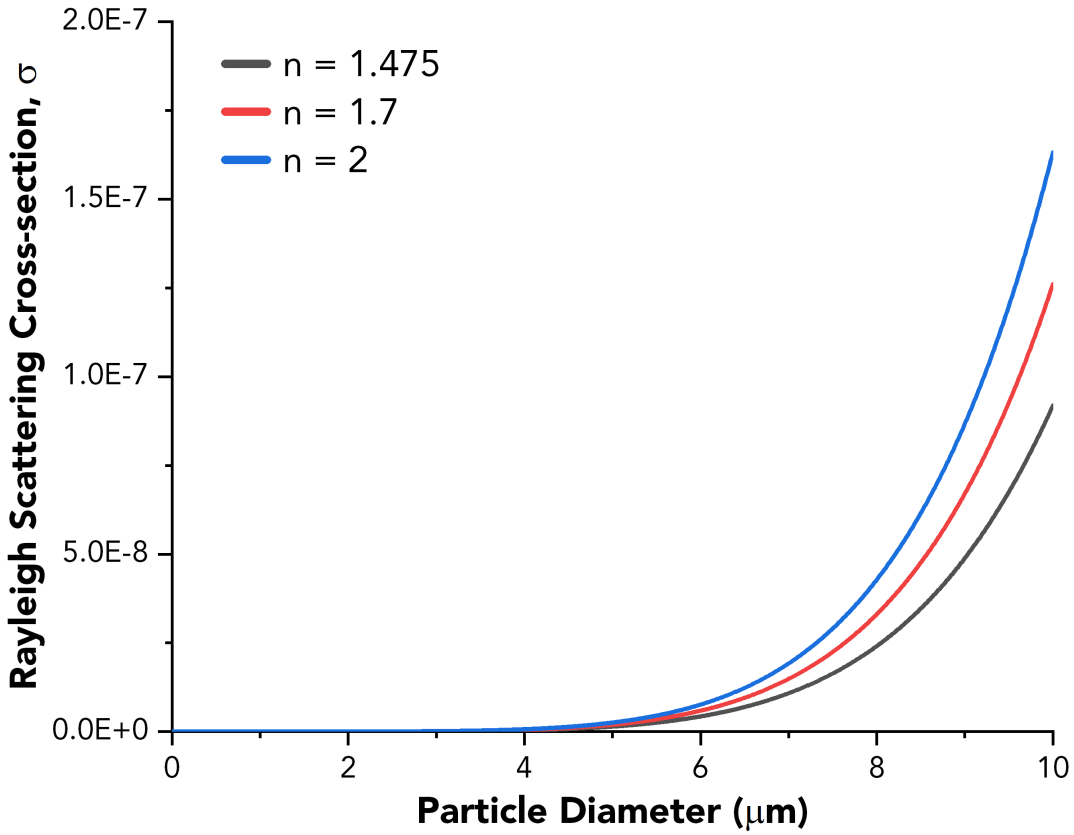

Figure A.1: Dependence of the Rayleigh scattering cross-section on particle size for a selection of 3 difference index of refractions corresponding to academically-relevant catalyst supports which are typically available as sub-20 nm nanoparticles (SiO_2, Al_2O_3, TiO_2). Clearly, there is a strong, exponential dependence of Rayleigh scattering cross-section on particle size for all particle sizes. A smaller dependence exists for particle index of refraction.

Using the equation above describing the cross-section of Rayleigh scattering, Figure A.1 shows the predicted effect of particle size and index of refraction on the Rayleigh scattering magnitude. It can be seen that there is an exponential influence of particle size on scattering cross-section, suggesting that particle size is an important consideration when determining the penetration depth in DRIFTS experiments. Specifically, the decreasing Rayleigh scattering coefficient with decreasing particle size is suggestive of the fact that with decreasing particle

size, a larger fraction of the light will undergo different light-matter interactions such as specular reflection or absorption. One might expect that in the case of the most specularly reflective surface, such as a mirror, the penetration depth for light would be exceedingly low as only a minimal fraction of the incident light would scatter or transmit into the next layer of particles.

Examining Eq. 2 also suggests that particle composition, namely through the index of refraction, should also influence the extent of scattering for particles of the same size. Considering the breadth of transition metal oxides used for modern-day catalyst supports, the effect of altering the index of refraction was also studied using the same approach. For this, SiO_2, Al_2O_3, and TiO_2 were investigated, with indexes of refraction of 1.4, 1.7, and 2.4, respectively. The results of this model, shown in Figure A.1, show that there is a weaker, but measurable, effect of particle composition on scattering alone relative to particle size as shown in Figure A.1.

The assessment above provides a cursory rationale as to why the influence of particle size must be taken into account when determining the penetration depth during a DRIFTS experiment. Specifically, modern nanomaterials that exhibit a diminished Rayleigh scattering cross-section as defined by Eq. 2 likely result in a suppressed depth of penetration of incident light, demanding a revisiting of experimental penetration depth determination for these systems. Additionally, the results suggest that particle identity may play a role through changes in the index of refraction. In order to validate these theoretical trends, an experimental system was developed using thin oxide films to explore these effects in more detail.

A.2.2 Model Film System

In order to experimentally validate the results of the theoretical assessment initially conducted above, a model system was required. However, these results and previous literature reports have suggested that the penetration depth of DRIFTS can be significantly smaller than even 100 microns, representing a significant experimental challenge to probe. For instance, in the work discussed above using $Ce_xZr_{1-x}O_2$ wafers pressed at known thicknesses, the limit of wafer thickness was set at 100 microns[43]. Thus, realistically, a different approach was required to achieve controllable film thicknesses smaller than this.

For this purpose, drop-cast films were selected. Drop-casting refers to the use of a film created by the dropwise addition of a solvent to a substrate, wherein the solvent either contains a suspended particle or dissolved solute[45,46]. As the solvent, typically a low-boiling point alcohol or organic, evaporates from the substrate, the solid or dissolved solute is deposited on the substrate in a manner that can be controlled by a number of factors, including evaporation rate, solvent selection, and thermal gradients, among others[47]. In the ideal case, drop-casting can achieve conformal, thin films with thicknesses determined by the deposited species of interest. In this case, the employment of SiO_2 nanoparticles as the suspended species in the solvent allows for theoretical film thicknesses on the order of the diameter of the SiO_2 nanoparticles themselves, enabling film thickness control far below the 100 microns previously studied. Additionally, whereas pressed wafers exhibit a significant change in bulk density compared to typically prepared powder beds used in DRIFTS, which may influence the light-matter interactions and scattering path, drop-cast films should in theory deposit in relatively similar bulk densities to the unpressed powder beds employed commonly in DRIFTS of loose powders, common to heterogeneous catalysts.

For the substrate upon which the films of SiO_2 would be deposited, a material was needed that might give a strong signal in DRIFTS as a reference, such that the loss of this signal might be monitored as the film thickness increased, thus giving a quantitative measure of penetration depth into the film. For this purpose, Pt/SiO_2 pellets were prepared that fit into the bed of commercially available environmental cells for DRIFTS (Harrick Sci.) such that CO probe molecule DRIFTS could be performed on film-covered pellets. CO DRIFTS has the benefit of being the same probe molecule of interest for a number of studies[41,48,49], thus excluding any wavelength-dependent changes in the penetration depth between model and realistic catalyst samples, though the results here likely hold for a range of vibrations relevant to mid-IR DRIFTS, broadly (for example, the wavelength of 1500 cm^{-1} in mid-IR DRIFTS is equivalent to only 6.6 μm, relatively comparable to the 5 μm wavelength assumed here). Additionally, the molar extinction coefficient for CO bound to metal surfaces is relatively large compared to other analytes[50], increasing the total sensitivity of the method to penetration depth. Thus, penetration depth as described here may in fact represent conservative estimates that will change based on the strength of the extinction coefficient in a given system.

A summary of the model system is shown in Figure A.2. The drop-casting procedure and the resulting pellets used in all subsequent DRIFTS studies are shown in Figure A.2a. Scanning electron microscopy (SEM) using a back-scatter detector geometry to provide elemental phase contrast was utilized to assess the general composition and state of the films, shown in Figure A.2b. It can be seen that although the films are not perfectly conformal, an appreciable coverage of the underlying Pt/SiO_2 base pellet is achieved.

Figure A.3a shows the CO DRIFTS spectra taken of base Pt/SiO_2 pellets loaded into a DRIFTS cell and exposed to 10% CO/Ar until saturation of the exposed Pt sites as a function

of drop-cast film thickness using 20-30 nm, spherical SiO_2 nanoparticles as the scattering film matrix. The primary feature, corresponding to CO bound linearly to Pt nanoparticle surfaces[51–53], drops rapidly in intensity with increasing film thickness. This can be further represented by integrating the total peak area and plotting against the film thickness as in Figure A.3b. It can

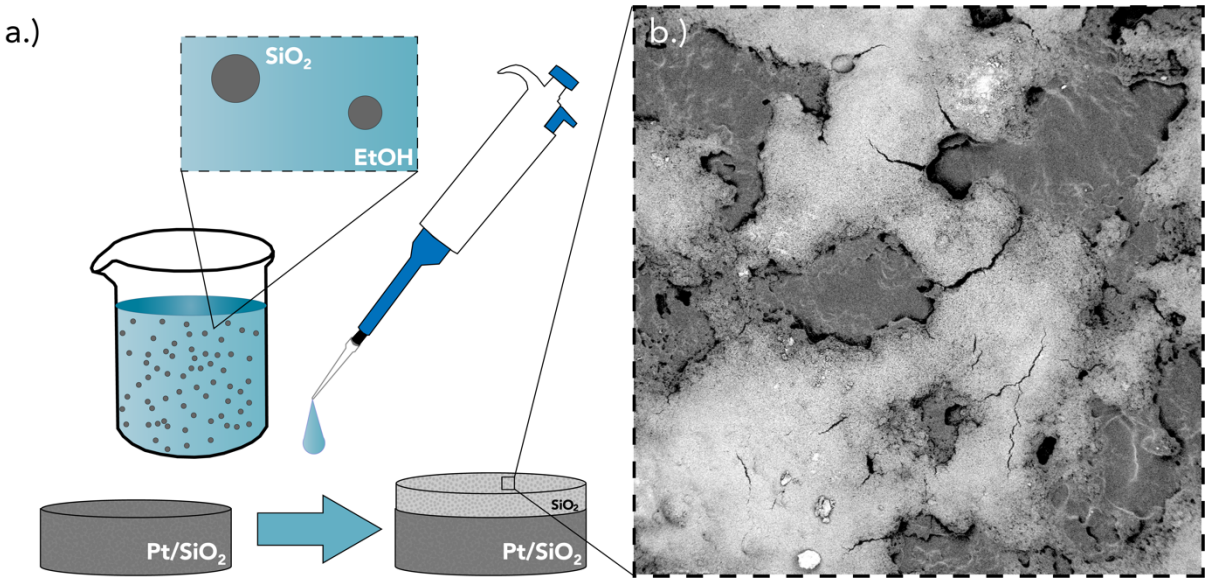

Figure A.2: a.) Synthesis of model A@Pt/SiO_2, where A represents the desired nanoparticle composition of the film, allowing for changes to both nanoparticle size and identity b.) SEM image of the 16 µm TiO_2 film (light areas) on Pt/SiO_2 pellet (dark areas), showing appreciable, but non-conformal, coverage of the underlying Pt/SiO_2 pellet.

be seen that peak area drops exponentially with thickness, as would be expected from the reflection of incident DRIFTS light by the deposited SiO_2 nanoparticle film prior to reaching the Pt/SiO_2 pellet. This confirms the ability of even the non-conformal SiO_2 film to fully attenuate the ability of DRIFTS to detect the Pt/SiO_2 surface at sufficiently thick films.

The same procedure is followed to cast films using spherical SiO_2 nanoparticles of 200 and 800 nm in diameter to assess the effect of particle size on DRIFTS penetration depth. The resulting profiles of CO peak area against film thickness shown in Figure A.4a exhibit a stark particle size effect. The decline in CO peak area is far less severe for films composed of 200 and 800 nm nanoparticles, respectively, indicating that infrared light is able to penetrate the

film and probe the surface of the Pt/SiO_2 pellet more effectively. This is consistent with the greater cross-section of Rayleigh scattering, thus promoting the penetration of incident infrared radiation farther into the catalyst bed for particle sizes greater than 15 nm. Indeed, in the case of the film composed of 800 nm SiO_2 particles, an additional effect may be the influence of Mie scattering rather than Rayleigh scattering, further providing a directional probe into the film as shown in Scheme A.1.

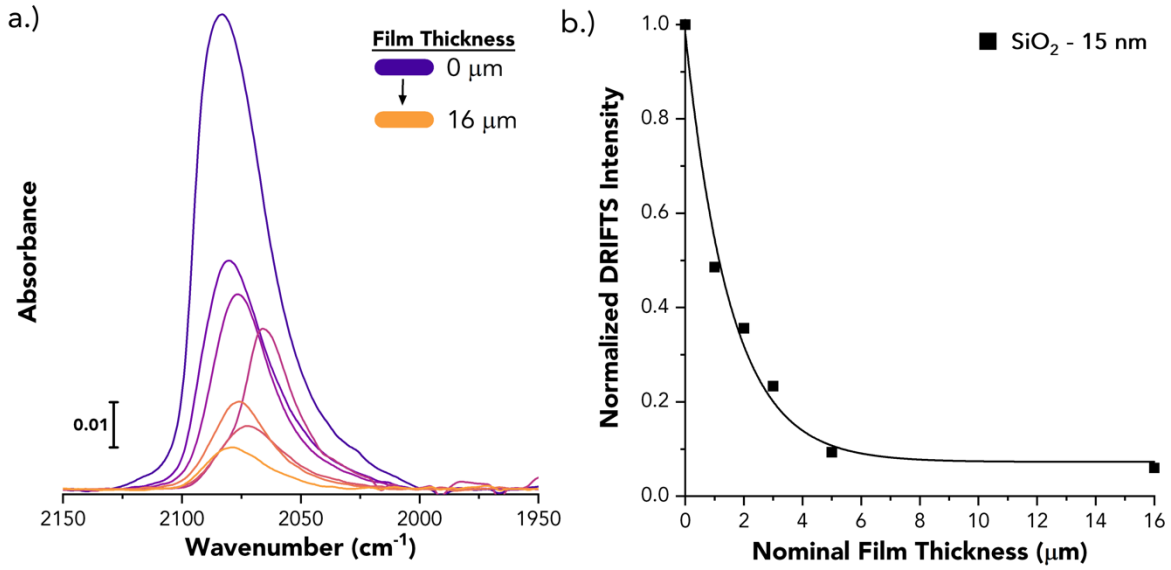

Figure A.3: a.) CO DRIFTS spectra collected for increasing film thicknesses of 20 nm SiO_2 nanoparticles atop 6wt% Pt/SiO_2 pellets. Spectra collected after exposure of the pellets to 10% CO/Ar until saturation of the surface with CO as measured by DRIFTS, typically greater than 15 minutes. b.) Integrated peak areas of the CO-Pt feature shown in a.), showing that the intensity of measured CO area decreases strongly with increasing film thickness. CO intensity is essentially negligible for films greater than 5 µm.

The effect of powder identity is also explored through the drop-casting method as shown in Figure A.4b. Particle size was kept as close as possible in these experiments, but nevertheless, there are some differences as SiO_2 powder was 20-30 nm in diameter compared to the 5 nm TiO_2 and Al_2O_3 samples. TiO_2 and Al_2O_3 samples were also not spherical, and TEM images of similar samples indicate more elongated shapes. Nevertheless, CO DRIFTS of

Pt/SiO_2 pellets decorated with these oxides show very little trend of oxide identity with penetration depth, with all oxides behaving similarly to the 20-30 nm SiO_2 nanoparticles originally studied. This is consistent with the theoretical model which suggested a small influence of particle identity (modeled solely as index of refraction changes) on the depth of penetration. One explanation for this trend could be that changes to the index of refraction are overshadowed by the stronger effect of particle size. At the limit of small particle size, the absolute differences in the Rayleigh scattering coefficient become negligible between different oxides, whereas a greater difference exists for larger particles in this model.

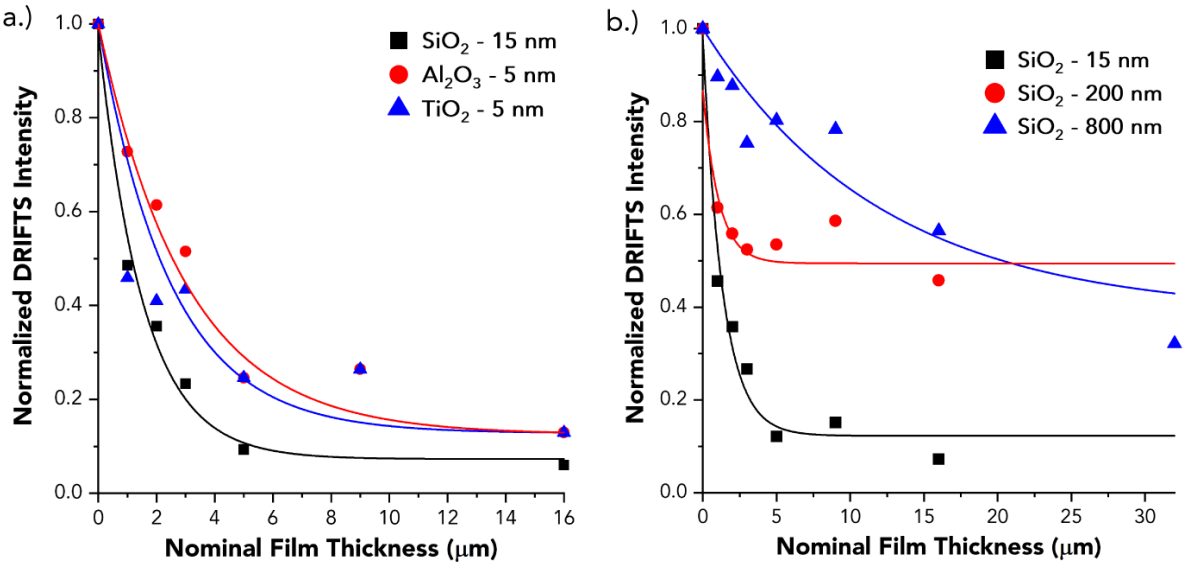

Figure A.4: a.) Integrated peak areas of the CO-Pt feature as a function of film thickness deposited on Pt/SiO_2 pellets for a range of different oxide nanoparticles representing relevant catalytic supports. b.) Integrated peak areas of the CO-Pt feature as a function of film thickness deposited on Pt/SiO_2 pellets for a range of different nanoparticle sizes for SiO_2. The results show a much stronger dependence of penetration depth as measured by the trends in CO-Pt integrated intensity on particle size than on particle identity, as predicted by the Rayleigh scattering cross-section.

A.3 Conclusions

The penetration depth of incident light in DRIFTS is an essential component in determining the quantifiability of spectral information, particularly in the case of temperature-programmed desorption techniques where re-adsorption effects can skew experimental results. To assess the influence of particle size and material identity (i.e. index of refraction) on the penetration depth in DRIFTS, a model system was developed utilizing drop-cast films of varying thickness, composition, and particle size on top of a Pt/SiO_2 surface to elucidate the influence of each characteristic on the penetration of incident infrared radiation using CO probe molecule DRIFTS. The model system shows that there is a significant influence of particle size on the penetration depth of light in DRIFTS, with small nanoparticles around 20 nm in size significantly attenuating the DRIFTS radiation, resulting in a minimal penetration depth measured by CO DRIFTS of ~ 5 μm. Importantly, this value is far smaller than the expected length of re-adsorption for CO temperature-programmed desorption (TPD), suggesting that CO DRIFTS may be an ideal method for the measurement of CO binding energy through TPD approaches in the case of small support nanoparticles. The model system shows that the penetration depth of DRIFTS increases with increasing particle size, as predicted from the theoretical Rayleigh scattering cross-section dependence on particle size. However, there appears to be a weaker influence of particle identity, or index of refraction, on the nature of light scattering here. Although a weaker influence was expected using the theoretical Rayleigh scattering cross-section alone, the lack of experimentally measurable effect of particle identity may stem from differences in the index of refraction for nanoparticles compared to the bulk components, shape effects, or differences in particle size distribution. Overall, it is shown that for sub-20 nm nanoparticles, the

penetration depth of DRIFTS is smaller than has been previously reported, underscoring the importance of considering particle size when designing DRIFTS experiments.

A.4 Methods

A.4.1 Film@Pellet Model System

The base 6wt% Pt/SiO_2 catalyst was described as was done in other chapters of this dissertation, described again briefly here. The desired amount of 15-20 nm spherical, non-porous SiO_2 (USNano) was dispersed under vigorous stirring in a volume of deionized water (Sigma) that had been adjusted to pH ~10 through the addition of NH_4OH (Sigma). To this, a 5 mL aqueous solution of the desired amount of tetraamineplatinum nitrate (TAPN) was added rapidly to reach the desired weight loading, in this case, 6% by mass of the initial silica. The combined SiO_2 and TAPN solution was allowed to stir without heating for 30 minutes to ensure homogeneity before the temperature was increased to 80˚C. Stirring was continued until all of the solution had evaporated. The resulting powder was collected and placed in an oven overnight at 110˚C to dry. Final catalysts were prepared by calcining the dry powder under 50 sccm dry air (Airgas) at 600˚C for 6 hours in a tube furnace.

To create pellets from the synthesized 6% Pt/SiO_2 catalysts, the prepared catalyst was first pressed and sieved between 100 and 250 mesh. To this, 50% by mass of hydroxypropylcellulose (Sigma) was added to act as a binder. The catalyst/cellulose mixture was then ground by hand using a mortar and pestle to distribute the cellulose well amongst the catalyst powder. Attempts to press catalyst pellets in the absence of a binder resulted in structurally weak pellets that often flaked and otherwise degraded during handling, which was undesirable for this model system. The prepared catalyst/cellulose mixture was then pressed

into pellets in a 7 mm diameter die under a Carver press at 4 metric tons of pressure. The resulting pellets were cylindrical and structurally sound, with diameters of 7 mm and heights of ~3 mm.

For the drop-casting of films onto the pellets, anhydrous ethanol (Sigma) was used as the solvent carrier for nanoparticles. Typically, 5 mL of anhydrous ethanol was placed in a vial, to which a known mass of nanoparticles was added, depending on the desired film composition and thickness. Nanoparticle concentrations were calculated by dividing the total surface area provided by the cylindrical, 7 mm pellet by the projected 2-D surface area of the nanoparticles of a given diameter. The mass of nanoparticles contained in this ideal film was then calculated as follows:

$$M_{Particle} = \rho_{Bulk} V_{Particle} N_{Particle}$$

Where ρ_{Bulk} is the bulk density of the nanoparticles being used, $V_{Particle}$ is the spherical volume of the nanoparticles based on their diameter, and $N_{Particle}$ is the number of particles in a monolayer calculated as described above. This obviously assumes a packing density that cannot be realistically achieved but gives a first approximation of the powder concentrations that were needed for a given film. Powder thicknesses were similarly approximated by dividing the desired thickness by the diameter of the nanoparticles themselves, providing an approximation for the number of monolayers (ML) of nanoparticles needed to form films of the desired thickness. For film deposition, a single 20 uL drop of nanoparticle suspension was used. The final concentration of nanoparticles in the ethanol solution can then be described as:

$$C_{NP} = \frac{M_{Particle}}{V_{Drop}} ML$$

Films were drop-cast by placing the pellets on hot plates under gentle heating to assist in the rapid evaporation of solvent, which has been shown previously to assist in the formation of conformal films free from the "coffee-stain" effect, where transport effects during solvent evaporation can cause accumulation of suspended species at the edges of the substrate.

A.4.2 CO DRIFTS: Film Models

For all spectra described in this section, infrared measurements were carried out on a Nicolet iS50R FT-IR spectrometer equipped with a Praying Mantis Diffuse Reflection Accessory (Harrick Scientific) and a High-Temperature Reaction Chamber (Harrick Scientific) fitted with a thermocouple in the catalyst bed. Ar (99.995%), O_2 (99.50%), 10% CO/Ar, and 10% H_2/Ar were purchased from Airgas and used as received.

For CO DRIFTS measurements taken of the film model pellets, pellets were first loaded into the sample cup of the Harrick reaction chamber and flushed with Ar at 50 sccm for 30 minutes. After this time, a background was collected without further pre-treatment. Though *in situ* reduction is a typical step performed elsewhere in this dissertation, the presence of the cellulose binder in the pellet formulations prevented the heating of the pellet due to concerns about cellulose degradation and possible contamination of the Pt nanoparticle surface. As shown, CO DRIFTS spectra can be successfully collected in the absence of a reduction step. Since structural information about the Pt is not being derived from this study, but rather, the

CO-Pt signal is only acting as a reporter on the penetration depth of DRIFTS analysis, the reduction step is not an integral component.

After purging in Ar to remove air from the high-temperature chamber, pellets were exposed to 10% CO/Ar until saturation coverage was achieved, monitored by the continuous collection of DRIFTS spectra during this time. Saturation times were typically greater than 15 minutes but sometimes extended to as long as 30 minutes in the case of pellets with more substantial film thicknesses. This difference in saturation time is attributed to the diffusion of CO through the porous film to adsorb on Pt nanoparticles, highlighting that the presence of the film does not entirely inhibit the adsorption of CO to the pellet surface. After saturation coverage was reached, the gas-phase CO signal was purged by Ar and a final spectrum was collected of the pellet.

A.5 References

1. Chakrabarti, A. *et al.* A decade plus of operando spectroscopy studies. *Catal Today* **283**, 27–53 (2017).
2. Bartholomew, C. H., Farrauto, R. J., Bartholomew, C. H. & Farrauto, R. J. *CATALYST CHARACTERIZATION AND SELECTION. FUNDAMENTALS OF INDUSTRIAL CATALYTIC PROCESSES, 2ND EDITION* (2006). doi:10.1002/9780471730071.
3. Leofanti, G. *et al.* Catalyst characterization: Characterization techniques. *Catal Today* **34**, 307–327 (1997).
4. Stavitski, E. & Weckhuysen, B. M. Infrared and Raman imaging of heterogeneous catalysts. *Chem Soc Rev* **39**, 4615–4625 (2010).
5. Zaera, F. Infrared Absorption Spectroscopy of Adsorbed CO: New Applications in Nanocatalysis for an Old Approach. *ChemCatChem* **4**, 1525–1533 (2012).
6. Armaroli, T., Bécue, T. & Gautier, S. Diffuse reflection infrared spectroscopy (DRIFTS):: Application to the *in situ* analysis of catalysts. *OIL & GAS SCIENCE AND TECHNOLOGY-REVUE D IFP ENERGIES NOUVELLES* **59**, 215–237 (2004).
7. BLITZ, J. P. & AUGUSTINE, S. M. CHARACTERIZATION OF HETEROGENEOUS CATALYSTS BY FT-IR DIFFUSE-REFLECTANCE SPECTROSCOPY. *SPECTROSCOPY* **9**, 28–34 (1994).
8. RASBAND, P. B. & HECKER, W. C. CATALYST CHARACTERIZATION USING QUANTITATIVE FTIR - CO ON SUPPORTED RH. *J Catal* **139**, 551–560 (1993).

9. Zaera, F. New advances in the use of infrared absorption spectroscopy for the characterization of heterogeneous catalytic reactions. *Chem Soc Rev* **43**, 7624–7663 (2014).
10. Guerrero-Pérez, M. O. & Patience, G. S. Experimental methods in chemical engineering: Fourier transform infrared spectroscopy-FTIR. *CANADIAN JOURNAL OF CHEMICAL ENGINEERING* **98**, 25–33 (2020).
11. Bürgi, T. & Baiker, A. Attenuated total reflection infrared spectroscopy of solid catalysts functioning in the presence of liquid-phase reactants. in *ADVANCES IN CATALYSIS, VOL 50* (eds. Gates, B. C. & Knozinger, H.) vol. 50 227–283 (2006).
12. Andanson, J. M. & Baiker, A. Exploring catalytic solid/liquid interfaces by *in situ* attenuated total reflection infrared spectroscopy. *Chem Soc Rev* **39**, 4571–4584 (2010).
13. Hamminga, G. M., Mul, G. & Moulijn, J. A. Reaction kinetics and intermediate determination of solid acid catalysed liquid-phase hydrolysis reactions:: A real-time *in situ* ATR FT-IR study. *Catal Letters* **109**, 199–206 (2006).
14. Mojet, B. L., Ebbesen, S. D. & Lefferts, L. Light at the interface: the potential of attenuated total reflection infrared spectroscopy for understanding heterogeneous catalysis in water. *Chem Soc Rev* **39**, 4643–4655 (2010).
15. Jentoft, F. C., Kröhnert, J., Subbotina, I. R. & Kazansky, V. B. Quantitative Analysis of IR Intensities of Alkanes Adsorbed on Solid Acid Catalysts. *JOURNAL OF PHYSICAL CHEMISTRY C* **117**, 5873–5881 (2013).
16. Couble, J., Gravejat, P., Gaillard, F. & Bianchi, D. Quantitative analysis of infrared spectra of adsorbed species using transmission and diffuse reflectance modes Case study: Heats of adsorption of CO on TiO_2 and CuO/Al_2O_3. *APPLIED CATALYSIS A-GENERAL* **371**, 99–107 (2009).
17. Roedel, E., Urakawa, A., Kureti, S. & Baiker, A. On the local sensitivity of different IR techniques: Ba species relevant in NO_x storage-reduction. *PHYSICAL CHEMISTRY CHEMICAL PHYSICS* **10**, 6190–6198 (2008).
18. Drochner, A., Fehlings, M., Krauss, K. & Vogel, H. A new DRIFTS cell for the *in-situ* investigation of heterogeneously catalyzed reactions. *Chem Eng Technol* **23**, 319-+ (2000).
19. Ma, X. Y., Zhang, W. Y., Ye, K., Jiang, K. & Cai, W. B. Electrolyte-Layer-Tunable ATR-SEIRAS for Simultaneous Detection of Adsorbed and Dissolved Species in Electrochemistry. *Anal Chem* **94**, 11337–11344 (2022).
20. Kortum, G., Braun, W. & Herzog, G. Principles and Techniques of Diffuse-Reflectance Spectroscopy. *Angewandte Chemie* **2**, 333–404 (1963).
21. Torrent, J. & Barrón, V. Diffuse Reflectance Spectroscopy. in *Methods of Soil Analysis. Part 5: Mineralogical Methods* 367–385 (2008).
22. Yang, P. W. & Mantsch, H. H. Diffuse reflectance infrared spectrometry: characteristics of the diffuse and specular components. *Appl Opt* **26**, 326–330 (1987).
23. Zhou, Y., Doronkin, D. E., Chen, M. L., Wei, S. Q. & Grunwaldt, J. D. Interplay of Pt and Crystal Facets of TiO_2: CO Oxidation Activity and *Operando* XAS/DRIFTS Studies. *ACS Catal* **6**, 7799–7809 (2016).
24. Bobadilla, L. F., Santos, J. L., Ivanova, S., Odriozola, J. A. & Urakawa, A. Unravelling the Role of Oxygen Vacancies in the Mechanism of the Reverse Water-Gas Shift Reaction by *Operando* DRIFTS and Ultraviolet-Visible Spectroscopy. *ACS Catal* **8**, 7455–7467 (2018).

25. Gamarra, D. & Martínez-Arias, A. Preferential oxidation of CO in rich H_2 over CuO/CeO_2: *Operando*-DRIFTS analysis of deactivating effect of CO_2 and H_2O. *J Catal* **263**, 189–195 (2009).
26. Sirita, J., Phanichphant, S. & Meunier, F. C. Quantitative analysis of adsorbate concentrations by diffuse reflectance FT-IR. *Anal Chem* **79**, 3912–3918 (2007).
27. Bredy, P., Fine, L., Farrusseng, D., Schuurman, Y. & Meunier, F. C. Evolution of sample optical pathlength during diffuse reflectance FT-IR analyses. *Catal Today* **424**, (2023).
28. Kale, M. J. & Christopher, P. Utilizing Quantitative in Situ FTIR Spectroscopy to Identify Well-Coordinated Pt Atoms as the Active Site for CO Oxidation on Al2O3-Supported Pt Catalysts. *ACS Catal* **6**, 5599–5609 (2016).
29. Marlowe, J., Ford, P. C., Abu-Omar, M. M. & Christopher, P. Structure sensitivity in Pt-catalyzed hydrodeoxygenation of multi-oxygenated lignol model compounds. *Catal Sci Technol* **13**, 5662–5678 (2023).
30. Hopper, J. T., Ma, R., Rawlings, J. B., Ford, P. C. & Abu-Omar, M. M. Markedly Improved Catalytic Dehydration of Sorbitol to Isosorbide by Sol-Gel Sulfated Zirconia: A Quantitative Structure-Reactivity Study. *ACS Catal* **13**, 10137–10152 (2023).
31. Bredy, P., Fine, L., Farrusseng, D., Schuurman, Y. & Meunier, F. C. Evolution of sample optical pathlength during diffuse reflectance FT-IR analyses. *Catal Today* **424**, (2023).
32. Choe, E. K., Lee, M., Park, K. S. & Chung, C. Characterization of cotton fabric scouring by Fourier transform-infrared attenuated total reflectance spectroscopy, gas chromatography-mass spectrometry and water absorption measurements. *TEXTILE RESEARCH JOURNAL* **89**, 2305–2315 (2019).
33. Pearl, M. R., Brooke, H., McCutcheon, J. N., Morgan, S. L. & Myrick, M. L. Coating Effects on Mid-Infrared Reflection Spectra of Fabrics. *Appl Spectrosc* **65**, 876–884 (2011).
34. Pálinkó, I., Sipos, P., Berkesi, O. & Varga, G. Distinguishing Anionic Species That Are Intercalated in Layered Double Hydroxides from Those Bound to Their Surface: A Comparative IR Study. *JOURNAL OF PHYSICAL CHEMISTRY C* **126**, 15254–15262 (2022).
35. ZAVARIN, E., JONES, S. J. & COOL, L. G. ANALYSIS OF SOLID WOOD SURFACES BY DIFFUSE REFLECTANCE INFRARED FOURIER-TRANSFORM (DRIFT) SPECTROSCOPY. *JOURNAL OF WOOD CHEMISTRY AND TECHNOLOGY* **10**, 495–513 (1990).
36. Olinger, J. M. & Griffiths, P. R. Quantitative effects of an absorbing matrix on near infrared diffuse reflectance spectra. *Anal Chem* **60**, 2427–2435 (1988).
37. Alcaraz de la Osa, R., Iparragirre, I., Ortiz, D. & Saiz, J. M. The extended Kubelka–Munk theory and its application to spectroscopy. *ChemTexts* **6**, (2020).
38. Christy, A. A., Kvalheim, O. M. & Velapoldi, R. A. Quantitative analysis in diffuse reflectance spectrometry: A modified Kubelka-Munk equation. *Vib Spectrosc* **9**, 19–27 (1995).
39. Myrick, M. L. *et al.* The kubelka-munk diffuse reflectance formula revisited. *Appl Spectrosc Rev* **46**, 140–165 (2011).
40. DeRita, L. *et al.* Catalyst Architecture for Stable Single Atom Dispersion Enables Site-Specific Spectroscopic and Reactivity Measurements of CO Adsorbed to Pt Atoms,

Oxidized Pt Clusters, and Metallic Pt Clusters on TiO2. *J Am Chem Soc* **139**, 14150–14165 (2017).
41. Zakem, G., Ro, I., Finzel, J. & Christopher, P. Support functionalization as an approach for modifying activation entropies of catalytic reactions on atomically dispersed metal sites. *J Catal* **404**, 883–896 (2021).
42. Gorte, R. J. *Design Parameters for Temperature Programmed Desorption from Porous Catalyst9*. *JOURNAL OF CATALYSIS* vol. 75 (1982).
43. Mondelli, C. *et al.* An operando DRIFTS-MS study on model Ce0.5Zr0.5O 2 redox catalyst: A critical evaluation of DRIFTS and MS data on CO abatement reaction. in *Catalysis Today* vol. 113 81–86 (2006).
44. Lockwood, D. J. Rayleigh and Mie Scattering. *Encyclopedia of Color Science and Technology* 1097–1136 (2016) doi:10.1007/978-1-4419-8071-7.
45. Zhao, C. *et al.* Formation of uniform reduced graphene oxide films on modified PET substrates using drop-casting method. *Particuology* **17**, 66–73 (2014).
46. Zuo, C. & Ding, L. Drop-Casting to Make Efficient Perovskite Solar Cells under High Humidity. *Angewandte Chemie - International Edition* **60**, 11242–11246 (2021).
47. Kaliyaraj Selva Kumar, A., Zhang, Y., Li, D. & Compton, R. G. A mini-review: How reliable is the drop casting technique? *Electrochemistry Communications* vol. 121 Preprint at https://doi.org/10.1016/j.elecom.2020.106867 (2020).
48. Asokan, C., Xu, M., Dai, S., Pan, X. & Christopher, P. Synthesis of Atomically Dispersed Rh Catalysts on Oxide Supports via Strong Electrostatic Adsorption and Characterization by Cryogenic Infrared Spectroscopy. *The Journal of Physical Chemistry C* **126**, 18704–18715 (2022).
49. Thang, H. V., Pacchioni, G., DeRita, L. & Christopher, P. Nature of stable single atom Pt catalysts dispersed on anatase TiO2. *J Catal* **367**, 104–114 (2018).
50. WAKABAYASHI, F., KONDO, J. N., DOMEN, K. & HIROSE, C. DIRECT COMPARISON OF N-2 AND CO AS IR-SPECTROSCOPIC PROBES OF ACID SITES IN H-ZSM-5 ZEOLITE. *JOURNAL OF PHYSICAL CHEMISTRY* **99**, 10573–10580 (1995).
51. Kappers, M. J. & Van Der Maas, J. H. Correlation between CO frequency and Pt coordination number. A DRIFT study on supported Pt catalysts. *Catal Letters* **10**, 365–374 (1991).
52. Meunier, F. C., Elgayyar, T., Dembélé, K. & Kaper, H. Stability of Pt-Adsorbed CO on Catalysts for Room Temperature-Oxidation of CO. *Catalysts* **12**, 1–12 (2022).
53. Podkolzin, S. G., Shen, J., De Pablo, J. J. & Dumesic, J. A. Equilibrated Adsorption of CO on Silica-Supported Pt Catalysts. *Journal of Physical Chemistry B* **104**, 4169–4180 (2000).